UAV-Enabled Wireless Power Transfer and Communications

by

Hua Yan

Thesis submitted to the University of Warwick

for the degree of

Doctor of Philosophy

School of Engineering

September 2021

THE UNIVERSITY OF WARWICK

Contents

Acknowledgments

I would like to give my greatest gratitude to those who give me supports for completing this thesis.

First and foremost, As a student of Joint Ph.D. Training Program offered by the University of Warwick (UoW) and Southern University of Science and Technology (SUSTech), I would like to express my heartfelt gratitude to my supervisors, Prof. Yunfei Chen at UoW and Prof. Shuang-Hua Yang at SUSTech, for their great support, careful guidance, insightful suggestions and ongoing encouragement over many years as well as to UoW and SUSTech for their support for my studies in both universities. Especially, I would like to thank SUSTech for awarding me the full scholarship, which has made my Ph.D. study in UK possible.

Then, I would like to thank members of the two research groups led by Prof. Shuang-Hua Yang and Prof. Yunfei Chen, respectively, for their discussion, encouragement and friendship. They are Dr. Yulong Ding, Dr. Jie Jiang, Miss Jing Wu, Miss Yujue Zhou, Mr. Zezheng Feng, Mr. Chenguang Liu, Mr. Youjie Ye, Miss Xueyun Gu, Mr. Fengyun Zhang, Mr. Shengguang Hong, Mr. Daniel Perez Fiadzeawu, Mr. Pengjie Liu, Mr. Zhihao Dai, Mr. Yuhuan Liu, Miss Lihua Cai, Mr. Zhicong Sun, Mr. Hao Li, Mr. Yuxin Zhou and Mr. Kai Liu, etc. I would like to give my special thanks to Dr. Yulong Ding for his valuable guidance

on both engineering projects and academia. The time I spent at both universities is one of the most precious memories in my schooldays.

Moreover, my thanks also go to Dr. Tardi Tjahjadi and Prof. Michail (Michalis) Matthaiou for being examiners of my Ph.D. viva. Besides, it is lucky to meet my girl friend, Lisa Huang, during my Ph.D. study. I would like to thank her for standing together with me through storm and stress.

Last but not least, I would like to express my deepest gratitude to my beloved parents for their encouragement and endless love. I am very grateful for their understanding and continuous supports. I would like to dedicate this thesis to them.

Declarations

This thesis is submitted in partial fulfillment for the degree of Doctor of Philosophy under the regulations set out by the Graduate School at the University of Warwick. This thesis is solely composed of research completed by Hua Yan, except where stated, under the supervision of Prof. Yunfei Chen and Prof. Shuang-Hua Yang between the dates of January 2018 and September 2021. This thesis has not previously been presented in identical or similar form to any other examination board.

Hua Yan

September, 2021

Abstract

Unmanned aerial vehicles (UAVs) have been considered as a promising technology in both military and civil communications. This thesis studies UAV-enabled wireless communications considering UAV propulsion consumption which has not been well studied in the existing literature.

To this end, first, wireless power transfer (WPT) efficiency in UAV-enabled wireless powered communication networks (WPCNs) is studied, where a rotary-wing UAV is dispatched as an energy carrier to charge the remote sensors after it is charged by a charging station such as a base station (BS). In the study, the propulsion consumption for different UAV manoeuvres has been taken into account. Two schemes for UAV-enabled WPT have been proposed and compared with the conventional scheme without using a UAV. By solving the energy equations, a distance threshold beyond which the new schemes show superiority over the conventional scheme is derived.

Then, in order to maximize the sum-energy received by all sensors, the optimal strategy for UAV deployment is studied. In this study, the UAV power consumption, the radio frequency to direct current (RF-to-DC) energy conversion efficiency and the BS charging process have all been taken into account. Both

one-dimensional (1D) and two-dimensional (2D) topologies of sensors have been considered. By maximizing the sum-energy received by all sensors, the optimal locations for the UAV have been derived.

Next, the use of UAVs in a WPCN as an energy transmitter and a data collector is investigated. In the study, the UAV is first charged from a BS before it flies to the sensors for data collection. Upon arrival, the UAV first charges the sensors via WPT in the down-link, followed by data transmission from the sensors in the up-link. After that, the UAV flies back to the BS to offload data to the BS. Both distance-dependent path loss and small-scale fading are considered. To maximize the amount of data offloaded to the BS given a fixed total time, the optimal time allocation in different phases has been derived.

In the aforementioned studies, we focus on the full process of UAV-enabled WPCN where wireless charging from the BS to the UAV and the UAV return trip have been considered. To maximize the available energy when the UAV arrives at destinations, the optimum battery weight in UAV-enabled wireless communication networks is studied. Numerical results show that both vertical flight and horizontal flight speeds and the gross weight of the UAV have a great impact on the optimal battery weight.

Motivated by studying the optimal battery weight, it is found that accurate and convenient energy consumption models (ECM) for rotary-wing UAVs are also, or even much more important for UAV-enabled wireless communications because energy is the guarantee of UAV operation. As a result, a simple and easy-to-use model with closed-form expression as a function of the initial velocity, acceleration and time duration is further studied. Numerical results show the validity and reliability of the new derived ECM.

List of Publications

Journal Papers

[J1] **Hua Yan**, Yunfei Chen and Shuang-Hua Yang, "Analysis of energy transfer efficiency in UAV-enabled wireless networks", *Physical Communication*, vol. 37, Dec. 2019.

[J2] **Hua Yan**, Yunfei Chen and Shuang-Hua Yang, "UAV-Enabled Wireless Power Transfer with Base Station Charging and UAV Power Consumption", *IEEE Transactions on Vehicular Technology*, vol. 69, no. 11, pp. 12883–12896, Nov. 2020.

[J3] **Hua Yan**, Yunfei Chen and Shuang-Hua Yang, "Time Allocation and Optimization in UAV-enabled Wireless Powered Communication Networks", *IEEE Transactions on Green Communications and Networking.* Doi: 10.1109/TGCN.2021.3117312.

[J4] **Hua Yan**, Shuang-Hua Yang, Yunfei Chen and Suhaib A. Fahmy, "Optimum Battery Weight for Maximizing Available Energy in UAV-Enabled Wireless Communications", *IEEE Wireless Communications Letters*, vol. 10, no. 7, pp. 1410-1413, July 2021.

[J5] **Hua Yan**, Yunfei Chen and Shuang-Hua Yang, "New Energy Consumption Model for Rotary-Wing UAV Propulsion", *IEEE Wireless Communications Letters*, vol. 10, no. 9, pp. 2009-2012, Sept. 2021.

List of Figures

List of Tables

Abbreviations

1D One-dimensional

1G The first generation

2D Two-dimensional

5G The fifth generation

6G The sixth generation

A2G Air-to-ground

AF Amplify-and-forward

AWGN Additive white Gaussian noise

B5G Beyond the fifth generation

BLE Bluetooth low energy

BS Base station

CMA Cyclical multiple access

DC Direct current

DL Downlink

ECM Energy consumption model

eMTC Enhanced machine type communication

EPS Electric propulsion systems

ER Energy receiver

FD full-duplex

FSPL Free space path loss

G2A Ground-to-air

GDRDB Global drone regulations database

HAP High altitude platform

IoT Internet of Things

LAP Low altitude platform

LCAC Load-carry-and-charge

LCAD Load-carry-and-deliver

LFAC Load-ferry-and-charge

LFCAO Load-ferry-charge-and-offloading

LiPo Lithium polymer

LoRa Long Range

LoS Line-of-sight

LPWAN Lower power wireless area network

MEC Mobile edge computing

MIMO Multiple-input multiple-output

NB-IoT Narrow band-Internet of Things

NFC Near-field communication

NLoS Non-line-of-sight

PDF Probability density function

RF Radio frequency

RF-to-DC Radio frequency to direct current

SAR Search and rescue

SNR Signal-to-noise ratio

SWIPT Simultaneous wireless information and power transfer

TDMA Time-division multiple access

TEM Total energy minimization

TWR Thrust-to-weight

UAV Unmanned aerial vehicle

UGV Unmanned ground vehicle

UL Uplink

UWB Ultra wide band

WET Wireless energy transfer

Wi-Fi Wireless fidelity

WIT Wireless information transfer

WPCN Wireless powered communication network

WPT Wireless power transfer

WSN Wireless sensor network

Important Symbols

$\arg\max(\cdot)$ Inverse function of maximum

$\arg\text{tag}(\cdot)$ Inverse function of tangent

$\max(\cdot)$ Maximum function

$\min(\cdot)$ Minimum function

$\lg\{\cdot\}$ The logarithm to the base 10

$\text{random}(\cdot,\cdot,\cdot)$ Random number function obeying a certain distribution

$E(\cdot)$ Expectation operator

$I_0(\cdot)$ The zero-th order modified Bessel function of the first type

K Rician factor

κ_v Visibility

λ Wavelength

$O(\cdot)$ Complexity operator

P_ϵ The minimum power

ρ_e Battery energy density

$\mathcal{CN}(\cdot,\cdot)$ Circularly-symmetric complex normal distribution

$\|\cdot\|$ Absolute value operator

$\lceil\cdot\rceil$ Ceiling function

$\lfloor\cdot\rfloor$ Floor function

Chapter 1

Introduction

1.1 Background

Over the past few decades, unmanned aerial vehicles (UAVs), well known as drones, have seen a growing interest as enablers in many public, military and civil applications [1–3]. Due to their advantages of flexibility, mobility, rapid deployment and high adaptability, UAVs have been widely studied by researchers from a range of areas in both academia and industry. In general, typical examples include, but not limited to, search and rescue (SAR), wireless coverage, mobile relay, aerial base station (BS), remote sensing and monitoring, emergency response, smart agriculture and delivery of goods, etc. [3–5]. Recently, UAVs have been presenting a promising technology in wireless networks, i.e., the fifth-generation (5G) and beyond 5G (B5G) communication networks, Internet of Things (IoTs) and the sixth-generation (6G) communication networks [6–12]. In this section, the basic background of UAV-enabled wireless communications, UAV-enabled wireless powered communication networks (WPCNs) are presented, followed by discussions of

the potential challenges.

1.1.1 UAV-enabled Wireless Communications

Throughout the evolution history from the first-generation (1G) to 5G and B5G technology, it is a process of continuously meeting users' experiences and requirements including higher data rate, lower latency, more connections and higher reliability, etc. As supplements and extensions of 5G and B5G, UAV-enabled wireless communications have been playing an important role due to the fact that deploying more 5G BSs will require higher costs. For example, the UAV can be deployed on-demand as an aerial BS to provide service where needed. In particular, for areas where communications infrastructure is damaged because of natural disaster, UAV can be deployed to provide communication service with fast response to the emergency. A typical example is that a Wing Loong-2H UAV was deployed to successfully restore telecommunications services [13–15] in China's Henan Province in July 2021, where an exceptionally heavy rainfall inundated the city Zhengzhou, leaving communications infrastructure damaged and people without access to the network. Besides, UAVs are also the best candidates to operate in environments which are dangerous or hard to reach [9], and in cases where the communication signals are blocked or inaccessible due to obstacles such as mountains.

Under such circumstances, plenty of researchers from both academia and industry had started their technical research in theory and practice. According to [4], three typical application scenarios for UAVs in wireless communications—Coverage, relaying and information dissemination/data collection have been highlighted, and there have been quite a few works on optimization in UAV-enabled Wireless communications [16–22]. With further research and extensive application

exploration. New opportunities and challenges coexist.

1.1.2 UAV-enabled Wireless Powered Communication Networks

Similar to UAV technologies, IoTs have also been playing an extremely important role in 5G and B5G wireless communication networks and thus have underpinned a large number of applications including smart agriculture, environment monitoring, and geological explorer, etc. In these applications, IoT end devices, well known as sensor nodes, have been deployed for wireless sensing, including collecting data and communicating with other sensor nodes or IoT gateway. Take smart agriculture as an example, sensors are deployed to collect environment data such as temperature and humidity and then transmit these data to the IoT gateway for further computing and decision-making. Here, another concept worth mentioning is wireless sensor network (WSN). A WSN is by definition a wireless network composed of a set of sensors, and it is usually deployed for wireless sensing. In this field, data collection, data transmission and data processing have been widely studied. Besides, different wireless technologies such as ZigBee, wireless fidelity(Wi-Fi), blue-tooth low energy (BLE), near field communication (NFC), ultra wide band (UWB), etc. have also been studied for communications among sensors. Nevertheless, sensors are generally energy-limited nodes due to their small size and limited battery capacity. As a result, periodically changing battery is needed. This is not an efficient way and thus lower power wide area network (LPWAN) has been proposed, where different wireless technologies such as long range (LoRa), narrow band IoT (NB-IoT), sigfox and enhanced machine-type communication (eMTC), etc. have been widely used in LPWAN applications. In LPWAN applications, the lifespan of batteries can reach ten years, which is considered to be a more efficient

way than changing battery frequently. However, the data rate is low due to long distance transmission compared with Wi-Fi or UWB, etc.

To overcome the dilemma of unbalanced battery life and data rate, WPCNs [23] have been studied, where radio frequency (RF) based wireless energy transfer (WET) has been regarded as a promising solution. Thanks to the flexibility and high adaptability of UAVs, there has been recently an increasing interest in studying UAV-enabled WPCN [24], [25], where the UAV is deployed as a flying charger to power sensors wirelessly. Besides, UAVs, in fact, have also been widely studied as flying gateways [26], mobile BSs or relays [18–20] and data collectors [25,27–29].

1.2 Research Motivation and Objectives

1.2.1 Motivation

Although UAVs have been widely studied as enablers in both military and civil applications, and also have been providing promising solutions for future wireless networks, several challenges in this field remain. This thesis mainly focuses on UAV-enabled WPCNs considering these challenges motivated by the following issues.

- First of all, in the earlier studies, there were quite a few works on UAV-enabled wireless communications, but UAVs were usually assumed to have inexhaustible energy for convenience. However, this is unrealistic in practical applications and thus, the UAV onboard energy should be carefully considered. Generally speaking, the energy consumption of the UAV mainly comes from two parts. The first part is from communication-related en-

ergy consumption, such as data receiving and transmitting. The second part comes from manoeuvre-related consumption, such as hovering, acceleration or deceleration. In practice, the manoeuvre-related energy is usually much larger than the energy required for communications [30]. Therefore, communication-related energy is usually ignored in the study [30]. Instead, manoeuvre-related energy cannot be ignored and must be considered. In particular, for the applications where the UAV trajectory optimization is considered, more propulsion energy is needed. As a result, it is necessary to consider the power consumption of the UAV for various manoeuvres in these applications, because it affects the operational efficiency of the UAV.

- Secondly, the UAV is also an energy-limited node that does not generate energy itself. Hence, it needs to be charged by a charging station wirelessly or with wire before being dispatched. However, this issue has been largely ignored by many existing works. Although renewable energy harvesting from solar energy or wind energy is a low-cost alternative and has been studied in [31], the amount of energy harvested is uncertain. As a result, it may not be enough as the main energy source of the UAV, instead as a supplement it could be a good choice. Compared with wired charging, wireless charging shows many advantages. For example, wireless charging can charge different brands of UAVs on demand, while wired charging needs the specific charger matched with brand [32]. At this point, wireless charging has better user experience. Another example is wireless charging provides much greater freedom of movement and supports simultaneous charging of multiple UAVs [33]. Considering wireless charging for UAVs has been regarded as a promising solution [34] and has achieved some initial successes in industry [35], the research field of UAV-enabled WPCNs will be further expanded.

- Then, in earlier researches on UAV-enabled wireless power transfer (WPT), radio frequency to direct current (RF-to-DC) conversion efficiency has been ignored [36–39] by assuming perfect conversion at the energy receiver. However, this is not practical in real applications. Afterwards, some of researchers started to consider RF-to-DC conversion efficiency, but only a linear conversion model [40] was simply considered in earlier researches [24, 41–47]. According to [48], the RF-to-DC conversion efficiency actually depends on the input RF power, which means the RF-to-DC conversion efficiency is non-linear. Therefore, it is necessary and important to bridge this gap, whether for the wireless charging from the charging station to the UAV, or WPT from the UAV to the sensors.

- Last but not least, the purpose of collecting data from sensors is to offload them to the BS for further computing or decision making. In particular, for monitoring and data sampling applications, data processing is as important as data collecting, or even more important. Hence, data offloading at the BS is also an important process that ignored in existing works. To the best of the author's knowledge, work on UAV-enabled WPCNs considering UAV wireless charging, UAV propulsion consumption and data offloading has not been studied yet.

1.2.2 Objectives

The main objective of this thesis is to study the performance of UAV-enabled WPCNs considering the UAV energy consumption, charging, discharging and round-trip flight, including the UAV-enabled WPT efficiency, the optimal UAV locations and the optimal time allocation, etc. The specific research objectives are

listed as follows.

1. Taking the conventional long distance direct WPT as a baseline, we first need to study the UAV-enabled WPT, and aim to derive a critical distance beyond which the UAV-enabled WPT may show better performance over the conventional scheme in terms of energy transfer efficiency.

2. Based on the research results of the first objective, we continue to optimize the UAV locations, aiming to maximize the sum-energy received by all ground sensors.

3. Considering the purpose of data collection and data offloading to the BS for further computing and decision-making in UAV-enabled WPCNs, the optimal time allocation between different processes, i.e., time for UAV wireless charging from a charging station, WPT, data collection and offloading, is studied to maximize the data offloading to the BS. This can be used as a performance index of the UAV-enabled WPCNs system.

4. To save the time cost of the UAV charging, a battery-powered UAV also needs to be considered. Since the UAV is usually restricted by operation time due to limited onboard energy, it is necessary and meaningful to study the optimal battery weight that maximizes the available energy for WPT or communications.

5. In order to calculate the energy consumption of UAV in different manoeuvres more simply and accurately, a new energy consumption mode (ECM) with closed-form expression needs to be further studied.

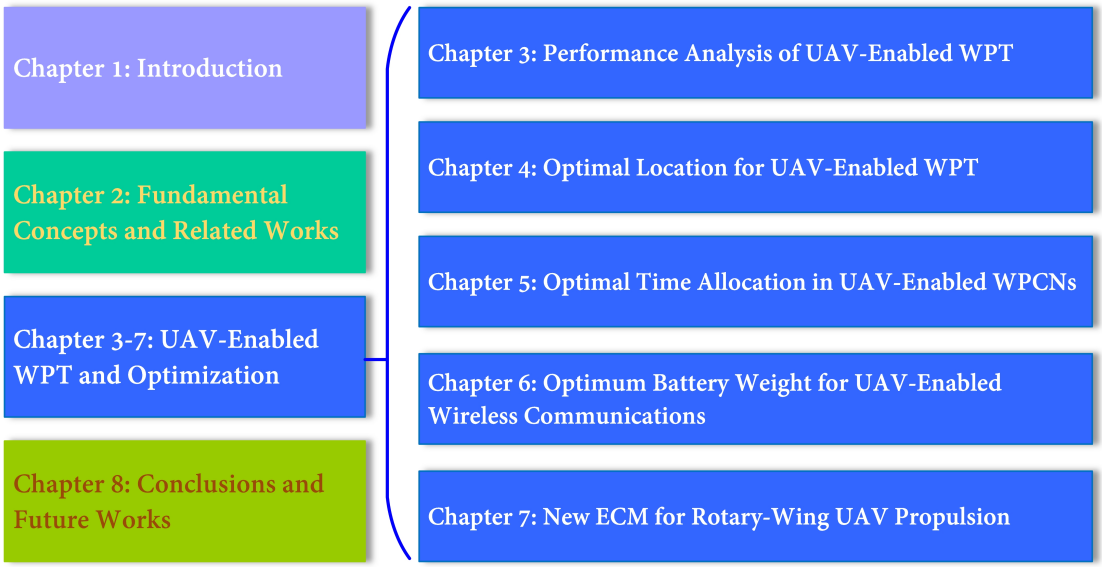

Figure 1.1: The overall structure of the thesis.

1.3 Thesis Outline and Contributions

Motivated by the above observations and objectives, in this thesis, UAV-enabled WPCN is studied, whilst taking UAV energy replenishment and propulsion consumption into consideration. The rest of this thesis is organized as follows. In Chapter 2, some fundamental concepts and related works are introduced. Then, we successively construct five technical chapters, i.e., from Chapter 3 to Chapter 7, to deal with the challenges and issues observed from the motivations in Section 1.2. Finally, the conclusions and some suggested future work are summarized in Chapter 8. Fig. 1.1 shows the overall structure of the thesis. The main contributions of each chapter is summarized below.

Chapter 2: Fundamental Concepts and Related Works. In this chapter, we first introduce some fundamental concepts used in this thesis, followed by a comprehensive literature review where the start-of-the-art of UAV-related works in wireless communications is presented, based on which our work emerged.

Chapter 3: Performance Analysis of UAV-Enabled WPT. Energy transfer efficiency of a UAV-enabled WPT system, where the UAV is deployed as an energy charger to charge the remote sensors considering UAV propulsion consumption is studied in this chapter. In the study, we propose two new schemes following a *Load-Ferry-and-Charge* (LFAC) paradigm for UAV-enabled WPT, and they are compared with the conventional schemes where long distance direct wireless charging without using a UAV is adopted. In the comparison, RF energy transfer model, UAV energy consumption model and RF-to-DC conversion efficiency model are analyzed. A critical distance beyond which the new schemes have a higher energy transfer efficiency than the conventional direct charging scheme is derived. Numerical results are also presented to show the influences of the RF-to-DC conversion efficiency and the UAV flight heights on the critical distance of the new schemes.

Chapter 4: Optimal Location for UAV-Enabled WPT. This chapter explores the optimal location of the UAV in a UAV-enabled WPT system, where the UAV is deployed to charge the ground sensors after being charged by a BS. The same paradigm as in Chapter 3 is considered, but the difference is that the power consumption at the UAV in this chapter is calculated using the energy consumption model firstly reported in [49]. Two different charging schemes for 1D and 2D topologies of the ground sensors are considered. By maximizing the sum-energy received by all ground sensors, the optimal location of the UAV is derived. Numerical results show that the optimal locations of the UAV have to be closer to the BS than what was reported in previous works that did not consider the propulsion consumption of the UAV.

Chapter 5: Optimal Time Allocation in UAV-Enabled WPCNs. In this chapter, the use of the UAV in a WPCN serving as both a data collector

and a wireless energy transmitter is investigated. In the study, the data offloading from the UAV to the BS is considered along with other processes, i.e., LFAC, as in Chapters 3 and 4. Both distance-independent path loss and small-scale fading are considered to maximize the data volume and transmission efficiency, defined as the ratio of the amount of data offloaded to the BS to the amount of data collected from the ground sensors, given in a fixed total time. The closed-form expression for the optimal time allocation between different processes, i.e., *Loading-Ferry-Charging-and-Offloading (LFCAO)*, is derived. Simulation results are also presented to show that the optimal time allocation can maximize the amount of data at the BS without wasting any time and energy.

Chapter 6: Optimal Battery Weight for UAV-Enabled Wireless Communications. In Chapter 3, Chapter 4 and Chapter 5, wireless charging from the BS to the UAV is considered. For applications in practice if wired charging at the BS is convenient and available, the results in above studies are still valid by assuming a very high RF-to-DC conversion efficiency. However, for some emergency response applications such as UAV-aided SAR, fast deployment on-demand is needed. Battery-powered UAVs with an automatic replacement mechanism [50] could be the best candidate because they reduce a large amount of time for charging from the BS. In this chapter, from the perspective of UAV onboard-energy maximization, we study the optimum battery weight for maximizing available energy in UAV-enabled wireless communication networks, where both vertical and horizontal flights are considered. Both numerical and approximate solutions to the optimal battery weight are derived. Numerical results are presented to show that the optimal battery weight that optimizes the flight performance is determined by the flight height, flight distance, vertical/horizontal flight speed and the gross mass of the UAV excluding battery mass.

Chapter 7: New ECM for Rotary-Wing UAV Propulsion. From the perspective of UAV onboard energy consumption, this chapter aims to derive a new ECM for UAV that overcomes the shortcomings of the existing models, i.e., there is no closed-form expression, and neither acceleration nor deceleration are considered. To this end, we decompose the power consumption of the UAV with acceleration/deceleration into vertical and horizontal directions using force analysis, based on which a new UAV ECM for arbitrary 2D level flight with closed-form expression as a function of the initial velocity, acceleration and time duration is derived. Using this model, the UAV flight control parameters such as polling force and tilt angle are also analyzed in analytical form. Numerical results show the validity and reliability of the new derived ECM.

Chapter 8: Conclusions and Future Work. In this chapter, we first summarize the main conclusions of this thesis. Then, possible future work is discussed and suggested based on this thesis.

1.4 Summary

In this chapter, we first introduced the background of UAV-enabled applications and pointed out there are some challenges and potential opportunities in UAV-aided wireless communications. Then, we clarified the research motivation and objectives in this thesis. Finally, the thesis outline has been provided and the main contributions of each chapter have also been summarized.

Chapter 2

Fundamental Concepts and Related Works

2.1 Wireless Channel Models

In wireless communications, electromagnetic waves are used to carry and transmit information. As it is well known that there is a reduction when the electromagnetic wave propagates through space, and that refraction, diffraction and reflection exist when encountering obstacles. As a result, the physical properties of electromagnetic wave determine the characteristics of wireless communications channel. In the following, some channel models used in this thesis are introduced.

2.1.1 Free Space Path Loss and Fading

Due to the air filtration, there is a power loss when the RF wave is transmitted from a transmitter to a receiver through free space. This power loss is defined as free space path loss (FSPL). According to [51], the FSPL model is given by

$$PL_{FS} = 20\lg\{f\} + 20\lg\{d\} - 147.55\ dB, \tag{2.1}$$

where d ($d \geqslant 1$) is the distance between the transmitter and the receiver, and f is the carrier frequency. Note that in the FSPL model $d \geqslant 1$, because the received power per unit area starts at a reference distance of 1 m [51]. Apart from being influenced by distance, the transmitting signal also experiences fading caused by refraction, diffraction and reflection, etc. As a result, the propagation model encompasses both the distance-dependent path loss and small-scale fading.

In UAV-enabled WPCNs, the air-to-ground (A2G) communication links between the UAV and ground sensors are mainly dominated by line-of-sight (LoS) and thus, Rician fading is a reasonable model to describe the fading in UAV communications. Let X denote a Rician random variable, the probability density function (PDF) of X is described in terms of the mean μ and variance σ as

$$f_X(x) = \frac{x}{\sigma^2} e^{-\frac{x^2+v^2}{2\sigma^2}} I_0(\frac{xv}{\sigma^2}), \quad x \geq 0 \tag{2.2}$$

where v is non-central parameter, $I_0(x)$ is the zero-th order modified Bessel function of the first type [52, eq.(8.406.1)].

For the environment where both LoS and non-LoS (NLoS) channels exist,

a new path loss model is derived in [16] as

$$PL = \frac{A}{1 + a_e exp(-b_e[\arctan(\frac{h}{R_c}) - a_e])} + 10\lg\left\{h^2 + {R_c}^2\right\} + 20\lg\left\{\frac{4\pi f}{c}\right\} + \eta_{NLOS}, \tag{2.3}$$

where $A = \eta_{LOS} - \eta_{NLOS}$, η_{LOS} and η_{NLOS} refer to the mean value of the excessive path loss caused by LoS channel and NLoS channel, respectively, h and R_c are vertical and horizontal distances from the transmitter to the receiver, a_e and b_e are constants related to the propagation environments.

2.1.2 Channel Capacity

According to the Shannon theorem, the maximum achievable rate R in bits/Hz can be expressed as

$$R = B\log_2\left(1 + \frac{S}{N_0}\right), \tag{2.4}$$

where B is the bandwidth, S is the received power in watts (W), N_0 denotes the additive white Gaussian noise (AWGN) in W, and $\frac{S}{N_0}$ is the signal-to-noise ratio (SNR) at the receiver.

2.2 Wireless Charging

2.2.1 Wireless Power Transfer

In UAV-enabled WPCNs, there has been a growing interest in studying WPT from the UAV to ground sensors, where RF signal is regarded as a promising solution. Considering the UAV is also an energy-limited node that does not generate energy

itself, wireless charging to UAVs has also been highlighted in both academia [34] and industry [35]. Denote the transmit power in dB by P_{Tx}, the received power P_{RF} can be expressed as

$$P_{RF} = P_{Tx} + G_{Tx} + G_{Rx} - PL_{FS}, \tag{2.5}$$

where G_{Tx} and G_{Rx} are the antenna gains of the transmitter and the receiver in dBi, respectively, PL_{FS} is the path loss defined in (2.1). However, the received RF power P_{RF} needs to be converted into DC before it can be used directly. In practice, this conversion is usually implemented by a rectifier, and the RF-to-DC conversion efficiency varies with different received power.

2.2.2 RF-to-DC Conversion Efficiency

In [40] and [48], both linear and non-linear models for the RF-to-DC conversion efficiency have been discussed. Wherein, the linear model has been adopted in most existing works [24, 41, 42, 44–47] for simplifying the calculation. Denote the converted DC power at the receiver by P_{DC}, using (2.5), one has the relationship between P_{RF} and P_{DC} as

$$P_{DC} = \eta \cdot 10^{\frac{P_{RF}}{10}}, \ 0 < \eta < 1. \tag{2.6}$$

The above model assumes that the RF-to-DC conversion efficiency is a constant that is linear and independent of the input RF power. However, in practice, the converted DC power actually depends on the input RF power, which means the RF-to-DC conversion efficiency is non-linear. One has the relationship between

the received RF power P_{RF} and the converted DC power P_{DC} as [48]

$$P_{DC} = f(P_{RF}) = \frac{a_0 10^{\frac{P_{RF}}{10}} + b_0}{10^{\frac{P_{RF}}{10}} + c_0} - \frac{b_0}{c_0}, \tag{2.7}$$

where a_0, b_0 and c_0 are constants obtained by standard curve-fitting. As a result, the non-linear RF-to-DC conversion efficiency η can be expressed as

$$\eta = \frac{P_{DC}}{10^{\frac{P_{RF}}{10}}} = \frac{\frac{a_0 10^{\frac{P_{RF}}{10}} + b_0}{10^{\frac{P_{RF}}{10}} + c_0} - \frac{b_0}{c_0}}{10^{\frac{P_{RF}}{10}}}, \ 0 < \eta < 1. \tag{2.8}$$

2.2.3 Energy Harvesting

According to the received RF power in (2.5) at the UAV, and the RF-to-DC conversion efficiency η in (2.8), the received DC energy can be calculated as

$$E_{DC-harvest} = P_{DC} \cdot T_{charge} = \eta \cdot 10^{\frac{P_{RF}}{10}} \cdot T_{charge}, \tag{2.9}$$

where T_{charge} is the charging time, and it is usually less than or equal to the time to fully charge the UAV.

2.3 UAV Types

In the past decade, there has been an increasing development in UAVs, resulting in a wide variety of UAVs. In the light of different metrics, UAVs can be divided into many different categories. For example, UAVs can be classified into military and civil according to the purpose. Other classifications such as by weight, by size or by fuel type have been detailed in [3, Table. (3)]. However, UAVs enabling in

the field of wireless communications are generally grouped by flight altitude [3, 11] and wings type [7, 12].

2.3.1 By Flight Altitude

- Low altitude platform (LAP): UAVs with flight height less than 10 km can be seen as a LAP for communications [3]. LAPs are generally easy to deploy, but limited by onboard energy.
- High altitude platform (HAP): Accordingly, HAP operates at an altitude of more than 10 km [3]. UAVs with this altitude show better performance on endurance, whist higher operational cost is needed.

2.3.2 By Wings Type

- Fixed-Wing: Fixed-wing UAVs usually have higher maximizing flying speed and payload. However, a runway is indispensable for taking off and landing.
- Rotary-Wing: Compared with fixed-wing UAVs, rotary-wing UAVs show advantages in taking off and landing vertically. In particular, they are able to hover somewhere in the air, which allows them to show more flexible mobility in communications. Nevertheless, the key limitations of rotary-wing UAVs are their low payload and endurance.

Table 2.1: Parameters for fixed-wing and rotary-wing UAVs

Notations	**Description**
ρ	Air density
m	the total mass of the UAV
g	Gravitational acceleration
W	$W = mg$ is the weight of the UAV
C_{D_0}	Zero-lift drag coefficient
S	Wing area of the fixed-wing UAV
e_0	Oswald efficiency
$\mathcal{A}_{\Re}$	The ratio of the fixed-wing span to its aerodynamic breadth
b	Number of blades
R	Rotor radius in meter m
A	Rotor disc area in m^2, $A = \pi R^2$
c	Blade or airfoil chord length
s	Rotor solidity, $s \triangleq \frac{bc}{\pi R}$
δ	Profile drag coefficient
Ω	Blade angular velocity in radians/second
k	Incremental correction factor to induced power
U_{tip}	Tip speed of the rotor blade, $U_{tip} \triangleq \Omega R$
v_0	Mean rotor induced velocity, $v_0 = \sqrt{\frac{W}{2\rho A}}$
S_{FP}	Fuselage equivalent flat plate area in m^2
d_0	Fuselage drag ratio, $d_0 \triangleq \frac{S_{FP}}{sA}$

2.4 UAV Propulsion Energy Consumption Models

In UAV-enabled WPCNs, in addition to the energy transferred to the ground sensors via WPT and the energy for communications, the UAV also requires energy for various manoeuvres such as hovering, acceleration/deceleration and flying at a constant speed of V. According to the existing works, fixed-wing and rotary-wing UAVs are two main types of UAVs that have been widely studied. In the following, the energy consumption models of these two types of UAVs are introduced.

2.4.1 Energy Consumption Model for Fixed-wing UAVs

According to [30], the propulsion consumption energy for a fixed-wing UAV with level flight without abrupt acceleration/deceleration $\bar{E}$ can be expressed as a function of a given trajectory $\mathbf{q}(t)$ [30, eq. (5)], one has

$$\begin{aligned}\bar{E}(\mathbf{q}(t)) = &\int_0^T \left[c_1 \|\mathbf{v}(t)\|^3 + \frac{c_2}{\|\mathbf{v}(t)\|} \left(1 + \frac{\|\mathbf{a}(t)\|^2 - \frac{(\mathbf{a}^T(t)\mathbf{v}(t))^2}{\|\mathbf{v}(T)\|^2}}{g^2} \right) \right] dt \\ &+ \frac{1}{2} m \left(\|\mathbf{v}(T)\|^2 - \|\mathbf{v}(0)\|^2 \right),\end{aligned} \tag{2.10}$$

where $\mathbf{v}(t) \triangleq \frac{\partial \mathbf{q}(t)}{\partial t}$ and $\mathbf{a}(t) \triangleq \frac{\partial^2 \mathbf{q}(t)}{\partial t^2}$ denote the instantaneous velocity and acceleration of the UAV, respectively. $c_1 = \frac{1}{2}\rho C_{D_0} S V^2$ and $c_2 = \dfrac{2W^2}{(\pi e_0 \mathcal{A}_{\Re})\rho S}$ are two constants related to the UAV's weight W, wing area S, air density ρ, etc., $g = 9.8\ m/s^2$ is the gravitational acceleration, m is the total mass of the UAV. Other parameters are detailed in Table 2.1.

2.4.2 Energy Consumption Model for Rotary-wing UAVs

Compared with fixed-wing UAVs, rotary-wing UAVs show better flexibility and mobility due to its characteristics of hovering and vertical flight. In [49], an analytical propulsion power consumption model for rotary-wing UAVs in forward level flight with speed of V, $P(V)$, was reported as

$$P(V) = P_0 \left(1 + \frac{3V^2}{U_{tip}^2} \right) + P_1 \left(\sqrt{1 + \frac{V^4}{4v_0^4}} - \frac{V^2}{2v_0^2} \right)^{\frac{1}{2}} + \frac{1}{2} d_0 \rho s A V^3, \tag{2.11}$$

where $P_0 = \frac{\delta}{8}\rho s A \Omega^3 R^3$ and $P_1 = (1+k)\sqrt{\frac{(mg)^3}{2\rho A}}$ are two constants related to the physical properties of the UAV and the flight environment, including profile drag

coefficient δ, air density ρ, rotor solidity s, etc., as detailed in Table 2.1. Denote the energy consumption during hovering, acceleration (deceleration) and flying at speed of V as E_{hover}, $E_{Acc}(E_{Dec})$ and E_V, respectively. By substituting $V = 0$ into (2.10), the power consumption for hovering, P_{hover}, can be derived as

$$P_{hover} = P(0) = P_0 + P_1, \tag{2.12}$$

and thus, the energy required for hovering during period of T_{hover} can be calculated as

$$E_{hover} = P(0) \cdot T_{hover}. \tag{2.13}$$

For flying at speed of V, one has

$$E_V = P(V) \cdot T_{flying}, \tag{2.14}$$

where T_{flying} is the flying time at constant speed of V. For linear acceleration or deceleration, one has the relationship between the speed $V(t)$, initial velocity $\mathbf{v}_0$ and acceleration $\mathbf{a}$ as

$$V(t) = \|\mathbf{v}_0\| \pm \|\mathbf{a}\|t, \tag{2.15}$$

where t is the time for acceleration (deceleration). As a result, the energy consumed by the UAV during the acceleration can be approximately calculated as

$$E_{Acc} = \int_0^{\frac{V - \|\mathbf{v}_0\|}{\|\mathbf{a}\|}} P\left[V(t)\right]. \tag{2.16}$$

Similarly, the energy consumed during deceleration can be derived using symmetry. It is unnecessary to go into details. Note that, (2.16) is only valid for forward level flight as specified in [49].

For vertical flight, the authors in [53] derived a power consumption model

as

$$P_v\left(\mathbf{V}_v, \mathbf{a}\right) = P_2 + \frac{T}{2}\left(\mathbf{V}_v + \sqrt{\|\mathbf{V}_v\|^2 + \frac{2T}{\rho A}}\right), \tag{2.17}$$

where $T = m(\mathbf{a} + g)$ is the rotor thrust, $\mathbf{V}_v$ is the velocity of vertical flight, $P_2 = \frac{\delta}{8}\rho s A \Omega^3 R^3 + k\sqrt{\frac{(mg)^3}{2\rho A}}$, $g = 9.8\ m/s^2$ is the gravitational acceleration, $a > 0$ (upward) is the acceleration for ascending and $a < 0$ (downward) for descending.

2.5 UAV-Related Works

2.5.1 UAV-enabled WPT

There have been quite a few works on the use of UAVs for WPT. In these works, the UAV is deployed to broadcast wireless energy to ground sensors. Due to the LoS links between the UAV and ground sensors, UAV-enabled WPT system can improve the energy transfer efficiency greatly by deploying UAV as a mobile energy transmitter. For example, in [41], a WPT system with a UAV-mounted energy transmitter was considered and for a basic two-user scenario, the energy region and the amount of energy transferred over a fixed period of time were studied jointly with the mobility and trajectory design of the UAV. In [42], the authors extended the two-user scenario in [41] to more users and maximized the minimum of the energy harvested by all users via optimizing the trajectory of the UAV. In [36], both UAV's optimal hovering locations for the sum-energy maximization and UAV's optimal hovering time allocations for maximizing the minimum received energy among all energy receivers were investigated by trajectory optimization. In [37], a one-dimensional (1D) UAV trajectory was designed for a multi-user WPT system, where all ground users stay on a line, such as a motorway or river. Also,

reference [38] considered a two-user scenario, but the UAV was equipped with a directional antenna for improving the energy transfer efficiency. In [54], the scenario was further extended to the case of multi-UAVs and multiple ground users, and the throughput was maximized by optimizing the user scheduling through considering the UAV trajectory and power control jointly. In [24], a new UAV-enabled wireless powered communication network was studied, where a UAV is deployed as a mobile access point to charge the ground users in the A2G link and collect information from ground users in the ground-to-air (G2A) link. The up-link minimum throughput was maximized by optimizing both the UAV trajectory and other resources. In [39], the maximum network throughput was discussed in a UAV-enabled relaying system where the UAV receives both energy and information from a BS, and then forwards the information to the ground user. The authors in [55] studied the use of a rotary-wing UAV as an energy transmitter to charge a set of energy receivers (ERs) taking into account the UAV's flight altitude and coverage performance. The energy harvested by all ERs was maximized via jointly optimizing the UAV's placement, beam pattern and charging time. Finally, in [56], a UAV-aided A2G cooperative non-orthogonal multiple access system for cellular users was studied, where the energy efficiency and spectrum efficiency were improved by jointly scheduling cellular users and the UAV. Reference [57] studied the energy trade-off between the up-link transmission energy of the ground terminals and the propulsion energy for UAV's movement. In [58], the authors considered a framework for UAV-aided wireless charging of sensor nodes using RF energy transfer. Other works include the related technologies, principles and applications of wireless charging in [32, 33, 59–62], RF energy models and energy transfer channel models in [63, 64], mobile charging technologies [65–67] and wireless energy harvesting [68]. All these works have provided very valuable guidance on the use of UAV-enabled WPT system.

2.5.2 UAV-aided Data Collection

In view of the fact that UAVs can be flexibly deployed on-demand when required, UAV-aided data collection has attained significant research attention. To name a few, the authors in [69] proposed a novel UAV-aided sensor network, where a UAV was employed as a mobile data collector for data collection and also as an anchor node to help terrestrial BS with sensor positioning. Similarly, a UAV-aided data collection scheme for WSNs was studied in [70], where both single UAV and multiple UAVs were considered. In [71], a UAV-enabled WSN was studied, where a flying UAV was dispatched to collect data from multiple sensors, and the minimum average data rate was maximized via optimizing the UAV communication scheduling and 3D trajectory. In [72], the shortest path for UAV-aided data collection was derived to achieve a high delivery rate and a low energy usage. Reference [73] studied UAV-aided data collection from time-constrained sensors via jointly optimizing the trajectory of the UAV and the radio resource allocation. In [74], UAV operations and traffic data collection have been reviewed for driving behavior analysis. In [75], energy-efficient data collection was studied, where sensor wake-up schedule and UAV trajectory were jointly optimized to minimize the maximum energy consumption for all sensors. Furthermore, reference [76] extended the work in [75] to multiple UAVs, in which the mission completion time among all UAVs was minimized. In [77], a UAV was dispatched to collect data from a set of sensors distributed on a straight line. The total flight time of the UAV was minimized via jointly optimizing sensor transmit power and the UAV speed. The authors in [78] proposed four UAV-aided data collection algorithms considering the dynamic network topology where sensors were mobile with constant velocities. In [79], a UAV trajectory planning model for data collection was proposed taking into account the message expiration. Also, in [80], age of information was considered as a perfor-

mance metric to measure the data freshness in UAV-aided IoT networks. In [81], a UAV-aided data collection design was proposed, where the UAV's trajectory, velocity, altitude and data link were all considered to minimize the mission time. In [82], a UAV acting as a mobile sink was dispatched to collect data from the cluster node of a WSN, and a direct future prediction model was proposed for UAV's trajectory plan. In [83], a rotary-wing UAV with limited onboard energy was employed to collect data from sensors. The maximum energy consumption among all sensors was minimized by jointly optimizing the communication schedule, the transmit power and the UAV trajectory.

As sensors deployed in IoTs are energy-limited nodes and they need to be charged until the energy exceeds the circuit activation threshold to start transmitting data [25], works on UAV-enabled WPCNs [25, 27–29, 44, 45] began to study the performance of combining WPT and data collection. Similarly, considering the UAV consumes energy in different manoeuvres, some recent works have started to take UAV propulsion energy into account [46, 47]. In [46], a rotary-wing UAV equipped with a hybrid access point was employed to serve energy-limited sensors, where sum throughput problem, total time minimization problem and total energy minimization (TEM) problem were optimized. For the TEM problem, UAV's propulsion energy was considered. Similarly, in [47], a rotary-wing UAV considering propulsion energy was considered to serve multiple ground users, where the ground users first harvested radio frequency energy from the UAV, and then transmitted information to the UAV. The energy-time trade-off was solved by jointly optimizing the user scheduling, UAV trajectory and mission completion time. All these works have provided very valuable insights on the use of UAV-enabled WPT and data collection.

2.6 Summary

In this chapter, some basic concepts and mathematical models to be used in this thesis have been first introduced in detail. Then, UAV-related works including UAV-enabled WPT and UAV-aided data collection have also been reviewed and discussed.

Chapter 3

Performance Analysis of UAV-Enabled WPT

This chapter is based on our work published in [J1]. ([43])

3.1 Introduction

In recent years, there has been increasing popularity in UAVs, as it has been widely used in many public, military and civil applications [1, 2, 4]. For example, UAVs have been adopted in environmental and natural disaster monitoring, for area or network coverage, as aerial BSs or relays, and for delivery of goods and construction.

In particular, as an aerial BS or relay, UAVs play a very important role in UAV-enabled wireless networks. The authors in [16] optimized the altitude of a LAP to provide the maximum radio coverage for the ground users. In [17], the

authors considered this problem in a relaying setting and studied the optimum placement of a relaying UAV for the maximum reliability. Furthermore, works on mobile relaying and mobile BS were also studied in [18] and [19], respectively. Zeng *et al.* [18] studied the throughput maximization problem in mobile relaying system by optimizing the transmit power, while Lyu *et al.* [19] focused on minimizing the number of mobile BSs needed to provide effective wireless coverage for several distributed ground terminals so that each ground terminal can have an effective communication connection with the mobile BS. In the seminal paper [20], the authors proposed a new cyclical multiple access (CMA) scheme to explore the periodic channel variations between a mobile BS served by a UAV and ground terminals for maximum throughput. The results show that there exists a trade-off between throughput and access delay in their proposed CMA scheme. For UAV relaying networks or systems, the authors in [21] jointly investigated the optimization problem of UAV node placement and communication resource allocation to achieve the maximum throughput. In [22], a solution that jointly optimizes the trajectory design and power control was proposed to minimize the outage probability of the UAV relaying network. All of the above works have provided very useful insights on the applications of UAV as a relay or a BS to provide information relay or information coverage. However, energy is as important as information in communications systems, especially in wireless sensor networks where the sensors are of limited battery life.

Although works on UAV-enabled WPT in 2.5.1 have considered the scenario where the UAV acts as a traditional static relay or an aerial BS to provide energy relay or energy coverage by WPT, a realistic and important issue that has been largely ignored is the power consumption of UAV. Some of these works (i.e., [36], [37], [38] and [39]) have also ignored the RF-to-DC energy conversion efficiency at energy receivers. Besides, the path loss caused by the transmission

distance seriously reduces the energy transfer efficiency. To improve the energy transfer efficiency, one efficient method is to reduce the path loss caused by long transmission distance. For this purpose, one interesting work is data ferry, where a third transceiver receives the data from the BS in its close proximity and then carry the data to the sensors for another transmission in close proximity. For example, in [84], the authors considered the method of using one or more UAVs to relay messages between two distant ground nodes. A "load-carry-and-deliver" (LCAD) paradigm was proposed to let the UAV load data from a source node, carry the data to the destination node, and finally deliver the data to the destination node. It has been shown in these works that data ferry is more efficient than traditional direct transmission. Moreover, works on cooperative communications, such as two-way multi-antenna cooperative relaying with comparison of one-hop direct transmission and two-hop relay-aided transmission [85–89], have also provided very valuable insights on relay-aided transmission strategies, and it is interesting to use UAV as a mobile relay following the idea of these works.

Motivated by the above observations, in this chapter, we study the WPT efficiency in a UAV-enabled wireless network, where a UAV is used to charge the remote unmanned ground vehicle (UGV). We propose two new schemes for UAV-enabled WPT. The new and conventional schemes (long distance direct wireless charging without using a UAV) are compared by analyzing their RF energy transfer model, UAV energy consumption model and RF-to-DC conversion efficiency model. A critical distance beyond which the new schemes have a higher energy transfer efficiency than the conventional direct charging is derived. Numerical results are presented to show the influences of the RF-to-DC conversion efficiency and the UAV flight height on the critical distance of the new schemes. Specifically, the critical distance is reduced from 192.99 m to 75.0 m when the RF-to-DC conversion efficiency increases from 0.6 to 1.0 for a fixed UAV height of 6.4 m

Table 3.1: Symbols in Chapter 3

Notations	**Description**
L_{FS}^{s1-1}	path loss from the BS to the UAV in Scheme 1
L_{FS}^{s1-2}	path loss from the UAV to the UGV in Scheme 1
L_{FS}^{s2-1}	path loss from the BS to the UAV in Scheme 2
L_{FS}^{s2-2}	path loss from the UAV to the UGV in Scheme 2
d_{s1-1}	transmission distance from the BS to the UAV in Scheme 1
d_{s1-2}	transmission distance from the UAV to the UGV in Scheme 1
d_{s2-1}	transmission distance from the BS to the UAV in Scheme 2
d_{s2-2}	transmission distance from the UAV to the UGV in Scheme 2
L_1	horizontal distance on both sides of the BS during the *load* stage
L_2	horizontal distance on both sides of the UGV during the *charge* stage
P_{uav-r}^{s1}	received RF power at the UAV in Scheme 1
P_{uav-r}^{s2}	received RF power at the UAV in Scheme 2
P_{uav-t}^{s1}	transmit RF power from the UAV in Scheme 1
P_{uav-t}^{s2}	transmit RF power from the UAV in Scheme 2
P_{ugv}^{s1}	received RF power at the UGV in Scheme 1
P_{ugv}^{s2}	received RF power at the UGV in Scheme 2
E_{uav-DC}^{s1}	received DC energy of UAV from the BS in Scheme 1
E_{uav-DC}^{s2}	received DC energy of UAV from the BS in Scheme 2
E_{fly-to}^{s1}	energy consumption during the *carry* stage in Scheme 1
E_{fly-to}^{s2}	energy consumption during the *carry* stage in Scheme 2
$E_{fly-back}^{s1}$	energy consumption for flying back in Scheme 1
$E_{fly-back}^{s2}$	energy consumption for flying back in Scheme 2

above ground level. Also, when the RF-to-DC conversion efficiency is set to 0.6, the critical distance increases from about 59.69 m to 192.99 m when the UAV height increases from 6.0 m to 6.4 m. The main contributions of this work can be summarized as follows:

- We propose two new schemes for UAV-enabled WPT in wireless networks.
- We derive and quantify the exact critical distance and the effective range beyond which the new schemes have superiority over the conventional direct charging.

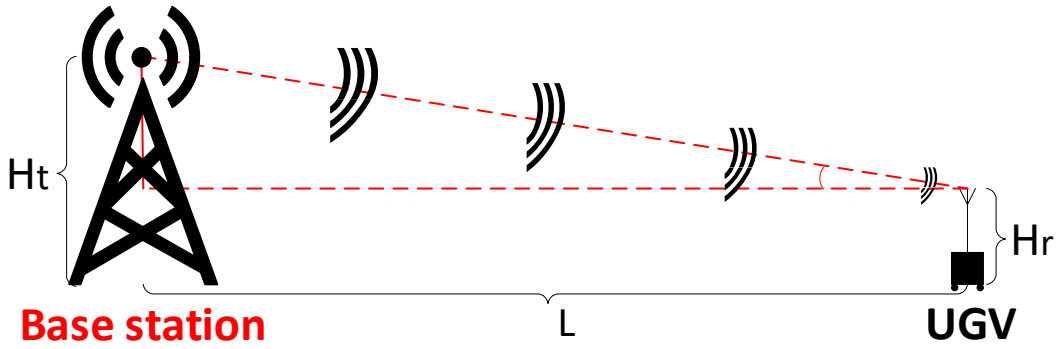

Figure 3.1: The conventional direct energy transfer scheme.

- We examine the effects of different system parameters on the performance of the proposed schemes to give useful guidance for system designs.

The remainder of this chapter is organized as follows. In Section 3.2, the system models used in the proposed schemes are introduced. The new schemes and the critical distance are studied in Section 3.3. Numerical results are presented in Section 3.4. Finally, we conclude the work in Section 3.5. Some frequently used symbols in this chapter are summarized in Table 3.1.

3.2 System Model

Consider three wireless charging scenarios as depicted in Figs. 3.1, Fig. 3.2 and Fig.3.3. In Fig. 3.1, an UGV, located L meters away from the BS, is charged via direct RF energy transfer. This is the conventional direct energy transfer scheme. In Fig. 3.2 and Fig. 3.3, a multi-rotor UAV is used to load the energy near the BS and then deliver the energy to the UGV by charging it from a short distance. These are the two new schemes.

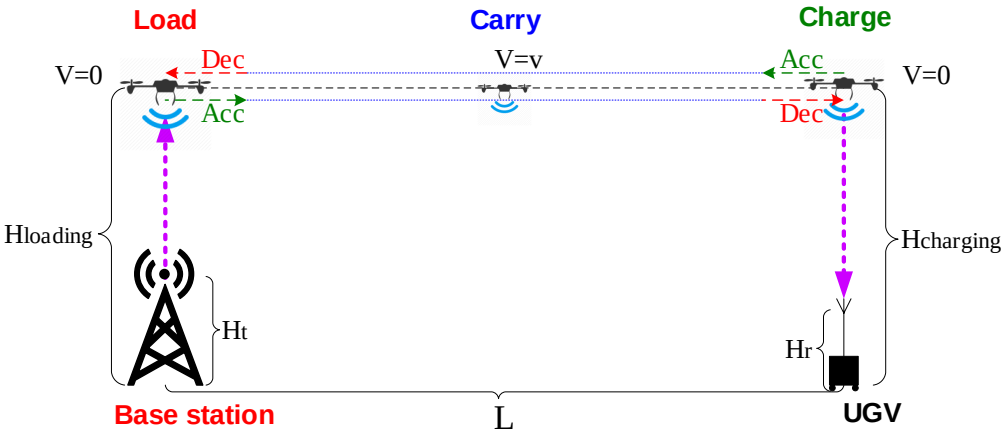

Figure 3.2: The proposed Scheme 1.

To determine which scheme is more energy efficient, we need to know the energy consumption of different parts of the system. For the conventional scheme, the energy consumption only comes from the transmission loss from the BS to the UGV and the conversion loss from RF to DC at the UGV. For the proposed schemes, the energy consumption comes from the transmission loss from the BS to the UAV and from the UAV to the UGV, the conversion loss from RF to DC at the UAV and at the UGV, and the UAV internal loss due to hovering, acceleration, deceleration and flying operations.

3.2.1 Transmission Loss

We assume a LoS communication link between the BS and the UAV, and between the UAV and the UGV as in [36–38, 41, 42]. Also, the communication link between the BS and the UGV comes with extra power loss caused by shadowing and NLoS. Denote the heights of the BS and the UGV as H_t and H_r, respectively. According

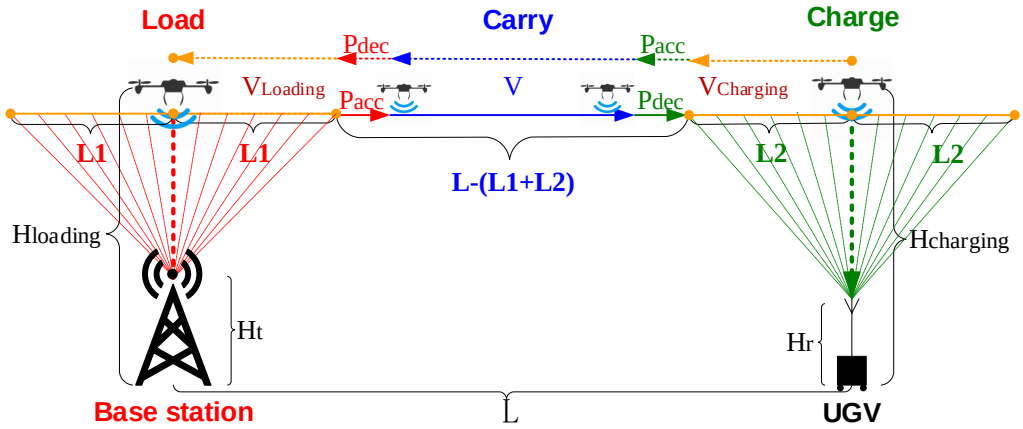

Figure 3.3: The proposed Scheme 2.

to the FSPL model [51], the transmission loss L_{FS} is expressed as

$$L_{FS(dB)} = 20\lg\{f_c\} + 20\lg\{d\} - 147.55\ dB, \tag{3.1}$$

where d (d $\geq$ 1 m) is the distance between the transmitter and the receiver and f_c is the operating frequency.

In Fig. 3.1, for the conventional direct transfer scheme, since the distance between the BS and the UGV is L, one has

$$d_0 = \sqrt{L^2 + (H_t - H_r)^2}, d_0 \geq 1\ m. \tag{3.2}$$

Hence, the transmission loss is

$$L^c_{FS(dB)} = 20\lg\{f_c\} + 20\lg\{d_0\} - 147.55 + X\ dB, \tag{3.3}$$

where X represents the extra power loss caused by shadowing.

In Fig. 3.2, for the proposed Scheme 1, the transmission distance from the

BS to the UAV is

$$d_{s1-1} = H_{loading} - H_t,\ d_{s1-1} \geq 1\ m, \tag{3.4}$$

and the distance from the UAV to the UGV is

$$d_{s1-2} = H_{charging} - H_r,\ d_{s1-2} \geq 1\ m, \tag{3.5}$$

where $H_{loading} > H_t$ and $H_{charging} > H_r$. Therefore, the transmission loss from the BS to the UAV can be expressed as

$$L_{FS(dB)}^{s1-1} = 20\lg\{f_c\} + 20\lg\{d_{s1-1}\} - 147.55\ dB, \tag{3.6}$$

and the transmission loss from the UAV to the UGV can be expressed as

$$L_{FS(dB)}^{s1-2} = 20\lg\{f_c\} + 20\lg\{d_{s1-2}\} - 147.55\ dB. \tag{3.7}$$

For the proposed Scheme 2 in Fig. 3.3, the UAV is charged while flying over the horizontal distance of L_1 meters on both sides of the BS. We denote each L_1 meters as one flight. Then, the flights within a horizontal distance of L_1 on both sides of the BS are symmetric, and thus we only need to consider the process within one L_1 meter distance. In essence, Scheme 2 charges and discharges the UAV while it is flying instead of hovering. In order to simplify the calculation, we use the average speed of $v_{loading}$ to approximately calculate the energy obtained during the *load* stage. Since the UAV flies at a fixed speed of $v_{loading}$ around the BS within a distance of L_1 meters during loading and we denote the instant time within L_1 meters as t, the instantaneous transmission distance at time instant t

from the BS to the UAV can be expressed as

$$d_{s2-1}(t) = \sqrt{(H_{loading} - H_t)^2 + (L_1 - v_{loading}t)^2}, \tag{3.8}$$

where $H_{loading} > H_t$ and $L_1 \geq v_{loading}t$ so that $0 \leq t \leq \frac{L_1}{v_{loading}}$, and $d_{s2-1}(t) \geq 1$ m. Similarly, if the UAV flies at a fixed speed of $v_{charging}$ around the UGV within a distance of L_2 meters during charging, the instantaneous transmission distance at time instant t from the UAV to the UGV can be expressed as

$$d_{s2-2}(t) = \sqrt{(H_{charging} - H_r)^2 + (L_2 - v_{charging}t)^2}, \tag{3.9}$$

where $H_{charging} > H_r$ and $L_2 \geq v_{charging}t$ so that $0 \leq t \leq \frac{L_2}{v_{charging}}$, and $d_{s2-2}(t) \geq 1$ m. Accordingly, the instantaneous transmission loss from the BS to the UAV can be expressed as

$$L_{FS(dB)}^{s2-1}(t) = 20\lg\{f_c\} + 20\lg\{d_{s2-1}(t)\} - 147.55\ dB, \tag{3.10}$$

and the instantaneous transmission loss from the UAV to the UGV can be expressed as

$$L_{FS(dB)}^{s2-2}(t) = 20\lg\{f_c\} + 20\lg\{d_{s2-2}(t)\} - 147.55\ dB. \tag{3.11}$$

3.2.2 UAV Internal Loss

In [90], the authors reported some computational models for the energy consumed by a UAV for its various manoeuvres (i.e. hovering, acceleration, deceleration and flying) based on experimental results. We will use these models here. Assume that the energy consumption during UAV acceleration is E_{acc}, and during UAV

deceleration is E_{dec}. Also, E_{hover} and E_v denote energy consumption during hovering and during normal flight at an average speed of v, respectively. According to the results in [90], the internal energy consumption at the UAV during different manoeuvres can be calculated as

$$E_{hover} = P_{hover} t_1, \tag{3.12}$$

$$E_{acc} = P_{\overline{acc}} \left(t_2 - t_1\right), \tag{3.13}$$

$$E_v = P_v \left(t_3 - t_2\right), \tag{3.14}$$

$$E_{dec} = P_{\overline{dec}} \left(t_4 - t_3\right), \tag{3.15}$$

where P_{hover} (watt) is the hovering power, $P_{\overline{acc}}$ (watt) is the average acceleration power, P_v (watt) is the average flying power at a speed of v and $P_{\overline{dec}}$ (watt) is the average deceleration power. Also, t_1 is the hovering time at a speed of 0, $t_2 - t_1$ is the acceleration time, $t_3 - t_2$ is the flying time at a speed of v, and $t_4 - t_3$ is the deceleration time. In this case, the UAV hovers for t_1 seconds, followed by an acceleration for $t_2 - t_1$ seconds to a fixed speed of v, a flying time of $t_3 - t_2$ and finally a deceleration for $t_4 - t_3$ seconds to become static again.

For the proposed Scheme 1 in Fig. 3.2, the UAV hovers above the BS for charging, then accelerates to a constant speed of v to deliver the energy. When it is close to the UGV, the UAV decelerates and then hovers above the UGV to deliver the energy before flying back to the BS. Thus, hovering, acceleration, deceleration and flying are the only four operations that need to be considered for this scheme.

For the proposed Scheme 2 shown in Fig. 3.3, the UAV flies at a fixed speed of $v_{loading}$ around the BS within a distance of L_1 meters for charging, then accelerates to a constant speed of v to carry the energy. When it flies close to the

UGV, it decelerates to a fixed speed of $v_{charging}$ and within a distance of L_2 meters for energy delivery before flying back to the BS. Hence, flying (i.e. at a fixed speed of $v_{loading}$, v and $v_{charging}$, respectively), acceleration and deceleration are the only three operations that need to be considered for this scheme. No hovering is performed in this case.

3.2.3 RF-to-DC Conversion Loss

The RF-to-DC model in (2.6) is adopted in this Chapter, because it can simplify the calculation without affecting the simulation results. Assume that the input power is denoted as P_{RF}, and that the constant RF-to-DC conversion efficiency is η. Therefore, the received DC power P_{DC} can be expressed as

$$P_{DC} = \eta * 10^{\frac{P_{RF}}{10}}. \tag{3.16}$$

3.3 The Proposed New Schemes

In this section, two wireless charging schemes using RF energy harvesting are proposed, where a UAV used as a carrier is studied. Specifically, four different cases, a conventional scheme with a single receiver on UGV, the new schemes with a single receiver on UGV, the conventional scheme with multiple receivers on UGV and the new schemes with multiple receivers on UGV, will be compared and discussed.

3.3.1 Conventional Scheme with a Single Receiver

In this case, the RF energy from the BS is harvested by a single receiver on the UGV located L meters away directly, as shown in Fig. 3.1. Accordingly, the received RF power at the UGV can be expressed as

$$P_{ugv} = P_t + G_t + G_{ugv} - 20\lg\{f_c\} - 20\lg\{d_0\} + 147.55 - X\ dB, \tag{3.17}$$

where P_{ugv} (dB) is the received RF power at the UGV, P_t (dB) is the transmit power, G_t and G_{ugv} are the transmitting antenna gain and receiving antenna gain (dBi), respectively, X is the extra power loss, $d_0 = \sqrt{L^2 + (H_t - H_r)^2}$ is the transmission distance between the BS and the UGV, and the transmission loss $L^c_{FS(dB)}$ in (3.3) has been used here. If the charging time is denoted as $T_{loading}$, the converted DC energy at the UGV is

$$E_{ugv\_DC} = \eta E_{ugv\_RF} = \eta 10^{\frac{P_{ugv}}{10}} T_{loading}, \tag{3.18}$$

where η is the constant RF-to-DC conversion efficiency defined in (3.16) and $T_{loading}$ is the loading time which equals to the charging time in this case. Note that, when P_t and $T_{loading}$ are fixed, the received DC energy is affected by the path loss, which is mainly determined by the transmission distance.

3.3.2 New Schemes with a Single Receiver

For the new schemes. a UAV is used to charge the remote wireless sensors after it is charged by the BS. This method reduces the transmission distance and therefore may be more energy-efficient due to the reduced path loss. In this case, the UAV has to hover above the BS to be charged by the BS. After it has been charged, it

flies towards the UGV and then hovers above the UGV to charge the UGV. Fig. 3.2 and Fig. 3.3 illustrate the process of the proposed new schemes.

From Fig. 3.2 and Fig. 3.3, the process of the new schemes can be divided into three stages: *load*, *carry* and *charge*, which is similar to the paradigm in [84] for data ferry. In the first stage, the UAV is charged with certain amount of energy by the BS. This is the *load* stage. The second stage is the *carry* stage in which the UAV carries the stored energy and flies towards the UGV. Then, the UGV will be powered by the UAV. This is the *charge* stage. We consider the two different schemes in the following.

The Proposed Scheme 1 in Fig. 3.2

a) Load

During the first stage, the UAV stays static above the BS at a height of $H_{loading}$. In this case, the received RF power at the UAV can be expressed as

$$P_{uav-r}^{s1} = P_t + G_t + G_{uav} - L_{FS(dB)}^{s1-1}, \tag{3.19}$$

where G_{uav} is either transmitting or receiving antenna gain of the UAV and P_{uav-r}^{s1} (dB) is the received RF power at the UAV. $L_{FS(dB)}^{s1-1}$ is the transmission loss from the BS to the UAV in (3.6). Then, the received DC energy is

$$E_{uav-DC}^{s1} = \eta 10^{\frac{P_{uav-r}^{s1}}{10}} T_{loading}^{s1}. \tag{3.20}$$

Note that, during the *load* stage, the UAV hovering operation consumes energy as well, because it has to stay above the BS with a power of P_{hover} (dB). This energy

consumption can be calculated as

$$E_{hover}^{s1} = P_{hover} T_{loading}^{s1}. \tag{3.21}$$

Besides, in order to ensure that the UAV does not fall and is in the state of charge, the received DC power should be greater than the hovering power P_{hover}. i.e., $\eta 10^{\frac{P_{uav-r}^{s1}}{10}} > P_{hover}$.

b) Carry

During the second stage, an *acceleration-fly-deceleration* operation of the UAV will be performed to carry energy to the destination. The energy consumption of the *carry* stage can be calculated as

$$E_{fly-to}^{s1} = \begin{cases} E_{acc}^{s1} + E_{v}^{s1} + E_{dec}^{s1} = P_{\overline{acc}}^{s1}\left(\frac{v}{a}\right) + P_{v}^{s1}\frac{\left(L - \frac{v^2}{a}\right)}{v} + P_{\overline{dec}}^{s1}\left(\frac{v}{a}\right), L > \frac{v^2}{a}, \\ E_{acc}^{s1} + E_{v}^{s1} + E_{dec}^{s1} = P_{\overline{acc}}^{s1}\left(\frac{v}{a}\right) + P_{\overline{dec}}^{s1}\left(\frac{v}{a}\right), L \leq \frac{v^2}{a} \end{cases} \tag{3.22}$$

where v is the final constant flight speed, a is the acceleration and L is the total distance from the BS to the UGV. Note that, there is no *carry* stage when $L \leq \frac{v^2}{a}$ from (3.22). Since the UAV needs to fly back to its initial position after each delivery, to ensure that the UAV has enough energy to fly back, the energy consumption for flying back should at least be the same as that for flying to the destination. Thus, this energy consumption of flying back can be given by $E_{fly-back}^{s1} = E_{fly-to}^{s1}$, assuming that the flying back operation is symmetric to the flying to operation.

c) Charge

In the third stage, the UAV is hovering above the UGV at a height of H_{charge} , which is chosen to be the same as the height of loading $H_{loading}$ in the first stage to reduce flight distance and simplify the flight process because we are not aiming at trajectory optimization [22, 36–38, 41, 42, 54]. Then, the UAV charges the UGV with a transmitted RF power of P^{s1}_{uav-t} (dB). In this way, the received RF power at the UGV can be derived as

$$P^{s1}_{ugv} = P^{s1}_{uav-t} + G_{uav} + G_{ugv} - L^{s1-2}_{FS(dB)}, \tag{3.23}$$

where $L^{s1-2}_{FS(dB)}$ is the path loss between the UAV and the UGV given by (3.7) before. The final amount of energy that is available for charging can be derived as

$$E^{s1}_{available} = E^{s1}_{uav-DC} - E^{s1}_{hover} - E^{s1}_{fly-to} - E^{s1}_{fly-back}. \tag{3.24}$$

Note that, during the *charge* stage the UAV also consumes energy with a power of P^{s1}_{hover} for hovering, similar to the *load* stage (i.e. hovering consumption). Thus, the charging time in this stage can be calculated as

$$T^{s1}_{charging} = \frac{E^{s1}_{available}}{10^{\frac{P^{s1}_{uav-t}}{10}} + P_{hover}}. \tag{3.25}$$

As a result, the energy that the UGV can receive is derived as

$$E^{s1}_{ugv-DC} = \eta E^{s1}_{ugv\_RF} = \eta 10^{\frac{P^{s1}_{ugv}}{10}} T^{s1}_{charging}. \tag{3.26}$$

Comparing (3.18) and (3.26), it can be seen that the conventional scheme is mainly affected by the transmission distance, while the proposed Scheme 1 is mainly

affected by the UAV's own energy consumption and the RF-to-DC conversion (i.e. from the BS to the UAV and from the UAV to the UGV) efficiency. The proposed Scheme 1 saves energy by significantly reducing the transmission distance but has extra energy consumption due to hovering and flight operations. Thus, there might exist a trade-off between the transmission loss and the extra UAV operations. We will investigate this trade-off by finding the transmission distance beyond which the proposed Scheme 1 will have advantages over the conventional direct transfer.

To do this, we need to study the critical distance beyond which the cost of UAV-enabled WPT is lower than the transmission loss caused by path loss in the conventional direct transfer. Using (3.18) for the conventional direct transfer scheme, one has

$$\begin{aligned} E_{ugv-DC} &= \frac{\eta T_{loading} 10^{\frac{P_t+G_t+G_{ugv}-20\lg\{f_c\}+147.55-X}{10}}}{10^{\frac{20\lg\left\{\sqrt{L^2+(H_t-H_r)^2}\right\}}{10}}} \\ &= \frac{\eta T_{loading} 10^{\frac{P_t+G_t+G_{ugv}-20\lg\{f_c\}+147.55-X}{10}}}{L^2+(H_t-H_r)^2}. \end{aligned} \tag{3.27}$$

Since all parameters in (3.27) are constants except L, denote $A = T_{loading} 10^{\frac{P_t+G_t+G_{ugv}-20\lg\{f_c\}+147.55dB}{10}}$ and let $H = H_t - H_r$, one has

$$E_{ugv-DC} = \eta \frac{A}{L^2+H^2}. \tag{3.28}$$

Similarly, using (3.26) for the proposed Scheme 1, one has

$$E^{s1}_{ugv-DC} = \eta 10^{\frac{P^{s1}_{ugv}}{10}} \frac{E^{s1}_{available}}{10^{\frac{P^{s1}_{uav-t}}{10}} + P_{hover}}. \tag{3.29}$$

Denote $B = 10^{\frac{P^{s1}_{ugv}}{10}}$, $C = \eta 10^{\frac{P^{s1}_{uav-r}}{10}} T^{s1}_{loading} - E^{s1}_{hover} - 2\left(P^{s1}_{\overline{acc}}(\frac{v}{a}) + P^{s1}_{\overline{dec}}(\frac{v}{a})\right)$, $D =$

$10^{\frac{P^{s1}_{uav-t}}{10}} + P_{hover}$, $E = \frac{2P_v}{v}$ and $F = \frac{v^2}{a}$. Then from (3.29), one has

$$E^{s1}_{ugv-DC} = \eta \frac{B}{D} \left(C - E \left(L - F \right) \right). \tag{3.30}$$

Using (3.28) and (3.30), the critical distance can be found by letting $E_{ugv-DC} = E^{s1}_{ugv-DC}$ and $T_{loading} = T^{s1}_{loading}$ (i.e. assuming that the energy released from the BS to UAV is fixed.) to give

$$\frac{A}{L^2 + H^2} = \frac{B}{D} \left(C - E \left(L - F \right) \right). \tag{3.31}$$

It can be seen that (3.31) is an equation of the distance L only, and it can be solved by transforming it using the *Cardano* formula. The solution to (3.31) can be found in Appendix A.1. This gives the two critical distances as

$$cd_1 = 2\sqrt[3]{\sqrt{-\left(\frac{p}{3}\right)^3}} \cos\left(\frac{1}{3} \arccos\left(-\frac{q}{2} \right) + 240^\circ \right), \tag{3.32}$$

and

$$cd_2 = 2\sqrt[3]{\sqrt{-\left(\frac{p}{3}\right)^3}} \cos\left(\frac{1}{3} \arccos\left(-\frac{q}{2} \right) \right) - \frac{b}{3a}, \tag{3.33}$$

where $cd_1 < cd_2$, $a = BE$, $b = -\left(BC + BEF\right)$, $c = BEH^2$, $d = -BCH^2 - BEFH^2 + AD$, $p = \frac{c}{a} - \frac{b}{3a^2}$, $q = \frac{2b^3}{27a^3} - \frac{bc}{3a^2} + \frac{d}{a}$, and A, B, C, D, E, F, H are defined as before. Accordingly, the critical range is derived as

$$cd_1 \leq critical\ range \leq cd_2. \tag{3.34}$$

The Proposed Scheme 2 in Fig. 3.3

Now consider the proposed Scheme 2 in Fig. 3.3. In this scheme, instead of hovering above the BS in a static position for charging or discharging, the UAV starts at L_1 meters to the right of the BS and flies along both sides of the BS within a distance L_1 meters to be charged, and similarly within a distance of L_2 meters to be discharged. The main reason for this is that it is found that the hovering power P_{hover} is higher than the flying power P_v when the flying speed of v is relatively low [49] so that it may save more energy if the UAV stays mobile than staying static. The process of Scheme 2 in Fig. 3.3 can also be divided into three stages, *load*, *carry* and *charge*.

a) Load

During this stage, within a horizontal distance of L_1 meters on both sides of the BS, the UAV is being charged. In order to ensure that the received power at the UAV is not too small or the amount is reasonable when the UAV is located at a horizontal distance of L_1 meters from the BS, we set a threshold of P_ϵ, so that the maximum value of L_1 when $P^{s2}_{uav-r} = P_\epsilon$ can be calculated according to

$$P^{s2}_{uav-r}(t) = P_t + G_t + G_{uav} - L^{s2-1}_{FS(dB)}(t) = P_\epsilon \ dB, \tag{3.35}$$

where $L^{s2-1}_{FS(dB)}(t)$ is the transmission loss from the BS to the UAV given in (3.10). The threshold of P_ϵ can be changed to any other value, depending on the application. Thus, the maximum L_1 can be derived as

$$L_1 = \sqrt{10^{\frac{P_t+G_t+G_{uav}-20\lg\{f_c\}+147.55-P_\epsilon}{10}} - {H_1}^2}, \tag{3.36}$$

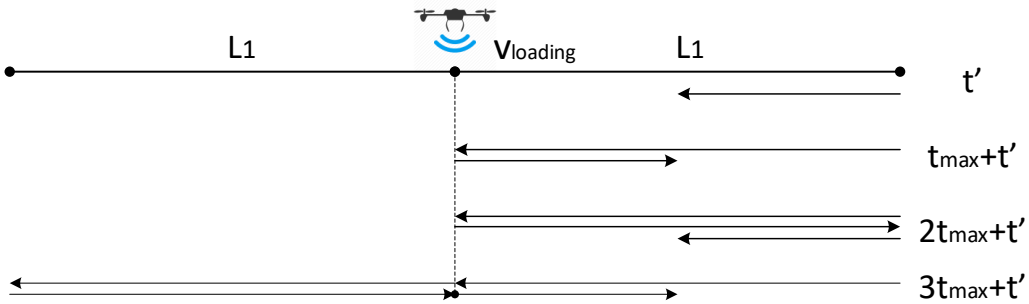

Figure 3.4: Different loading cases (Scheme 2).

where $H_1 = H_{loading} - H_t$. Also, we assume that the UAV flies at a fixed speed of $v_{loading}$ during loading. The instantaneous distance between the UAV and the BS within a horizontal distance of L_1 meter is

$$d_{s2-1}(t) = \sqrt{{H_1}^2 + (L_1 - v_{loading}t)^2}, \tag{3.37}$$

where $L_1 \geq v_{loading}t$ so that $0 \leq t \leq \frac{L_1}{v_{loading}}$. Accordingly, the received instantaneous power at the UAV can be expressed as

$$P_{uav-r}^{s2}(t) = \Omega - 20\lg\{d_{s2-1}(t)\}\ dB, \tag{3.38}$$

where $\Omega = P_t + G_t + G_{uav} - 20\lg\{f_c\} + 147.55$. Denote $t_{max} = \frac{L_1}{v_{loading}}$ as the maximum flight time on both sides of the BS. Since the received power at the UAV is changing with the time due to the flight, the total energy loaded during this time is

$$\begin{aligned} E_{t_{max}} &= \eta 10^{\frac{\Omega}{10}} \int_0^{t_{max}} \frac{1}{{H_1}^2 + (L_1 - v_{loading}t)^2}\, dt \\ &= \eta 10^{\frac{\Omega}{10}} \left[\xi \tan^{-1}\frac{v_{loading}t_{max} - L_1}{H_1} - \xi \tan^{-1}\frac{-L_1}{H_1}\right], \end{aligned} \tag{3.39}$$

where $\xi = \frac{1}{v_{loading} H_1}$, and we have used the integral in [52, eq. (2.103.4)]. It can be seen that the flight of the UAV is symmetric about the center point right above the BS. In other words, the time that is taken to fly to the right or the left is the same and the total energy loaded is also the same. It takes four flights for the UAV to complete a cycle and go back to the starting position. Thus, the total energy loaded for a complete cycle is $4E_{t_{max}}$. Also, denote the total loading time as $T^{s2}_{loading}$, Thus, it takes $\left\lceil \frac{T^{s2}_{loading}}{t_{max}} \right\rceil$ flights to finish the energy loading. Several cases can be discussed as shown in Fig. 3.4.

In the first case, in addition to the full cycles, there is some time t' ($t' < t_{max}$) left due to an incomplete flight when the UAV flies towards the BS. We calculate the energy loaded within t' that is less than t_{max} as

$$\begin{aligned} E^{s2-1}_{t'} &= \eta 10^{\frac{\Omega}{10}} \int_0^{t'} \frac{1}{{H_1}^2 + (L_1 - v_{loading} t)^2} \, dt \\ &= \eta 10^{\frac{\Omega}{10}} \left[\xi \tan^{-1} \frac{v_{loading} t' - L_1}{H_1} - \xi \tan^{-1} \frac{-L_1}{H_1} \right], \end{aligned} \tag{3.40}$$

where $0 \leq t' < t_{max}$. In this case, denote the total number of full cycles as $n_{4t_{max}}$. Then , we can calculate the total energy loaded within $T^{s2}_{loading}$ as

$$E^{s2}_{uav-DC} = n_{4t_{max}} * 4E_{t_{max}} + E^{s2-1}_{t'}. \tag{3.41}$$

In the second case, there is $t_{max} + t'$ left due to one complete flight and one incomplete flight. For time t', since the UAV flies away from the BS, we calculate

the energy loaded for this time as

$$\begin{aligned} E_{t'}^{s2-2} &= \eta 10^{\frac{\Omega}{10}} \int_0^{t'} \frac{1}{{H_1}^2 + (v_{loading} t)^2} \, dt \\ &= \eta 10^{\frac{\Omega}{10}} \left[\frac{1}{v_{loading} H_1} \tan^{-1} \left(t' \frac{v_{loading}}{H_1} \right) \right], \end{aligned} \tag{3.42}$$

where we have also used the integral [52, eq. (2.103.4)] in (3.42). Thus, the total energy loaded in this case can be calculated as

$$E_{uav-DC}^{s2} = n_{4t_{max}} * 4E_{t_{max}} + E_{t_{max}} + E_{t'}^{s2-2}. \tag{3.43}$$

In the third case, there is $2t_{max} + t'$ left due to two complete flights and one incomplete flight. According to the Fig. 3.4, the total energy loaded in this case can be calculated as

$$E_{uav-DC}^{s2} = n_{4t_{max}} * 4E_{t_{max}} + 2E_{t_{max}} + E_{t'}^{s2-1}. \tag{3.44}$$

In the last case, there is $3t_{max} + t'$ left due to three complete flights and one incomplete flight. Thus, the total energy loaded in this case can be calculated as

$$E_{uav-DC}^{s2} = n_{4t_{max}} * 4E_{t_{max}} + 3E_{t_{max}} + E_{t'}^{s2-2}. \tag{3.45}$$

The following Algorithm 1 can be used to calculate the total energy loaded by the UAV during the first stage with a loading time of $T_{loading}^{s2}$ in different cases. Denote N as the total number of flights within $T_{loading}^{s2}$, $n_{4t_{max}}$ as the total number of full cycles and $n_{t_{max}}$ as the number of complete flights beyond the number of full cycles. Note that, during the *load* stage the UAV also consumes energy for loading at a fixed speed of $v_{loading}$ with a power of $P_{v_{loading}}$ (watt). Thus, the consumption

Algorithm 1: Calculate the total energy loaded within $T^{s2}_{loading}$

1: Calculate the total number of flights for a loading $N = \left\lfloor \frac{T^{s2}_{loading}}{t_{max}} \right\rfloor$.
2: Calculate the number of full cycles during the loading process $n_{4t_{max}} = \left\lfloor \frac{N}{4} \right\rfloor$. Each full cycle has four flights.
3: Exclude the number of flights during loading that does not make a full flight $t' = T^{s2}_{loading} - N * t_{max}$.
4: The total energy loaded during $T^{s2}_{loading}$ can be calculated as:
5: **if** $n_{t_{max}} = 0$ or $n_{t_{max}} = 2$ **then**
6: $\quad E^{s2}_{uav-DC} = n_{4t_{max}} * E_{4t_{max}} + n_{t_{max}} * E_{t_{max}} + E^{s2-1}_{t'}$
7: **else if** $n_{t_{max}} = 1$ or $n_{t_{max}} = 3$ **then**
8: $\quad E^{s2}_{uav-DC} = n_{4t_{max}} * E_{4t_{max}} + n_{t_{max}} * E_{t_{max}} + E^{s2-2}_{t'}$
9: **end if**

during *load* stage can be derived as

$$E^{s2}_{v_{loading}} = P_{v_{loading}} T^{s2}_{loading}. \tag{3.46}$$

2) Carry

In this stage, after being charged by the BS in the above four different cases, an *acceleration-fly-deceleration* operation of the UAV will be performed to carry energy. Here is a summary of operations —the UAV starts to accelerate from $v_{loading}$ to a higher flight speed of v to deliver the energy. Then, it starts to decelerate from v to $v_{charging}$. As a result, the energy consumption of the *carry* stage can be expressed as

$$E^{s2}_{fly-to} = \begin{cases} \Phi + P_{v_{loading}} t', \\ \Phi + P_{v_{loading}} \left(t_{max} - t'\right), \end{cases} \tag{3.47}$$

where $\Phi = P_{\frac{s2}{acc}}\left(\frac{v-v_{loading}}{a}\right) + P_{\frac{s2}{dec}}\left(\frac{v-v_{charging}}{a}\right) + P_{v}^{s2}\frac{\left(L-(L_1+L_2)-\frac{v^2-{v_{loading}}^2}{a}\right)}{v}$ and $L-(L_1+L_2)-\frac{v^2-{v_{loading}}^2}{a} > 0$. Otherwise, there is no *carry* stage, similar to what discussed in (3.22), $P_{v_{loading}}t'$ and $P_{v_{loading}}\left(t_{max}-t'\right)$ in (3.47) are the consumption during the rest of the *load* stage caused by incomplete flights when $n_{t_{max}} = 0, 2$ and $n_{t_{max}} = 1, 3$ respectively.

3) Charge

In the third stage, we firstly derived the received RF power at the UGV as

$$P_{ugv}^{s2} = P_{uav-t}^{s2} + G_{uav} + G_{ugv} - L_{FS(dB)}^{s2-2}\left(t\right), \tag{3.48}$$

where $L_{FS(dB)}^{s2-2}\left(t\right)$ is the transmission loss from the UAV to the UGV given in (3.11). And the instantaneous distance in this case is given as

$$d_{s2-2}\left(t\right) = \sqrt{{H_2}^2 + \left(L_2 - v_{charging}t\right)^2}, \tag{3.49}$$

where $H_2 = H_{charging} - H_r$, $H_{charging} > H_r$, $L_2 \geq v_{charging}t$ so that $0 \leq t \leq \frac{L_2}{v_{charging}}$, L_2 is the maximum distance when $t = 0$ by letting $P_{ugv}^{s2} = -33$ dBm to give

$$L_2 = \sqrt{10^{\frac{\Omega'-16}{10}} - {H_2}^2}, \tag{3.50}$$

where $\Omega' = P_{uav-t}^{s2} + G_{uav} + G_{ugv} - 20\lg\left\{f_c\right\} + 147.55$. Hence, the received instantaneous power at the UGV can be expressed as

$$P_{ugv}^{s2}\left(t\right) = \Omega' - 20\lg\left\{d_{s2-2}\left(t\right)\right\}. \tag{3.51}$$

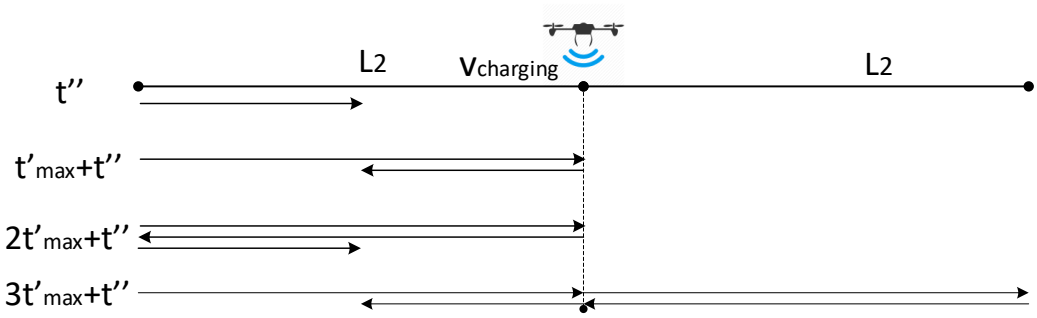

Figure 3.5: Different charging cases (Scheme 2).

Similar to the *load* stage, denote the $t'_{max} = \frac{L_2}{v_{charging}}$ as the maximum flight time on both sides of the UGV. Since the received power at the UGV is changing with the time because of the flight. the total energy received at the UGV during this time is

$$\begin{aligned} E_{t'_{max}} &= \eta 10^{\frac{\Omega'}{10}} \int_0^{t'_{max}} \frac{1}{{H_2}^2 + (L_2 - v_{charging} t)^2} \, dt \\ &= \eta 10^{\frac{\Omega'}{10}} \left[\xi' \tan^{-1} \frac{v_{charging} t'_{max} - L_2}{H_2} - \xi' \tan^{-1} \frac{-L_2}{H_2} \right], \end{aligned} \tag{3.52}$$

where $\xi' = \frac{1}{v_{charging} H_2}$ and [52, eq. (2.103.4)] is used here again. Note that, in order to make sure that the UAV can fly back to its initial position, the energy consumption for flying back, which is denoted as $E^{s2}_{fly-back}$, need to be considered. Then, $E^{s2}_{fly-back}$ can be calculated as

$$E^{s2}_{fly-back} = \begin{cases} \Phi' + P_{v_{charging}} t'', \\ \Phi' + P_{v_{charging}} \left(t'_{max} - t'' \right), \end{cases} \tag{3.53}$$

where $\Phi' = P^{s2}_{\overline{acc}} \left(\frac{v - v_{charging}}{a} \right) + P^{s2}_{\overline{dec}} \left(\frac{v - v_{loading}}{a} \right) + P^{s2}_{v} \frac{\left(L - (L_1 + L_2) - \frac{v^2 - {v_{charging}}^2}{a} \right)}{v}$, $L - (L_1 + L_2) - \frac{v^2 - {v_{charging}}^2}{a} > 0$, $P_{v_{charging}} t''$ and $P_{v_{charging}} (t'_{max} - t'')$ in (3.53) are the

power consumption during the rest of the *charge* stage due to incomplete flights when $n_{t'_{max}} = 0, 2$ and $n_{t'_{max}} = 1, 3$, respectively. However, it is difficult to calculate $E^{s2}_{fly-back}$ without knowing t'', because t'' is derived from $E^{s2}_{available}$ which is derived assuming knowledge of $E^{s2}_{fly-back}$. Thus, for convenience and in order to make sure the UAV has enough energy for flying back, the upper bound time t'_{max} is used, i.e. $P_{v_{charging}} t'_{max}$, to calculate the power consumption in the rest of the *charge* stage in Section 3.3. Consequently, the available energy for *charging* can be derived as

$$E^{s2}_{available} = E^{s2}_{uav-DC} - E^{s2}_{vloading} - E^{s2}_{fly-to} - E^{s2}_{fly-back}. \tag{3.54}$$

Fig. 3.5 shows different charging cases. It can be also seen that the flight of the UAV is symmetric about the center point right above the UGV. Thus, the time taken to fly to the right or the left is the same and the total energy to be charged is the same as well. It takes four flights for the UAV to complete a cycle and go back to the initial position. Therefore, the total energy received at the UGV for a complete cycle is $4E_{t'_{max}}$. Denote the total charging time as $T^{s2}_{charging}$ and in this case it can be calculated as

$$T^{s2}_{charing} = \frac{E^{s2}_{available}}{10^{\frac{P^{s2}_{uav-t}}{10}} + P_{v_{charging}}}. \tag{3.55}$$

Thus, it takes $\left\lceil \frac{T^{s2}_{charging}}{t'_{max}} \right\rceil$ flights to finish the energy discharging. Several cases in Fig. 3.5 can be discussed.

In the first case, there is only t'' ($t'' < t'_{max}$) seconds left for an incomplete flight when the UAV flies towards the UGV. The energy received at the UGV

during t'' is

$$\begin{aligned} E_{t''}^{s2-3} &= \eta 10^{\frac{\Omega'}{10}} \int_0^{t''} \frac{1}{{H_2}^2 + (L_2 - v_{charging} t)^2} \, dt \\ &= \eta 10^{\frac{\Omega'}{10}} \left[\xi' \tan^{-1} \frac{v_{charging} t'' - L_2}{H_2} - \xi' \tan^{-1} \frac{-L_2}{H_2} \right], \end{aligned} \tag{3.56}$$

where $H_2 = H_{charging} - H_r$ and $0 \leq t'' < t'_{max}$. Denote the total number of full cycles as $n_{4t'_{max}}$. Then, we can calculate the total energy discharged during $T^2_{charging}$ as

$$E^{s2}_{ugv-DC} = n_{4t'_{max}} * 4E_{t'_{max}} + E^{s2-3}_{t''}. \tag{3.57}$$

In the second case, there is $t'_{max} + t''$ left due to one complete flight and one incomplete flight. For time t'', since the UAV flies away from the UGV, we calculate the energy discharged during t'' as

$$E^{s2-4}_{t''} = \eta 10^{\frac{\Omega'}{10}} \int_0^{t''} \frac{1}{{H_2}^2 + (v_{charging} t)^2} dt = \eta 10^{\frac{\Omega'}{10}} \left[\xi' \tan^{-1} \left(t'' \frac{v_{charging}}{H_2} \right) \right], \tag{3.58}$$

where $0 \leq t'' < t'_{max}$. In this case, the total energy discharged can be calculated as

$$E^{s2}_{ugv-DC} = n_{4t'_{max}} * 4E_{t'_{max}} + E_{t'_{max}} + E^{s2-4}_{t''}. \tag{3.59}$$

In the third case, there is $2t'_{max} + t''$ left due to two complete flights and one incomplete flight. According to Fig. 3.5, the total energy discharged in this case can be calculated as

$$E^{s2}_{ugv-DC} = n_{4t'_{max}} * 4E_{t'_{max}} + 2E_{t'_{max}} + E^{s2-3}_{t''}. \tag{3.60}$$

In the last case, if there is $3t'_{max} + t''$ left due to three complete flights

Algorithm 2: Calculate the total energy charged within $T^{s2}_{charging}$

1: Calculate the total number of flights for charging process $N' = \left\lfloor \frac{T^{s2}_{charging}}{t'_{max}} \right\rfloor$.
2: Calculate the number of full cycles during charging process $n_{4t'_{max}} = \left\lfloor \frac{N'}{4} \right\rfloor$. Each full cycle has four flights.
3: Exclude the number of flights during charging that does not make a full cycle $t'' = T^{s2}_{charging} - N' * t'_{max}$
4: The total energy charged within $T^{s2}_{charging}$ can be calculated as
5: **if** $n_{t'_{max}} = 0$ or $n_{t'_{max}} = 2$ **then**
6: $\quad E^{s2}_{ugv-DC} = n_{4t'_{max}} * E_{4t'_{max}} + n_{t'_{max}} * E_{t'_{max}} + E^{s2-3}_{t''}$
7: **else if** $n_{t'_{max}} = 1$ or $n_{t'_{max}} = 3$ **then**
8: $\quad E^{s2}_{ugv-DC} = n_{4t'_{max}} * E_{4t'_{max}} + n_{t'_{max}} * E_{t'_{max}} + E^{s2-4}_{t''}$
9: **end if**

and one incomplete flight, Thus, the total energy discharged in this case can be calculated as

$$E^{s2}_{ugv-DC} = n_{4t'_{max}} * 4E_{t'_{max}} + 3E_{t'_{max}} + E^{s2-4}_{t''}. \tag{3.61}$$

Algorithm 2 can be used to calculate the total energy received by the UGV during the *charge* stage within time $T^{s2}_{charging}$. Denote N' as the total number of flights within $T^{s2}_{charging}$, $n_{4t'_{max}}$ as the total number of full cycles and $n_{t'_{max}}$ as the number of complete flights beyond the number of full cycles.

Next, We will investigate the trade-off by finding the transmission critical distance beyond which the proposed Scheme 2 has advantages over the conventional direct transfer. According to Algorithm 2, the total energy harvested by the UGV with $T^{s2}_{charging}$ can be expressed as

$$\begin{aligned} E^{s2}_{ugv-DC} = &\left\lfloor \frac{\lfloor \Psi \rfloor}{4} \right\rfloor * E_{4t'_{max}} + (\lfloor \Psi \rfloor \bmod 4) * E_{t'_{max}} \\ &+ (((\lfloor \Psi \rfloor \bmod 4) + 1) \bmod 2) * E^{s2-3}_{t''} + ((\lfloor \Psi \rfloor \bmod 4) \bmod 2) * E^{s2-4}_{t''}, \end{aligned} \tag{3.62}$$

where $\Psi = \frac{T^{s2}_{charging}}{t'_{max}}$. Using (3.28) and (3.62) (i.e.$E_{ugv-DC} = E^{s2}_{ugv-DC}$), we have

$$\eta \frac{A}{L^2 + H^2} = \left\lfloor \frac{\lfloor \Psi \rfloor}{4} \right\rfloor * E_{4t'_{max}} + (\lfloor \Psi \rfloor \bmod 4) * E_{t'_{max}} + (((\lfloor \Psi \rfloor \bmod 4) + 1) \bmod 2) * E^{s2-3}_{t''} + ((\lfloor \Psi \rfloor \bmod 4) \bmod 2) * E^{s2-4}_{t''}. \tag{3.63}$$

It is not easy to solve the above equation. The critical distance in Scheme 2 can be obtained numerically. We next consider the more general case when multiple receivers are charged.

3.3.3 Conventional Scheme with Multiple Receivers

In this case, n receivers on the UGV need to be powered. Assume that these receivers are very close to each other on the UGV so that their distance to the BS are approximately the same. Then, the total energy harvested by n receivers in this case can be calculated as

$$E_{ugvs-DC} = \sum_{i=1}^{n} E_{ugv_i-DC} = \sum_{i=1}^{n} \eta 10^{\frac{P_{ugv_i}}{10}} T_{loading}, \tag{3.64}$$

where $i = 1, 2, ..., n$ index different receivers, P_{ugv_i} is the received power of the i-th UGV, $E_{ugv_i\_RF}$ is the received RF energy of the i-th UGV and E_{ugv_i-DC} is the converted DC energy of the i-th UGV. One has

$$P_{ugv_i} = P_t + G_t + G_{ugv_i} - 20\lg\{f_c\} - 20\lg\{d_0\} + 147.55 - X\ dB, \tag{3.65}$$

$$E_{ugv_i\_RF} = 10^{\frac{P_{ugv_i}}{10}} T_{loading}, \tag{3.66}$$

$$E_{ugv_i\_DC} = \eta E_{ugv_i\_RF}. \tag{3.67}$$

3.3.4 New Schemes with Multiple Receivers

Similar to the above case, there are n receivers in this case. They are approximately of the same distance to the UAV. For the proposed Scheme 1, the total energy harvested by n receivers can be derived from (3.26) as:

$$E^{s1}_{ugvs-DC} = \sum_{i=1}^{n} E^{s1}_{ugv_i-DC} = \sum_{i=1}^{n} \eta 10^{\frac{P^{s1}_{ugv_i}}{10}} T^{s1}_{charging}, \tag{3.68}$$

where $i = 1, 2, ..., n$ index different receivers. For the proposed Scheme 2, the total energy harvested by n receivers can be derived based on Algorithm 2 as

$$\begin{aligned} E^{s2}_{ugvs-DC} = &\sum_{i=1}^{n} \left\lfloor \frac{\lfloor \Psi \rfloor}{4} \right\rfloor * E_{4t'_{max}} + (\lfloor \Psi \rfloor \bmod 4) * E_{t'_{max}} \\ &+ (((\lfloor \Psi \rfloor \bmod 4) + 1) \bmod 2) * E^{s2-3}_{t''} + ((\lfloor \Psi \rfloor \bmod 4) \bmod 2) * E^{s2-4}_{t''}. \end{aligned} \tag{3.69}$$

It is noted that the case when multiple receivers are not close to each other is an interesting issue for future works. Since this issue will lead to many optimization problems, such as optimal hovering position, trajectory design and power optimization, etc., it is beyond the scope of this work.

3.4 Numerical Results and Discussion

In this section, numerical examples are presented to show the energy performances of the proposed schemes. First, we compare the conventional scheme and the proposed schemes for a single receiver on the UGV. Then, we expand the discussion to the case of multiple receivers on the UGV. In the comparison, we set $P_t = 35.68$

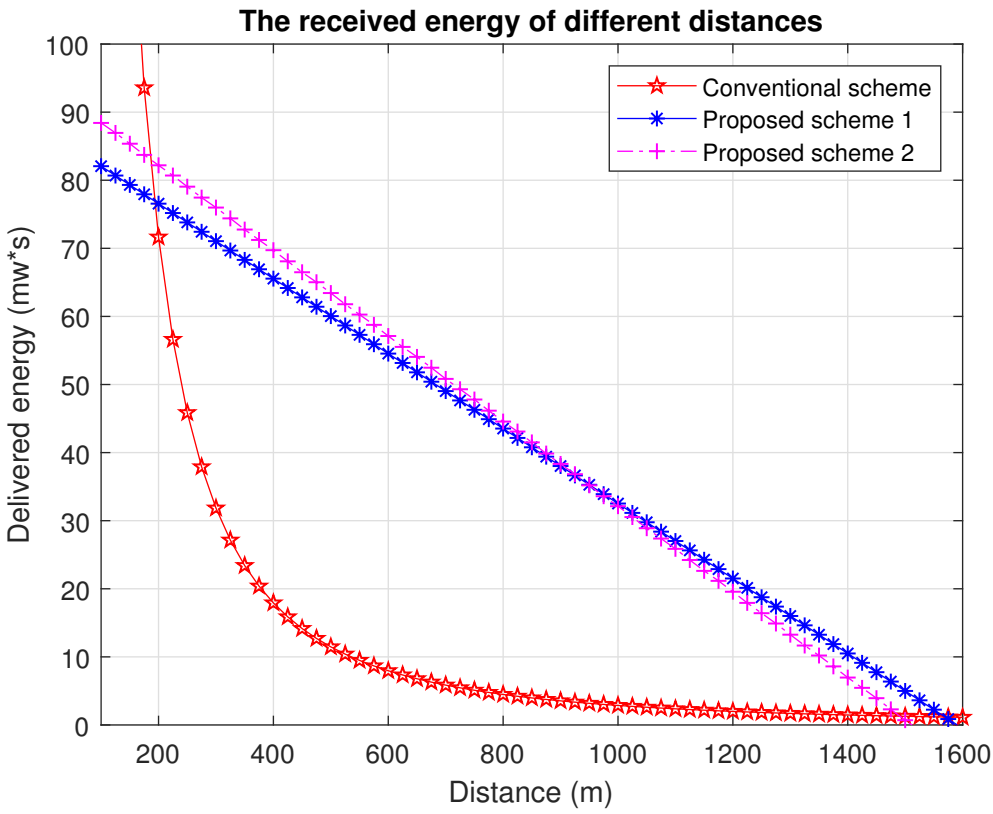

Figure 3.6: The comparison of the proposed Schemes 1 and 2.

dBw, $G_t = 15$ dBi [91], $G_{uav} = 2$ dBi, $G_{ugv} = 5$ dBi, $P^{s1}_{uav-t} = P^{s2}_{uav-t} = 40$ dBm, $H_{loading} = 6$ m, $H_t = 5$ m, $H_r = 0.5$ m, $f_c = 915$ MHZ, $T_{loading} = T^{s1}_{loading} = T^{s2}_{loading} = 1200$ s, $P_{hover} = 32.65$ W, $P_v = P^{s1}_v = P^{s2}_v = 20$ W, $P^{s1}_{acc} = P^{s1}_{dec} = P^{s2}_{acc} = P^{s2}_{dec} = 28$ W, $V = 10$ m/s, $a = 1$ m/s^2, $X = 18$ dB and the RF-to-DC conversion efficiency $\eta = 0.6$, if not stated otherwise[1]. Our expressions are general enough for arbitrary parameters and hence, these values are only used for illustration purpose. The value of the distance L is set from 100 m to 1600 m with a step size of 25 m.

Fig. 3.6 shows the amount of the received energy at the UGV versus distance

[1]Considering the distance between the BS and the UAV has a major impact on the efficiency of RF energy transfer, we try to select the parameter values as small as possible within a reasonable range, such as height H_t and power for different manoeuvres.

L. Firstly, we consider the proposed Scheme 1. One can see that, when the total energy transmitted by the BS is fixed, the energy received by the UGV decreases with the distance in both the conventional scheme and the proposed Scheme 1 because of the path loss and UAV internal loss. However, as seen in Fig. 3.6, the total energy obtained in the conventional scheme decreases exponentially with the transmission distance. This is due to the fact that the path loss is a logarithmic function of transmission distance. Beyond a transmission distance of about 1500 m, the received energy is very close to 0. On the other hand, the straight line with asterisks representing the proposed Scheme 1 shows that its received energy decreases linearly with a fixed slope and hence is a linear function of the transmission distance. This can be explained as follows. The UAV first harvests a certain amount of energy from the BS and then flies to the UGV. Due to the values of UAV speed and flight height are constants, the propulsion consumption is proportional to the distance. As a result, the available energy for charging UGV is in inverse proportion to the distance. This makes UAV-enabled WPT improve the energy transfer efficiency greatly. As shown in Fig. 3.6, there are two intersection points between the conventional scheme and the proposed Scheme 1. The corresponding X coordinates are the critical distances, which are 192.99 m and 1569.62 m in this case derived from (3.32) and (3.33). Thus, when the transmission distance is within this range, the proposed Scheme 1 shows superiority over the conventional direct transfer scheme. For the critical distance 192.99 m, beyond which the proposed scheme shows better performance than the conventional scheme over the distance. However, for the critical distance 1569.62, since the received energy at receivers is almost 0, the discussion is of little significance. Hence, the critical distance we discuss will refer to the X coordinate value of the left intersection, i.e., cd_1 in (3.34), if not stated otherwise.

Next, we investigate the proposed Scheme 2. In this case, we set $P_{v_{loading}} =$

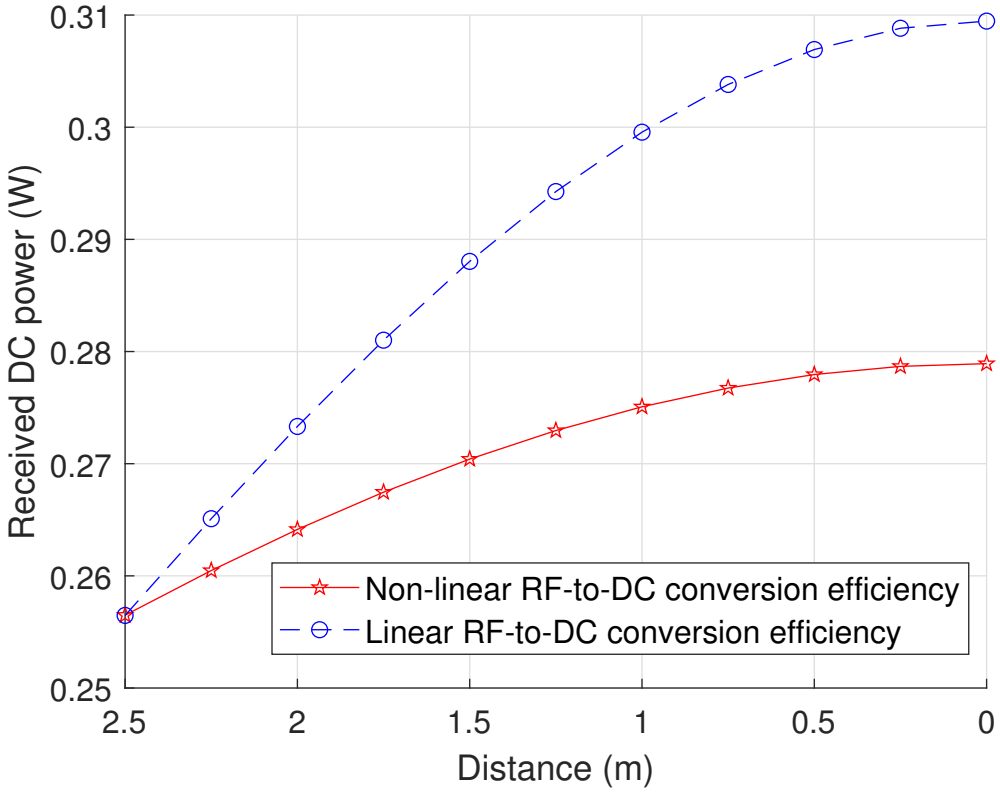

Figure 3.7: The comparison of received power using linear model and non-linear model.

25.5 W, and the minimum value of P^{s2}_{uav-r} is set to 21 dBw (i.e. $P_\epsilon = 21$ dBw). Fig. 3.6 also compares the conventional scheme and the proposed Scheme 2 represented by the straight line with plus signs. Similar observations can be made. Again, the received energy in the conventional scheme decreases exponentially with the distance, while it decreases linearly in the proposed Scheme 2. Also, compared with the Scheme 1, we can see that the energy loaded from the BS of Scheme 2 is higher than that of Scheme 1. For Scheme 1, the UAV hovers over the BS during loading. Although the path loss between the UAV and the BS is minimum and remains unchanged, it consumes larger energy to keep hovering with a power of P_{hover}. For Scheme 2, the UAV no longer hovers over the BS with a power of P_{hover}, but flies

around the BS during loading with at a fixed speed of $V_{loading}$, which means it suffers from larger path loss with longer distance. The path loss becomes larger when the UAV flies farther away from the BS. Although the distance between the UAV and the BS changes with time and in general is larger than that in Scheme 1, the propulsion power of $P_{v_{loading}}$ is smaller than P_{hover}. From Fig. 3.6, we can see that the critical range of Scheme 2 is between 188 m and 1490 m. This critical distance is smaller than that in Scheme 1.

From Fig. 3.6, one can see that the critical range in Scheme 1 is between 192.99 m and 1569.62 m, and that in Scheme 2 is between 188 m and 1490 m. The critical distances cd_1 and cd_2 in Scheme 2 is smaller than that in Scheme 1 (188<192.99 and 1490<1569.62), which means the Scheme 2 has advantages than Scheme 1 by having shorter distance cd_1. As shown in this figure, there is one intersection point between Scheme 1 and Scheme 2. The corresponding X coordinate value is about 942 m, beyond which Scheme 1 has better efficiency than Scheme 2. This is due to the fact that, although the energy loaded by the UAV in Scheme 2 from the BS during *load* stage is larger than that of Scheme 1 since the $P_{v_{loading}}$ is small than P_{hover}, it suffers from an even larger path loss during the *charge* stage. Although the UAV in Scheme 1 suffers from an even larger consumption of hovering in these two stages. the path loss between the UAV and the UGV is minimum and remains unchanged. Next, we will examine the effects of different system parameters on the critical range.

Fig. 3.7 compares the received DC power over distance using linear and non-linear RF-to-DC models. In this figure, the horizontal distance between the UAV and the receiver is set from 2.5 m to 0 m with a step size of 0.5 m. One can see that, for both models, the received DC power increases with the decrease of the distance between the UAV and the receiver. This is because the reduction

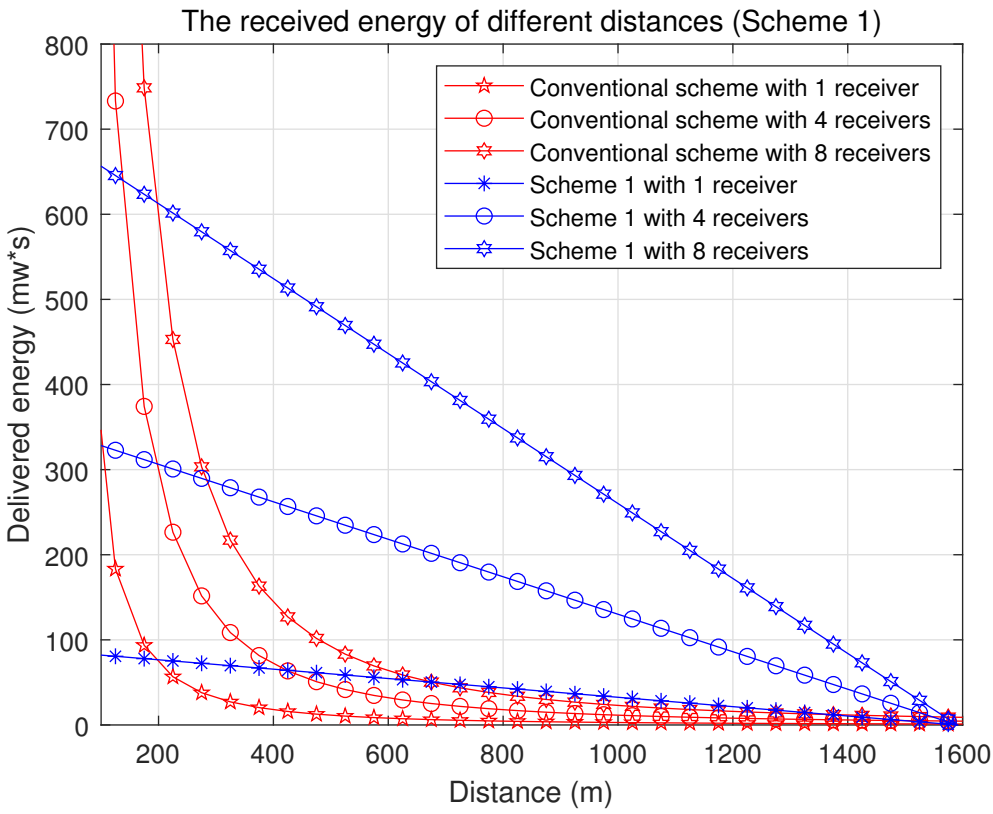

Figure 3.8: Comparison of the conventional scheme and the proposed Scheme 1 with multiple receivers. (The number is 1, 4 and 8 respectively.)

of the distance reduces the path loss and increases the received power. However, the received DC power using non-linear model is smaller than using linear model. This means that with the increase of received power, the non-linear RF-to-DC conversion efficiency decrease.

Fig. 3.8 uses the proposed Scheme 1 as an example to compare the conventional scheme and the proposed Scheme 1 for multiple receivers. We set the number of the receivers to 1, 4 and 8 using (3.64) and (3.68). As shown in this figure, the curves in Fig. 3.8 have exactly the same trend as those in Fig. 3.6, except that the rate of decrease is proportional to the number of receivers. There are six

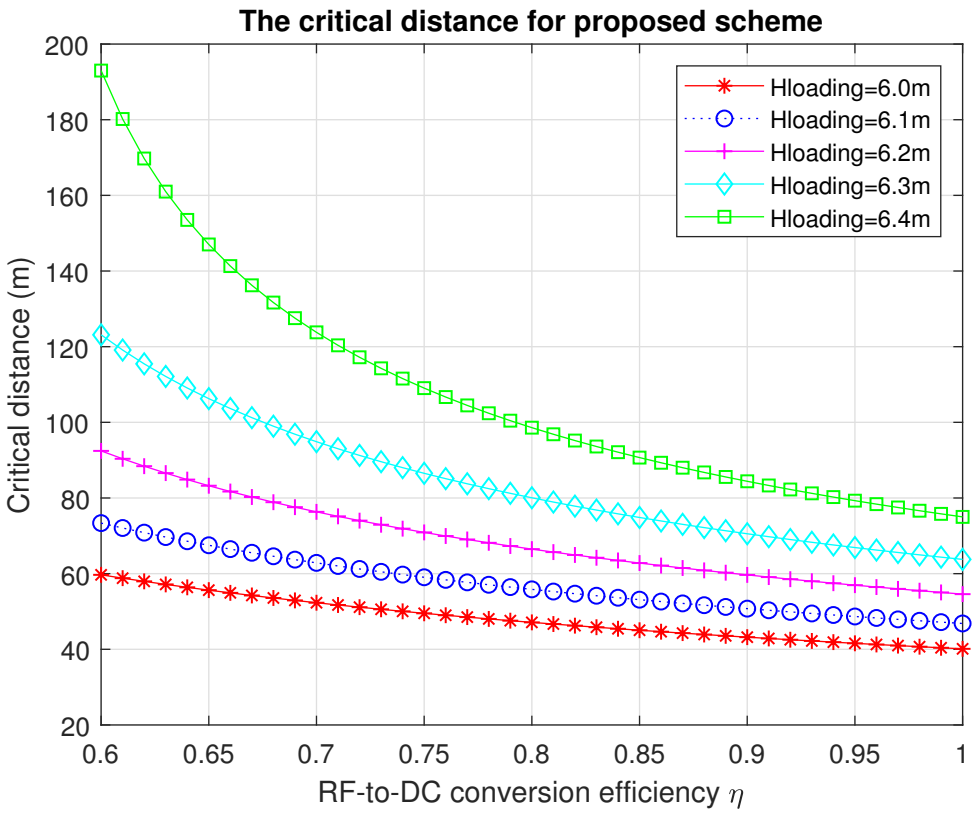

Figure 3.9: The effects of RF-to-DC conversion efficiency η on the proposed scheme 1 performance for different flight heights.

intersection points in the figure. Note that the critical range observed in Fig. 3.6 remains the same in this figure, as all the parameters are the same except for the number of receivers but this number does not change the intersection points.

Fig. 3.9 examines the effect of the RF-to-DC conversion efficiency η on the critical distance. First, one can see that the critical distance decreases with η. This is because a higher conversion efficiency leads to more loaded or charged energy and hence, gives the proposed Scheme 1 more advantages with a shorter critical distance. It can also be seen that the higher the flight altitude is, the greater the critical distance will be. In these curves, we consider the starting point

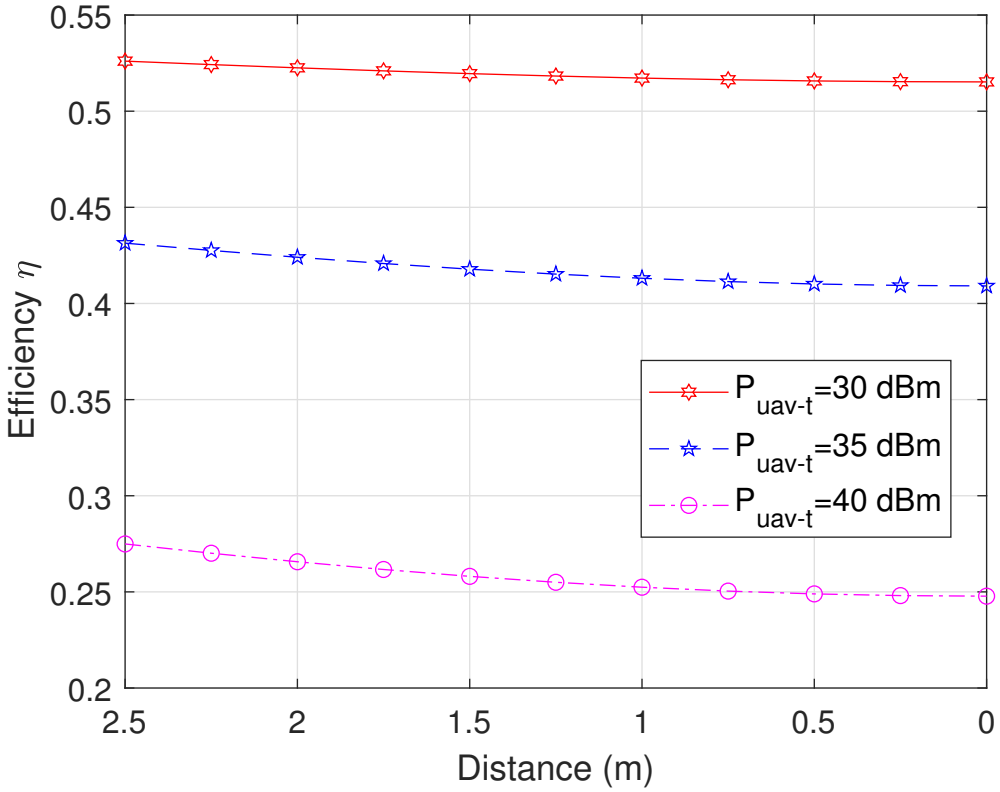

Figure 3.10: Non-linear RF-to-DC conversion efficiency VS distance.

of the critical range. When the transmission distance exceeds this critical distance without exceeding the critical range, the Scheme 1 shows better energy transfer efficiency performance. The same performance can also be seen for Scheme 2.

Fig. 3.10 examines the change of non-linear RF-to-DC conversion efficiency when the transmission distance decreases. In the figure, the transmission distance is set from 2.5 m to 0 m as in Fig. 3.7. One sees that the non-linear efficiency decreases as the distance reduces. In other words, the reduction of transmission distance means that the received power increases, but the conversion efficiency decreases. This can be also observed by comparing the efficiency under different transmit power when the distance is fixed. Taking the transmission distance of

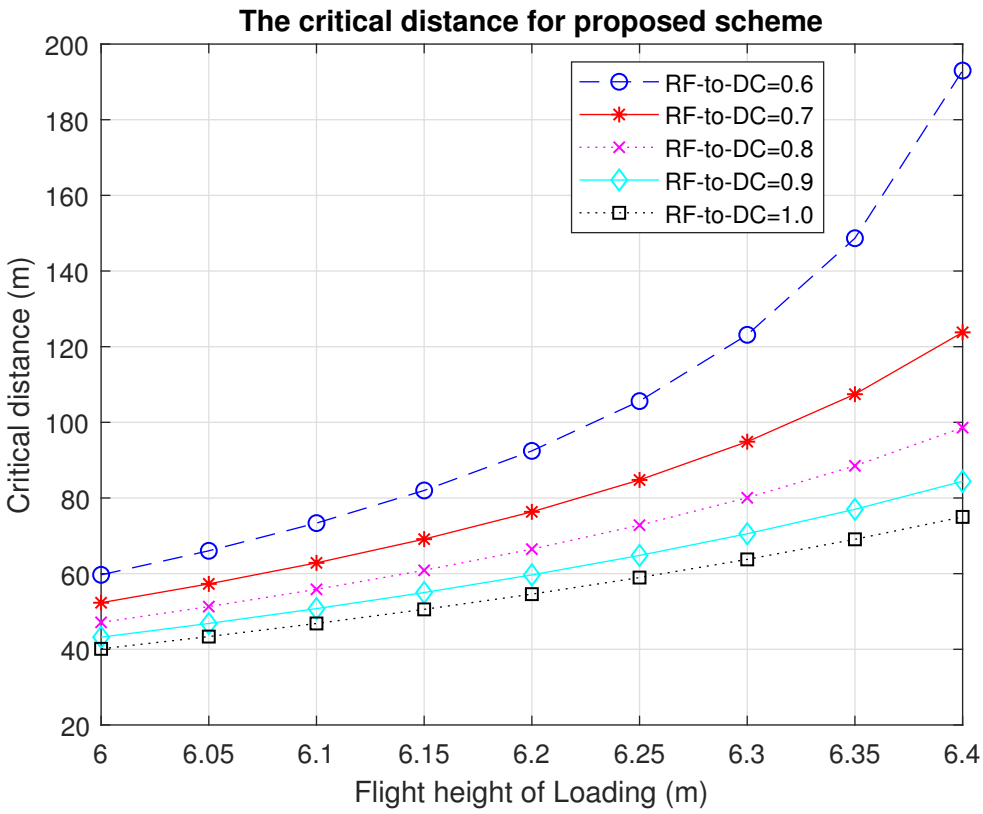

Figure 3.11: The effects of the loading height of the UAV on the proposed Scheme 1 performance for different RF-to-DC conversion efficiency η.

1.5 m as an example. one can see that when $P_{uav-t} = 40$ dBm, the efficiency η is smaller than that when $P_{uav-t} = 35$ dBm, and the efficiency when $P_{uav-t} = 35$ dBm is smaller than that when $P_{uav-t} = 30$ dBm. As a result, increasing the transmission power can improve the energy harvested by the receiver, but it is at the cost of large conversion loss.

Fig. 3.11 examines the effect of the flight height on the critical distance. The height of the BS is assumed to be 5 m, and the height of the UGV is set as 0.5 m. First, one can see that the critical distance increases with the flight height of loading. This is because a lower height of loading leads to more loaded

or charged energy and thus, gives the proposed Scheme 1 and Scheme 2 more advantages with a shorter critical distance. When the loading height increases, the path loss increases. As a result, the energy obtained by the UAV is reduced, which is unfavorable to the proposed schemes. Note that, the conventional direct transfer scheme is the existing algorithm. There is no other energy ferry work in the literature.

3.5 Summary

In this chapter, we have studied the WPT efficiency in UAV-enabled wireless networks. We have proposed two schemes for UAV-enabled WPT. By solving the energy equations, critical ranges have been derived. Numerical results have shown that the energy received by the UGV decreases with the transmission distance because of the path loss and UAV internal loss in both schemes. Within the critical range, the proposed two schemes have been shown to have better performances than the conventional scheme. The lower the loading height or the larger the RF-to-DC conversion efficiency is, the smaller the critical distance will be. To improve the performance of the proposed schemes further, one needs to carefully adjust parameters, such as task time, antenna gain, transmit power, energy conversion efficiency, battery capacity on the UAV, and the UAV velocity, which could require optimization with extra costs.

Chapter 4

Optimal Location for UAV-Enabled WPT

This chapter is based on our work published in [J2]. ([92])

4.1 Introduction

In recent years, UAVs have found a significant number of applications in wireless communication and transportation systems due to their decreasing expense and increasing functionality [2, 4]. From the viewpoint of communications, the UAV can be used as an aerial BS for wireless coverage, or as a mobile relay to provide reliable communication links for distant users [17, 93]. For example, in remote areas when the communication infrastructure is damaged by natural disasters, UAVs can serve as an aerial BS to provide wireless services [94]. Other UAV applications include UAV-aided wireless networking [95–97], future intelligent and

secure UAV networks for 6G [98]. This chapter mainly focuses on the application where a UAV employs RF WPT to charge a set of ground sensors in a remote area, that is, UAV-enabled WPT.

Wireless charging [32, 33] has been recognized as a promising technique to provide energy supply for battery-limited nodes, such as IoT devices and sensors. For example, works reviewed in Section 2.5.1 have provided very valuable guidance on the use of UAV-enabled WPT system. However, several challenges in this field remain. Firstly, the power consumption of the UAV (i.e., power consumption from its hovering for charging and discharging, and from its propulsion for flight) is very important in these applications, but this issue has been largely overlooked in the existing works. Secondly, the UAV is an energy-limited node itself. Thus, it has to be charged by a BS wirelessly without landing [35] before transferring power to remote nodes. Most works only consider the power transfer from the UAV to the remote sensors but do not consider the power transfer from the BS to the UAV. In [43], the energy transfer efficiency from BS to sensors by employing UAV as a mobile energy transmitter has been analyzed without optimizing the location of UAV in multiple sensors case. Thirdly, many of the previous works (i.e., [36–38] and [39]) have ignored the RF-to-DC energy conversion efficiency by assuming perfect discharging at the energy receiver. Due to the increased use of UAVs in communication systems [99–101], these issues require urgent attention. To the best of the authors' knowledge, the UAV-enabled WPT problem considering all these three issues has not been studied yet.

Motivated by these observations, in this chapter, we study the use of the UAV in a UAV-enabled WPT system, where the UAV is deployed to charge the ground sensors after being charged by the BS. In the study, we take into account the power consumption at the UAV, the power transfer from the BS to UAV and

the practical conversion efficiency at the energy receiver. To do this, we will first derive the optimal location of the UAV when the ground sensors are deployed in a 1D topology, as the case in [37]. Then, we will investigate the more complicated case when the ground sensors are deployed in a two-dimensional (2D) topology. For both cases, the optimal locations of UAVs will be derived by maximizing the sum-energy received by all ground sensors. Numerical results will be presented to show that the optimal locations have to be closer to the BS than what was reported in previous works that did not consider the power consumption of the UAV. The main contributions of this work can be summarized as follows:

- Two different charging schemes for both 1D and 2D topologies in UAV-enabled WPT systems are studied by considering the BS charging process and the UAV power consumption.
- The optimal locations of the UAV in WPT system in these two different cases are derived analytically.
- The effects of different system parameters on the energy transfer performance are examined to give useful guidance for system designs.

The remainder of this chapter is organized as follows. In Section 4.2, the system model is explained. Section 4.3 and 4.4 derive the optimal location of UAVs in WPT system in 1D and 2D cases, respectively. Section 4.5 presents numerical results. Finally, the work is concluded in Section 4.6.

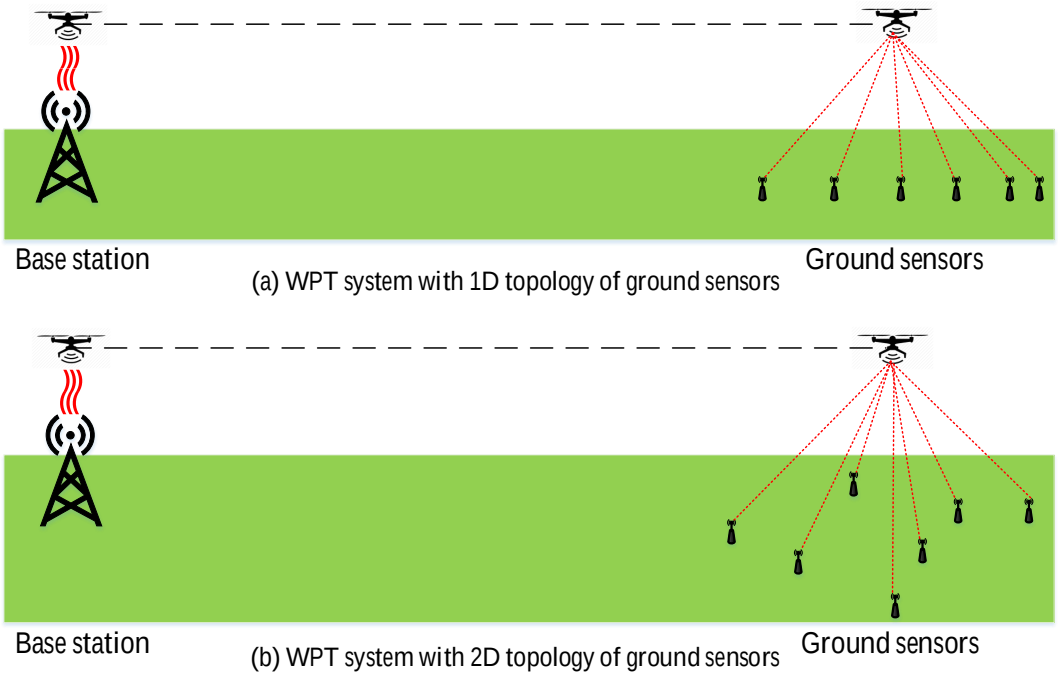

Figure 4.1: 1D and 2D topologies.

4.2 System Model

Consider two typical scenarios, where the ground sensors are distributed either in a 1D or 2D topology, as shown in Fig. 4.1. A rotary-wing UAV is first charged by a BS wirelessly in its close proximity, then flies to $K \geqslant 2$ remote ground sensors to charge them wirelessly for sustained operations. Let k index the sensors with $1 \leqslant k \leqslant K$. In our study, only the locations of the sensors are needed. The structure and topology of the ground sensor network will not affect the derivation. In Fig. 4.1(a), all ground sensors are located on a straight line, as the case in [37]. In Fig. 4.1(b), they are assumed to be located on a 2D surface. Let $(0, 0, H_{bs})$ denote the location of the BS with a height of H_{bs}, and the kth ground sensor is located at (x_k, y_k, H_{sr}) with a common antenna height of H_{sr}, i.e., $(x_k, 0, H_{sr})$ for

1D and (x_k, y_k, H_{sr}) for 2D. The UAV is assumed to fly at a fixed height H above the ground [24, 36–38, 41, 42], because there is always a "near-far" issue which may aggravate the fairness among sensors. Thus, its location can be denoted as (x, y, H). Also, it is assumed that all sensors have enough battery capacity for charging.

In this work, we assume wireless charging by the BS to the UAV. This is the case when there is no dedicated landing dock at the BS for wired charging, as in conventional BSs. This is also the case when it is not convenient or safe for the UAV to land due to the complicated environment surrounding the BS. In the case when wired charging is available at the BS, the following results are still valid by ignoring the *Load* stage of the BS charging or assuming zero loss from the BS to the UAV. In order to quantify the energy consumption of the UAV during the WPT from the UAV to ground sensors, the energy consumption in different phases of the process will be analyzes. The energy consumption mainly comes from the transmission loss from the BS to the UAV, and from the UAV to the ground sensors, the conversion loss from RF to DC at both the UAV and ground sensors, and the UAV power consumption due to the UAV manoeuvre, such as hovering, acceleration, deceleration and flying at a constant speed. These will be discussed in the following.

4.2.1 Transmission Loss

As the UAV hovers above the BS in its close proximity to be charged, a LoS link can be established between the BS and the UAV[1]. Similarly, we assume a LoS link

[1]Note that fading or probability of LoS may exist when H is large [17, 24, 29, 32, 33, 35–39, 41–43, 55, 56, 93–101]. When H is small, as in works [24, 36–39, 41, 42], fading and probability of LoS can be ignored because H is small and the channel link is dominated by LoS. We use the same system model as [24, 36–39, 41, 42] by ignoring fading and LoS probability. However, the result

between the UAV and ground sensors, as in [24, 36–39, 41, 42]. According to the FSPL model, the transmission loss in these links can be expressed as

$$PL_{FS} = 20\lg\{f\} + 20\lg\{d\} - 147.55\ dB, \tag{4.1}$$

where d ($d \geqslant 1$) is the distance between the transmitter and the receiver, and f is the carrier frequency. Note that in FSPL model $d \geqslant 1$, because the received power per unit area starts at a reference distance of 1 m [51].

As the channel between the BS and the UAV is dominated by LoS, the transmission loss from the BS to the UAV in both Fig. 4.1(a) and Fig. 4.1(b) can be expressed as

$$PL_{bs-uav} = 20\lg\{f\} + 20\lg\{H - H_{bs}\} - 147.55\ dB, \tag{4.2}$$

where $H - H_{bs} \geqslant 1$ m is the distance between the BS and the UAV.

Also, since the wireless channel between the UAV and each ground sensor is dominated by LoS, similar to [24, 36–39, 41, 42], the transmission loss from the UAV to the kth sensor in Fig. 4.1(a) can be expressed by adopting the FSPL model in (4.1) as

$$PL^{1D}_{uav-gs} = 20\lg\{f\} + 20\lg\left\{d^{1D}_{uav-gs_k}\right\} - 147.55\ dB, \tag{4.3}$$

and in Fig. 4.1(b) as

$$PL^{2D}_{uav-gs} = 20\lg\{f\} + 20\lg\{d^{2D}_{uav-gs_k}\} - 147.55\ dB, \tag{4.4}$$

of this chapter can be extended to the scenario considering fading or LoS probability where the channel link is dominated by both LoS and NLoS.

where $d^{1D}_{uav-gs_k} = \sqrt{(x - x_k)^2 + (H - H_{sr})^2}$ is the distance between the UAV and the kth sensor in the 1D case, $d^{2D}_{uav-gs_k} = \sqrt{(x - x_k)^2 + (y - y_k)^2 + (H - H_{sr})^2}$ in the 2D case, and $H - H_{sr} \geqslant 1$.

4.2.2 UAV Power Consumption

In addition to the energy transferred to the ground sensors, the UAV also requires energy for various manoeuvres (i.e. hovering, acceleration, deceleration and flying to fly to the sensors). For example, the authors in [102] studied the trade-off between power consumption and flight performance of fixed wing UAV. We will calculate the internal energy consumption of UAV using the model in (2.11). In this study, for forward level flight, we consider the process when the UAV accelerates from an initial velocity of 0 to V and continues to fly to the sensors at the speed of V, and finally decelerates from V to 0 to hover over the sensors for charging. Hence, the energy consumed by the UAV during the acceleration can be calculated as

$$E_{Acc} = \int_0^{\frac{V}{a}} P(t)\ dt, \tag{4.5}$$

where $\frac{V}{a}$ is the acceleration time, as $v_0 = 0$, $P(t) = P[V(t)] = P_0\left(1 + \frac{3(at)^2}{U_{tip}^2}\right) + P_i\left(\sqrt{1 + \frac{(at)^4}{4v_0^4}} - \frac{(at)^2}{2v_0^2}\right)^{1/2} + \frac{1}{2}d_0\rho sA(at)^3$ by substituting (2.15) into (2.11). Since acceleration and deceleration in this study are symmetric, the energy consumed during deceleration is the same as that during acceleration, i.e., $E_{Acc} = E_{Dec}$. The calculation of (4.5) is given in Appendix B.1.

For both the 1D case in Fig. 4.1(a) and the 2D case in Fig. 4.1(b), the UAV hovers above the BS to be charged wirelessly, then accelerates to a constant speed of V and flies to the sensors. When it approaches the ground sensors, it

decelerates from V to 0 and then hovers above the sensors to charge them before flying back to the BS in the same way. Thus, hovering, acceleration, deceleration, and flying are the four operations that need to be considered in our study.

4.2.3 RF-to-DC Conversion Loss

From the simulation results in [40], it was found that the conversion efficiency depends on the input power. When the input power is below a threshold, the output power increases linearly with the input power. Thus, we assume that the energy harvester works in this linear region and the linear model is used in this case as assumed in [24, 41–43]. Using (2.6), one has

$$P_{DC} = \eta \cdot 10^{\frac{P_{RF}}{10}}, \tag{4.6}$$

where P_{RF} is the received RF power, η is the constant RF-to-DC conversion efficiency and P_{DC} is the converted DC power at the harvester.

Remark 1

Note that many factors could affect the optimal location of the UAV that maximizes the sum-energy received by all sensors, such as the number of sensors, the trajectory and the velocity of the UAV, etc. The UAV has to fly back to the BS after charging the sensors but needs to maximize the energy delivered to sensors. Firstly, the actual topology of the 1D and 2D WPT systems may be less important, as long as they are within the coverage area of the UAV WPT. If the area is too large, although the sum-energy is maximized, it may lead to unfairness among the sensors, especially those at the edge of the cell. Secondly, placing the UAV at

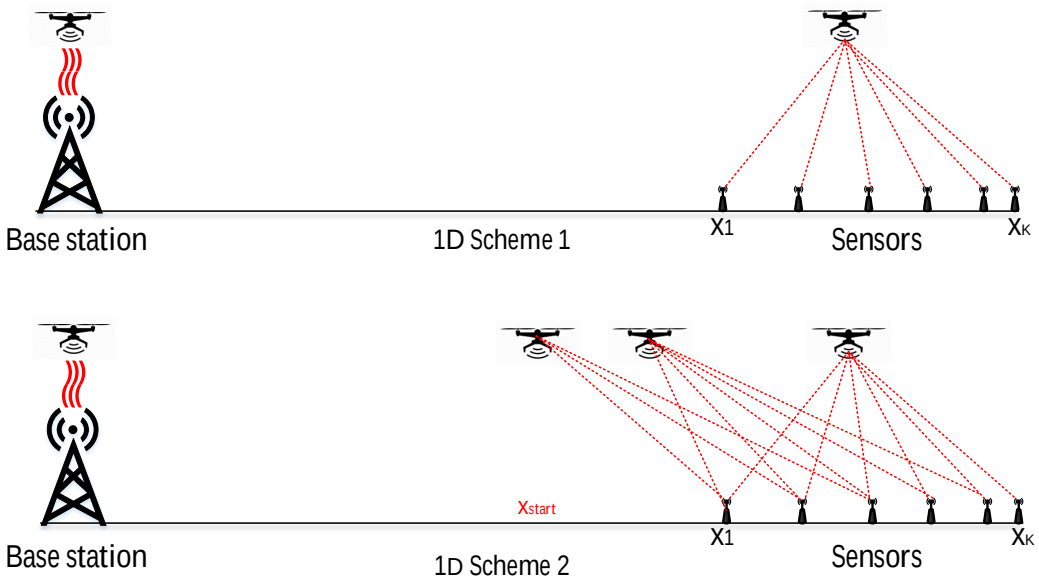

Figure 4.2: Schemes 1 and 2 of 1D case.

different optimal locations for different sensors by exploiting the UAV's trajectory designs, such as [42] and [36], will inevitably consume much more energy because of the extra propulsion power. This is not energy-efficient compared with our scheme that fixes the UAV at some point during charging and discharging to only consume hovering power.

4.3 Optimal Location of UAV for Maximizing Sum-Energy in 1D Case

In this section, in order to study the optimal location of UAV that maximizes the sum-energy received by all sensors, the 1D case is considered first. As mentioned before, the UAV hovers above the BS to be charged, and then accelerates to a

constant speed of V to fly to the destination. When it approaches the ground sensors, it decelerates and finally hovers above these sensors to charge them. Two schemes are considered, as shown in Fig. 4.2. In Scheme 1, the UAV only charges the sensors when it arrives and hovers at their top. This minimizes the transmission loss by having the shortest distance but limits the charging time. In Scheme 2, the UAV starts to charge the sensors before it arrives at their top, that is, the UAV starts charging while it is flying close to the sensors. This increases the charging time but suffers from possible larger transmission loss for each sensor.

4.3.1 1D Scheme 1

This scheme can be divided into three stages: *load*, fly, and *charge*. In the first stage, the UAV is charged by the BS. This is the *load* stage. In the second stage, the UAV carries the stored energy and flies towards the ground sensors. This is the fly stage. Finally, the UAV hovers above these sensors to charge them by transferring wireless power. This is the *charge* stage.

a) Load

In the first stage, the received RF power in dB by the UAV can be derived as [43]

$$P_{uav-r}^{1Ds1} = P_t + G_t + G_{uav} - PL_{bs-uav}, \tag{4.7}$$

where P_t is the transmitted power in dBw, G_t is the gain of the transmitting antenna at the BS in dBi, G_{uav} is the receiving antenna gain at the UAV in dBi (assumed to be the same as the transmitting antenna gain later), PL_{bs-uav} is the path loss between the BS and the UAV in dB, as defined in (4.2). Then, the

received DC energy can be calculated by applying the RF-to-DC conversion model in (4.6) as

$$E_{uav-r}^{1Ds1} = \eta 10^{\frac{P_{uav-r}^{1Ds1}}{10}} T_{loading}^{1Ds1}, \tag{4.8}$$

where $T_{loading}^{1Ds1}$ is the loading time. Note that, during the *load* stage, the UAV also consumes energy as it needs energy to keep aloft above the BS. This energy consumption can be calculated as

$$E_{hover}^{T_{loading}^{1Ds1}} = P(0) \cdot T_{loading}^{1Ds1}. \tag{4.9}$$

Also, to ensure that the UAV does not fall and is being charged, the received DC power must be greater than the hovering power $P(0)$, i.e., $\eta 10^{\frac{P_{uav-r}^{1Ds1}}{10}} > P(0)$.

b) Fly

Then, an *acceleration – fly(v) – and – deceleration* operation will be performed by the UAV to carry the charged energy to the sensors. We denote the final hovering position of the UAV as $(x_h, 0, H)$ in 1D Case since the BS and all sensors are located in a straight line. The energy required during the second stage can be calculated according to the propulsion power consumption model in (2.11) as

$$\begin{aligned} E_{fly-to}^{1Ds1} &= E_{Acc}^{1Ds1} + E_{V}^{1Ds1} + E_{Dec}^{1Ds1} \\ &= 2\int_0^{\frac{V}{a}} P(t)\ dt + P(V)\,\frac{x_h - \frac{V^2}{a}}{V}, \end{aligned} \tag{4.10}$$

where V is the final constant flight speed, a is the acceleration, and $P(t)$ is the power consumption at time t. Note that, in order to ensure that the UAV has enough energy to fly back to the BS after charging the sensors, the energy for flying back should be considered and must not be less than that in the fly stage.

Thus, the minimum energy required for flying back is $E^{1Ds1}_{fly-back} = E^{1Ds1}_{fly-to}$, assuming that the flying back operation is symmetric to the flying to operation.

c) Charge

After the UAV decelerates to a speed of 0 and hovers at $(x_h, 0, H)$, it starts to transfer wireless power to the ground sensors. In this case, the amount of energy available for transfer can be derived as

$$E^{1Ds1}_{available} = E^{1Ds1}_{uav-r} - E^{T^{1Ds1}_{loading}}_{hover} - 2E^{1Ds1}_{fly-to}. \tag{4.11}$$

During this stage, the received RF power at the kth sensor can be expressed as

$$P^{1Ds1}_{gs-k} = P_{uav-t} + G_{uav} + G_{gs} - PL^{1D}_{uav-gs_k}, \tag{4.12}$$

where P_{uav-t} is the transmission power of the UAV in dBw, G_{uav} is the transmitting antenna gain, the same as the receiving antenna gain G_{uav} in (4.7), G_{gs} is the receiving antenna gain at each sensor in dBi, assumed to be the same for all sensors, $PL^{1D}_{uav-gs_k}$ is the path loss between the UAV and the kth sensor in dB, defined in (4.3). Note that, during this stage, the UAV also consumes energy with a power of $P(0)$ in watt to stay aloft, similar to the *load* stage. As a result, the charging time can be obtained as

$$T^{1Ds1}_{charging} = \frac{E^{1Ds1}_{available}}{10^{\frac{P_{uav-t}}{10}} + P(0)}. \tag{4.13}$$

Consequently, the DC energy received by the kth sensor when the UAV hovers at $(x_h, 0, H)$ can be derived as

$$Q_{gs-k}^{1Ds1}(x_h, 0, H) = \eta 10^{\frac{P_{gs-k}^{1Ds1}}{10}} T_{charging}^{1Ds1}. \tag{4.14}$$

The sum-energy received by all sensors can be calculated as

$$E_{sum}^{1Ds1}(x_h, 0, H) = \sum_{k=1}^{K} Q_{gs-k}^{1Ds1}(x_h, 0, H). \tag{4.15}$$

The optimization problem can be formulated as

$$(x^*, 0, H) = \arg\max_{x_h} E_{sum}^{1Ds1}(x_h, 0, H), \tag{4.16a}$$

$$\text{s.t.: } E_{available}^{1Ds1} \geq 0, \tag{4.16b}$$

where x^* in (4.16a) is the optimal UAV location which maximizes the sum-energy function $E_{sum}^{1Ds1}(x_h, 0, H)$, (4.16b) is the constraint on available energy to ensure the UAV can fly back.

d) Optimization

The solution to (4.16) is summarized in Algorithm 3, as it is challenging to derive its closed-form solution when K is large. The step-size setting in the algorithm determines the accuracy of x^*, and it can be changed according to the accuracy requirement. As a result, the complexity of Algorithm 3 can be calculated as

$$\boldsymbol{O}(X \times S), \tag{4.17}$$

Algorithm 3: Optimization of (4.16)

Input: Sensors' location array $S = [x_1, \cdots, x_k, \cdots, x_K]$, P_t, G_t, G_{uav}, G_{gs}, P_{uav-t}, V, a, H, $X = \min(S)$: Step-size: $\max(S)$ and $T^{1Ds1}_{loading}$.

Output: Optimal location x^*.

```
for i=1: length(X) do
    Initialize E^{1Ds1}_{sum}
    Calculate E^{1Ds1}_{available}(i) using (4.11)
    if E^{1Ds1}_{available}(i) ≥ 0 then
        for k=1: length(S) do
            Calculate Q^{1Ds1}_{gs-k}(k) using (4.12) – (4.15)
            E^{1Ds1}_{sum}(i) = E^{1Ds1}_{sum}(i) + Q^{1Ds1}_{gs-k}(k)
    else
        break;
```

Result: $x^* = X(i^*) \leftarrow i^* = \arg\max E^{1Ds1}_{sum}(i)$

where X is the number of iterations of the first "for" loop and S is the number of sensors.

4.3.2 1D Scheme 2

The main difference between Scheme 1 and Scheme 2 is that in Scheme 2 the UAV starts to charge the sensors before it arrives at the top of sensors. Hence, in both deceleration and hovering operations, the sensors can receive power from the UAV. We denote the charging time in these two phases as $T^{1Ds2}_{charge1}$ and $T^{1Ds2}_{charge2}$, and the energy received by sensors as $E^{1Ds2}_{received1}$ and $E^{1Ds2}_{received2}$, respectively. Since the energy harvester has an activation energy, a minimum power of P_ϵ dB needs to be ensured at the closest sensor. This leads to a threshold value of x_{start}, at which the UAV starts energy transfer, as

$$P_{uav-t} + G_{uav} + G_{gs} - PL^{1D}_{uav-gs_1} \geqslant P_\epsilon \; dB, \tag{4.18}$$

where $PL^{1D}_{uav-gs_1}$ is defined in (4.3), the distance between the UAV and the first sensor is $d^{1D}_{uav-gs_1} = \sqrt{(x_1 - x_{start})^2 + \Delta H^2}$, $\Delta H = H - H_{sr}$, and

$$x_{start} \geqslant x_1 - \sqrt{10^{\frac{P_{uav-t}+G_{uav}+G_{gs}-20\lg\{f\}+147.55-P_\epsilon}{10}} - \Delta H^2}. \tag{4.19}$$

Denote the final static hovering position of the UAV as $(x_h, 0, H)$. Two sub-cases needs to be discussed, as shown in Fig. 4.3.

Case a)

In Fig. 4.3(a), when $x_h - x_{start} \leqslant \Delta X_{Dec}$, the UAV is in the deceleration when it arrives at x_{start}. Thus, the velocity of the UAV when it starts energy transfer can be calculated as

$$V_{start} = \sqrt{-2a(x_h - x_{start})}, \tag{4.20}$$

where $a\,(a < 0)$ is the deceleration. In the special case when $x_h - x_{start} = \Delta X_{Dec}$, we have $V_{start} = V$. Then, the charging time during deceleration is

$$T^{1Ds2}_{charge1} = \frac{0 - V_{start}}{a},\ a < 0. \tag{4.21}$$

Since deceleration from V_{start} to 0 is symmetric to the acceleration from 0 to V_{start}, the received RF power by the kth sensor in $T^{1Ds2}_{charge1}$ period can be calculated as

$$P^{1Ds2}_{gs-k} = \Omega - 20\lg\{d^{1D}_{uav-gs_k}\}, \tag{4.22}$$

where $\Omega = P_{uav-t} + G_{uav} + G_{gs} - 20\lg\{f\} + 147.55$, $d^{1D}_{uav-gs_k} = \sqrt{\left(x_h - \frac{1}{2}at^2 - x_k\right)^2 + \Delta H^2}$, $0 \leqslant t \leqslant T^{1Ds2}_{charge1}$, and a in $d^{1D}_{uav-gs_k}$ is the acceleration when the UAV accelerates from x_h to x_{start} with the velocity from 0 to V_{start},

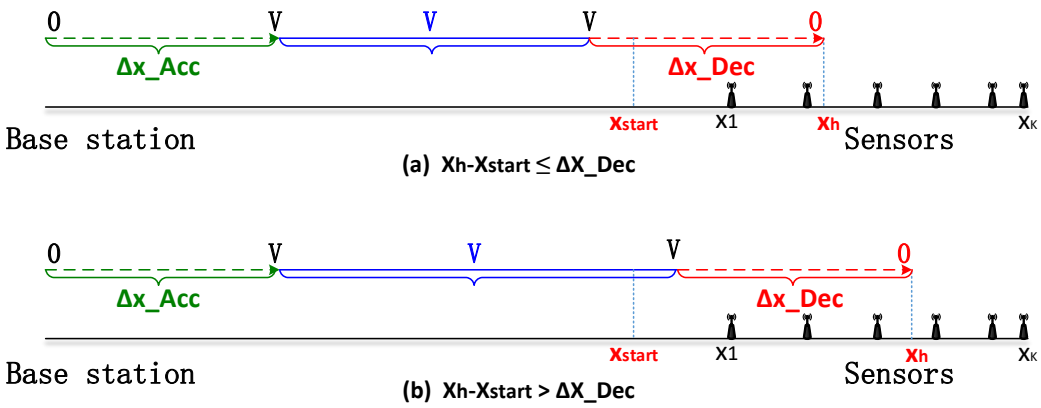

Figure 4.3: Two cases in 1D Scheme 2.

which is the same as deceleration from V_{start} to 0 when the UAV decelerates from x_{start} to x_h. As a result, the total energy received by the kth sensor can be obtained as

$$\begin{aligned} Q_{gs-k}^{1Ds2} &= \eta \int_0^{T_{charge1}^{1Ds2}} 10^{\frac{P_{gs-k}^{1Ds2}}{10}} \, dt \\ &= \frac{\eta 10^{\frac{\Omega}{10}}}{4C_1 q^3 \sin\alpha} \sin\frac{\alpha}{2} \ln \frac{\tau^2 + 2q\tau\cos\frac{\alpha}{2} + q^2}{\tau^2 - 2q\tau\cos\frac{\alpha}{2} + q^2} \\ &\quad + \frac{\eta 10^{\frac{\Omega}{10}}}{2C_1 q^3 \sin\alpha} \cos\frac{\alpha}{2} \left(\arctan \frac{\tau^2 - q^2}{2q\tau\sin\frac{\alpha}{2}} + \pi/2 \right), \end{aligned} \tag{4.23}$$

where $\alpha = \arccos(-\frac{B_1}{2\sqrt{A_1 C_1}})$, $\tau = T_{charge1}^{1Ds2}$, $q = \sqrt[4]{\frac{A_1}{C_1}}$, $A_1 = (x_h - x_k)^2 + \Delta H^2$, $B_1 = -a\,(x_h - x_k)$, $C_1 = \frac{1}{4}a^2$, and we have used the integral in [52, eq. (2.161.1)]. Finally, the total energy received by all sensors in this case can be calculated as

$$E_{received1}^{1Ds2} = \sum_{k=1}^{K} Q_{gs-k}^{1Ds2}. \tag{4.24}$$

Case b)

In Fig. 4.3(b), when $x_h - x_{start} > \Delta X_{Dec}$, the UAV has to fly at the constant speed of V for some time before decelerating, although it has already started energy transfer. Denote the time flying at a constant speed of V and decelerating as $T_{charge1}^{1Ds2-1}$ and $T_{charge1}^{1Ds2-2}$, respectively. Then, one has

$$\begin{aligned}
&T_{charge1}^{1Ds2-1} = \frac{x_h - x_{start} - \Delta X_{Dec}}{V}, \\
&T_{charge1}^{1Ds2-2} = \frac{0 - V}{a}, \ a < 0, \\
&T_{charge1}^{1Ds2} = T_{charge1}^{1Ds2-1} + T_{charge1}^{1Ds2-2}.
\end{aligned} \tag{4.25}$$

If the received RF power at the kth sensor during $T_{charge1}^{1Ds2-1}$ and $T_{charge1}^{1Ds2-2}$ are denoted by P_{gs-k}^{1Ds2-1} and P_{gs-k}^{1Ds2-2}, respectively. one has

$$\begin{aligned}
&P_{gs-k}^{1Ds2-1} = \Omega - 20\lg\{d_{uav-gs_k}^{1Ds2-1}\}, \\
&P_{gs-k}^{1Ds2-2} = \Omega - 20\lg\{d_{uav-gs_k}^{1Ds2-2}\},
\end{aligned} \tag{4.26}$$

where

$$\begin{aligned}
&d_{uav-gs_k}^{1Ds2-1} = \sqrt{(x_{start} + Vt - x_k)^2 + \Delta H^2}, \\
&0 \leqslant t \leqslant T_{charge1}^{1Ds2-1}, \\
&d_{uav-gs_k}^{1Ds2-2} = \sqrt{\left(x_h - \frac{1}{2}at^2 - x_k\right)^2 + \Delta H^2}, \\
&a > 0, \ 0 \leqslant t \leqslant T_{charge1}^{1Ds2-2}.
\end{aligned} \tag{4.27}$$

Denote the total energy received by the kth sensor during $T_{charge1}^{1Ds2-1}$ and $T_{charge1}^{1Ds2-2}$ as Q_{gs-k}^{1Ds2-1} and Q_{gs-k}^{1Ds2-2}, respectively. Then, one has

$$\begin{aligned} Q_{gs-k}^{1Ds2-1} &= \eta \int_0^{T_{charge1}^{1Ds2-1}} 10^{\frac{P_{gs-k}^{1Ds2-1}}{10}} \, dt \\ &= \frac{2\eta 10^{\frac{\Omega}{10}}}{\sqrt{4A_2C_2 - B_2^2}} \arctan \frac{B_2 + 2C_2 T_{charge1}^{1Ds2-1}}{\sqrt{4A_2C_2 - B_2^2}} \\ &\quad - \frac{2\eta 10^{\frac{\Omega}{10}}}{\sqrt{4A_2C_2 - B_2^2}} \arctan \frac{B_2}{\sqrt{4A_2C_2 - B_2^2}}, \end{aligned} \tag{4.28}$$

where $A_2 = (x_{start} - x_k)^2 + \Delta H^2$, $B_2 = 2V(x_{start} - x_k)$, $C_2 = V^2$, and the integral in [52, eq. (2.172)] is used here (or [52, eq. (2.103.4)]). Similarly, during $T_{charge1}^{1Ds2-2}$, one has

$$\begin{aligned} Q_{gs-k}^{1Ds2-2} &= \eta \int_0^{T_{charge1}^{1Ds2-2}} 10^{\frac{P_{gs-k}^{1Ds2-2}}{10}} \, dt \\ &= \frac{\eta 10^{\frac{\Omega}{10}}}{4C_1 q^3 \sin\alpha} \sin\tfrac{\alpha}{2} \ln \frac{T^2 + 2qT\cos\frac{\alpha}{2} + q^2}{T^2 - 2qT\cos\frac{\alpha}{2} + q^2} \\ &\quad + \frac{\eta 10^{\frac{\Omega}{10}}}{2C_1 q^3 \sin\alpha} \cos\tfrac{\alpha}{2} \left(\arctan \frac{T^2 - q^2}{2qT\sin\frac{\alpha}{2}} + \pi/2 \right), \end{aligned} \tag{4.29}$$

where $\alpha = \arccos(-\frac{B_1}{2\sqrt{A_1C_1}})$, $T = T_{charge1}^{1Ds2-2}$, $q = \sqrt[4]{\frac{A_1}{C_1}}$, $A_1 = (x_h - x_k)^2 + \Delta H^2$, $B_1 = -a\,(x_h - x_k)$, $C_1 = \frac{1}{4}a^2$, and the integral in [52, eq. (2.161.1)] has been used here. Hence, the total energy received by the kth sensor during $T_{charge1}^{1Ds2}$ can be calculated as

$$Q_{gs-k}^{1Ds2} = Q_{gs-k}^{1Ds2-1} + Q_{gs-k}^{1Ds2-2}, \tag{4.30}$$

and the sum-energy received by all sensors in this case can be calculated as

$$E_{received1}^{1Ds2} = \sum_{k=1}^{K} Q_{gs-k}^{1Ds2}. \tag{4.31}$$

After the UAV decelerates to the speed of 0, the energy available for transfer can be calculated as

$$\begin{aligned} E_{available}^{1Ds2} =& E_{uav-r}^{1Ds2} - E_{hover}^{T_{loading}^{1Ds2}} - 2E_{fly-to}^{1Ds2} \\ & - 10^{\frac{P_{uav-t}}{10}} \cdot T_{charge1}^{1Ds2}, \end{aligned} \tag{4.32}$$

where E_{uav-r}^{1Ds2}, $E_{hover}^{T_{loading}^{1Ds2}}$, E_{fly-to}^{1Ds2} can be calculated using the method in Scheme 1, $P_{uav-t}T_{charge1}^{1Ds2}$ is the total energy delivered by the UAV from x_{start} to x_h. The received RF power at the kth sensor can be expressed as

$$P_{gs-k}^{1Ds2} = \Omega - 20\lg\{d_{uav-gs_k}^{1D}\}, \tag{4.33}$$

where $d_{uav-gs_k}^{1D} = \sqrt{(x_h - x_k)^2 + \Delta H^2}$. The delivery time can be derived as

$$T_{charge2}^{1Ds2} = \frac{E_{available}^{1Ds2}}{10^{\frac{P_{uav-t}}{10}} + P(0)}. \tag{4.34}$$

Hence, the DC energy received by k^{th} sensor in this time can be calculated as

$$Q_{gs-k}^{1Ds2}(x_h, 0, H) = \eta 10^{\frac{P_{gs-k}^{1Ds2}}{10}} T_{charge2}^{1Ds2}, \tag{4.35}$$

and the energy received by all sensors in $T_{charge2}^{1Ds2}$ can be derived as

$$E_{received2}^{1Ds2} = \sum_{k=1}^{K} Q_{gs-k}^{1Ds2}(x_h, 0, H). \tag{4.36}$$

Finally, the sum-energy can be expressed as

$$E_{sum}^{1Ds2} = E_{received1}^{1Ds2} + E_{received2}^{1Ds2}, \tag{4.37}$$

Algorithm 4: Optimization of (4.38)

Input: Sensors' location array $S = [x_1, \cdots, x_k, \cdots, x_K]$, P_t, G_t, G_{uav}, G_{gs}, P_{uav-t}, V, a, H, P_ϵ, $X = \min(S)$: Step-size : $\max(S)$ and $T^{1Ds2}_{loading}$ which is equal to $T^{1Ds1}_{loading}$.

Output: Optimal location x^*.

```
for i=1: length(X) do
    x_start, ΔX_Dec ← calculate x_start using min(S), V, a and P_ϵ
    Initialize E^1Ds2_sum, E^1Ds2_received1 and E^1Ds2_received2
    Calculate E^1Ds2_available(i) using (4.32)
    if E^1Ds2_available(i) ≥ 0 then
        if X(i) − x_start ≤ ΔX_Dec then
            for j=1: length(S) do
                Calculate E^1Ds2_received1(i) using (4.22) – (4.24)
        else
            for j=1: length(S) do
                Calculate E^1Ds2_received1(i) using (4.25) – (4.31)
        for k=1: length(S) do
            Calculate E^1Ds2_received2(i) using (4.33) – (4.36)
        E^1Ds2_sum(i) = E^1Ds2_received1(i) + E^1Ds2_received2(i)
    else
        break;
i* = arg max E^1Ds2_sum(i)
```

Result: $x^* = X(i^*)$

which leads to the optimization problem

$$(x^*, 0, H) = \arg\max_{x_h} E^{1Ds2}_{sum}\left(x_h, 0, H\right), \tag{4.38a}$$

$$\text{s.t.: } E^{1Ds2}_{available} \geq 0, \tag{4.38b}$$

where x^* in (4.38a) is the optimal UAV location that maximizes the sum-energy function E^{1Ds2}_{sum}, (4.38b) is the constraint on the available energy to ensure the UAV can fly back to the BS. The objective function is determined by the delivery time allocation, velocity V, acceleration a ($a > 0$ or $a < 0$), and the number and

distribution of sensors. It is too complicated to be solved analytically. We will solve it numerically. Details on the numerical solution to (4.38) is summarized in Algorithm 4. For this algorithm, the complexity can be calculated as

$$\boldsymbol{O}\left(X \times 2 \times S\right), \tag{4.39}$$

where X is the number of iterations of the first "for" loop and S is the number of sensors. Because there are two phases in Case b for sensors to receive energy, it needs to multiply by 2. Note that, x_{start} in our work is calculated by using (4.19) to satisfy the minimum power P_ϵ. However, x_{start} can also be jointly optimized with x_h. This will be a future work.

4.3.3 Further Discussion

The above results assume the RF-to-DC conversion efficiency is a constant that is linear and independent of the input power whether the input power is large or small. Nevertheless, it has been revealed that the RF-to-DC conversion efficiency actually depends on the input power [48] when the input power is relatively small, which means the RF-to-DC conversion efficiency is non-linear. Using (2.7), one has the relationship between the input RF power x and output DC power $f(x)$ of the energy harvester as [48]

$$f(x) = \frac{a_0 10^{\frac{x}{10}} + b_0}{10^{\frac{x}{10}} + c_0} - \frac{b_0}{c_0}, \tag{4.40}$$

where a_0, b_0 and c_0 are constants derived by standard curve-fitting. As a result, the non-linear RF-to-DC conversion efficiency at the kth sensor can be expressed

as

$$\eta_k = \frac{f(x)}{10^{\frac{x}{10}}}, \tag{4.41}$$

where P_{RF} is the received RF power at the kth sensor, and $P_{DC} = f(x)$ is the output DC power changed non-linearly by P_{RF}.

According to [48], it is found that the η_k remains unchanged when the P_{RF} is below a threshold and thus, the conversion efficiency in (4.8) in *Load* stage can be seen as a constant when P_t at the BS is chosen carefully. For the 1D Scheme 1, the UAV only charges sensors when hovering at the top of sensors. Hence, using (4.40) and (4.41), the RF-to-DC conversion efficiency in (4.14) is $\eta_k = f(P_{gs-k}^{1Ds2})/10^{\frac{P_{gs-k}^{1Ds2}}{10}}$.

For the 1D Scheme 2, as the UAV charges sensors before it arrives at the top of the sensors. Therefore, the RF-to-DC conversion efficiency changes with the time in both deceleration and flying operation. In *Case a*, using (4.40) and (4.41), the total energy received by the kth sensor in (4.23) can be obtained as

$$\begin{aligned} Q_{gs-k}^{1Ds2} &= \int_0^{T_{charge1}^{1Ds2}} \left(\frac{a_0 * 10^{\frac{P_{gs-k}^{1Ds2}}{10}} + b_0}{10^{\frac{P_{gs-k}^{1Ds2}}{10}} + c_0} - \frac{b_0}{c_0} \right) dt \\ &= \frac{(a_0 c_0 - b_0) 10^{\frac{\Omega}{10}}}{4 F_1 q^3 \sin\alpha} \sin\tfrac{\alpha}{2} \ln \frac{\tau^2 + 2q\tau\cos\frac{\alpha}{2} + q^2}{\tau^2 - 2q\tau\cos\frac{\alpha}{2} + q^2} \\ &\quad + \frac{(a_0 c_0 - b_0) 10^{\frac{\Omega}{10}}}{2 F_1 q^3 \sin\alpha} \cos\tfrac{\alpha}{2} \left(\arctan \frac{\tau^2 - q^2}{2q\tau\sin\frac{\alpha}{2}} + \pi/2 \right), \end{aligned} \tag{4.42}$$

where $\alpha = \arccos(-\frac{E_1}{2\sqrt{D_1 F_1}})$, $\tau = T_{charge1}^{1Ds2}$, $q = \sqrt[4]{\frac{D_1}{F_1}}$, $D_1 = c_0(x_h - x_k)^2 + c_0 \Delta H^2 + c_0 10^{\frac{\Omega}{10}}$, $E_1 = -a\,(x_h - x_k)\,{c_0}^2$, $F_1 = \frac{1}{4} a^2 {c_0}^2$, and the integral in [52, eq. (2.161.1)] is used. In *Case b*, since the calculation during the deceleration is the same as that in *Case a*, we only calculate the energy received by the kth sensor during $T_{charge1}^{1Ds2-1}$ at constant speed. Using (4.40) and (4.41), the energy received by the kth sensor

in (4.28) can be obtained as

$$
\begin{aligned}
Q_{gs-k}^{1Ds2-1} &= \int_0^{T_{charge1}^{1Ds2-1}} \left(\frac{a_0 * 10^{\frac{P_{gs-k}^{1Ds2-1}}{10}} + b_0}{10^{\frac{P_{gs-k}^{1Ds2-1}}{10}} + c_0} - \frac{b_0}{c_0} \right) dt \\
&= \frac{2(a_0c_0 - b_0)10^{\frac{\Omega}{10}}}{\sqrt{4D_2F_2 - E_2^2}} \arctan \frac{E_2 + 2F_2T_{charge1}^{1Ds2-1}}{\sqrt{4D_2F_2 - E_2^2}} \\
&\quad - \frac{2(a_0c_0 - b_0)10^{\frac{\Omega}{10}}}{\sqrt{4D_2F_2 - E_2^2}} \arctan \frac{E_2}{\sqrt{4D_2F_2 - E_2^2}},
\end{aligned}
\tag{4.43}
$$

where $D_2 = {c_0}^2(x_{start} - x_k)^2 + {c_0}^2\Delta H^2 + c_0 10^{\frac{\Omega}{10}}$, $E_2 = 2{c_0}^2V(x_{start} - x_k)$, $F_2 = {c_0}^2V^2$, and the integral in [52, eq. (2.172)] is used here. Finally, considering the non-linear RF-to-DC conversion efficiency, the DC energy received by k^{th} sensor during hovering in (4.35) can be calculated as

$$
Q_{gs-k}^{1Ds2}(x_h, 0, H) = f(10^{\frac{P_{gs-k}^{1Ds2}}{10}})T_{charge2}^{1Ds2}. \tag{4.44}
$$

4.4 Optimal Location of UAV for Maximizing Sum-Energy in 2D Case

In this section, we extend the result from 1D to 2D. Two schemes are depicted in Fig. 4.4.

4.4.1 2D Scheme 1

The charging process is similar to the 1D case in Scheme 1.

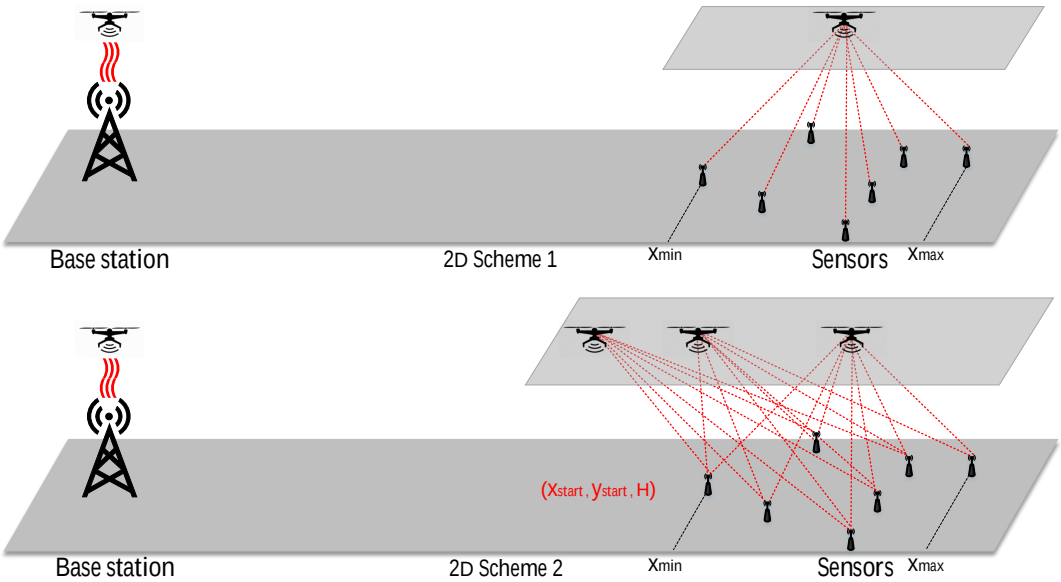

Figure 4.4: Schemes 1 and 2 of 2D case.

a) Load

The received RF power in dB during the *load* stage can be expressed as

$$P_{uav-r}^{2Ds1} = P_t + G_t + G_{uav} - PL_{bs-uav}, \tag{4.45}$$

where the symbols are defined the same as before. Thus, the received DC energy can be calculated as

$$E_{uav-r}^{2Ds1} = \eta 10^{\frac{P_{uav-r}^{2Ds1}}{10}} T_{loading}^{2Ds1}, \tag{4.46}$$

where $T_{loading}^{2Ds1}$ is the loading time. Since the UAV also consumes energy during hovering with a power of $P(0)$ in watt, this can be calculated as

$$E_{hover}^{T_{loading}^{2Ds1}} = P(0) \cdot T_{loading}^{2Ds1}. \tag{4.47}$$

Again, to ensure that the UAV does not fall, $\eta 10^{\frac{P_{uav-r}^{2Ds1}}{10}} > P\left(0\right)$ needs to be satisfied.

b) Fly

Denote the energy required for carrying the obtained energy to the destination as E^{2Ds1}_{fly-to}. In the fly stage, one has

$$\begin{aligned} E^{2Ds1}_{fly-to} &= E^{2Ds1}_{Acc} + E^{2Ds1}_{V} + E^{2Ds1}_{Dec} \\ &= 2\int_0^{\frac{V}{a}} P\left(t\right)\ dt + P\left(V\right)\frac{x_h - \frac{V^2}{a}}{V}, x_h > \frac{v^2}{a}. \end{aligned} \tag{4.48}$$

Since the UAV also needs energy to fly back after each charging, we let $E^{2Ds1}_{fly-back} = E^{2Ds1}_{fly-to}$.

c) Charge

In the final stage, the amount of energy available for transmission is

$$E^{2Ds1}_{available} = E^{2Ds1}_{uav-r} - E^{T^{2Ds1}_{loading}}_{hover} - 2E^{2Ds1}_{fly-to}. \tag{4.49}$$

Then, the received RF power at the kth sensor can be expressed as

$$P^{2Ds1}_{gs-k} = P_{uav-t} + G_{uav} + G_{gs} - PL^{2D}_{uav-gs_k}, \tag{4.50}$$

where G_{uav} is the transmitting antenna gain at the UAV in dBi, G_{gs} is the receiving antenna gain at the sensors in dBi, $PL^{2D}_{uav-gs_k}$ is the path loss between the UAV and the kth sensor in dB, which is defined in (4.4). Due to the extra energy for hovering, the charging time can be calculated as

$$T^{2Ds1}_{charging} = \frac{E^{2Ds1}_{available}}{10^{\frac{P_{uav-t}}{10}} + P(0)}. \tag{4.51}$$

Algorithm 5: Optimization of (4.54)

Input: Sensors' location array
$S = [(x_1, y_1), \cdots, (x_k, y_k), \cdots, (x_K, y_K)]$, P_t, G_t, G_{uav}, G_{gs},
P_{uav-t}, V, a, H, $X = \min(S \to x)$: Step-size : $\max(S \to x)$,
$Y = \min(S \to y)$: Step-size : $\max(S \to y)$ and $T^{2Ds1}_{loading}$.

Output: Optimal location x^* and y^*.

```
for i=1: length(X) do
    for j=1: length(Y) do
        Initialize E^{2Ds1}_{sum}
        index(i,j) = (X(i) − min(X)) * length(Y) + Y(j) − min(Y) + 1
        Calculate E^{2Ds1}_{available}(index(i,j)) using (4.45) – (4.49)
        if E^{2Ds1}_{available}(index(i,j)) ≥ 0 then
            for k=1: length(S) do
                Calculate Q^{2Ds1}_{gs−k}(k) using (4.50) – (4.52)
                E^{2Ds1}_{sum}(index(i,j)) = E^{2Ds1}_{sum}(index(i,j)) + Q^{2Ds1}_{gs−k}(k)
        else
            break;
index*(i,j) = arg max E^{2Ds1}_{sum}(index(i,j))
i,j ← index*(i,j)
```

Result: $x^* = X(i)$, $y^* = Y(i)$

Consequently, the DC energy received by the kth sensor during $T^{2Ds1}_{charging}$ period can be obtained as

$$Q^{2Ds1}_{gs-k}(x_h, y_h, H) = \eta 10^{\frac{P^{2Ds1}_{gs-k}}{10}} T^{2Ds1}_{charging}, \tag{4.52}$$

and the sum-energy received by all sensors is

$$E^{2Ds1}_{sum}(x_h, y_h, H) = \sum_{k=1}^{K} Q^{2Ds1}_{gs-k}(x_h, y_h, H). \tag{4.53}$$

Then, the optimization becomes

$$(x_h^*, y_h^*, H) = \arg\max_{x_h, y_h} E_{sum}^{2Ds1}(x_h, y_h, H), \tag{4.54a}$$

$$\text{s.t.: } E_{available}^{1Ds2} \geq 0, \tag{4.54b}$$

where (x_h^*, y_h^*, H) in (4.54a) is the optimal location of the UAV that maximizes the sum-energy received by all sensors, and (4.54b) is the constraint on the energy to ensure the UAV can fly back to the BS.

d) Optimization

The solution to (4.54) is summarized in Algorithm 5. For this algorithm, the complexity can be calculated as

$$\boldsymbol{O}\left(X \times Y \times S\right), \tag{4.55}$$

where X is the number of iterations of the first "for" loop, Y is the number of iterations of the second "for" loop, and S is the number of sensors.

4.4.2 2D Scheme 2

Compared with Scheme 1, the UAV in Scheme 2 can fly at any directions as long as its destination is within the box mentioned earlier, as shown in Fig. 4.5. Let $T_{charge1}^{2Ds2}$ and $T_{charge2}^{2Ds2}$ denote the delivery time of these two phases, and $E_{received1}^{2Ds2}$, $E_{received2}^{2Ds2}$ denote the energy received by sensors, respectively. Since the received

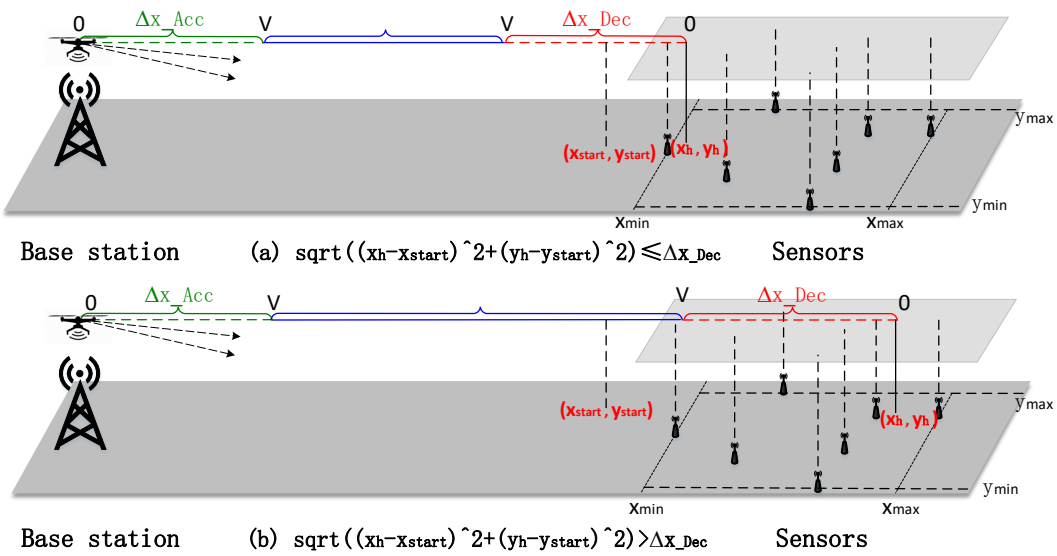

Figure 4.5: Sub-cases (a) and (b) of 2D Scheme 2.

RF power by sensors is expressed as

$$P_{gs-k}^{2Ds2} = P_{uav-r} + G_{uav} + G_{gs} - PL_{uav-gs_k}^{2D}, \tag{4.56}$$

P_ϵ can be calculated through $P_{gs-k}^{2Ds2} > P_\epsilon$, where k depends on the flying direction. Denote the final hovering location of the UAV as (x_h, y_h, H).

Case a)

In Fig. 4.5(a), when $\sqrt{(x_h - x_{start})^2 + (y_h - y_{start})^2} \leqslant \Delta X_{Dec}$, the UAV is in deceleration when it passes over point (x_{start}, y_{start}). Hence, the velocity of the UAV when it starts to broadcast wireless power can be expressed as

$$V_{start} = \sqrt{-2a\sqrt{(x_h - x_{start})^2 + (y_h - y_{start})^2}}, \tag{4.57}$$

where a ($a < 0$) is deceleration. When $\sqrt{(x_h - x_{start})^2 + (y_h - y_{start})^2} = \Delta X_{Dec}$, we have $V_{start} = V$. As a result, the delivery time in this case can be expressed as

$$T_{charge1}^{2Ds2} = \frac{0 - V_{start}}{a}, \ a < 0. \tag{4.58}$$

The received RF power by the kth sensor in $T_{charge1}^{2Ds2}$ is

$$P_{gs-k}^{2Ds2} = \Omega - 20\lg\left\{\sqrt{(x(t) - x_k)^2 + (y(t) - y_k)^2 + \Delta H^2}\right\}, \tag{4.59}$$

where $\Omega = P_{uav-t} + G_{uav} + G_{gs} - 20\lg\{f\} + 147.55$, $x(t) = x_h - \frac{1}{2}a_x t^2$, $y(t) = y_h - \frac{1}{2}a_y t^2$, $0 \leqslant t \leqslant T_{charge1}^{2Ds2}$, $a_x = a\cos\arctan(\frac{y_h}{x_h})$ and $a_y = a\sin\arctan(\frac{y_h}{x_h})$. Herein, a_x and a_y are the projected acceleration to x and y coordinates, as shown in Fig. 4.6, a ($a > 0$) is acceleration when the UAV accelerates from (x_h, y_h, H) to $(x_{start}, y_{start}, H)$. Note that, although the UAV can fly in any direction, its trajectory is still a straight line to save flying time and internal power consumption. Thus its direction can be given by $\theta = \arctan(\frac{y_h}{x_h})$ as shown in Fig. 4.6. Then, the total energy received by the kth sensor during $T_{charge1}^{2Ds2}$ can be calculated as

$$\begin{aligned} Q_{gs-k}^{2Ds2} = & \frac{\eta 10^{\frac{\Omega}{10}}}{4C_3 q^3 \sin\alpha} \sin\frac{\alpha}{2} \ln\frac{\tau^2 + 2q\tau\cos\frac{\alpha}{2} + q^2}{\tau^2 - 2q\tau\cos\frac{\alpha}{2} + q^2} \\ & + \frac{\eta 10^{\frac{\Omega}{10}}}{2C_3 q^3 \sin\alpha} \cos\frac{\alpha}{2}\left(\arctan\frac{\tau^2 - q^2}{2q\tau\sin\frac{\alpha}{2}} + \pi/2\right), \end{aligned} \tag{4.60}$$

where $\alpha = \arccos(-\frac{B_3}{2\sqrt{A_3 C_3}})$, $\tau = T_{charge1}^{2Ds2}$, $q = \sqrt[4]{\frac{A_3}{C_3}}$, $A_3 = (x_h - x_k)^2 + (y_h - y_k)^2 + \Delta H^2$, $B_3 = -\left[a_x(x_h - x_k) + a_y(y_h - y_k)\right]$, $C_3 = \frac{1}{4}\left({a_x}^2 + {a_y}^2\right)$, and we have used the integral in [52, eq. (2.161.1)]. Finally, the sum-energy received by all sensors in $T_{charge1}^{2Ds2}$ can be calculated as

$$E_{received1}^{2Ds2} = \sum_{k=1}^{K} Q_{gs-k}^{2Ds2}. \tag{4.61}$$

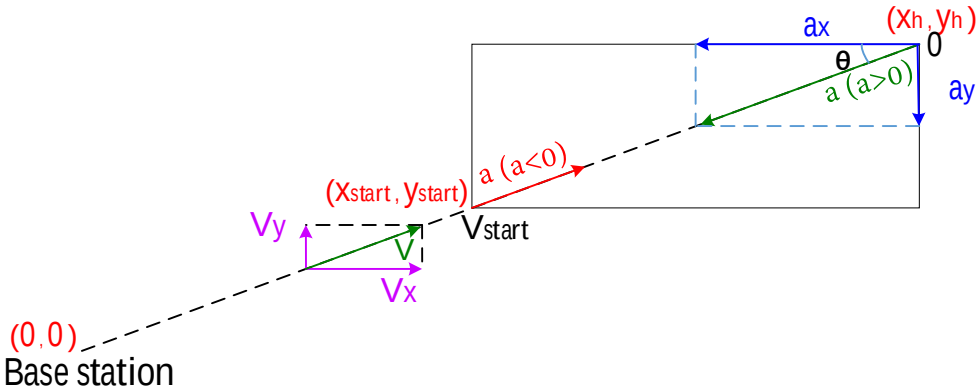

Figure 4.6: Symmetrical process of 2D Scheme 2.

Case b)

In Fig. 4.5(b), when $\sqrt{(x_h - x_{start})^2 + (y_h - y_{start})^2} > \Delta X_{Dec}$, the UAV starts to transfer wireless power at a the speed of V before deceleration. Denote the time flying at a constant speed of V and decelerating as $T_{charge1}^{2Ds2-1}$ and $T_{charge1}^{2Ds2-2}$, respectively. Then, one has

$$\begin{aligned}
T_{charge1}^{2Ds2-1} &= \frac{\sqrt{(x_h - x_{start})^2 + (y_h - y_{start})^2} - \Delta X_{Dec}}{V}, \\
T_{charge1}^{2Ds2-2} &= \frac{0 - V}{a}, \ a < 0, \\
T_{charge1}^{2Ds2} &= T_{charge1}^{2Ds2-1} + T_{charge1}^{2Ds2-2}.
\end{aligned} \tag{4.62}$$

If we denote the received RF power by the kth sensor as P_{gs-k}^{2Ds2-1} and P_{gs-k}^{2Ds2-2}, respectively, we have

$$\begin{aligned} P_{gs-k}^{2Ds2-1} &= \Omega - 20\lg\{d_{uav-gs_k}^{2Ds2-1}\}, \\ P_{gs-k}^{2Ds2-2} &= \Omega - 20\lg\{d_{uav-gs_k}^{2Ds2-2}\}. \end{aligned} \tag{4.63}$$

Herein,

$$\begin{aligned} d_{uav-gs_k}^{2Ds2-1} &= \sqrt{{\chi_1}^2 + {\gamma_1}^2 + \Delta H^2}, \\ d_{uav-gs_k}^{2Ds2-2} &= \sqrt{{\chi_2}^2 + {\gamma_2}^2 + \Delta H^2}, \end{aligned} \tag{4.64}$$

where $\chi_1 = x_{start} + V_x t_1 - x_k$, $\gamma_1 = y_{start} + V_y t_1 - y_k$, $0 \leqslant t_1 \leqslant T_{charge1}^{2Ds2-1}$, $V_x = V\cos\theta$, $V_y = V\sin\theta$, $\chi_2 = x_h - \frac{1}{2}a_x {t_2}^2 - x_k$, $\gamma_2 = y_h - \frac{1}{2}a_y {t_2}^2 - y_k$, $0 \leqslant t_2 \leqslant T_{charge1}^{2Ds2-2}$, $a_x = a\cos\theta$, $a_y = a\sin\theta$, $\theta = \arctan(\frac{y_h}{x_h})$. Thus, the total energy received by the kth sensor during the $T_{charge1}^{2Ds2-1}$ can be expressed as

$$\begin{aligned} Q_{gs-k}^{2Ds2-1} = &\frac{2\eta 10^{\frac{\Omega}{10}}}{\sqrt{4A_4C_4 - {B_4}^2}} \arctan \frac{B_4 + 2C_4 T_{charge1}^{2Ds2-1}}{\sqrt{4A_4C_4 - {B_4}^2}} \\ &- \frac{2\eta 10^{\frac{\Omega}{10}}}{\sqrt{4A_4C_4 - {B_4}^2}} \arctan \frac{B_4}{\sqrt{4A_4C_4 - {B_4}^2}}, \end{aligned} \tag{4.65}$$

where $A_4 = (x_{start} - x_k)^2 + (y_{start} - y_k)^2 + \Delta H^2$, $B_4 = 2(x_{start} - x_k)V_x + 2(y_{start} - y_k)V_y$, $C_4 = {V_x}^2 + {V_y}^2$, and the integral in [52, eq. (2.172)] is used here. For $T_{charge1}^{2Ds2-2}$, the total energy received by k^{th} sensor can be expressed as

$$\begin{aligned} Q_{gs-k}^{2Ds2-2} = &\frac{\eta 10^{\frac{\Omega}{10}}}{4C_3 q^3 \sin\alpha} \sin\frac{\alpha}{2} \ln \frac{T^2 + 2qT\cos\frac{\alpha}{2} + q^2}{T^2 - 2qT\cos\frac{\alpha}{2} + q^2} \\ &+ \frac{\eta 10^{\frac{\Omega}{10}}}{2C_3 q^3 \sin\alpha} \cos\frac{\alpha}{2} \left(\arctan \frac{T^2 - q^2}{2qT\sin\frac{\alpha}{2}} + \pi/2 \right), \end{aligned} \tag{4.66}$$

where $\alpha = \arccos(-\frac{B_3}{2\sqrt{A_3 C_3}})$, $T = T_{charge1}^{2Ds2-2}$ $q = \sqrt[4]{\frac{A_3}{C_3}}$, $A_3 = (x_h - x_k)^2 + (y_h - y_k)^2 + \Delta H^2$, $B_3 = -\left[a_x\left(x_h - x_k\right) + a_y(y_h - y_k)\right]$, $C_3 = \frac{1}{4}\left({a_x}^2 + {a_y}^2\right)$, and we have used the integral in [52, eq. (2.161.1)].

The total energy received by the kth sensor during $T_{charge1}^{2Ds2}$ can be calculated as

$$Q_{gs-k}^{2Ds2} = Q_{gs-k}^{2Ds2-1} + Q_{gs-k}^{2Ds2-2}, \tag{4.67}$$

and the sum-energy received by all sensors in this period can be obtained as

$$E_{received1}^{2Ds2} = \sum_{k=1}^{K} Q_{gs-k}^{2Ds2}. \tag{4.68}$$

When the UAV decelerates to the speed of 0, and hovers above sensors at a location (x_h, y_h, H), the energy available for transfer can be calculated as

$$\begin{aligned} E_{available}^{2Ds2} = E_{uav-r}^{2Ds2} - E_{hover}^{T_{loading}^{2Ds2}} - 2E_{fly-to}^{2Ds2} \\ - 10^{\frac{P_{uav-t}}{10}} \cdot T_{charge1}^{2Ds2}, \end{aligned} \tag{4.69}$$

where E_{uav-r}^{2Ds2}, $E_{hover}^{T_{loading}^{2Ds2}}$, E_{fly-to}^{2Ds2} are calculated using the same method as in Scheme 1, $P_{uav-t}^{T_{charge1}^{2Ds2}}$ is the total energy delivered by the UAV in the process of from $(x_{start}, y_{start}, H)$ to (x_h, y_h, H). The received RF power at the kth sensor can be expressed as

$$P_{gs-k}^{2Ds2} = \Omega - 20\lg\{d_{uav-gs_k}^{2D}\}, \tag{4.70}$$

where $d_{uav-gs_k}^{2D} = \sqrt{(x_h - x_k)^2 + (y_h - y_k)^2 + \Delta H^2}$. As a result, the charge time is

$$T_{charge2}^{2Ds2} = \frac{E_{availabel}^{2Ds2}}{10^{\frac{P_{uav-t}}{10}} + P(0)}, \tag{4.71}$$

where $P(0)$ is the power for hovering. Hence, the DC energy received by the kth

sensor in $T_{charge2}^{2Ds2}$ can be expressed as

$$Q_{gs-k}^{2Ds2}\left(x_h, y_h, H\right) = \eta 10^{\frac{P_{gs-k}^{2Ds2}}{10}} T_{charge2}^{2Ds2}, \tag{4.72}$$

and the total energy received by all sensors in $T_{charge2}^{2Ds2}$ can be derived as

$$E_{received2}^{2Ds2}\left(x_h, y_h, H\right) = \sum_{k=1}^{K} Q_{gs-k}^{2Ds2}\left(x_h, y_h, H\right). \tag{4.73}$$

Algorithm 6: Optimization of (4.75)

Input: Sensors' location array $S = [(x_1, y_1), \cdots, (x_k, y_k), \cdots, (x_K, y_K)]$, P_t, G_t, G_{uav}, G_{gs}, P_{uav-t}, V, a, H, P_ϵ, $X = \min(S \rightarrow x)$: Step-size : $\max(S \rightarrow x)$, $Y = \min(S \rightarrow y)$: Step-size : $\max(S \rightarrow y)$ and $T^{2Ds2}_{loading}$ which is equal to $T^{2Ds1}_{loading}$.

Output: Optimal location x^* and y^*.

```
for i=1: length(X) do
    for j=1: length(Y) do
        Calculate x_start, y_start, ΔX_Dec ← using min(S), V, a and P_ε
        Initialize E^2Ds2_sum, E^2Ds2_received1 and E^2Ds2_received2
        index(i,j) = (X(i) − min(X)) * length(Y) + Y(j) − min(Y) + 1
        Calculate E^2Ds2_available(index(i,j)) using (4.32)
        if E^2Ds2_available(index(i,j)) ≥ 0 then
            if √((X(i) − x_start)^2 + (Y(j) − y_start)^2) ≤ ΔX_Dec then
                for k=1: length(S) do
                    Calculate E^2Ds2_received1(index(i,j)) ← using (4.56) – (4.61)
                        // Case a
            else
                for k=1: length(S) do
                    Calculate E^2Ds2_received1(index(i,j)) ← using (4.62) – (4.68)
                        // Case b
            for k=1: length(S) do
                calculate E^2Ds2_received2(index(i,j)) ← using (4.70) – (4.74)
            E^2Ds2_sum(index(i,j)) =
              E^2Ds2_received1(index(i,j)) + E^2Ds2_received2(index(i,j))
        else
            break;
index*(i,j) = arg max E^2Ds2_sum(index(i,j))
i,j ← index*(i,j)
```

Result: $x^* = X(i)$, $y^* = Y(i)$

Finally, the sum-energy can be derived as

$$E_{sum}^{2Ds2}\left(x_h, y_h, H\right) = E_{received1}^{2Ds2} + E_{received2}^{2Ds2}, \tag{4.74}$$

and the optimization problem is obtained as

$$\left(x^*, y^*, H\right) = \arg\max_{x_h, y_h} E_{sum}^{2Ds2}\left(x_h, y_h, H\right). \tag{4.75a}$$

$$\text{s.t.: } E_{available}^{2Ds2} \geq 0, \tag{4.75b}$$

where (x^*, y^*, H) in the objective function (4.75a) is the optimal UAV location which maximizes the sum-energy function E_{sum}^{2Ds2}, (4.75b) is the constraint on the energy to ensure the UAV can fly back to the BS. Details on the solution to (4.75) is summarized in Algorithm 6. For this algorithm, the complexity can be calculated as

$$\boldsymbol{O}\left(X \times Y \times 2 \times S\right), \tag{4.76}$$

where X and Y are the number of iterations of the first and second "for" loops, respectively, S is the number of sensors. Similar to the Algorithm 4, because there are two phases for sensors to receive energy, it also needs to be multiplied by 2. The calculation using non-linear RF-to-DC model is similar to the 1D case, and they are not discussed here to make this chapter compact.

Table 4.1: UAV parameters.

Notation	**Physical meaning**	**Value**
m	Air-frame mass in kg	0.8
W	Aircraft weight in Newton, $g = 9.8$ m/s^2	7.84
ρ	Air density in kg/m^3	1.225
b	Number of blades	4
R	Rotor radius in meter m	0.2
A	Rotor disc area in m^2, $A = \pi R^2$	0.1256
c	Blade or airfoil chord length	0.0196
s	Rotor solidity, $s \triangleq \frac{bc}{\pi R}$	0.1248
δ	Profile drag coefficient	0.012
Ω	Blade angular velocity in radians/second	400
k	Incremental correction factor to induced power	0.05
U_{tip}	Tip speed of the rotor blade, $U_{tip} \triangleq \Omega R$	80
v_0	Mean rotor induced velocity, $v_0 = \sqrt{\frac{W}{2\rho A}}$	5.0463
S_{FP}	Fuselage equivalent flat plate area in m^2	0.0079
d_0	Fuselage drag ratio, $d_0 \triangleq \frac{S_{FP}}{sA}$	0.5009
P_0	Blade power, $P_0 = \frac{\delta}{8}\rho s A \Omega^3 R^3$	14.7517
P_i	Induced power, $P_i = (1+k)\frac{W^{\frac{3}{2}}}{\sqrt{2\rho A}}$	41.5409

4.5 Numerical Results and Discussion

In this section, numerical examples are presented to show the optimal UAV location maximizing the sum-energy received by all sensors. In the simulation, we set $P_t = 35.68$ dBw, $G_t = 15$ dBi [91], $G_{uav} = 2$ dBi, $G_{gs} = 5$ dBi, $P_{uav-t} = 10$ dBw,

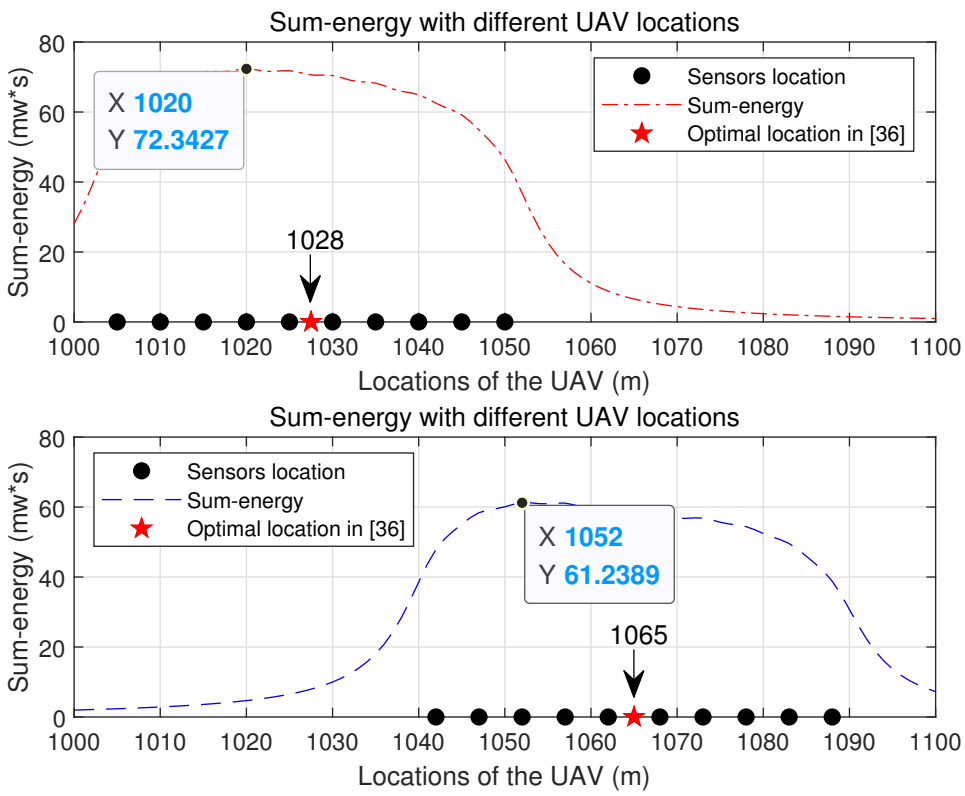

Figure 4.7: Optimal location of UAV in 1D Scheme 1.

$H_{bs} = 4.5$ m, $H = 5.5$ m, $H_{sr} = 0.5$ m, $f = 915$ MHz, $a = 1$ m/s^2, $K = 10$ and the RF-to-DC conversion efficiency $\eta = 0.6$, if not stated otherwise. Our expressions are general enough for all possible values of parameters but these values are chosen as examples. The time for the UAV to load energy from the BS is set to 600 s, and the parameters of the UAV are summarized in Table 4.1.

Fig. 4.7 shows the optimal location that maximizes the sum-energy in 1D Scheme 1, and compares it with the optimal location derived in [36]. In this figure, V is set to 10 m/s. In the upper part of the figure, ten sensors with X coordinates (1005, 1010, 1015, 1020, 1025, 1030, 1035, 1040, 1045, 1050) are used as a case study. One can see that the curve of the sum-energy increases first and then

decreases when the flight distance increases, as expected as, when the UAV flies from the left side of the sensors to the right side, the distance-dependent path loss decreases first and then increases. The optimal location derived in [36] marked by five-pointed star is $x = 1028$, which is at the center position of the sensors. However, the optimal location in our study is $x = 1020$, smaller than that in [36] or closer to the BS. This is because we have taken the UAV power consumption and BS charging process into account, while [36] ignored them. When the UAV flies from $x = 1020$ to $x = 1028$, more propulsion energy is needed, which will reduce the energy harvested by the sensors. Here, the difference, i.e., 8 meters, seems marginal because of the compact coordinates. When the distance between sensors is large, the performance improvement will stand out. In the lower part of the figure, another ten sensors with X coordinates (1042, 1047, 1052, 1057, 1062, 1068, 1073, 1078, 1083, 1088) are used. Similar observations can be made. Note that the optimal locations of our study and [36] are 1052 and 1065, respectively in this case. The gap between these two optimal locations is 13 m, which is larger than 8 m in the upper part. This is due to the fact that, when the sensors are placed further away from the BS, the UAV needs to consume more extra energy, which in turn leads to less energy that can be transferred to the sensors, 61.24 mw·s and 72.34 mw·s in the figure. As a result, the optimal location has to be closer to the BS.

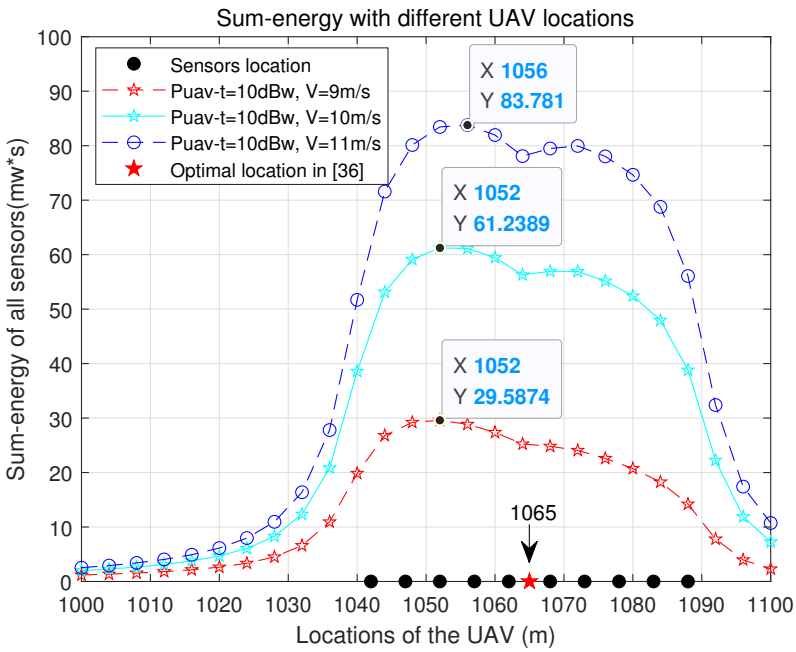

(a) The effect of the speed on 1D Scheme 1.

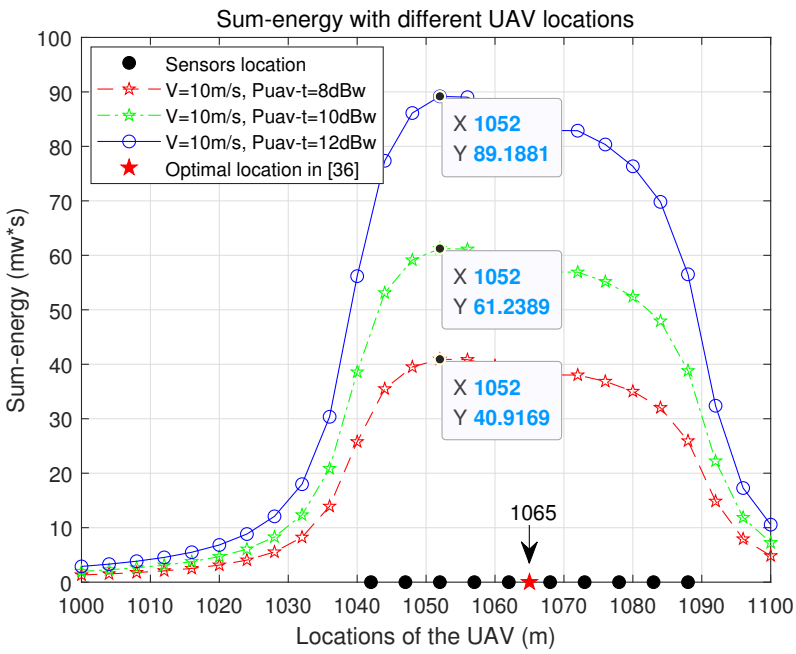

(b) The effect of the transmit power on 1D Scheme 1.

Figure 4.8: The effects of different system parameters on 1D Scheme 1.

Fig. 4.8 examines the effects of the speed and the UAV transmit power on the sum-energy received by all sensors at different hovering locations in 1D Scheme 1. Ten sensors with X coordinates (1042, 1047, 1052, 1057, 1062, 1068, 1073, 1078, 1083, 1088) are used as a case study. In Fig. 4.8(a), we fix $P_{uav-t} = 10$ dBw to examine the speed. From Fig. 4.8(a), one can see that the sum-energy received by all sensors increases with the speed. This is because the propulsion power of the UAV decreases when the UAV speed increases from 0 to the *maximum-endurance speed* [49], and hence this reduces the UAV power consumption and the gap between the optimal location in our study and the one in [36]. However, as seen from Fig. 4.8(a), the change in energy becomes marginal when the speed is large. This is because high speed requires more time to accelerate from and decelerate to the speed of 0 for hovering and acceleration or deceleration consume extra energy. Next, we examine the transmit power by fixing $V = 8$ m/s in Fig. 4.8(b). One can see that the sum-energy received by all sensors increases with the transmit power. This is because the time for hovering decreases with the increase of the transmit power and the power consumption for hovering can be saved or reduced to transfer more energy to sensors. Note that there is a valley near the five-pointed star position. This is because the sensors are not placed equidistant. As shown in the lower or right part of Fig. 4.7 and Fig. 4.8, the distance between the 5th sensor and the 6th sensor is larger than others and thus, it leads to a relatively low sum-energy with local peak points. In this case, the UAV can be dispatched to the two peak points alternately to charge them in turn to improve fairness.

For the optimal sum-energy shown in Fig. 4.8, Fig. 4.9 shows the energy received by the individual sensors. In this figure, V is set to 10 m/s, and P_{uav-t} is set 10 dBw. Firstly, we compare the optimal location of [36] with the one derived in our study. As seen from Fig. 4.9, there is unfairness among different sensors.

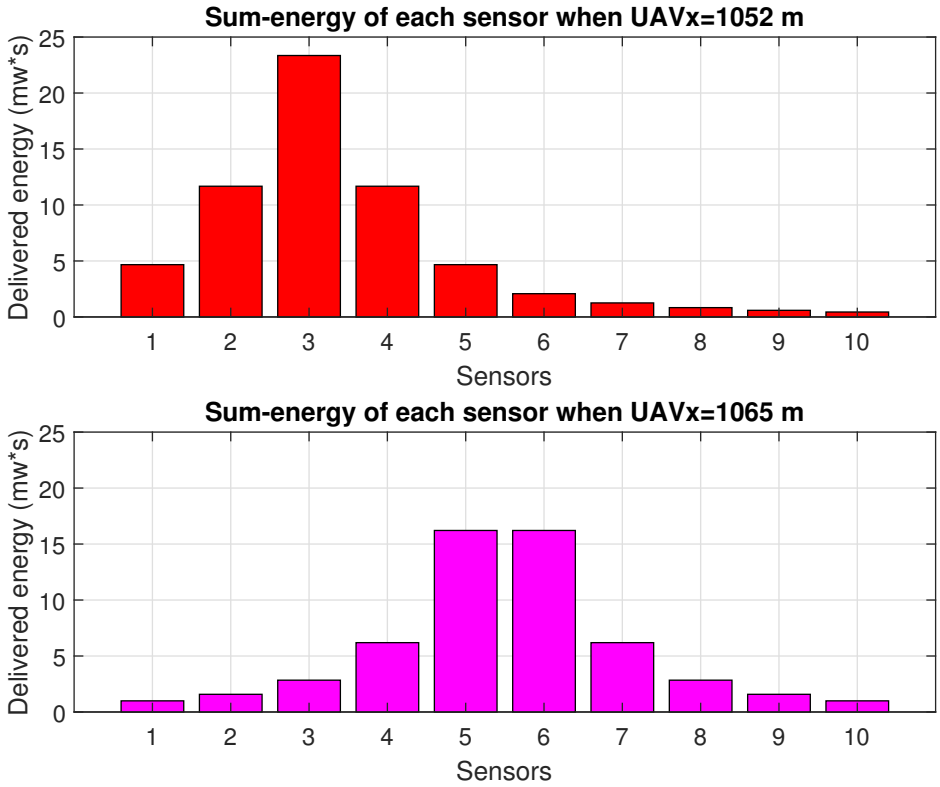

Figure 4.9: Comparison of total energy received by each sensors in 1D Scheme 1.

In the upper part of the figure, the sensors located closer to the BS harvest more energy than those further away from the BS. In the lower part of the figure, the sensors located in the middle have much more energy than those at the edge. This is because the optimal location in [36] is the physical center of the sensors. Besides, the total energy received by $1^{st}, 2^{nd}$, 3rd and t^{th} sensor, when $x^* = 1052$, is much higher than that in [36] when $x^* = 1065$. From the viewpoint of the sum-energy, the optimal location derived in our study has a higher WPT efficiency. However, for a fixed spatial distribution, the unbalanced energy among sensors is a problem. One possible solution is to use multiple UAVs.

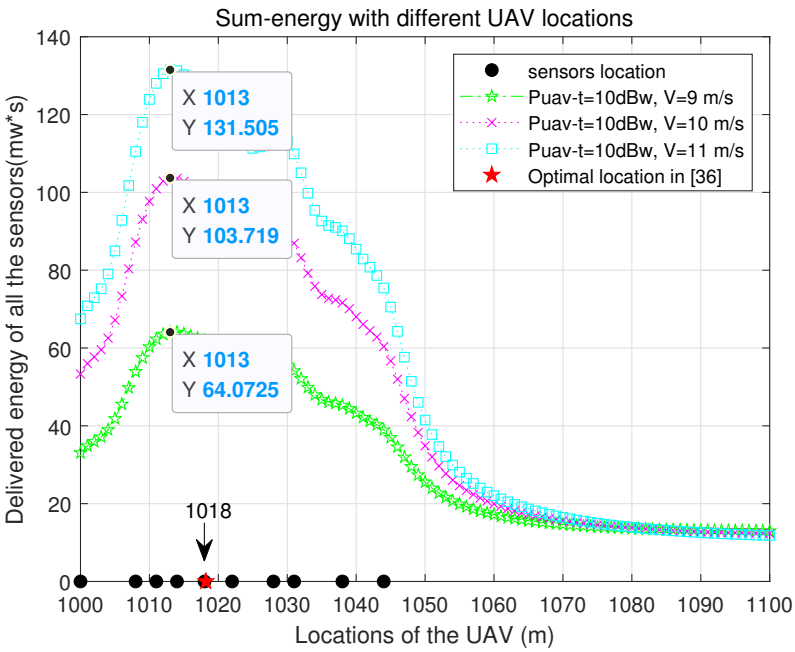

(a) The effect of the speed on 1D Scheme 2.

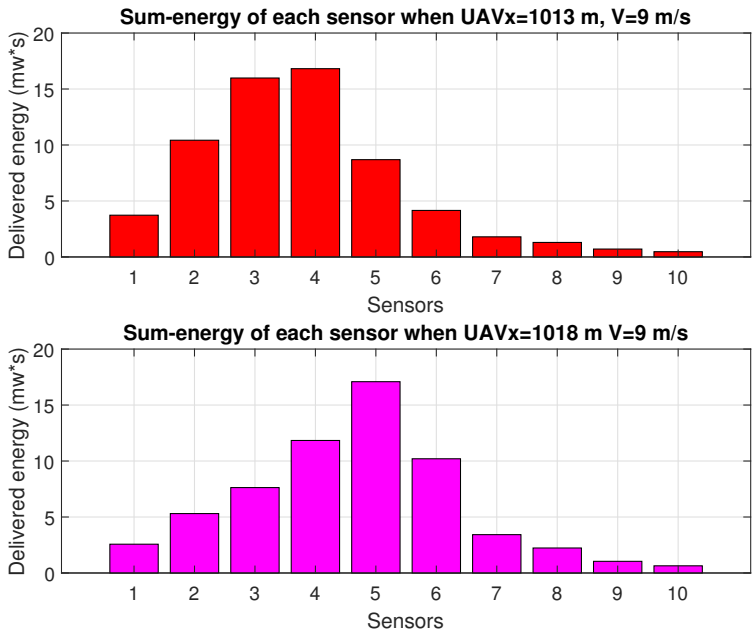

(b) Comparison of the received energy by each sensor.

Figure 4.10: Simulation results of 1D Scheme 2.

Fig. 4.10 shows the optimal location that maximizes the sum-energy in 1D Scheme 2. Ten sensors with X coordinates (1000, 1008, 1011, 1014, 1018, 1022, 1028, 1031, 1038, 1044) are used in this simulation. In Fig. 4.10(a), one can see that the sum-energy received by all sensors increases with the speed when the transmit power is fixed. The optimal locations derived in [36] $x^* = 1018$. In our study, when the speed is set to 9 m/s, 10 m/s and 11 m/s, the optimal location is $x^* = 1013$. Again, this is because when the speed increases, the propulsion power reduces and the flight time reduces to save more energy transferred to the sensors. This was ignored in [36]. However, the change in energy becomes marginal when the speed is large, as in Fig. 4.8(a). Next, we examine the total energy received by individual sensors for $V = 9$ m/s and $P_{uav-t} = 10$ dBw. As seen in Fig. 4.10(b), the first four sensors receive more energy when $x^* = 1013$ m than when $x^* = 1018$ m. As expected, the maximum sum-energy received by all sensors in our schemes is much more than that in previous works, and thus it has much higher energy efficiency. Comparing with Scheme 1 and Scheme 2 of 1D case, as seen from Fig. 4.7 and Fig. 4.10(a), Scheme 2 has much higher energy efficiency than Scheme 1. Hence, a longer charging time is more beneficial than a lower transmission loss in this case.

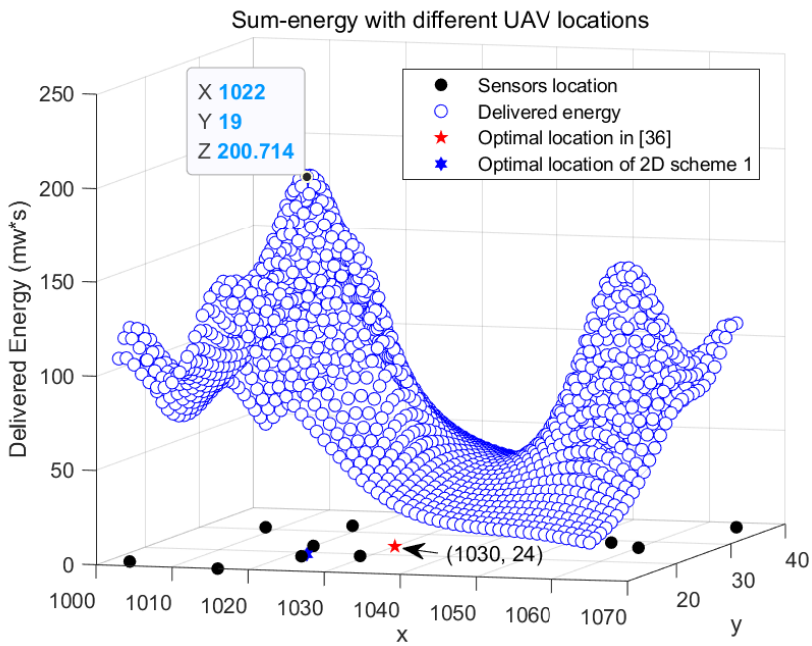

(a) The sum-energy of hovering at different locations.

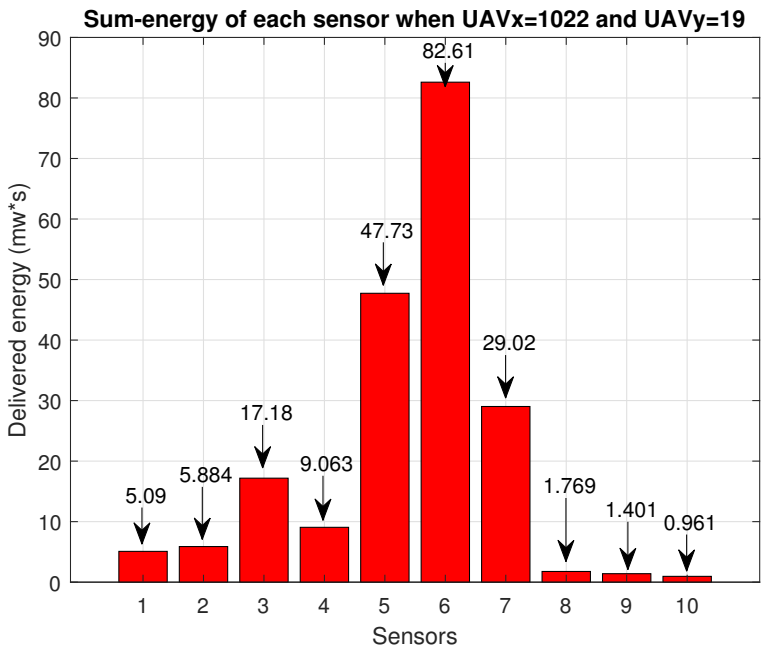

(b) Comparison of the received energy by each sensor.

Figure 4.11: Simulation results of 2D Scheme 1.

Fig. 4.11 shows the optimal location that maximizes the sum-energy, and compares the energy received by individual sensors when the UAV hovering at the optimal location in Scheme 1 of 2D case. In this simulation, ten sensors with $(1003, 13)$, $(1008, 31)$, $(1016, 11)$, $(1018, 33)$, $(1020, 23)$, $(1022, 18)$, $(1029, 19)$, $(1055, 29)$, $(1060, 27)$, $(1065, 38)$ as 2D coordinates are used and we set $V = 9$ m/s. As seen from Fig. 4.11(a), the optimal location tends to be above the area where sensors are denser. In this scheme, the optimal location is $(x^* = 1020, y^* = 23)$ with a sum-energy of 200.7 mw·s. Compared with the one $(x^* = 1030, y^* = 24)$ from the previous works, it tends to be closer to the BS. In Fig. 4.11(b), one can see that the total energy received by individual sensors decreases as the distance from the UAV increases. In particular, as the UAV hovers above the 6th sensor, the sum-energy reaches its maximum, as expected. The 10th sensor receives the minimum energy as it is the farthest. Next, we investigate Scheme 2.

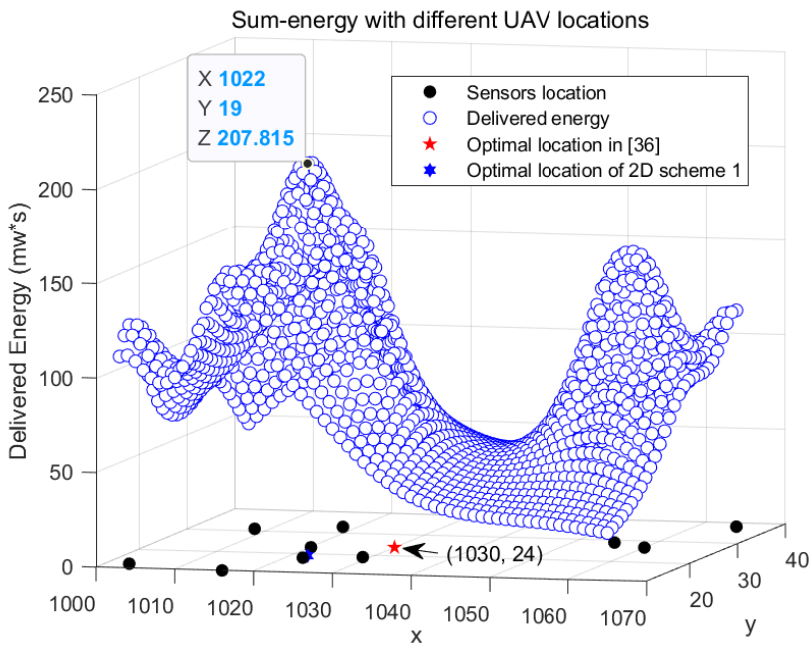

(a) The sum-energy of hovering at different locations.

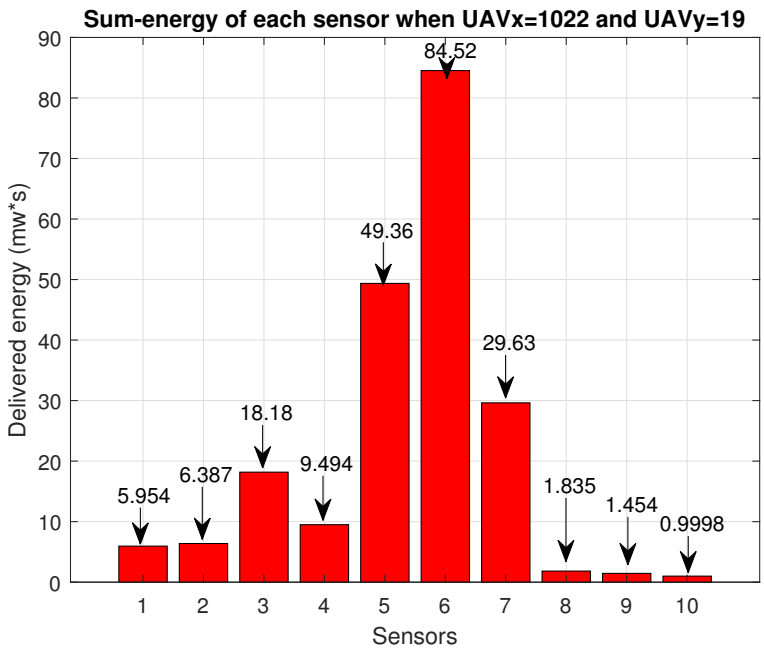

(b) Comparison of the received energy by each sensor.

Figure 4.12: Simulation results of 2D Scheme 2.

Fig. 4.12 shows the optimal location that maximizes the sum-energy in Scheme 2 of 2D case. Similar observations can be made. Again, the denser the sensors are, the higher the sum-energy they can receive. As shown in Fig. 4.12(a), it reaches the maximum 207.8 mw·s when the UAV hovers at $(x^* = 1022, y^* = 19)$, and hence $(x^* = 1022, y^* = 19)$ is the optimal location in this scheme. In Fig.4.12(b), the energy received by individual sensors is presented when the UAV hovering at the optimal location. The 6th sensor receives more energy than others, as expected, as it is the closest to the UAV. Comparing Scheme 1 and Scheme 2 in 2D case, as can be seen from Fig.4.11 and Fig. 4.12, both the maximum sum-energy and the energy received by individual sensor in Scheme 2 are larger than Scheme 1. The optimal locations in Scheme 1 and 2 are the same when V is not large. Both are close to the BS.

4.6 Summary

In this chapter, we have studied the optimal location of UAV-enabled WPT by taking the UAV power consumption, the conversion loss and the BS charging process into account. We have proposed two schemes for UAV-enabled WPT in both 1D and 2D cases. Algorithms 5 and 6 in the 2D case are similar to Algorithms 3 and 4 in the 1D case. However, the calculations in Algorithms 5 and 6 are more complicated, because the velocity in the 2D case is decomposed to V_x and V_y, and so does the acceleration a. By maximizing the sum-energy received by all sensors, the optimal locations for the UAV have been derived. Numerical results have shown that the optimal locations of the UAV tend to be close to the BS compared with the optimal locations in previous works that ignore the BS charging process or the UAV power consumption. In both 1D and 2D cases, Scheme 2 shows a better

energy efficiency than Scheme 1. Moreover, the higher the speed and transmit power, the higher the sum-energy will be.

Chapter 5

Optimal Time Allocation in UAV-Enabled WPCNs

This chapter is based on our work published in [J3].

5.1 Introduction

Recently, UAVs have been presenting a promising technology in 5G, IoTs and the six-generation (6G) communication networks [103], [104]. In particular, there has been a growing interest in studying UAV-enabled WPCNs [44] – [45], where the UAV was dispatched to collect data from remote sensors, charge remote sensors or both [25, 27–29, 44, 45]. For example, the authors in [44] combined the WPT and wireless information transfer (WIT) in a WPCN, where a UAV with a constant power supply coordinated the WPT/WIT to/from a set of ground users. The up-link (UL) sum-rate was maximized by jointly optimizing time allocation and

the UAV position. In [45], the outage probability of the UAV-enabled WPCN was analyzed by identifying the optimum time ratio of the WPT and the WIT under the assumption of the Rician fading channel. The authors in [27] employed UAVs to collect data from the sensors as well as recharge the sensors. In [28], a UAV was used as a flying base station to serve battery-limited sensors. Both data collection and sensor charging have been studied. In [29], a novel energy-efficient data collection and WPT system using a multiple-input multiple-output (MIMO) full-duplex (FD) UAV was proposed, where simultaneous wireless information and power transfer was explored. In [25], the outage and coverage performance of the UAV-aided WPT and data collection have been studied, where the Rician fading and path loss caused by UAV's elevation angle were considered. In practical applications, one challenge is to schedule the full process of a UAV mission when considering its own energy supply and propulsion in a given time. That is, the UAV is first charged with a certain amount of energy by a charging station and then dispatched to charge the remote sensors, and then collect data from sensors and bring it back to the charging station. There may exist an optimal time allocation at different phases of this full process.

Works reviewed in Section 2.5 have provided very valuable insights on the use of UAV-enabled WPT and data collection. However, in these works, there are three important issues that have been more or less ignored. Firstly, the power consumption of the UAV has not been considered in most of these applications [25, 27–29, 44, 45, 69–77]. This affects the operational efficiency of the UAV. Secondly, UAV is an energy-limited node that does not generate energy itself. All these works [25, 27–29, 44–47, 69–83] have ignored the energy charging process from a charging station[1], such as a BS, to the UAV, either with wired power supply or

[1]Note that UAV can be recharged wirelessly by a wireless charger without landing, and the output power of the wireless charger can reach 12 KW [35].

wirelessly. In [31], UAV energy harvesting from solar energy or wind energy has been studied. However, the amount of energy harvested is random and thus, it may not be enough as the main energy source of the UAV, but as a supplement, it could be a good choice. Also, data collection has not been considered in this work. Thirdly, the purpose of collecting data from the sensors is to offload them to the BS, i.e., the mobile edge computing (MEC) server [105, 106], for computing and decision-making [25]. Thus, data offloading at the BS is an important process that has been ignored in these works. To the best of the authors' knowledge, UAV-aided WPT and data collection considering all these three important issues has not been studied yet and thus, it represents contribution.

Motivated by the above observations, this chapter studies the use of the UAV in a WPCN serving as both a data collector and a wireless energy transmitter. In the study, the energy consumption at the UAV, the energy transfer from the BS to the UAV, and the data offloading from the UAV to the BS will all be considered along with other processes in the UAV-enabled WPCN. In detail, four phases are needed to be considered. First, since the UAV does not generate energy itself, it needs to be firstly charged by a charge station, i.e., a BS, and then flies to the sensors at the cost of propulsion consumption. Second, the UAV, upon arrival, first charges all the sensors distributed in a given area in the down-link (DL) as all sensors are assumed to be in a low power state with solar energy acquisition capability and can only be used for sensing, followed by data transmission from the sensors to the UAV in the UL in a time-division-multiple-access (TDMA) manner. This is the third phase. Note that, for one sensor, simultaneously WPT and data collection could save time. However, in practical applications, there are usually multiple sensors. To avoid the inter-user interference caused by data transmission among different sensors, TDMA is employed [25], [23]. After data collection, the UAV flies back to the BS with propulsion energy consumption again, and offloads

the collected data to the BS for further processing in the fourth phase. In the study, both distance-dependent path loss and small-scale fading are considered to maximize the data volume and transmission efficiency, defined as the ratio of the amount of data offloaded to the BS to the amount of data collected from the sensors, given a fixed total time. The closed-form expression for the optimal time allocation between different phases will be derived. Simulation results will be presented to give useful guidance for system designs. The main contributions of this work can be summarized as follows:

- The UAV-enabled WPCNs is studied by considering energy transfer from the BS to the UAV, the UAV power consumption and the data offloading from the UAV to the BS.
- The closed-form expressions of the optimal time allocation are derived analytically.
- Two TDMA mechanisms, i.e., TDMA with equal transmission times for all sensors and TDMA with optimal transmission times for all sensors are studied.
- The effects of different system parameters on the transmission efficiency and the optimal time allocation are examined to provide useful guidance for system designs.

The remainder of this chapter is organized as follows. In Section 5.2, the system model is explained. Section 5.3 derives the optimal time allocation. Section 5.4 further discusses and analyzes the time allocation problem. Section 5.5 presents numerical results. Finally, the work is concluded in Section 5.6.

5.2 System Model

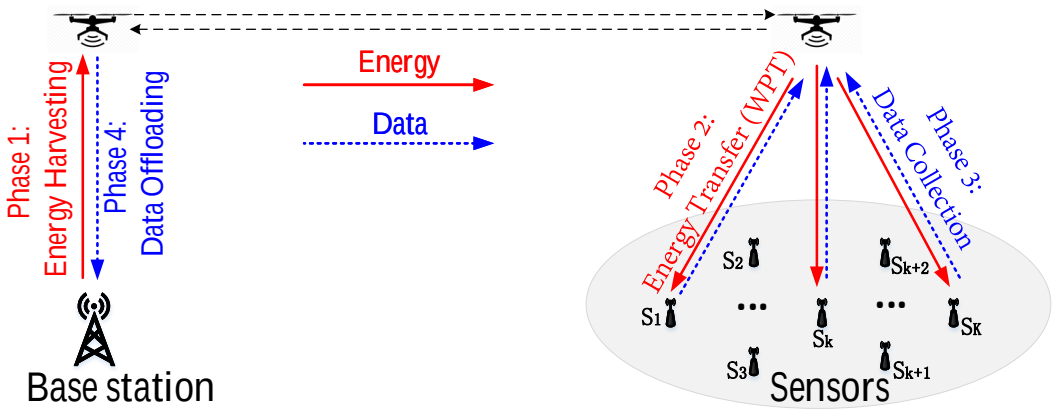

Figure 5.1: Illustration of system model.

Consider a UAV-enabled WPCN. As depicted in Fig. 5.1, the system consists of one BS, one UAV and K sensors distributed in a given area and denoted by S_k with $1 \leq k \leq K$. All the sensors are assumed to be located on a 2D surface. The position of the BS is denoted as $(0, 0, H_{bs})$ with a height of H_{bs}. The location of the kth sensor is denoted as (x_k, y_k, H_{sr}) with a common antenna height of H_{sr}. The UAV is assumed to fly at a fixed height of H above the ground [46, 47, 83], and hence its location can be denoted as (x, y, H). The UAV-aided data collection process works as follows. First, a rotary-wing UAV is charged by a BS wirelessly in its close proximity [35], [43, 92]. After being charged for a period of time, the UAV flies to the destination area where all sensors are located. Then, the UAV charges all sensors via WPT in the DL for a certain period of time, followed by the orthogonal data transmission from the sensors to the UAV in the UL in a TDMA manner. Finally, the UAV flies back to the BS and offloads data to the BS wirelessly. The main reason for the use of UAV, instead of performing WPT and data collection directly between the BS and the sensors [23, 43, 92, 107], is to reduce the

transmission range and therefore to improve the efficiency of the BS and sensor operations, as the path loss will be greatly reduced by performing transmission and reception in a close proximity [43, 92].

In this work, we assume wireless charging by the BS to the UAV [34, 43, 92]. This is the case when there is no dedicated landing dock at the BS for wired charging, as in conventional BSs. This is also the case when it is not convenient or safe for the UAV to land due to the complicated environment surrounding the BS. In the case when wired charging is available at the BS, the following results are still valid by ignoring the first phase of the BS charging or by assuming a very high conversion efficiency. Besides, one wireless charging station can charge multiple UAVs at the same time, which is an advantage over wired charging on the ground [35].

As shown in Fig. 5.1, the communication link between the BS and the UAV as well as that between the UAV and sensors on the ground are assumed to be dominated by LoS. This is another benefit of using UAVs. In this case, the propagation model encompasses both the distance-dependent path loss and small-scale fading. It may be noted that there have been path loss models for UAVs [108, 109]. However, fading was ignored in these works. In this work, we assume Rician fading [45], [25], [110]. We consider WPT from the BS to the UAV in Phase 1 and from the UAV to the sensors in Phase 2. Consequently, data collection from ground sensors to the UAV is considered in Phase 3 after charging sensors, and data offloading from the UAV to the BS is considered in Phase 4. Note that there is also a round-trip flight, i.e., the UAV flies to the sensors after harvesting energy from the BS in Phase 1, and flies back to the BS after collecting data from the sensors in Phase 3. The goal is to derive the optimal time allocation for these four phases given a fixed flight distance and a fixed total time. The round-trip

process is not included in the time allocation, as the flight time is determined by the flight distance and UAV speed and both are fixed.

5.2.1 Phase 1 – Energy Harvesting

In Phase 1, the BS charges the UAV, as shown in Fig. 5.1. The received power in dB at the UAV due to path loss can be expressed as [43, 92]

$$P_{uav-r} = P_{bs-t} + G_{bs} + G_{uav} - PL_{bs-uav}, \tag{5.1}$$

where P_{bs-t} denotes the transmit power at the BS, G_{bs} and G_{uav} are the antenna gains of the BS and the UAV in dBi, respectively, $PL_{bs-uav} = 20\lg\{f\} + 20\lg\{d_{bs-uav}\} - 147.55$ dB is the free-space path loss between the BS and the UAV, f denotes the operating frequency, and $d_{bs-uav} = H - H_{bs}$ with $d_{bs-uav} \geq 1$ is the distance between the BS and the UAV for wireless charging in far-field. Let $g_{b,u} \sim \mathcal{CN}(0, \sigma^2_{b,u})$ denote the complex channel coefficient from the BS to the UAV, where $\sigma^2_{b,u}$ is the average fading power. Thus, the far-field wireless energy harvested by the UAV during Phase 1 can be expressed as

$$E_{uav-h} = \eta 10^{\frac{P_{uav-r}}{10}} |g_{b,u}|^2 T_{phase1}, \tag{5.2}$$

where $0 < \eta < 1$ is the energy conversion efficiency [48], i.e., RF-to-DC, at the UAV, and T_{phase1} is the operating time in Phase 1 or the charging time. For time sensitive tasks, such as emergency and rescue, T_{phase1} is usually less than the time to fully charge the UAV. Thus, in a given time, reasonable time allocation may improve the efficiency of UAV missions.

It is worth noting that there are different technologies for UAV wire-

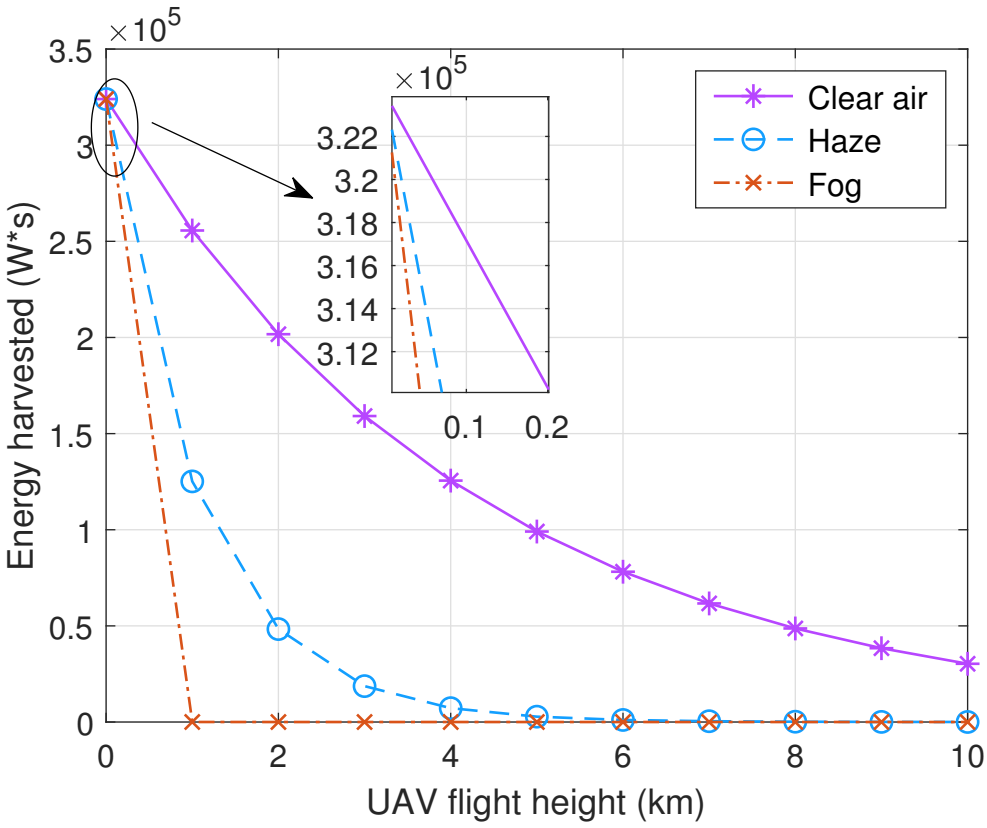

Figure 5.2: Energy harvested via laser vs UAV flight heights.

less charging, such as inductive coupling, magnetic resonance coupling, capacitive coupling, RF power beam-forming and laser beaming [32, 33, 111, 112]. For wired charging or near-field wireless charging, η is close to 1, $g_{b,u} = 1$ and $PL_{bs-uav} = G_{bs} = G_{uav} \approx 0$ dB. For inductive coupling [113], $g_{b,u} = 1$, $PL_{bs-uav} = G_{bs} = G_{uav} \approx 0$ dB, the distance d_{bs-uav} in PL_{bs-uav} can be 3 cm [114], and η can be any value between 0 and 1 depending on P_{uav-r}. For laser beaming [112], $g_{b,u} = 1$, $G_{bs} = G_{uav} \approx 0$ dB, $PL_{bs-uav} = 10\frac{C_\epsilon}{\kappa_v}(\frac{\lambda}{C_\chi})^{-\rho_{sd}} d_{bs-uav} \lg\{e\}$ and η can be 0.54 [115], C_ϵ and C_χ are two constants, κ_v is the visibility, λ is the wavelength, ρ_{sd} is the size distribution of the scattering particles and depends on κ_v, and e is the Euler number. Thus, E_{uav-h} in (5.2) is general and applicable to different transmission powers and distances from the charger. Fig. 5.2

shows the energy harvested at the UAV via laser charging versus different flight heights under three scenarios [115]. In the figure, $P_{bs-t} = 30$ dBW, $T_{phase} = 10$ minutes, $\eta = 0.54$, and other parameters follow [115, Table III]. One can see that the energy harvested at the UAV decreases with the UAV flight height. This is due to the fact that PL_{bs-uav} increases with the distance between the BS and the UAV. Besides, the harvested energy is also influenced by weather. When the UAV flight height is fixed at 1 km, one sees that the energy harvested at the UAV in clear air is the largest, followed by in a haze, and in fog. This is because the laser with high frequency is easily obscured by fog. From the global drone regulations database (GDRDB), most countries, such as European countries, USA and China, have a maximum altitude of 120 meters, and Canada of 90 meters for UAVs [116], and there is no minimum altitude as long as it is reasonable. In China, the flight height of the UAV for assisting agricultural spraying shall not exceed 15 meters [116]. Thus, Fig. 2 shows that at least wireless charging of UAV via laser is promising under the regulations.

5.2.2 Phase 2 – WPT

Upon arrival, in Phase 2, the UAV hovers at a height of H above the sensors and broadcasts wireless energy to all sensors on the ground to charge them in the DL. Let P_{uav-t} denote the transmit power at the UAV and $h_{u,k} \sim \mathcal{CN}(0, \sigma^2_{u,k})$ denote the complex channel coefficient from the UAV to the kth sensor, where $\sigma^2_{u,k}$ is the average fading power. Thus, the received power at the kth sensor in the DL due to path loss can be expressed as

$$P_{k-r} = P_{uav-t} + G_{uav} + G_k - PL_{uav-k}, \tag{5.3}$$

where $PL_{uav-k} = 20\lg\{f\} + 20\lg\{d_{uav-k}\} - 147.55$ dB is the free-space path loss between the UAV and the kth sensor, $d_{uav-k} = \sqrt{(x-x_k)^2+(y-y_k)^2+(H-H_{sr})^2}$ with $d_{uav-k} \geq 1$ is the distance between the UAV and the kth sensor, G_k is the antenna gain of the kth sensor and all other symbols are denoted as before. For convenience, it is assumed that $G_1 = \cdots = G_K = G_{sr}$ so that all sensors have the same antenna gains. As a result, the amount of energy harvested by the kth sensor is

$$E_k = \eta_k 10^{\frac{P_{k-r}}{10}} |h_{u,k}|^2 T_{phase2}, \tag{5.4}$$

where T_{phase2} is the charging time for energy replenishing in Phase 2, $0 < \eta_k < 1, k = 1, \ldots, K$, is the energy conversion efficiency at the kth sensor. In most previous works [44, 45], [46, 47], it has been assumed that the conversion efficiency is a constant that is linear and independent of the input power whether the input power is large or small. However, it has been revealed that the conversion efficiency actually depends on the input power [48], which means the output harvested power is non-linear. One has the relationship between the input power P_{RF} and the output power $f(P_{RF})$ of the energy harvester as [48]

$$f(P_{RF}) = \frac{a_0 10^{\frac{P_{RF}}{10}} + b_0}{10^{\frac{P_{RF}}{10}} + c_0} - \frac{b_0}{c_0}, \tag{5.5}$$

where a_0, b_0 and c_0 are constants obtained by standard curve-fitting. In this case, the conversion efficiency at the kth sensor can be expressed as

$$\eta_k = \frac{f(P_{k-r})}{10^{\frac{P_{k-r}}{10}}}, \quad k = 1, \ldots, K, \tag{5.6}$$

which changes with the input power, i.e., P_{k-r}, at the kth sensor. Thus, for WPT in Phase 2, we assume an energy conversion efficiency that varies with input power

at different sensors. Note that the energy conversion efficiency η in Phase 1 is also non-linear actually, and it is determined by PL_{bs-uav} in (5.1).

5.2.3 Phase 3 – Data Collection

After charging the sensors, the UAV will collect data from the sensors using TDMA in the corresponding UL in Phase 3 with a total transmission time of T_{phase3}. It is assumed that all the energy harvested at each sensor will be used for its UL information transmission [23] and that the amount of time allocated for each sensor in the UL is denoted by t_k. Since the total time for Phase 3 is T_{phase3}, we have

$$\sum_{k=1}^{K} t_k \leq T_{phase3}, \;\; k = 1, \ldots, K. \tag{5.7}$$

Consequently, the transmission power of the kth sensor, denoted by P_{k-t}, is proportional to E_k in (5.4). One has

$$P_{k-t} = \frac{E_k}{t_k} = \frac{\eta_k 10^{\frac{P_{k-r}}{10}} |h_{u,k}|^2 T_{phase2}}{t_k}. \tag{5.8}$$

The received power at the UAV from the kth sensor in the UL due to path loss can be expressed as

$$P_{uav-r_k} = 10 \lg \{P_{k-t}\} + G_k + G_{uav} - PL_{uav-k}. \tag{5.9}$$

We denote $g_{k,u} \sim \mathcal{CN}(0, \sigma_{k,u}^2)$ as the complex channel coefficient from the kth sensor to the UAV. The overall received signal at the UAV in the UL is given by

$$y_{k,u} = \sqrt{10^{\frac{P_{uav-r_k}}{10}}} g_{k,u} s_{k,u} + n_{k,u}, k = 1, \ldots, K, \tag{5.10}$$

where $s_{k,u}$ is the signal transmitted by the kth sensor with $E\left\{|s_{k,u}|^2\right\} = 1$, and $n_{k,u} \sim \mathcal{CN}(0, \sigma_{k,u}^2)$ is the noise at the UAV during t_k with mean zero and variance $\sigma_{k,u}^2$. From (5.4) – (5.10), the sum-data received by UAV from K sensors after Phase 3 can be formulated as

$$D_{K,u} = \sum_{k=1}^{K} t_k B \log_2 \left(1 + \frac{10^{\frac{P_{uav-r_k}}{10}} |g_{k,u}|^2}{\sigma_{k,u}^2}\right). \tag{5.11a}$$

$$\text{s.t.: } \sum_{k=1}^{K} t_k \leq T_{phase3},\ k = 1, \ldots, K, \tag{5.11b}$$

where B is bandwidth.

5.2.4 Phase 4 – Data Offloading

In Phase 4, the UAV hovers above the BS for data offloading. The received power at the BS from the UAV due to path loss can be expressed as

$$P_{bs-r} = P_{uav-t} + G_{uav} + G_{bs} - PL_{bs-uav}, \tag{5.12}$$

where P_{uav-t} is the transmission power of the UAV during data-offloading as that in (5.3). During Phase 4, let $h_{u,b} \sim \mathcal{CN}(0, \sigma_{u,b}^2)$ denote the complex channel coefficient from the UAV to BS, the overall received signal at the BS from the UAV considering both path loss and fading is

$$y_{u,b} = \sqrt{10^{\frac{P_{bs-r}}{10}}} h_{u,b} s_{u,b} + n_{u,b}, \tag{5.13}$$

where $s_{u,b}$ is the transmitted signal of the UAV with $E\left\{|s_{u,b}|^2\right\} = 1$, and $n_{u,b} \sim \mathcal{CN}(0, \sigma_{u,b}^2)$ denotes the noise at the BS. Then, the amount of data that can be

offloaded at the BS in Phase 4 can be expressed as

$$D_{u,b} = T_{phase4} B \log_2 \left(1 + \frac{10^{\frac{P_{bs-r}}{10}} |h_{u,b}|^2}{\sigma_{u,b}^2} \right). \tag{5.14}$$

5.2.5 UAV Propulsion Consumption for Round-Trip Flight

Between Phase 1 and Phase 4, the UAV also requires energy for various manoeuvres, such as hovering, acceleration, deceleration and flying at a speed of V. In this study, we consider the process when the UAV accelerates from an initial velocity of 0 to V and continues to fly to the sensors at the speed of V, and finally decelerates from V to 0 to hover over the sensors. Hence, using (2.11) and (2.15), the energy consumed by the UAV during the acceleration can be calculated approximately as [92] and [117] as

$$E_{Acc} = \int_0^{\frac{V}{a}} P\left[V\left(t\right)\right] \, dt, \tag{5.15}$$

where a is acceleration. Since acceleration and deceleration in this study are symmetric, the energy consumed during deceleration is the same as that during acceleration, i.e., $E_{Acc} = E_{Dec}$. Note that (5.15) is valid only for forward level flight as specified in [49]. For vertical flight and arbitrary 2D level flight, the energy consumption can be calculated using [117, eq. (3)] and [118, eq. (12)], respectively. As a result, complex path planning for the UAV may consume more energy and thus, affects the system performance. This will be considered as future work.

5.2.6 Compound Convex Optimization Problem

It is challenging to directly optimize the time allocation among the above four phases to maximize the amount of data offloaded to the BS, because this target is constrained by both time and energy. The convergence of the target function cannot be guaranteed. However, it is found that more data collected by the UAV is a necessary condition for maximizing the data offloaded to the BS. Thus, the target can be regarded as two sub-problems and both are convex. As a result, the target optimization problem can be solved in the following two steps.

Step 1

We first maximize the data collected by the UAV, i.e., optimize the time allocation between Phase 2 and Phase 3 [23].

Step 2

Once the optimal time ratio between Phase 2 and Phase 3 is derived, it can be combined and taken as a whole. In doing so, the original optimization can be regarded as a time allocation problem with only three processes, i.e., Phase 1, "Phase 2 and Phase 3", and Phase 4.

5.3 Problem Formulation and Optimization

In this section, we will solve an optimization problem that maximizes the amount of data offloaded at the BS to derive the closed-form expression of the optimal time

allocation for the four phases described in Fig. 5.1. To analyze the performance of this process, two cases will be studied. In Case 1, TDMA with optimal transmission times for all sensors is studied. While in Case 2, TDMA with equal transmission times for all sensors is considered.

5.3.1 Case 1

In Phase 1, the UAV hovers above the BS to be charged. It is assumed that the initial position of the UAV is $(0, 0, H)$ with the minimum initial energy of the system E_ϵ. Since the UAV consumes power for keeping aloft (i.e., hovering) while being charged, the sum energy harvested by the UAV at the end of T_{phase1} can be calculated as

$$E_0 = E_\epsilon + E_{uav-h} - E_{hover1}, \tag{5.16}$$

where E_{uav-h} is the energy harvested by the UAV from the BS in (5.2) with $E_{uav-h} > E_{hover1}$, $E_{hover1} = P(0) \cdot T_{phase1}$ is the energy consumed by hovering in Phase 1, $P(0)$ is the power for hovering and T_{phase1} is the hovering time. We denote as E_{fly-to} and $E_{fly-back}$ the energy consumed by the UAV flying to the sensors and flying back to the BS, respectively. One has

$$E_{fly-to} = E_{fly-back} = E_{Acc} + E_V + E_{Dec}. \tag{5.17}$$

In Phase 2, the UAV broadcasts wireless energy to the sensors by WPT. The total energy transferred from the UAV can be calculated as

$$E_{wpt} = 10^{\frac{P_{uav-t}}{10}} * T_{phase2}, \tag{5.18}$$

and the energy consumed for hovering during this process is

$$E_{hover2} = P\left(0\right) * T_{phase2}. \tag{5.19}$$

After this, the sensors start to transmit their data to the UAV via TDMA using the harvested energy.

In Phase 3, the UAV still needs to keep aloft while receiving data from the sensors. Hence, it continues consuming energy in hovering as

$$E_{hover3} = P\left(0\right) * T_{phase3}. \tag{5.20}$$

Next, the UAV flies back to the BS with the collected data to consume an amount of energy $E_{fly-back}$ given in (5.17).

In Phase 4, when the UAV reaches the BS, the available energy at the UAV is

$$\begin{aligned} E_{available} = E_0 - E_{fly-to} - E_{fly-back} \\ - E_{wpt} - E_{hover2} - E_{hover3}. \end{aligned} \tag{5.21}$$

To deliver as much data collected from the sensors to the BS as possible, $E_{available} - E_\epsilon$ will be used for offloading. The reason to keep an amount of energy E_ϵ at the end of offloading is to prepare the UAV for the next round of data collection. Hence, $E_{available} \geq E_\epsilon$. Meanwhile, since the UAV has to keep hovering, the offloading time for Phase 4 can be calculated as

$$T_{phase4} = \frac{E_{available} - E_\epsilon}{P\left(0\right) + 10^{\frac{P_{uav-t}}{10}}}, \quad T_{phase4} \geq 0. \tag{5.22}$$

Based on the above discussion, we can finally formulate the time allocation problem that maximizes the amount of data received by the BS under the constraint of a fixed time $\tau = T - T_{flying}$, where T is the total time and T_{flying} is the time for round trip which is determined by the flight distance and UAV speed and both are fixed. The variables to be optimized are T_{phase1}, T_{phase2}, T_{phase3} and T_{phase4}. As a result, the problem is formulated as

$$(P1): \max_{T_{phase1}, T_{phase2}, T_{phase3}, T_{phase4}} D_{u,b}, \tag{5.23a}$$

$$\text{s.t.: } 0 \leq T_{phase1} \leq \tau, \tag{5.23b}$$

$$0 \leq T_{phase2} \leq \tau, \tag{5.23c}$$

$$0 \leq T_{phase3} \leq \tau, \tag{5.23d}$$

$$0 \leq T_{phase4} \leq \tau, \tag{5.23e}$$

$$E_{available} \geq E_{\epsilon}, \tag{5.23f}$$

$$D_{u,b} \leq D_{K,u}, \tag{5.23g}$$

$$\tau = T_{phase1} + T_{phase2} + T_{phase3} + T_{phase4}, \tag{5.23h}$$

where (5.23a) is the objective function, (5.23b) – (5.23e) are the constraints on T_{phase1}, T_{phase2}, T_{phase3} and T_{phase4}, (5.23f) is the constraint on available energy at the UAV in Phase 4 given by (5.16) and it has already included the constraint $E_{uav-h} > P(0) \cdot T_{phase1}$ in (5.16), (5.23g) is the constraint on data volume between $D_{u,b}$ and $D_{K,u}$ that the amount of received data cannot exceed the amount of collected data, and (5.23h) is the constraint on the fixed time τ.

The optimization problem in (5.23) is complicated because the objective function is constrained by both energy and time, and its convergence cannot be guaranteed. This can be explained as follows. With given T_{phase1}, T_{phase2} and T_{phase3}, T_{phase4} can be derived by (5.23h). However, T_{phase4} is also given by (5.22),

the one for offloading data in Phase 4 with energy constraint included in (5.23f). It does not necessarily imply that the two are equal. When the one from (5.23h) is greater than the one from (5.22), it means there is a waste of time as the energy determines the time that can be used to offload data. Besides, it may be noted that $D_{K,u}$ is actually determined by T_{phase2} and T_{phase3} as T_{phase2} determines the energy used to transmit data from sensors to the UAV in Phase 3. Thus, the time allocation between T_{phase2} and T_{phase3} should be carefully chosen. Once this optimal allocation is derived, then they can be considered as a whole for optimizing the allocation of τ. To this end, we decompose this optimization into two steps.

5.3.2 Solution to Case 1

Step 1

In order to maximize the amount of data received at the BS, we first optimize the time allocation between T_{phase2} and T_{phase3} to maximize the amount of data received from sensors by fixing $T_{phase2} + T_{phase3}$. To do this, denote $T_{phase2\&3} = T_{phase2} + T_{phase3}$ as the sum of T_{phase2} and T_{phase3}, and $\mu_2 = \frac{T_{phase2}}{T_{phase2\&3}}$ and $\mu_3 = \frac{T_{phase3}}{T_{phase2\&3}}$ as the proportions of T_{phase2} and T_{phase3} in the sum, respectively. Once the optimal values of μ_2 and μ_3 are derived as μ_2^* and μ_3^*, the optimal time allocation of T_{phase2} and T_{pahse3} can be obtained as $\mu_2^* * T_{phase2\&3}$ and $\mu_3^* * T_{phase2\&3}$, respectively, for fixed $T_{phase2\&3}$ in this step. Mathematically, this problem after normalization

of $T_{phase2\&3}$ can be formulated as

$$(P1_{-S1}) : (\mu_2^*, \mu_3^*) = \underset{\mu_2,\mu_3}{\arg\max}\ \bar{D}_{K,u}\ (\mu_2, \mu_3) \tag{5.24a}$$

$$\text{s.t.: } \mu_2 + \mu_3 = 1, \tag{5.24b}$$

$$0 < \mu_2, \mu_3 < 1, \tag{5.24c}$$

where $\bar{D}_{K,u} = \frac{D_{K,u}}{T_{phase2\&3}}$ is the normalized achievable data rate with respect to time. The optimization problem in (5.24) is different from that in [44] and [23] as they used fixed energy conversion efficiency. In our work, we assumed that the energy conversion efficiency is non-linear and depends on the input power as in (5.6), since the received power at each sensor is different. The transmit power of each sensor, P_{k-t}, is determined by its harvested energy from the UAV, as in [44, 45] and [23]. To solve $(P1_{-S1})$ above, using (5.3) to (5.11) and replacing t_k in (5.11) with its time proportion λ_k, $(P1_{-S1})$ can be reformulated as

$$(P1_{-S1}) : (\mu_2^*, \mu_3^*) = \underset{\mu_2,\mu_3}{\arg\max} \sum_{k=1}^{K} \lambda_k \log_2 \left(1 + \gamma_k \frac{\lambda_0}{\lambda_k}\right) \tag{5.25a}$$

$$\text{s.t.: } \sum_{k=0}^{K} \lambda_k = 1, \tag{5.25b}$$

$$\lambda_k \geq 0,\ k = 0, \cdots, K, \tag{5.25c}$$

$$\mu_2 = \lambda_0, \tag{5.25d}$$

$$\mu_3 = \sum_{k=1}^{K} \lambda_k, \tag{5.25e}$$

where $\gamma_k = \frac{\eta_k 10^{\frac{P_{uav-t}+2G_k+2G_{uav}-2PL_{uav-k}}{10}} \left|h_{u,k}\right|^2 \left|g_{k,u}\right|^2}{\sigma_{k,u}^2}$, $\mu_2 = \lambda_0$ is allocated to the DL WPT in Phase 2, $\lambda_k \geq 0,\ k = 1, \cdots, K$, is the time portion assigned to the kth sensor and $\mu_3 = \sum_{k=1}^{K} \lambda_k$ is the total time portion for UL WIT in Phase 3.

Note that, for an arbitrary topology of sensors, one needs to study the optimal location of the UAV [92], as the geometric center may not be the middle of the area. This study is beyond the scope of the current work. Also, we do not consider UAV trajectory optimization, as in [71] and [73], because these works have ignored the UAV power consumption and the flying-to and flying-back processes while our work takes all of these into account. When UAV power consumption is considered, flying to each sensor may be disadvantageous to staying at a fixed location, due to the extra propulsion energy. Thus, the UAV will hover at one spot over the sensors.

From [23], (5.25) is a convex optimization problem and the optimal time allocation solution for $(P1_{-S1})$ in each block time of $T_{phase2\&3}$, denoted by ${\lambda_k}^\star,\ k = 0, \cdots, K$, is given by

$$
{\lambda_k}^\star = \begin{cases} \dfrac{z^\star - 1}{\Upsilon + z^\star - 1}, & k = 0, \\ \dfrac{\gamma_k}{\Upsilon + z^\star - 1}, & k = 1, \cdots, K, \end{cases} \tag{5.26}
$$

where $\Upsilon = \sum_{k=1}^{K} \gamma_k > 0$ and $z^\star$ is the solution of $z \ln z - z + 1 = \Upsilon,\ z \geq 0$ given in [23][1]. Hence, the values for Phase 2 and Phase 3 can be obtained as

$$
\begin{cases} \mu_2^* = {\lambda_0}^\star, \\ \mu_3^* = \displaystyle\sum_{k=1}^{K} {\lambda_k}^\star, \end{cases} \tag{5.27}
$$

[1]Remarks: Although (5.25) is the same problem as in [23], they are applied in different scenarios. In our work, the RF-to-DC conversion efficiency is non-linear but in [23] it is linear. In [23], Rayleigh fading is considered, while Rician fading is assumed in our work. Besides, the UAV has not been considered as an energy transmitter and a data collector in [23].

and the optimal time allocation between Phase 2 and Phase 3 can be derived as

$$\begin{cases} T^*_{phase2} = \mu^*_2 * T_{phase2\&3}, \\ T^*_{phase3} = \mu^*_3 * T_{phase2\&3}. \end{cases} \tag{5.28}$$

Also, the sum achievable data rate can be obtained by substituting (5.26) into (5.25) as

$$\bar{D}_{K,u} = \sum_{k=1}^{K} {\lambda_k}^\star \log_2 \left(1 + \gamma_k \frac{{\lambda_0}^\star}{{\lambda_k}^\star}\right). \tag{5.29}$$

Step 2

Once the achievable data in the sensor network is maximized in *Step* 1, the whole process can be treated as three phases because T_{phase2} and T_{phase3} can be combined as one phase denoted by $T_{phase2\&3} = T_{phase2} + T_{phase3}$, as *Step* 1. In this case, we let α and β be the ratio of T_{phase1} and $T_{phase2\&3}$ to the time $\tau = T_{phase1} + T_{phase2} + T_{phase3} + T_{phase4}$, and $(1 - \alpha - \beta)$ be the ratio of T_{phase4} to τ. Thus, $\alpha = \frac{T_{phase1}}{\tau}$, $\beta = \frac{T_{phase2\&3}}{\tau}$, $1 - \alpha - \beta = \frac{T_{phase4}}{\tau}$. As a result, the optimization problem in (5.23) can be rewritten as

$$(P1_{-S2}) : (\alpha^*, \beta^*) = \arg\max_{\alpha,\beta} \; D_{u,b}\,(\alpha, \beta) \tag{5.30a}$$

$$\text{s.t.: } 0 \le \alpha \le 1, \tag{5.30b}$$

$$0 \le \beta \le 1, \tag{5.30c}$$

$$0 \le \alpha + \beta \le 1, \tag{5.30d}$$

$$E_{available} \ge E_\epsilon, \tag{5.30e}$$

$$D_{u,b} \le D_{K,u}. \tag{5.30f}$$

where (5.30a) is the objective function, (5.30b) – (5.30d) are the constraints on T_{phase1}, $T_{phase2\&3}$ and T_{phase4}, respectively, (5.30e) is the constraint on energy when the UAV arrives at the top of the BS in Phase 4, and (5.30f) is the constraint on the data volume between $D_{u,b}$ and $D_{K,u}$.

Details on the solution to $(P1_{-S2})$ are summarized in Algorithm 7. In the Algorithm, some special cases causing $D_{u,b} = 0$ have also been considered. This comes from the lack of time ($1-\alpha-\beta \leq 0$) or energy ($E_{available} \leq E_{\epsilon}$), or the time proportion (β) for Phase 3 is 0. Once α^* and β^* are derived from the Algorithm 7, the optimal time allocation between T_{phase1}, $T_{phase2\&3}$ and T_{phase4} can be derived as

$$\begin{cases} T^*_{phase1} = \alpha^* \tau, \\ T^*_{phase2\&3} = \beta^* \tau, \\ T^*_{phase4} = (1 - \alpha^* - \beta^*)\, \tau. \end{cases} \tag{5.31}$$

Since the optimal time allocation proportions of T_{phase2} and T_{phase3} have been derived in $P1_{-S1}$, as μ_2^* and μ_3^*, the final optimal time allocation for the original problem $(P1)$ can be obtained as

$$\begin{cases} T^*_{phase1} = \alpha^* \tau, \\ T^*_{phase2} = \mu_2^* \beta^* \tau, \\ T^*_{phase3} = \mu_3^* \beta^* \tau, \\ T^*_{phase4} = (1 - \alpha^* - \beta^*)\, \tau. \end{cases} \tag{5.32}$$

Complexity Analysis of Algorithm 7

For Algorithm 7, the complexity to compute $D_{u,b}(i,j)$ mainly comes from the two "for" loops for parameters α and β, which are determined by the step-sizes of α

Algorithm 7: Optimization of (5.30)

Input: $\alpha = 0$: $step\_\alpha$: 1, $\beta = 0$: $step\_\beta$: 1

Output: $D_{u,b_{max}}$, $\alpha^*(i), \beta^*(j)$

```
for i=1: length(α) do
    for j=1: length(β) do
        /* E_4 is the available energy at Phase 4 calculated by α(i)
           and β(j) */
        if α(j) == 0 || β(j) == 0 || α(i) + β(j) ≥ 1 then
            D_{u,b}(i,j) = 0 // Data from the UAV to the BS
        else
            E_4(i,j) ← calculate the rest of energy using α(i), β(j)
            if E_4 ≤ 0 then
                D_{u,b}(i,j) = 0
            /* Compare the actual remaining time with the original
               planned allocation time */
            else if E_4(i,j) / (P_{uav-t} + P_{hover}) ≥ (1 − α(i,j) − β(i,j)) τ then
                /* TP_{ub} is the throughput from the UAV to the BS */
                if (1 − α(i,j) − β(i,j))τ * TP_{ub} ≥ β(j)τ * D̄_{K,u} then
                    D_{u,b}(i,j) = β(j)τ * D̄_{K,u}
                else
                    D_{u,b}(i,j) = (1 − α(i,j) − β(i,j))τ * TP_{ub}
            else
                if E_4(i,j) / (P_{uav-t} + P_{hover}) * TP_{ub} ≥ β(j)τ * D̄_{K,u} then
                    D_{u,b}(i,j) = β(j)τ * D̄_{K,u}
                else
                    D_{u,b}(i,j) = E_4(i,j) / (P_{uav-t} + P_{hover}) * TP_{ub}
```

Result: $D_{u,b_{max}} = \max D_{u,b}(i,j), \alpha^*(i), \beta^*(j) \leftarrow (i,j) = \arg\max D_{u,b}(i,j)$

or β. Assume that the number of iterations of the first "for" loop is m, and the second "for" loop is n. The complexity of Algorithm 7 is

$$\boldsymbol{O}\left(m \times n\right), \tag{5.33}$$

where $m = \frac{1}{step\_\alpha} + 1$, $n = \frac{1}{step\_\beta} + 1$.

5.3.3 Case 2

Compared with Case 1, in this case, the time allocated to each sensor is the same in Phase 3. Hence, there is no optimal time allocation for each sensor in Phase 3. This simplifies the network synchronization. As discussed in [23], there is always a "near-far" issue that affects the fairness among users. In [23], this was tackled by imposing a minimum rate on each user.

Now that the time allocated for each sensor in Phase 3 is the same, one has calculated as

$$t_k = \frac{T_{phase3}}{K}. \tag{5.34}$$

Consequently, the transmission power by the kth sensor, denoted by P_{k-t} as in (5.8) can be calculated by substituting (5.34) into (5.8) as

$$P_{k-t} = \frac{E_k}{t_k} = \frac{\eta_k 10^{\frac{P_{k-r}}{10}} |h_{u,k}|^2 T_{phase2} K}{T_{phase3}}. \tag{5.35}$$

As other processes and the final optimization problem, i.e., maximizing $\bar{D}_{K,u}$, are the same as in Case 1, the problem is also solved in two steps.

5.3.4 Solution to Case 2

Step 1

Step 1 can be formulated by using $\bar{D}_{K,u} = \sum_{k=1}^{K} \frac{\mu_3}{K} \log_2 \left(1 - KA_k + \frac{KA_k}{\mu_3}\right)$ and $\mu_2 = 1 - \mu_3$ as

$$\mu_3^* = \arg\max_{\mu_3} \sum_{k=1}^{K} \frac{\mu_3}{K} \log_2 \left(1 - KA_k + \frac{KA_k}{\mu_3}\right), \tag{5.36a}$$

$$\text{s.t.: } 0 < \mu_3 < 1, \tag{5.36b}$$

where $A_k = \frac{\eta_k 10^{\frac{P_{uav-t}+2G_k+2G_{uav}-2PL_{uav-k}}{10}} \left|h_{u,k}\right|^2 \left|g_{k,u}\right|^2}{\sigma_{k,u}^2}$. From (5.36), the objective function is a function of μ_3 for a given number of sensors K. This is because η_k and PL_{uav-k} in A_k can be regarded as constants given the topology of sensors. Besides, as in [23], it is assumed that both DL and UL channels are quasi-static flat-fading. Thus, $\left|h_{u,k}\right|^2$ and $\left|g_{k,u}\right|^2$ remain constant during each block in Phase 3. Note that A_k $(k = 1 \ldots K)$ are different for different sensors. Hence, $\bar{D}_{K,u}$ can be seen as a function of only one variable μ_3.

From (5.36), $\bar{D}_{K,u} = \sum_{k=1}^{K} \frac{\mu_3}{K} \log_2 \left(1 - KA_k + \frac{KA_k}{\mu_3}\right)$ is a concave function of μ_3 and thus, this is a convex optimization problem. However, the first order derivative of (5.36) includes an item in the form of "$x \ln x$", and it is challenging to derive its closed-form solution when K is large. Hence, for K sensors with a given topology, one-dimensional exhaustive search will be used to derive μ_3^* and corresponding $\bar{D}_{K,u}$. This is described in Algorithm 8. For the special case of only one sensor, i.e., $K = 1$, the optimal time proportion, μ_3^*, is also derived in Appendix C.1.

Algorithm 8: Optimization of (5.36)

Input: μ_3 =Initial value: $step\_\mu_3$: $1, G_k, G_{uav}, r, R,$
$K, P_{uav-t}, \sigma^2_{k,u}$, Sum_$\bar{D}_{K,u}$, Average_$\bar{D}_{K,u}$,
temp_$\bar{D}_{K,u}$, $\bar{D}_{K,u}$=0

Output: μ_3^*, $\bar{D}_{K,u}$

```
for i=1: length(μ3) do
    Initialize Sum_D̄K,u = 0
    for j=1:1000 do
        for k=1:K do
            // PDF_Rician is Probability Density Function of Rician distribution
            h_{u,k}(k) = random(PDF_Rician, 1, 1)
            g_{k,u}(k) = random(PDF_Rician, 1, 1)
            Calculate A_k
        Calculate temp_D̄K,u(j)=Σ_{k=1}^{K} D̄k,u ← using μ3(i)
        Sum_D̄K,u = Sum_D̄K,u + temp_D̄K,u(j)
    Average_D̄K,u(i) = Sum_D̄K,u / 1000
    if D̄K,u < Average_D̄K,u(i) then
        D̄K,u = Average_D̄K,u(i)
        μ3* = μ3(i)
```

Result: μ_3^*, $\bar{D}_{K,u}$

Complexity Analysis of Algorithm 8

For Algorithm 8, the complexity to calculate μ_3^* and $\bar{D}_{K,u}$ mainly comes from three "for" loops with indexes i, j and k. The increment index i is determined by the step-size $step\_\mu_3$, and k depends on the number of sensors K. Note that the last value of the index j is fixed, assumed to be 1000 as an example. As a result, denoting $l = \frac{1}{step\_\mu_3}$ as the number of iterations of the first "for" loop, the complexity of Algorithm 8 can be calculated as

$$\boldsymbol{O}\left(l \times 1000 \times K\right). \tag{5.37}$$

As a result, the optimal time proportion of T_{phase2} can then be calculated as $\mu_2^* = 1 - \mu_3^*$. Finally, the optimal time allocation for T_{phase2} and T_{phase3} can be obtained as (5.28).

Step 2

As other processes are the same as those in Case 1, the optimal time allocation for Phases 1 to 4 can be derived following the steps in Step 2 of Case 1.

5.4 Further Discussion

5.4.1 Wired Charging

Case 1 and Case 2 are the cases when there is no dedicated landing dock at the BS for wired charging or when it is not convenient or safe for the UAV to land due to the complicated environment. They require wireless charging. In this subsection, we discuss the case when wired charging is available.

Case 3

Following the discussion in Case 1, the UAV is first charged by the BS via a wired connection and thus, T_{phase1} will be greatly reduced because of high energy conversion efficiency. However, there may be an extra vertical flight when the height of the BS is lower than H, which in turn increases T_{flying} and consumes extra energy. Upon arrival, the method in $Step1$ of Case 1 is still valid and can be used to derive the optimal time proportion, μ_2^* and μ_3^*, for the WPT phase

and the WIT phase. In this case, T_{phase4} can be ignored because of the wired connection. As a result, $\tau = T - T_{flying} = T_{phase1} + T_{phase2\&3}$. To maximize the data offloaded to the BS, one needs to balance the relationship between time and energy. Specifically, with small T_{phase1}, E_0 is also small. In this regime, as E_0 increases with increasing T_{phase1} until it is fully charged. However, as T_{phase1} increases, $T_{phase2\&3}$ is decreased. As a result, the amount of data collected from sensors will be limited by time. In turn, it will be limited by energy. Therefore, there exists an optimal time allocation between T_{phase1} and $T_{phase2\&3}$. One has the following relationship

$$\begin{cases} \tau = T_{phase1} + T_{phase2\&3}, \\ E_{available} = E_{\epsilon}. \end{cases} \tag{5.38}$$

Case 4

In this case, we not only use wired charging to replace wireless charging as in Case 3, but also allocate equal times to the K sensors, as in Case 2. Thus, the optimal values of μ_2^* and μ_3^* in this are derived by Algorithm 8, instead of from equations (5.26) and (5.27). As other processes and steps are the same as those in the previous subsection, they will not be discussed further. It can be noted that, for the case of wired charging, T_{phase4} can be ignored as the collected data can be transmitted to the BS by a wired connection. Thus, more time can be used for WPT and WIT in Phases 2 and 3, respectively.

5.4.2 Transmission Efficiency

Using (5.11) and (5.14), the transmission efficiency of the UAV-aided data collection system can be defined as

$$TE = \frac{D_{u,b}}{D_{K,u}} = \frac{T_{phase4} B \log_2 \left(1 + \frac{10^{\frac{P_{bs-r}}{10}} |h_{u,b}|^2}{\sigma_{u,b}^2}\right)}{\sum_{k=1}^{K} t_k B \log_2 \left(1 + \frac{10^{\frac{P_{uav-r_k}}{10}} |g_{k,u}|^2}{\sigma_{k,u}^2}\right)}. \tag{5.39}$$

In Section 5.3, we have first maximized $D_{K,u}$ in (5.24) and then maximized $D_{u,b}$ in (5.30). The value of $D_{u,b}$ is always smaller than or equal to $D_{K,u}$. Thus, $TE \leq 1$. When $TE < 1$, there is some data loss, as the amount of data offloaded to the BS is smaller than the data collected from the sensors. Ideally, all the collected data should be delivered to the BS so that the transmission efficiency should be 1. Transmission efficiency of 1 does not guarantee that the data received by the BS is the maximum and vice versa. This is because there are many ways of achieving a transmission efficiency of 1. For example, the UAV can choose to collect a minimum amount of data from the sensors to be fully delivered to the BS so that both $D_{u,b}$ and $D_{K,u}$ are small but no data is lost for reliability to achieve a transmission efficiency of 1. Therefore, we can let the transmission efficiency be 1, and let time for Phase 4 all be used to offload the data. One has

$$\begin{cases} D_{u,b} = D_{K,u}, \\ E_{available} - E_{\epsilon} = (1 - \alpha - \beta)\tau * \left(P(0) + 10^{\frac{P_{uav-t}}{10}}\right). \end{cases} \tag{5.40}$$

Therefore, the optimal allocation can be derived by solving (5.40) as

$$\begin{aligned} \alpha^* &= \frac{MF - NW}{MF - NE}, \\ \beta^* &= \frac{MW - ME}{MF - NE}, \end{aligned} \tag{5.41}$$

where $M = \log_2\left(1 + \frac{10^{\frac{P_{bs-r}}{10}}\left|h_{u,b}\right|^2}{\sigma_{u,b}^2}\right)$, $N = M + \bar{D}_{K,u}$, $W = E_{fly-to} + E_{fly-back} + P(0)\tau + 10^{\frac{P_{uav-t}}{10}}\tau$, $E = \eta 10^{\frac{P_{uav-r}}{10}}\left|g_{b,u}\right|^2\tau + 10^{\frac{P_{uav-t}}{10}}\tau$, $F = \mu_3^*\tau 10^{\frac{P_{uav-t}}{10}}$. This solution ensures that all data collected from sensors will be offloaded to the BS without wasting any time and energy. For Cases 1 and 2 in wireless charging, the solution in (5.41) depends on μ_2^* and μ_3^* derived from (5.27) or Algorithm 8 although it has closed-form. Moreover, the random complex channel coefficient $h_{u,k}$ and $g_{k,u}$ also determines the solution in (5.41). Thus, it is dependent on the values of $h_{u,k}$ and $g_{k,u}$.

5.5 Numerical Results and Discussion

In this section, numerical results are presented to show the optimal time allocation maximizing the amount of data received by the BS. The simulation settings are similar to [43,49,91,92], and the detailed settings are summarized in Table 5.1. The average rate is obtained by generating 1000 random values of $\left|h_{u,k}\right|^2\left|g_{k,u}\right|^2$, adding them together and dividing the sum by 1000. For $\left|h_{b,u}\right|^2$ or $\left|g_{u,b}\right|^2$, the average value of 1000 random values is also taken. The total operating time τ including all phases and round trip flight is set to 3600 s. The RF-to-DC conversion efficiency from the BS to the UAV $\eta \approx 0.8$. The flight distance is set to 1000 m and the parameters of the UAV follow [92, Table I]. These values are only chosen for

Table 5.1: Simulation parameters

Notation	**Parameters**	**Values**
α	The ratio of T_{phase1} to the τ	—
β	The ratio of $T_{phase2\&3}$ to the τ	—
K	Rician factor	10 dB
P_{bs-t}	Transmit power at the BS	35.68 dBW
P_{uav-t}	Transmit power at the UAV	40 dBm
G_{bs}	Antenna gain of the BS	15 dBi
G_{uav}	Antenna gain of the UAV	5 dBi
G_k	Antenna gain of the kth sensor	5 dBi
H_{bs}	The height of the BS	4.5 m
H_{sr}	Sensors antenna height	0.5 m
H	Flight height of the UAV	5.5 m
f	Operating frequency	915 MHZ
B	Bandwidth	1 HZ
v	UAV speed	10 m/s
a	Acceleration/deceleration	1 m/s^2
a_0	Model parameter in (5.5)	2.463
b_0	Model parameter in (5.5)	1.635
c_0	Model parameter in (5.5)	0.826
$\sigma_{b,u}, \sigma_{u,b}, \sigma_{u,k}, \sigma_{k,u}$	Noise power	-80 dBm

illustration purpose but other values can also be used if different applications are considered.

Fig. 5.3 shows the effects of α and β on the data volume at the BS. In this figure, we take one sensor as an example. The upper part of the figure shows the data volume at the BS versus α, which is the charging time proportion in Phase 1, when β is fixed. One can see that all the curves look like a "square wave", as expected. This can be explained as follows. When α is small, the amount of energy harvested by the UAV from the BS is small, which will lead to the following results: i) the UAV has too little energy to fly to the sensors; ii) the UAV has no energy to receive data from the sensors, otherwise it cannot fly back; iii) the UAV can only fly back, but there is no energy to offload data to the BS. Therefore, the

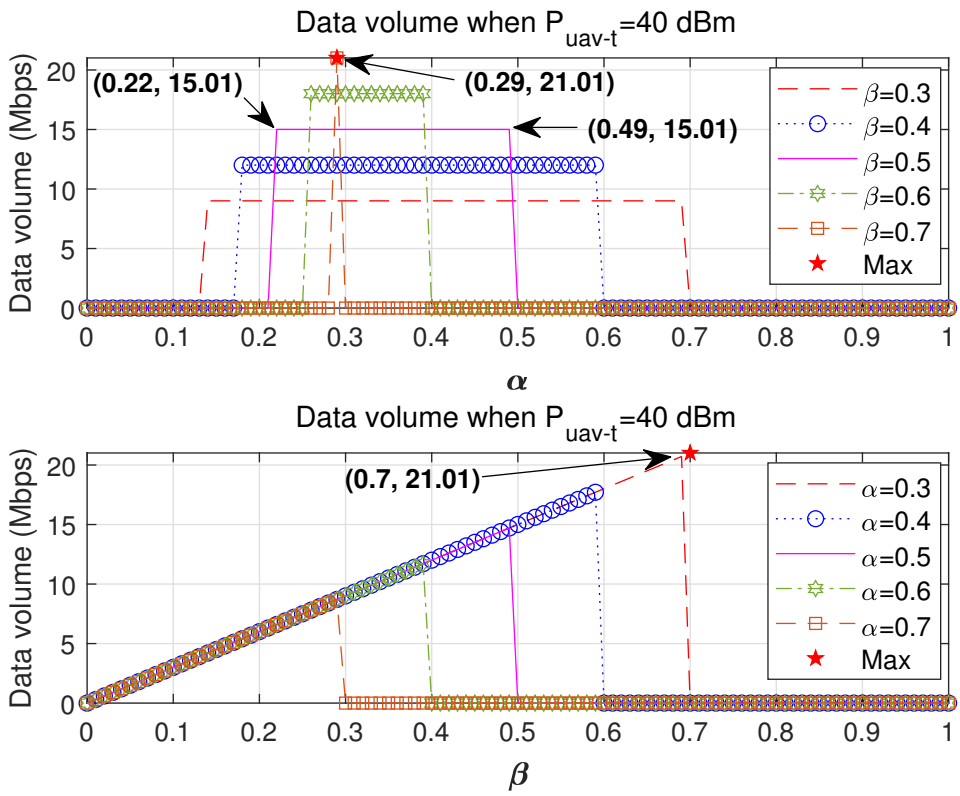

Figure 5.3: The influence of α and β on data volume.

data volume is 0. When α is large, the UAV has enough energy but there is limited time for WPT and WIT. This may lead to 1) no time to receive data from the sensors; 2) no time to fly back; 3) no time to deliver the received data to the BS. As a result, there is no data received by the BS either. When α is medium, reasonable values of α are available for fixed β. Take $\beta = 0.5$ as an example. The data volume remains unchanged when α increases from 0.22 to 0.49, which means $\alpha = 0.22$ is the minimum time portion requirement in this setting. Otherwise, there will be energy surplus after data delivery, such as when $\alpha = 0.4$. The lower part of the figure shows the data volume at the BS versus β, which is the proportion of the total time of Phase 2 and Phase 3 for WPT and WIT, when α is fixed. One sees that the data volume firstly increases with the increase of β, but then decreases to

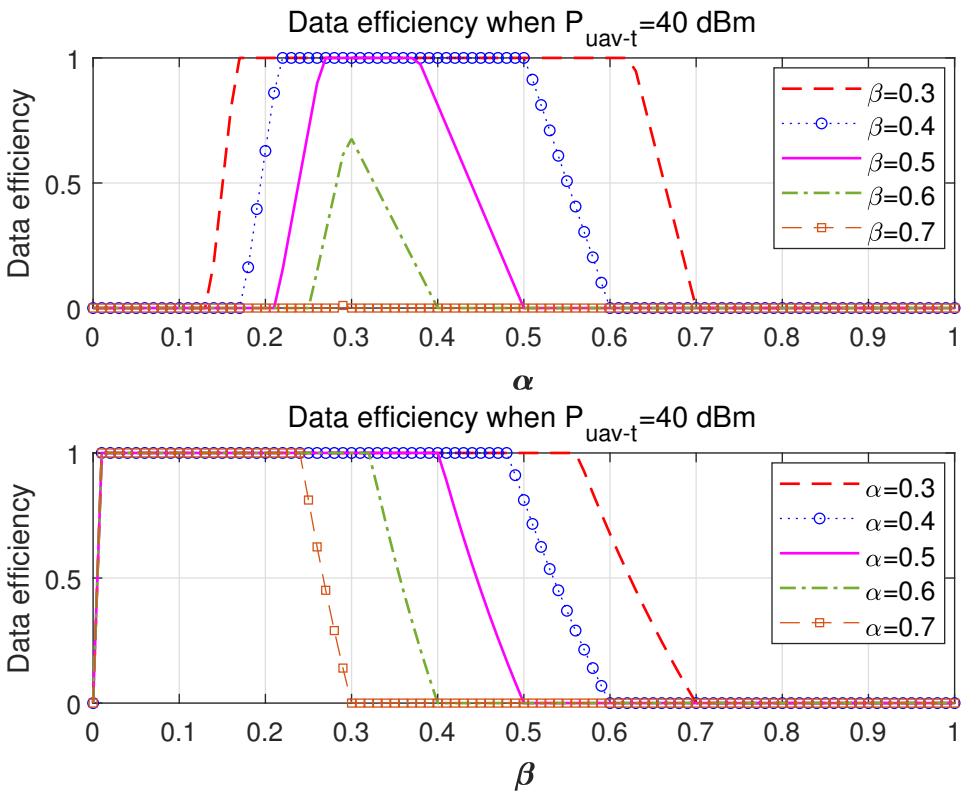

Figure 5.4: The influence of α and β on transmission efficiency.

0, because when α is fixed, the time for Phase 4, $1-\alpha-\beta$, decreases with increasing β. Take the case when $\alpha = 0.4$ as an example. The data volume increases when the value of β increases from 0 to 0.5. When $\beta = 0.6$, the data volume is 0. This is because there is no time left in Phase 4, i.e. $1 - \alpha - \beta = 0$. According to the Algorithm 7, the optimal α^* and β^* in this example are 0.29 and 0.7, respectively, as shown in the figure, and the maximum of data volume is 21.01.

Fig. 5.4 shows the effects of α and β on the transmission efficiency. Also, one sensor is used in this figure as a case study. The upper part of the figure shows the transmission efficiency at the BS versus α when β is fixed. One sees that all the curves start from 0 when β changes from 0.3 to 0.5, and then rise from 0 to 1

and remain unchanged at 1, until it drops from 1 to 0 again. This is explained as follows. When α is small, the amount of energy harvested by the UAV is also small so that there is no energy left for WPT and WIT, or for Phase 4. Therefore, no data can be received by the BS, resulting in an efficiency of 0. For example, when $\beta = 0.7$ and $\alpha = 0.3$, there is no time for data offloading in Phase 4 and thus, it makes data efficiency 0. When α is large, although the UAV has enough energy, there is no time left for Phase 4, as $1 - \alpha - \beta$ decreases with increasing α when β is fixed. Besides, when β increases from 0.3 to 0.5, one sees that the range for α in which the transmission efficiency remains at one narrows. In particular, when $\beta = 0.6$, the transmission efficiency is less than 1. This can also be explained from $1 - \alpha - \beta$. The lower part of the figure shows the transmission efficiency versus β when α is set from 0.3 to 0.7. Similar observations can be made.

Note that, although the transmission efficiency is 1, it does not mean that the data volume is maximized. On the other hand, a large data volume does not mean that the transmission efficiency is 1 either. Thus, Figs. 5.3 and 5.4 provide very useful guidance on the choices of α and β to either maximize data volume or ensure transmission efficiency. For example, in monitoring applications for prediction, all sensing data are necessary. Hence, it is of great importance to ensure that all the sensing data collected by the UAV can be delivered to the BS. In data sampling applications for big data analysis, collecting as much data as possible and ensuring data diversity are two priorities but there is redundancy in data to allow loss. Therefore, it is important to choose reasonable values of α and β to meet different requirements.

Fig. 5.5 compares the optimal time proportion for WPT in Phase 2 and WIT in Phase 3, i.e., μ_2^* and μ_3^*, for Case 1 and Case 2. In the figure, we take five sensors located on a circle with a radius of 1 meter as an example. The upper part

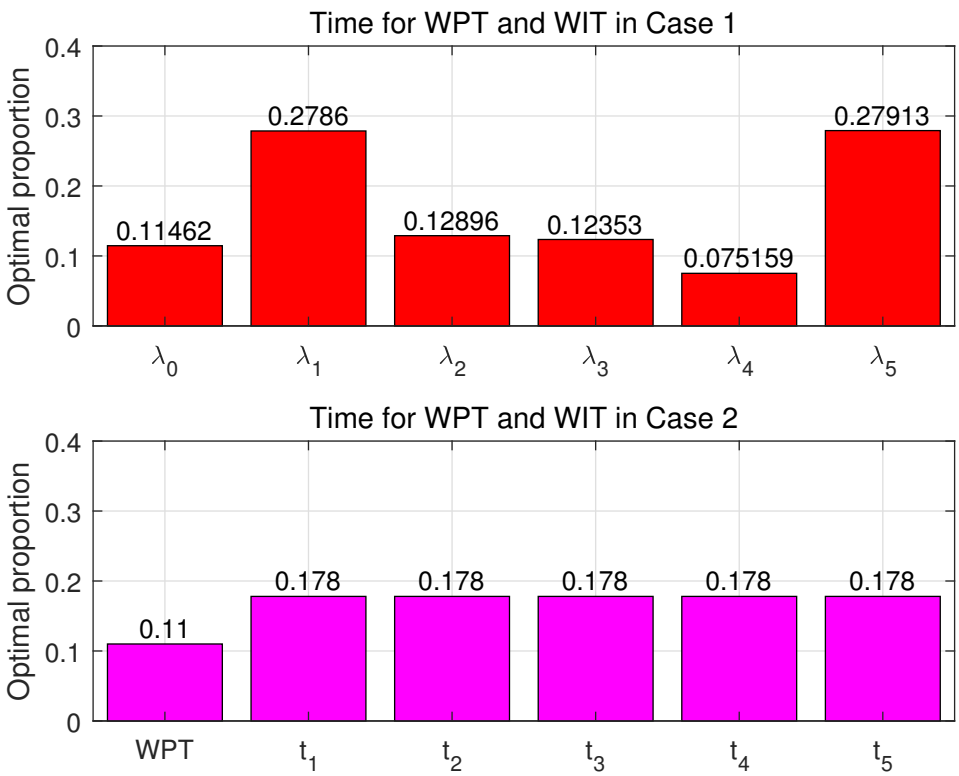

Figure 5.5: The optimal time proportion of WPT and WIT, Case 1 versus Case 2.

of the figure shows the optimal time proportion of WPT and WIT for each sensor, labeled as λ_0^* and λ_k^* respectively in (5.26) and (5.27). To maximize throughput, the time allocated for each sensor for WIT mainly depends on the channel state. As shown in the figure, the channel state between the UAV and the 1st and 5th sensors are the best among the five sensors so that their time proportion, i.e., 0.2786 and 0.27913, is the largest. On the contrary, the 4th sensor has the worst channel state and thus, its time proportion is the smallest. The lower part of the figure shows the optimal time proportion in Case 2 with equal times for different sensors. As shown in the figure, the time proportion for each sensor is equal to 0.178, and the ratio of WPT to WIT is 0.11/0.89, which is a bit small than that in Case 1.

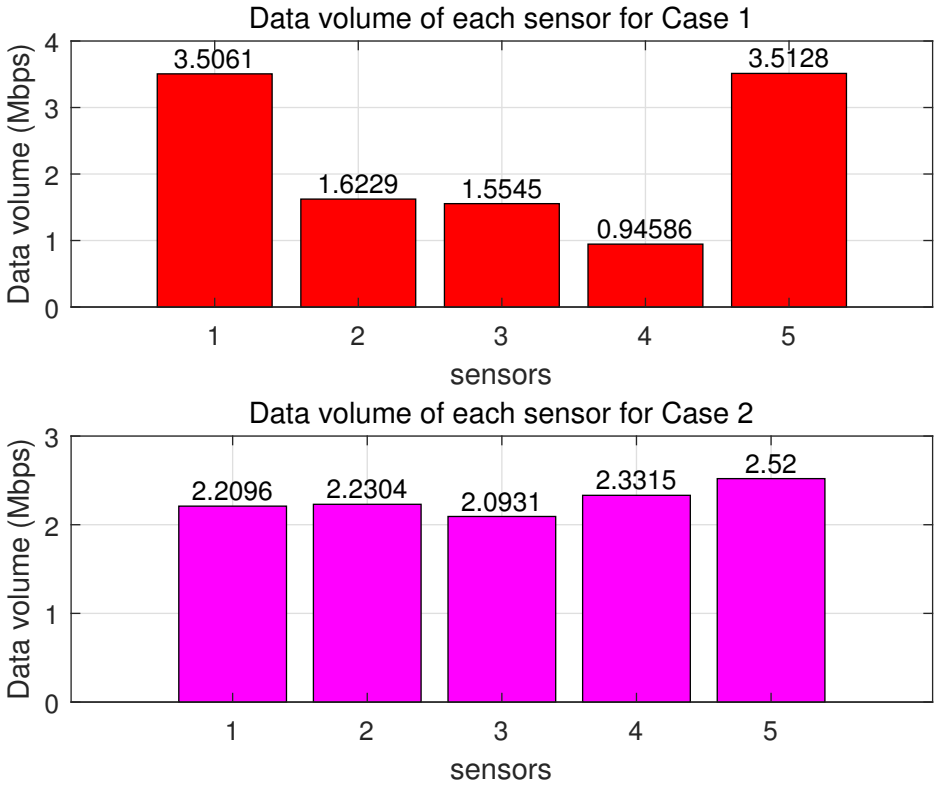

Figure 5.6: Data volume of each sensor, Case 1 versus Case 2.

Fig. 5.6 shows the data volume received from each sensor with time proportion from Fig. 5.5 per unit time in Case 1 and Case 2. The upper part of the figure shows the data sent by each sensor in Case 1, using the same allocation ratio as in Fig. 5.5. One sees that the data volume sent by each sensor is proportional to its allocated time and harvested energy. As the 5th sensor is allocated the largest proportion of 0.27913 shown in Fig. 5.5, its transmitted data is 3.5128, which is also the largest. The lower part of the figure shows the data sent by sensors in Case 2, the same observation can be made. However, the data volume sent by each sensor varies due to different channel conditions. From the viewpoint of data volume, the total amount of data in Case 1 is very close to that in Case 2. However, there is a data imbalance in Case 1. For example, the data received from the 5th sensor, i.e.,

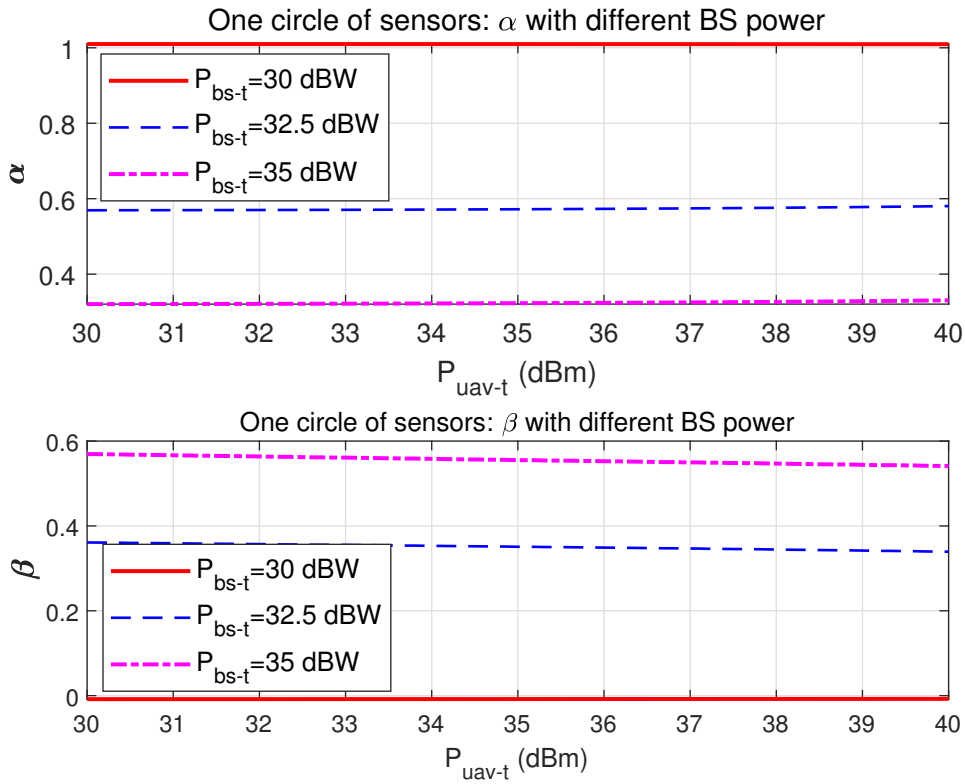

Figure 5.7: The influence of P_{uav-t} on α^* and β^*.

3.5128, is much greater than 0.94586 from the 4th sensor. Case 2 shows a better balance in terms of data volume among all sensors, because sensors in Case 2 have the same time allocated for transmitting data. Therefore, it is of great importance to choose Case 1 or Case 2 to meet different application requirements.

Fig. 5.7 studies the effect of P_{uav-t} on the optimal time allocation (α^*, β^*). In the figure, we take five sensors located on a circle with a radius of 10 meters as an example, and Algorithm 8 and equation (5.41) are used. Unless otherwise specified, this topology is also used as an example in Fig. 5.8 and Fig. 5.9. The upper part of the figure shows the influence of P_{uav-t} on α^* when P_{bs-t} is set as 30 dBw, 32.5 dBw and 35 dBw. One sees that the optimal value of α^* increases with

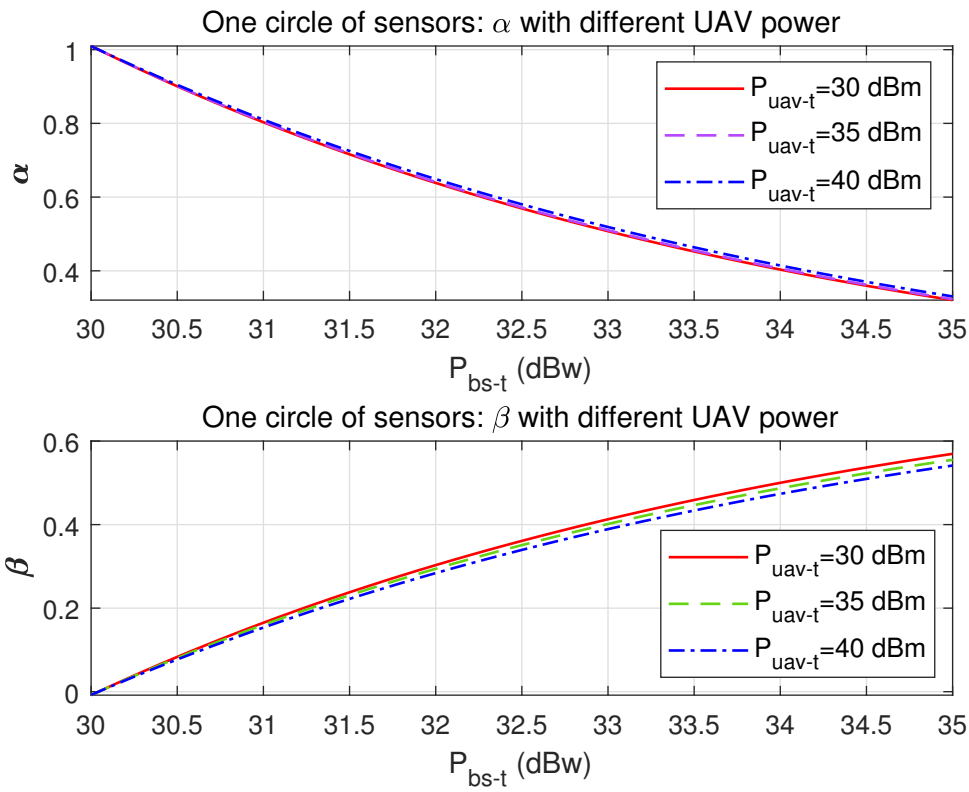

Figure 5.8: The influence of P_{bs-t} on α^* and β^*.

increasing P_{uav-t}, because larger transmitting power needs more energy reserve. When P_{uav-t} is fixed, one can see that the higher the transmitting power of the BS, the smaller the value of α^* will be. This is because the power is inversely proportional to the time when the total required energy is fixed. Note that, when $P_{bs-t} = 30$ dBw, due to the path loss, it is too small to fully charge the UAV. As a result, it needs more time. This is why the solid line above 1, although it is not reasonable as $0 \leq \alpha \leq 1$. The lower part of the figure shows the influence of P_{uav-t} on β^* when P_{bs-t} is set as 30 dBw, 32.5 dBw and 35 dBw. One sees that the value of β^* decreases with increasing P_{uav-t}, because the increase of P_{uav-t} leads to increased α^*, while β^* decreases with increasing α^* when the time for Phase 4, $1 - \alpha^* - \beta^*$, is fixed. Besides, when P_{uav-t} is fixed, one can see that β^*

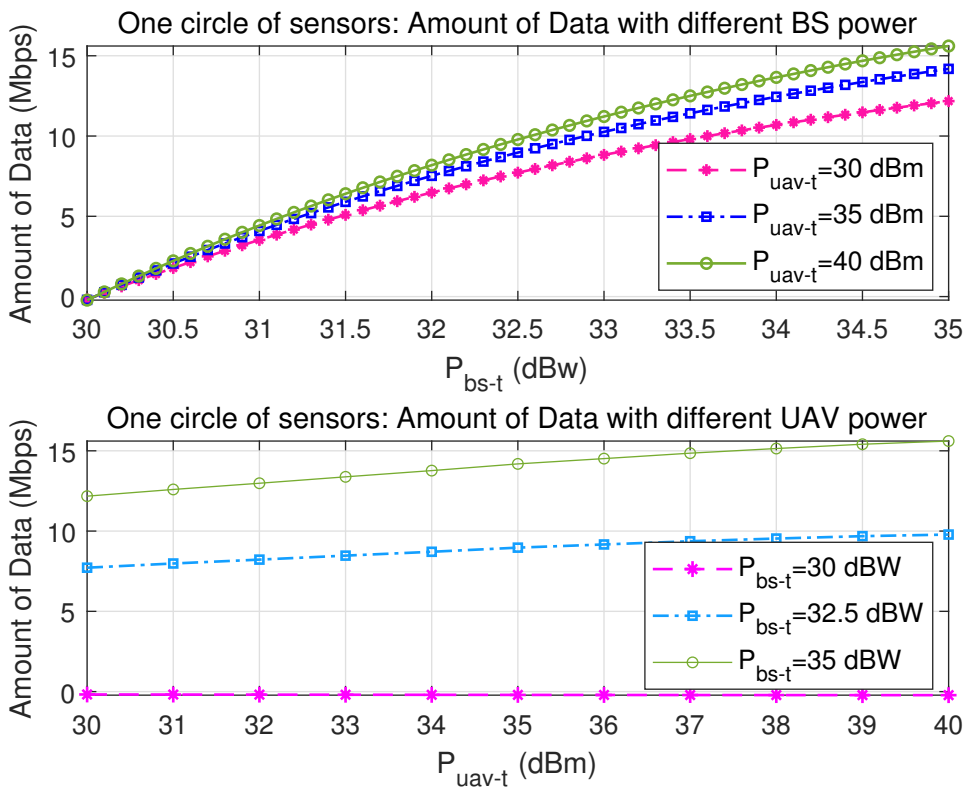

Figure 5.9: Data volume versus P_{bs-t} and P_{uav-t}.

increases with increasing P_{bs-t} as large P_{bs-t} leads to smaller α^*, thereby resulting in increased β^*. Also, the solid line shows that when $P_{bs-t} = 30$ dBw, it is not enough to fully charge the UAV as explained aforementioned.

Fig. 5.8 examines the effects of P_{bs-t} on α^* and β^*, respectively. The upper part and the lower part of the figure show the opposite trend as those in Fig. 5.7. In other words, both Fig. 5.7 and Fig. 5.8 imply that the increase of P_{bs-t} will decrease α^* and increase β^*, whilst the increase of P_{uav-t} will increase α^* and decrease β^*. Note that, changes to α^* and β^* will have an impact on data volume. Thus, we next investigate the effects of P_{bs-t} and P_{uav-t} on the data volume.

Fig. 5.9 examines the effects of P_{bs-t} and P_{uav-t} on the data volume. In

this figure, the upper part shows the effect of P_{bs-t} on the data volume when fixing P_{uav-t} as 30 dBm, 35 dBm and 40 dBm, and the lower part shows the effect of P_{uav-t} on the data volume when fixing P_{bs-t} as 30 dBw, 32.5 dBw and 35 dBw. One sees that all the curves increase with the increase of either P_{bs-t} or P_{uav-t}. As analyzed in Figs. 5.7 and 5.8, increasing P_{bs-t} will lead to decrease α^* and increase β^*, while increasing P_{uav-t} will result in increasing α^* and decreasing β^*. According to this, there should be an optimal power allocation of P_{bs-t} and P_{uav-t} that can increase the data volume further. However, this power allocated is limited by the maximum value of P_{bs-t} allowed and the battery capacity of the UAV itself. This will be an very interesting future work. Beside, when $P_{bs-t} = 30$ dBw, the data volume is almost 0 as little energy makes the UAV unable to complete the given task. Since Case 3 and Case 4 are very similar with Case 1 and Case 2 except for the Phase 1, we do not discuss them here.

5.6 Summary

In this paper, we have studied the optimal time allocation for the UAV-aided data collection, where the BS charging process for the UAV, the UAV's propulsion consumption and the data offloading process are all taken into account. By maximizing the data volume and analyzing the transmission efficiency, the optimal time allocation in different phases has been derived. When the total time is fixed, we have also derived the closed-form expression of the optimal time allocation. Numerical results have shown that the optimal α^* and β^* can maximize the data volume without wasting any time or energy. These results have provided very useful guidance for UAV-enabled WPCN system designs. As future work, It would be interesting to consider the impact of hovering fluctuation. To this end, the effect

of antenna directivity gain under different UAV channel conditions needs to be considered. Besides, it is also interesting and challenging to consider the age of information in sensors with limited memory in time-limited UAV tasks.

Chapter 6

Optimum Battery Weight for UAV-enabled Wireless Communications

This chapter is based on our work published in [J4]. ([117])

6.1 Introduction

Battery-powered electric propulsion systems have been widely used for UAVs [119]. One challenge for battery-powered UAV communications is the choice of battery weight, as a larger battery weight leads to higher battery capacity for longer flight [120] but also heavier UAV to consume more propulsion power. There may exist an optimal battery weight for the best UAV performance, and this applies to both single and multiple UAV applications [121].

Several works have been conducted on battery-powered UAV electric propulsion systems (EPS). For example, the authors in [122] proposed a systematic design for EPS considering the UAV's payload capacity, flight time and battery pack. In [123], several factors, such as the battery-dumping system and battery packs, were studied to analyze the performance of UAVs. The authors in [124] extended the endurance of battery-powered UAVs by grouping battery packs, and the logarithmic growth trend of durability extension was obtained. In [125], different factors in the design of the EPS for UAVs were investigated. In [126], empirical power consumption models for an Intel Aero Ready to Fly Drone were derived for energy efficient UAV mission planning. All these works have provided very useful insights on the design of battery-powered UAVs. However, none of these works has considered optimal battery weight by accounting for UAV propulsion power consumption, which affects the UAV flight and hence communications performance in practice.

In this work, we study the optimal battery weight in UAV-enabled wireless sensor networks. Both vertical and horizontal flights are considered. Numerical results show that the best battery weight that optimizes the flight performance is determined by the flight height, flight distance, vertical/horizontal flight speed and the gross mass of the UAV excluding battery mass.

6.2 System Model

Consider the system shown in Fig. 6.1, where a set of batteries on the parking apron are used as energy for UAV communications. A battery-powered UAV is first equipped with the batteries through an automatic replacement mechanism [50], then flies vertically up to an altitude of H followed by a horizontal flight of distance

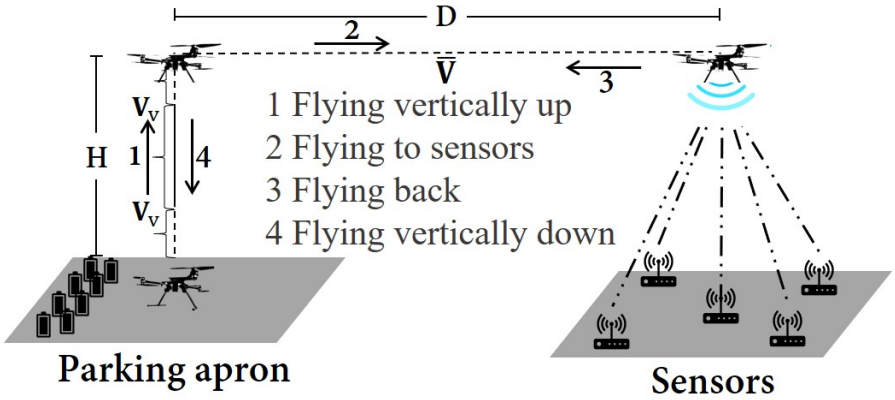

Figure 6.1: System model.

D to the remote sensors with propulsion consumption, denoted as Stages 1 and 2 in Fig. 6.1. Upon arrival, the UAV consumes an energy of E_{A2G} for different communications tasks, such as data collection/transmission and WPT [43, 92]. Finally, the UAV flies back to the parking apron to replace its batteries for the next flight, denoted as Stages 3 and 4 symmetric to Stages 2 and 1, respectively.

In this study, it is assumed that the mass of the UAV, including that of the fuselage and communications system but excluding the battery pack, is m_0, and the mass of the battery pack is m_b. Commonly used lithium polymer (LiPo) batteries are considered because of their high energy density [127]. Thus, the total mass of the UAV is $m = m_0 + m_b$. Using results in [120], [125] and [128], the battery energy capacity [1] E_b in W·s as a function of the battery mass m_b can be derived as

$$E_b\left(m_b\right) = \rho_e * 3600 * m_b * \eta_{DC-DC},\ 0 \leq m_b \leq m_{b,max}, \tag{6.1}$$

where ρ_e is the energy density (W· hr/kg) [120], η_{DC-DC} is the DC-DC conversion

[1]The battery energy capacity represents the maximum amount of energy that can be used from the battery. In this work, the battery energy capacity is measured by W · s.

efficiency ranging from 0.9 to 0.95 [129], $m_{b,max}$ is the maximum battery mass [125] limited by the rotor thrust.

Remarks

Note that, from [120], the energy density of the LiPo batteries is currently 150 Wh/kg, and can be increased to 250 Wh/kg. We set it to 150 Wh/kg in this work. In the case when the parking apron has a height of H, the vertical flight can be ignored. The following results are still valid by ignoring Stages 1 and 4. Also, in the case when there is no automatic battery replacement mechanism [50], charging through a charging station can be considered.

For the manoeuvre of the UAV, the energy consumption models for both horizontal and vertical flights have been discussed in (2.11) and (2.17). We will calculate the propulsion energy consumption using these models.

In general, the performance of a UAV depends on the battery weight m_b. For small m_b, the total mass m is small so that the amount of energy consumed by UAV manoeuvre operations is small. However, the available energy E_b is also small, which results in shorter flight time or less energy for communications. Therefore, there may exist an optimal m_b.

Denote the transmit power at the UAV as P_{uav-t} in dB. Considering path loss [16], the received power at the ground sensor using (2.3) is

$$P_r = P_{uav-t} - \frac{A_0}{1 + a_0 \mathrm{e}^{-b_0(\theta_0 - a_0)}} - B_0, \tag{6.2}$$

where $A_0 = \eta_{LOS} - \eta_{NLOS}$, $B_0 = 20\lg\{H\} + 20\lg\{4\pi f/c\} + \eta_{NLOS}$, c is the speed of light, θ_0 is the elevation angle, η_{LOS}, η_{NLOS}, a_0 and b_0 are constants related to

the propagation environments. The spectral efficiency in bits/Hz is

$$R = \tau \log_2 \left(1 + \frac{10^{\frac{P_r}{10}}}{10^{\frac{\sigma^2}{10}}} \right), \tag{6.3}$$

where $\tau = \frac{E_{A2G}}{10^{\frac{P_{uav-t}}{10}} + P(0)}$ is the time for data transmission while hovering, $P(0)$ is the hovering power when the speed is zero ($V = 0$ in (2.11)), and σ^2 is the received noise power in dB at the sensor.

6.3 Optimization of Battery Weight

In this section, we will maximize E_{A2G} to derive the optimal battery weight. E_{A2G} is given by

$$E_{A2G} = E_b\left(m_b\right) - 2\int_0^{T_v} P_v(V_v, a)\ dt - 2\int_0^{T_h} P(\overline{V})\ dt, \tag{6.4}$$

where 2 comes from the symmetric process of Stages 1 and 4, Stages 2 and 3, $T_v = \frac{H}{V_v} + \frac{V_v}{a}$ is the time for ascending in Stage 1 or the time for descending in Stage 4, assumed to be symmetric, $T_h = \frac{D}{\overline{V}}$ is the time for horizontal flight in Stage 2 or 3, $\overline{V}$ is the mean velocity used to calculate the propulsion energy without considering the acceleration or deceleration, as they are relatively small compared with the long flight at constant speed. The calculation of $\int_0^{T_v} P_v(V_v, a)\ dt$ is divided into three parts, acceleration, constant speed and deceleration, in which the rotor thrust T are $m\left(a+g\right)$, mg and $m\left(g-a\right)$. The integral $\int_0^{T_h} P(\overline{V})\ dt$ can be calculated directly. And both are provided as (6.5) and (6.6) at the top of the next page, where $T_{v1} = T_{v3} = \frac{V_v}{a}$, $T_{v2} = \frac{H}{V_v} - \frac{V_v}{a}$. respectively. Thus, one has

$$E_{A2G} = E_b\left(m_b\right) - E_{vF} - E_{hF}, \tag{6.7}$$

$$\int_0^{T_v} P_v(V_v, a)\ dt = \int_0^{T_{v1}} P_v(V_v)\ dt + \int_0^{T_{v2}} P_v(V_v)\ dt + \int_0^{T_{v3}} P_v(V_v)\ dt$$
$$= \frac{m\,(a+g)}{2}\left(\frac{T_{v1}}{2}\sqrt{a^2T_{v1}^2 + \frac{2m\,(a+g)}{\rho A}} + \frac{m\,(a+g)}{a\rho A}\ln\frac{aT_{v1} + \sqrt{a^2T_{v1}^2 + \frac{2m(a+g)}{\rho A}}}{\sqrt{\frac{2m(a+g)}{\rho A}}}\right)$$
$$+ \frac{mg}{2}\left(V_v + \sqrt{{V_v}^2 + \frac{2mg}{\rho A}}\right)T_{v2} + \frac{m\,(g-a)}{4}aT_{v3}^2$$
$$+ P_2\,(T_{v1} + T_{v2} + T_{v3}) + \frac{m\,(a+g)}{4}aT_{v1}^2$$
$$+ \frac{m\,(g-a)}{2}\left(\frac{T_{v3}}{2}\sqrt{a^2T_{v3}^2 + \frac{2m\,(g-a)}{\rho A}} + \frac{m\,(g-a)}{a\rho A}\ln\frac{aT_{v3} + \sqrt{a^2T_{v3}^2 + \frac{2m(g-a)}{\rho A}}}{\sqrt{\frac{2m(g-a)}{\rho A}}}\right), \tag{6.5}$$

$$\int_0^{T_h} P\left(\overline{V}\right)\ dt = \left[P_0\left(1 + \tfrac{3\overline{V}^2}{U_{tip}^2}\right) + P_1\left(\sqrt{1 + \tfrac{\overline{V}^4}{4v_0^4}} - \tfrac{\overline{V}^2}{2v_0^2}\right)^{\frac{1}{2}} + \frac{d_0\rho sA\overline{V}^3}{2}\right]T_h, \tag{6.6}$$

where

$$\begin{aligned} E_{vF} =& 2P_2\left(\frac{H}{V_v} + \frac{V_v}{a}\right) + mg\left(\sqrt{{V_v}^2 + \frac{2mg}{\rho A}}\right)\left(\frac{H}{V_v} - \frac{V_v}{a}\right) \\ &+ m\,(a+g)\left(\frac{V_v}{2a}\zeta_1 + \frac{m\,(a+g)}{a\rho A}\ln\frac{V_v + \zeta_1}{\xi_1}\right) + mgH \\ &+ m\,(g-a)\left(\frac{V_v}{2a}\zeta_2 + \frac{m\,(g-a)}{a\rho A}\ln\frac{V_v + \zeta_2}{\xi_2}\right), \end{aligned}$$

$$E_{hF} = 2\left[P_0\left(1 + \frac{3\overline{V}^2}{U_{tip}^2}\right) + P_1\varsigma_1 + \frac{d_0\rho sA\overline{V}^3}{2}\right]\frac{D}{\overline{V}},$$

are the total energy for vertical and horizontal flights, respectively, $\zeta_1 = \sqrt{{V_v}^2 + \frac{2m(a+g)}{\rho A}}$, $\xi_1 = \sqrt{\frac{2m(a+g)}{\rho A}}$, $\zeta_2 = \sqrt{{V_v}^2 + \frac{2m(g-a)}{\rho A}}$, $\xi_2 = \sqrt{\frac{2m(g-a)}{\rho A}}$ and

Algorithm 9: Solving the equation $\frac{\partial E_{A2G}}{\partial m_b} = 0$

Input: m_0, H, V_v, a, $\overline{V}$, D, $L_m = 0$, M_m, $R_m = m_{b,max}$

```
if g(L_m) > 0 && g(R_m) < 0 then
    while R_m − L_m ≤ ε do
        M_m = (Float) (L_m + R_m) /2
        g(M_m) > 0 ? L_m = M_m : R_m = M_m
m_b^* = (Float) (L_m + R_m) /2
Calculate E_A2G using (6.7)
```

Output: m_b^*, E_{A2G}

$\varsigma_1 = \sqrt{\sqrt{1 + \frac{\overline{V}^4}{4v_0^4}} - \frac{\overline{V}^2}{2v_0^2}}$. To maximize E_{A2G}, one further has

$$\frac{\partial E_{A2G}}{\partial m_b} = \rho_e * 3600 * \eta_{DC-DC} - \frac{\partial E_{vF}}{\partial m_b} - \frac{\partial E_{hF}}{\partial m_b}, \tag{6.8}$$

where

$$\frac{\partial E_{hF}}{\partial m_b} = \frac{\sqrt{2}D}{\overline{V}} (1+k)\, g \left(\sqrt{\varsigma_2 - \overline{V}^2} + \frac{m^2 g^2}{2\varsigma_2 \rho^2 A^2 \sqrt{\varsigma_2 - \overline{V}^2}} \right),$$

$$\begin{aligned}
\frac{\partial E_{vF}}{\partial m_b} &= g \left(\frac{H}{V_v} - \frac{V_v}{a} \right) \left(\sqrt{{V_v}^2 + \frac{2mg}{\rho A}} + \frac{mg}{\rho A \sqrt{{V_v}^2 + \frac{2mg}{\rho A}}} \right) \\
&+ \frac{V_v}{2} (\zeta_1 - \zeta_2) - \frac{V_v g}{2a} (\zeta_1 + \zeta_2) + \left(\frac{H}{V_v} + \frac{V_v}{a} \right) \frac{3k\sqrt{mg^3}}{\sqrt{2\rho A}} \\
&+ \frac{mV_v}{2a\rho A} \left(\frac{(a+g)^2}{\zeta_1} + \frac{(g-a)^2}{\zeta_2} \right) + gH \\
&+ \frac{2m}{a\rho A} \left((a+g)^2 \ln \frac{V_v + \zeta_1}{\xi_1} + (g-a)^2 \ln \frac{V_v + \zeta_2}{\xi_2} \right) \\
&+ \frac{m^2}{a\rho^2 A^2} \left(\frac{(a+g)^3}{(V_v + \zeta_1)\,\zeta_1} - \frac{(a+g)^3}{\xi_1^2} + \frac{(g-a)^3}{(V_v + \zeta_2)\,\zeta_2} - \frac{(g-a)^3}{\xi_2^2} \right),
\end{aligned}$$

$\varsigma_2 = \sqrt{4{v_0}^4 + \overline{V}^4}$. Taking the second-order derivative of (6.7), one has

$$\frac{\partial^2 E_{A2G}}{\partial {m_b}^2} = -\left(\frac{\partial^2 E_{vF}}{\partial {m_b}^2} + \frac{\partial^2 E_{hF}}{\partial {m_b}^2}\right),\ 0 \leq m_b \leq m_{b,max}. \tag{6.9}$$

Using the energy density of 150 Wh/kg in [120] and the parameters from Table I in [49], it is found that $\frac{\partial^2 E_{A2G}}{\partial {m_b}^2} < 0$, when m_b is between 0 and $m_{b,max} = 20$ kg [125]. This implies that the function E_{A2G} has a unique maximum at $m_b = m_b^*$. It is challenging to obtain the exact solution m_b^* by solving the equation $\frac{\partial E_{A2G}}{\partial m_b} = 0$. Denote $g(m_b) = \frac{\partial E_{A2G}}{\partial m_b}$. This can be solved using the binary search in Algorithm 9.

In Algorithm 9, $\varepsilon > 0$ is the given precision tolerance. Thus, its complexity is $O\left(\log_2 \frac{m_{b,max}}{\varepsilon}\right)$. Note that, if $g(L_m = 0) > 0$ and $g(R_m) \geq 0$, E_{A2G} will achieve its maximum at $m_b = R_m$. If $g(L_m = 0) \leq 0$ and $g(R_m) < 0$, it will achieve its maximum at $m_b = L_m$, but $m_b = L_m = 0$. Once the maximum energy of E_{A2G} is obtained, the spectral efficiency can be derived using (6.3).

Next, consider an approximation. In (2.11), $\left(\sqrt{1 + \frac{V^4}{4v_0^4}} - \frac{V^2}{2v_0^2}\right)^{1/2}$ can be approximated as $\dfrac{v_0}{V}$ by applying the first-order Taylor approximation $(1+x)^{1/2} \approx 1 + \frac{1}{2}x$ when $\left(\frac{v_0}{V}\right)^4 \ll 1$. Then,

$$E_{hF} \approx \frac{2P_0 D}{\overline{V}}\left(1 + \frac{3\overline{V}^2}{{U_{tip}}^2}\right) + \frac{(1+k)\, m^2 g^2 D}{\rho A \overline{V}^2} + d_0 \rho s A \overline{V}^2 D. \tag{6.10}$$

Also, if the acceleration time during vertical flight is less than that during constant speed, the consumption during vertical flight can be calculated using a mean velocity of $\overline{V_v}$ as

$$E_{vF} \approx \left(2P_2 + mg\overline{V_v} + mg\sqrt{\overline{V_v}^2 + \frac{2mg}{\rho A}}\right)\frac{H}{\overline{V_v}}. \tag{6.11}$$

Denote E_{vF} as $h(m_b)$ and use the second-order Taylor approximation at $m_b = 0$, one has

$$E_{vF} \approx h(0) + h'(0)m_b + \frac{1}{2}h''(0){m_b}^2, \tag{6.12}$$

where $h(0) = \left(\frac{\delta}{4}\rho s A\Omega^3 R^3 + 2k\sqrt{\frac{(m_0 g)^3}{2\rho A}} + m_0 g\overline{V_v} + m_0 g\zeta_3\right)\frac{H}{\overline{V_v}}$, $\zeta_3 = \sqrt{\overline{V_v}^2 + \frac{2m_0 g}{\rho A}}$, $h'(0) = \frac{3kgH}{2\overline{V_v}}\sqrt{\frac{2m_0 g}{\rho A}} + gH + \frac{gH\zeta_3}{\overline{V_v}} + \frac{m_0 g^2 H}{\overline{V_v}\rho A\zeta_3}$ and $h''(0) = \frac{3kgH}{4\overline{V_v}}\sqrt{\frac{2g}{m_0\rho A}} + \frac{2g^2 H}{\overline{V_v}\rho A\zeta_3} + \frac{m_0 g^3 H}{\overline{V_v}\rho^2 A^2 {\zeta_3}^3}$. Using (6.10) and (6.12), (6.7) can be rewritten as

$$\begin{aligned} E_{A2G} \approx &- \left(\frac{1}{2}h''(0) + \Phi\right){m_b}^2 - d_0\rho s A\overline{V}^2 D \\ &+ \left(\rho_e * 3600 * \eta_{DC-DC} - h'(0) - 2\Phi m_0\right)m_b \\ &- \frac{2P_0 D}{\overline{V}}\left(1 + \frac{3\overline{V}^2}{{U_{tip}}^2}\right) - \Phi{m_0}^2 - h(0), \end{aligned} \tag{6.13}$$

where $\Phi = \frac{(1+k)g^2 D}{\rho A\overline{V}^2}$. From (6.13), the optimal weight is

$$m_b^* \approx \frac{\rho_e * 3600 * \eta_{DC-DC} - h'(0) - 2\Phi m_0}{h''(0) + 2\Phi}. \tag{6.14}$$

6.4 Numerical Results and Discussion

In this section, numerical examples are given to show the optimal battery mass. In the examples, we set $\rho_e = 150$ Wh/kg [120], $\eta_{DC-DC} = 0.9$ [129], $m_0 = 5.5$ kg, $m_{b,max} = 20$ kg [125], $a = 2$ m/s^2, $P_{uav-t} = 40$ dBm, $f = 2$ GHz, $\sigma^2 = -80$ dBm, $D = 40$ km, $V_v = 4$ m/s and $\overline{V} = V = 25$ m/s. Also, a suburban environment is considered for communication, where $\eta_{LOS} = 0.1$ dB, $\eta_{NLOS} = 21$ dB, $a_0 = 5.0188$,

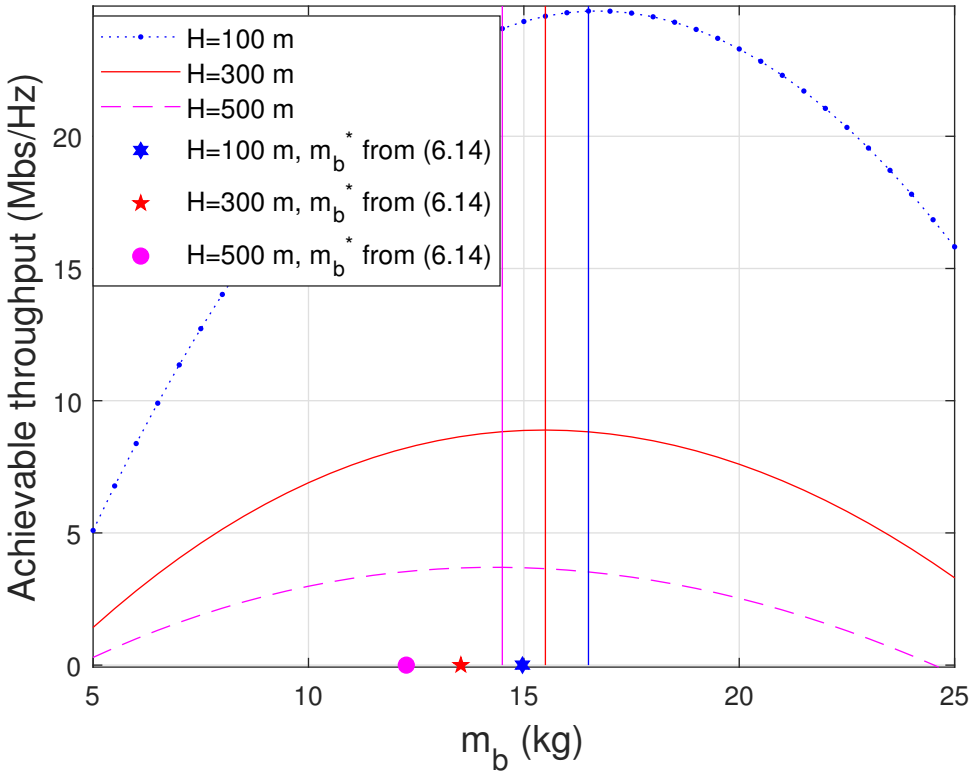

Figure 6.2: Spectral efficiency changing with m_b.

$b_0 = 0.3511$ [16], and other parameters of UAV are given in Table I of [49].

Fig. 6.2 shows the spectral efficiency versus the battery mass when the flight height changes from 100 m to 500 m. Consider one sensor below the UAV as an example, i.e., $\theta_0 = 0$. One sees that the spectral efficiency increases first and then decreases when the battery mass increases. This is consistent with the analysis in Sections 6.2 and 6.3. The higher the altitude H, the smaller the optimum m_b and the spectral efficiency will be. For example, when $H = 500$ m, the optimal m_b is about 14.5 kg, which is smaller than 16.5 kg when $H = 100$ m. This is because larger height consumes extra energy such that E_{A2G} is reduced. For a fixed H, the optimal m_b^* exists indicated by three straight lines. One can see that the values

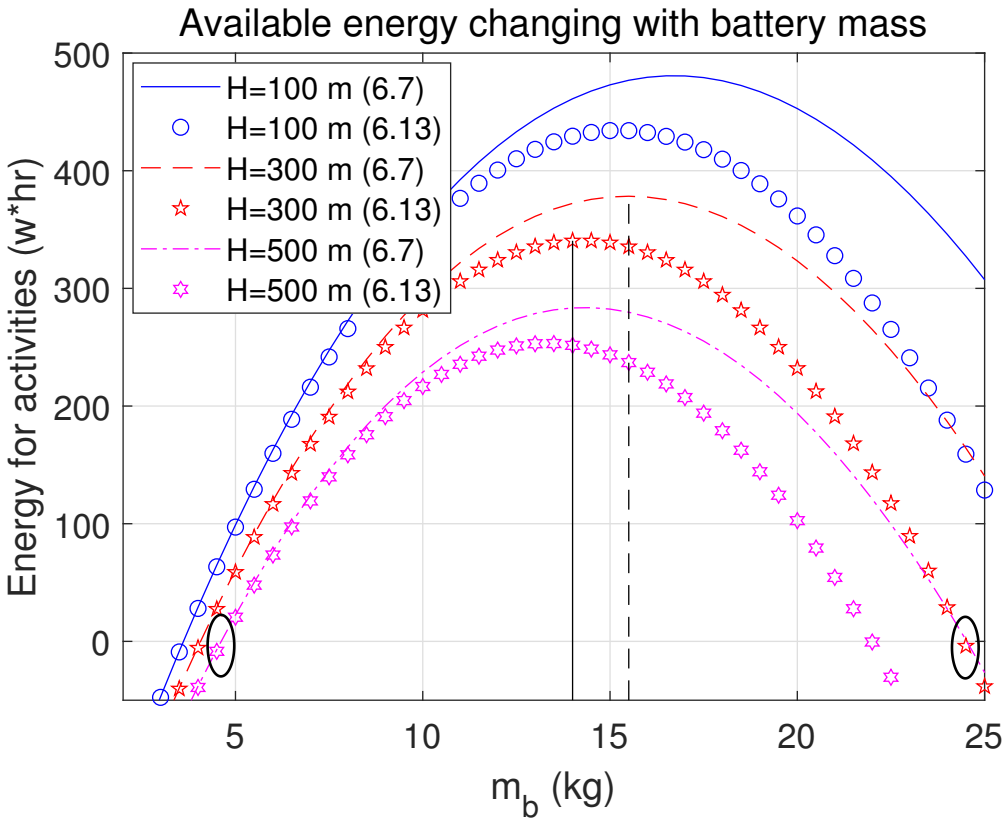

Figure 6.3: E_{A2G} changing with m_b.

from approximation are smaller than those from Algorithm 9. This is because when $\overline{V_v}$ is set to V_v, the approximation in (6.12) is larger than the actual value. Meanwhile, the approximation in (6.10) is also larger than the actual value, thus reducing E_{A2G}.

Fig. 6.3 shows E_{A2G} versus m_b. Similar observations can be made, because the spectral efficiency is proportional to E_{A2G} in this case. In this figure, (6.7) and (6.13) are used to compare the numerical results of E_{A2G} with the approximate results. Take $H = 300$ m as an example. The gap between the optimal m_b using (6.7) and the one using (6.13) is about 1.5 kg, almost consistent with the result in Fig. 6.2. Also, zero-crossing points marked with ellipse in Fig. 6.3 indicate

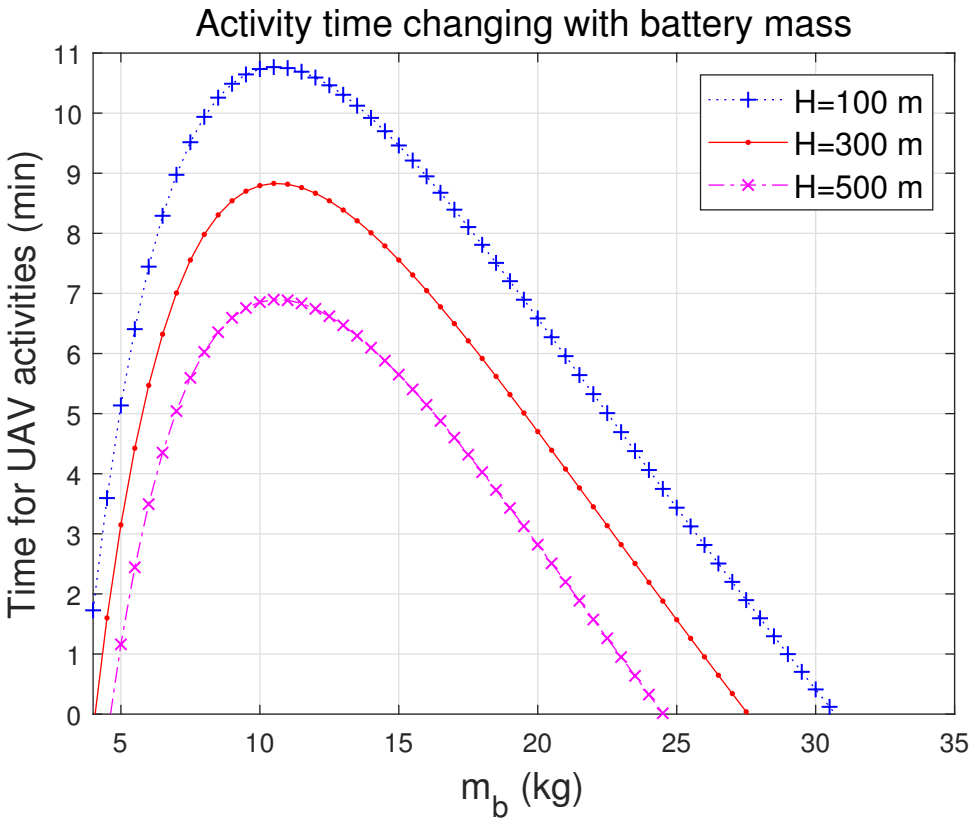

Figure 6.4: Activity time τ changing with m_b.

that $E_{A2G} = 0$ so that the energy provided by the battery can only be used for manoeuvre, not for UAV communications. Note that, for a given task, where E_{A2G} is certain and smaller than the peak value in Fig. 6.3, the optimal battery weight can be obtained by finding the root of the equation (6.13) with m_b^* as the unknown.

Fig. 6.4 shows the time for UAV activities using the same parameters as Fig. 6.2 and Fig. 6.3. One can see that, under the same conditions the optimal m_b is about 10.5 kg now, smaller than that in Fig. 6.2 and Fig. 6.3. This means that the optimal m_b for maximum energy does not necessarily maximize time. This can be explained as follows. With larger m_b, more energy is available. However, the power consumption for hovering increases to reduce the hovering time. Therefore,

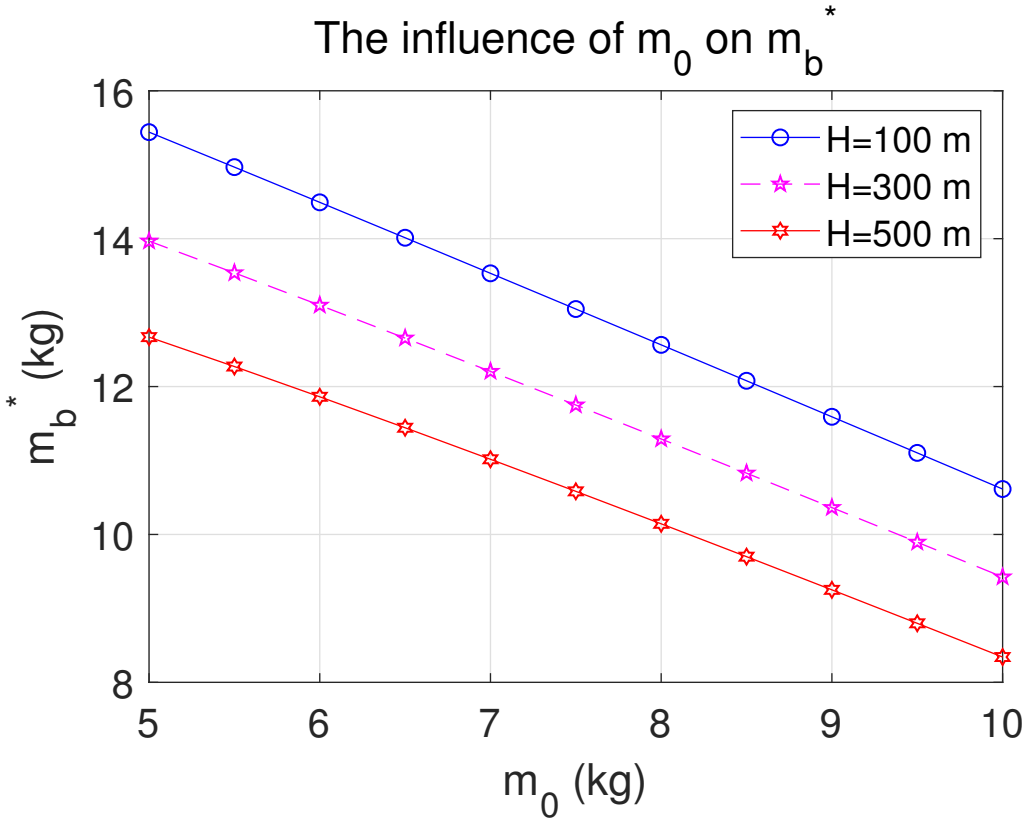

Figure 6.5: m_b^* changing with m_0.

it is important to carefully choose m_b for balanced energy and operation time.

Fig. 6.5 shows the optimal value m_b versus m_0, where H is set to 100 m, 300 m and 500 m. In this figure, (6.14) is used. One sees that the optimal value m_b decreases with increasing m_0. This is because, when other parameters are fixed, increasing m_0 results in an overall increase in weight, leading to more energy consumption.

Fig. 6.6 shows the effects of V_v on m_b^*. In this figure, (6.14) is used. One sees that m_b^* increases with V_v first and then approaches an upper limit, which means there should be an optimal V_v that exists for fixed H.

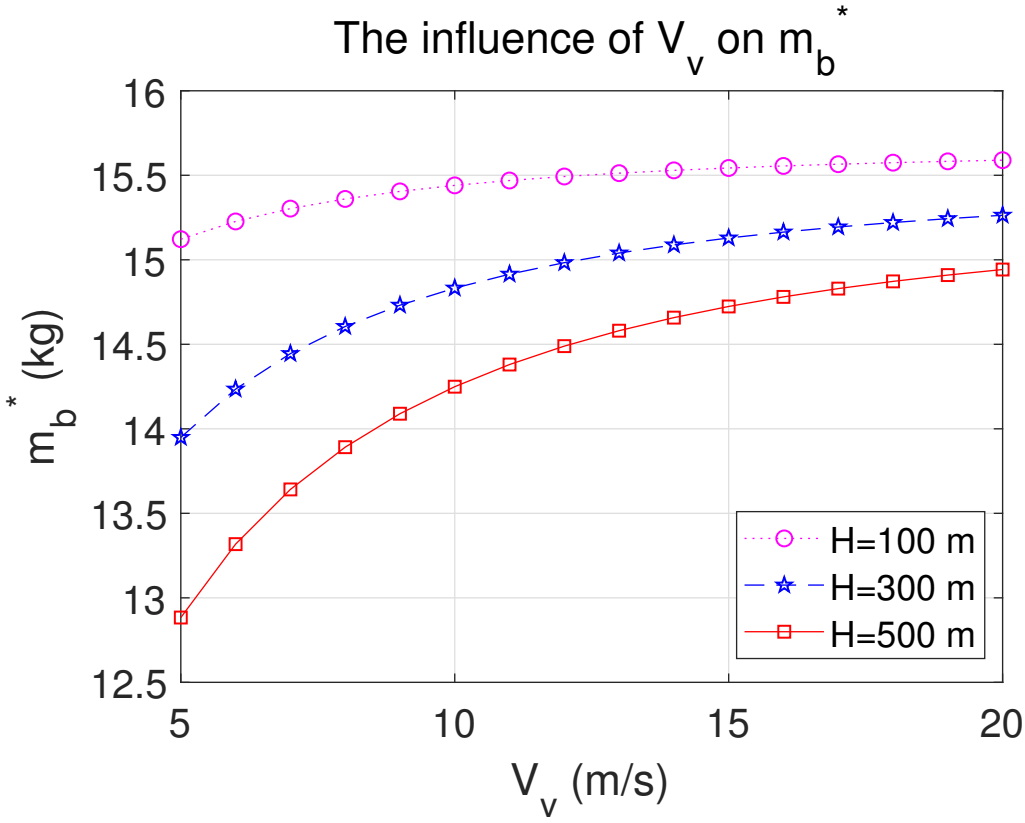

Figure 6.6: m_b^* changing with V_v.

Fig. 6.7 shows how m_b^* changes with V_h. In this figure, $H = 300$ m and (6.14) is used. One sees that m_b^* increases with V_h. Taking $D = 40$ km as an example, when $V_h = 15$ km/s, m_b^* is about 2 kg. However, according to Fig. 6.3, the available E_{A2G} is less than 0, and this is meaningless. When $V_h = 30$ km/s, m_b^* is beyond $m_{b,max} = 20$ kg. Thus, V_h should be carefully chosen.

6.5 Summary

In this chapter, the optimal weight for a battery in UAV electrical propulsion system has been studied, where the UAV's vertical and horizontal propulsion con-

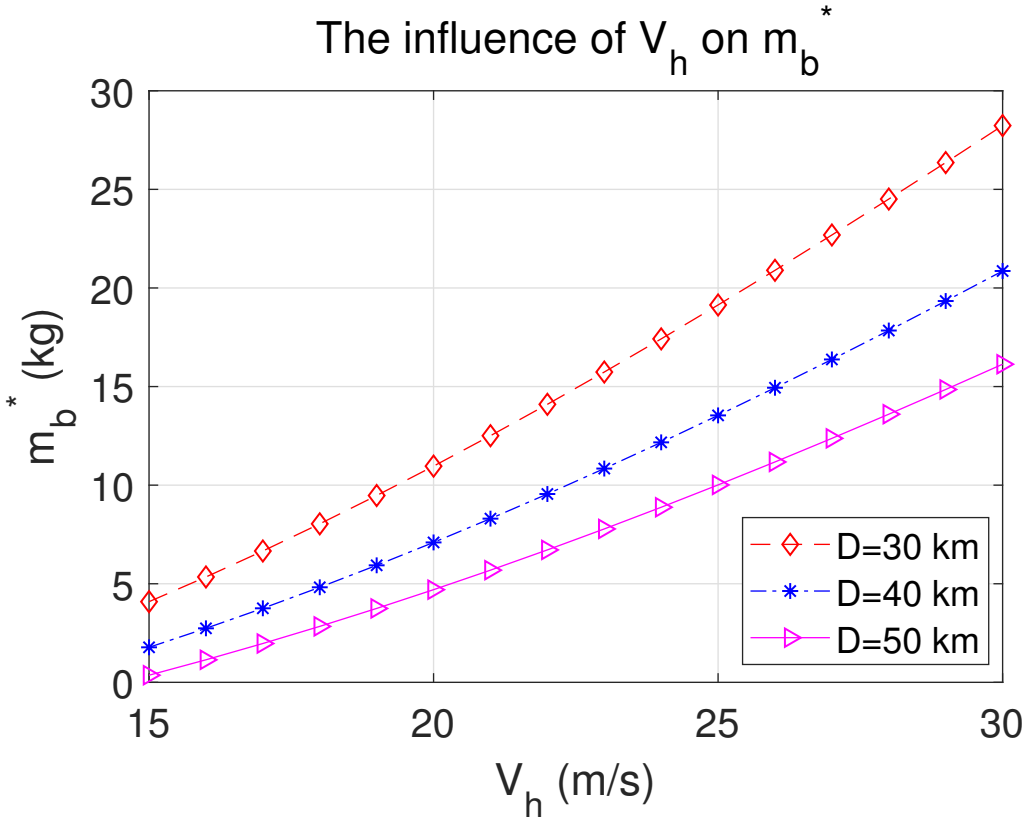

Figure 6.7: m_b^* changing with V_h.

sumption are taken into account. By maximizing the energy available for communications, both numerical and approximate solutions to the optimal battery mass have been derived. Numerical results have shown that the optimal battery mass that maximizes the flight performance is determined by m_0, vertical/horizontal flight speed V_v/V, flight height H and flight distance D. The larger H and D are, the smaller m_b^* will be. Besides, the optimal battery mass for maximum energy does not necessarily maximize the operation time. As future work, it is interesting to study the joint optimization of transmission power, time and altitude to optimize energy efficiency and the minimization of battery weight for fixed E_{A2G}. Energy efficiency determines the actual use of the maximized available energy and can be optimized via power and time allocation too.

Chapter 7

New ECM for Rotary-Wing UAV Propulsion

This chapter is based on our work published in [J5]. ([118])

7.1 Introduction

Propulsion energy consumption of UAVs is very important in the design of UAV-enabled communications systems [43, 92, 117]. The challenge is to accurately estimate the amount of energy consumed by different UAV missions. A simple and easy-to-use yet accurate propulsion ECM is required for this purpose.

There have been quite a few works on the modeling of propulsion energy [130], [131]. For example, the authors in [132] and [133] studied the energy consumption of electric-powered UAVs from the perspective of battery usage, and this method has been proved effective and feasible. However, the result depends on

the specific UAV and the type of battery adopted. In [134], a theoretical model for multi-rotor small unmanned aircraft power consumption based on helicopter theory was derived assuming a steady-state without acceleration. Similarly, in [49], the authors derived a closed-form propulsion power consumption model for rotary-wing UAVs in a 1D level flight at a constant speed without acceleration/deceleration. Considering the practical situation, the authors in [53] extended the result in [49] by deriving an analytical model for rotary-wing UAVs in straight-and-level flight with acceleration and deceleration. However, this model is very complex, as no closed-form expression and only an integral expression was provided in [53, eq. (A.8)]. Also, the model in [49] was further extended in [135] to an arbitrary 2D level flight, and the energy consumption was derived as a function of the flying speed, direction and acceleration using centrifugal acceleration [30]. This model is also very complicated without closed-form.

All these works have provided very valuable insights on modeling the propulsion energy consumption of rotary-wing UAVs. However, these models are either too complex, or do not consider acceleration/deceleration—a very important UAV manoeuvre in UAV-enabled communications [43, 92, 117], [49]. Thus, it is of great interest to derive a new ECM that is both simple and takes the acceleration/deceleration into account. Such an ECM can be used to calculate the energy consumed in different UAV missions, or as a target for UAV trajectory optimization.

Motivated by the above observation, this chapter aims to derive a new ECM that overcomes the shortcomings of the aforementioned works. To do this, we decompose the power consumption of the UAV with acceleration/deceleration into vertical and horizontal directions using force analysis, based on which a new ECM is derived. Numerical results show the validity and reliability of the new ECM and

that acceleration and speed have a great impact on the total energy consumption of the UAV. The novelty of the work is summarized as follows: compared with [49], this work considers both acceleration and deceleration, while [49] did not consider acceleration/deceleration. Compared with [53] and [135], our model is much simpler and easier to use with closed-form, while the model in [53] or [135] is complex and does not have closed-form expression.

7.2 Existing Energy Consumption Models

From [49], for forward level flight of a rotary-wing UAV at a constant speed of V, the propulsion power consumption can be modeled as

$$P\left(V,\widetilde{\kappa}\right)=P_0\left(1+\frac{3V^2}{U_{tip}^2}\right)+P_1\widetilde{\kappa}\left(\sqrt{\widetilde{\kappa}^2+\frac{V^4}{4v_0^2}}-\frac{V^2}{2v_0^2}\right)^{\frac{1}{2}}+\frac{d_0\rho sAV^3}{2}, \tag{7.1}$$

where $P_0\left(1+\frac{3V^2}{U_{tip}^2}\right)$ and $P_1\widetilde{\kappa}\left(\sqrt{\widetilde{\kappa}^2+\frac{V^4}{4v_0^2}}-\frac{V^2}{2v_0^2}\right)^{1/2}$ are functions of speed related to the physical properties of the UAV and the flight environment, including the UAV weight W, rotor solidity s, rotor disc area A, air density ρ, the tip speed of the rotor blade U_{tip} and the mean rotor induced velocity v_0, etc., as the *blade profile power* and *induced power* in hovering status, as detailed in [49], $\widetilde{\kappa}\triangleq\frac{T}{W}\approx 1$ is the thrust-to-weight ratio (TWR) [136, eq. (4.3)], d_0 denotes the fuselage drag ratio and $d_0\rho sAV^3/2$ denotes the *parasite power* (also known as power to overcome fuselage drag [136, eq. (4.5)] related to speed). Therefore, the energy consumption can be modeled as a function of V, which is neither convex nor concave, similar to [49]. Using (7.1), one has

$$E_v=P\left(V,1\right)\tau, \tag{7.2}$$

where τ is the time duration and $\widetilde{\kappa} = 1$.

From [53], for forward level flight, with a given trajectory $q(t)$, the propulsion energy is calculated as

$$\begin{aligned} E(q(t), T_0) = \int_0^{T_0} [P_0 \left(1 + c_1 v^2(t)\right) + c_5 v^3(t) + \\ P_1 \sqrt{1 + \left(c_2 v^2(t) + c_3 a(t) v(t)\right)^2} \\ \times \sqrt{\sqrt{1 + \left(c_2 v^2(t) + c_3 a(t) v(t)\right)^2 + c_4^2 v^4(t)} - c_4 v^2(t)}] \, dt, \end{aligned} \tag{7.3}$$

where T_0 is the time duration, $c_j, j = 1, \cdots, 5$, are the parameters detailed in [53], $v(t) = \frac{dq(t)}{dt}$ and $a(t) = \frac{d^2 q(t)}{dt^2}$ are the velocity and acceleration, respectively.

Also, from [135], for an arbitrary 2D level flight with given trajectory $\mathbf{q}(t)$, the propulsion energy is presented as

$$\begin{aligned} & E(\mathbf{q}(t)) \\ & = \int_0^{T_0} c_3 \sqrt{1 + \frac{a_\perp^2(t)}{g^2}} \left(\sqrt{1 + \frac{a_\perp^2(t)}{g^2} + \frac{\|\mathbf{v}(t)\|^4}{c_4^2}} - \frac{\|\mathbf{v}(t)\|^2}{c_4} \right)^{\frac{1}{2}} dt \\ & + \int_0^{T_0} c_1 (1 + c_2 \|\mathbf{v}(t)\|^2) \, dt + \int_0^{T_0} c_5 \|\mathbf{v}(t)\|^3 \, dt + \Delta_K, \end{aligned} \tag{7.4}$$

where T_0 is the time duration, $c_k, k = 1, \cdots, 5$ are the parameters detailed in [135], $\Delta_K = \frac{1}{2} m (\|\mathbf{v}(T_0)\|^2 - \|\mathbf{v}(0)\|^2)$ is the change in kinetic energy. Both (7.3) and (7.4) are very complex to use and do not have closed-form expression.

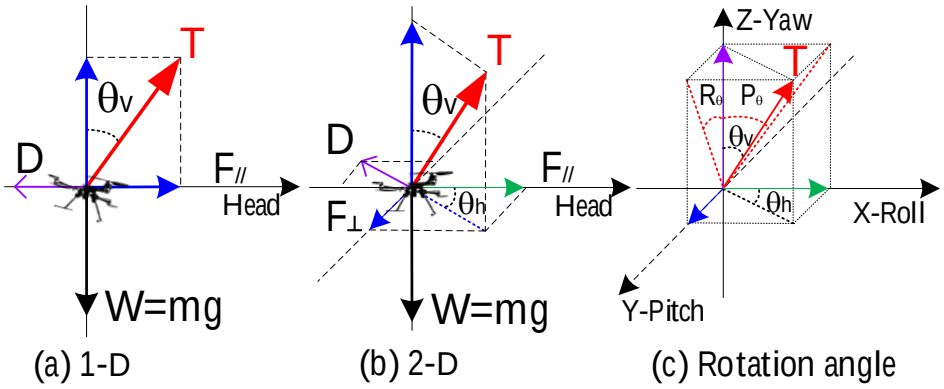

Figure 7.1: Force analysis of the UAV.

7.3 New Energy Consumption Model

In this section, we will study the power consumption of UAV with acceleration/deceleration from the initial velocity $\mathbf{V}_i$ (final velocity $\mathbf{V}_f$) to $\mathbf{V}_f(\mathbf{V}_i)$, using the same parameters as those in [49] to derive the new model. Since the 1D scenario is a special case of the 2D scenario, we will focus on 2D scenarios to derive a generic model.

As indicated in (7.1), for forward level flight, the UAV keeps balance in the vertical direction at the cost of *blade profile power* and *induced power*. On the other hand, in the horizontal direction, the UAV incurs the fuselage drag, i.e., *parasite power*. Based on this analysis, the required power consumption for a rotary-wing UAV can be studied by analyzing the vertical and horizontal power consumption. In the vertical direction, the UAV keeps balance at the cost of $P_0\left(1+\frac{3V^2}{U_{tip}^2}\right)+P_1\widetilde{\kappa}\left(\sqrt{\widetilde{\kappa}^2+\frac{V^4}{4v_0^2}}-\frac{V^2}{2v_0^2}\right)^{1/2}$. During acceleration/deceleration, $\widetilde{\kappa}=\sqrt{1+\frac{(\rho S_{FP}V^2+2ma)^2}{4W^2}}$ [53, eq. A.5], and $S_{FP}\triangleq d_0sA$ [49] is the fuselage equiv-

alent flat plate area. Using the parameters from Table I in [49] with a maximum speed of $V_{max} = 30$ m/s [49], it is found that $\widetilde{\kappa}$ approximately equals to 1 for different accelerations and UAV weights. As a result, the power consumption for acceleration/deceleration in vertical direction can be expressed as

$$\begin{aligned} P_{vertical}(t) =& P_0 \left(1 + \frac{3\|\mathbf{V}_i + \mathbf{a}t\|^2}{U_{tip}^2}\right) \\ &+ P_1 \left(\sqrt{1 + \frac{\|\mathbf{V}_i + \mathbf{a}t\|^4}{4v_0^4}} - \frac{\|\mathbf{V}_i + \mathbf{a}t\|^2}{2v_0^2}\right)^{\frac{1}{2}}, \end{aligned} \tag{7.5}$$

where $\mathbf{V}_i$ is the initial velocity and $\mathbf{a}$ is the acceleration or deceleration. Thus, $P_{vertical}(t)$ varies with the UAV speed, and it is not related to the orientation. In the horizontal direction, the power consumption at a speed of $\mathbf{v}(t)$ is [30]

$$P_{horizontal}(t) = \|\mathbf{F}\|\|\mathbf{v}(t)\|, \tag{7.6}$$

where $\mathbf{F}$ is the pulling force, $\mathbf{v}(t) = \|\mathbf{V}_i + \mathbf{a}t\|$ is the instantaneous velocity at time t. When flying at a constant speed of V, $\|\mathbf{F}\| = \frac{1}{2}d_0\rho sAV^2$ equals to the fuselage drag $D = \frac{1}{2}\rho S_{FP}V^2$ [136]. According to the above analysis, the power consumption for rotary-wing UAVs can be finally modeled as

$$P_{total}(t) = P_{vertical}(t) + P_{horizontal}(t). \tag{7.7}$$

Particularly, when $\|\mathbf{a}\| = 0$, (7.7) is the same as $P(V, 1)$ in (7.1) and [49, eq. 12]. Thus, (7.7) is general.

7.3.1 Acceleration/Deceleration

From [135] and [30], the UAV acceleration can be decomposed in the parallel and perpendicular directions of its head. Considering an arbitrary 2D level flight with acceleration $\mathbf{a}$ shown in Fig. 7.1(b), one has

$$\begin{aligned} &T \sin\theta_v \cos\theta_h - D_{\shortparallel} = m a_{\shortparallel}, \\ &T \sin\theta_v \sin\theta_h - D_{\perp} = m a_{\perp}, \\ &T \cos\theta_v - W = 0, \end{aligned} \tag{7.8}$$

where m is the total mass of the UAV, θ_h is the initial angle between $\mathbf{a}$ and $\mathbf{V}_i$ and it can be derived by rotation of the UAV, i.e., rotation of angle P_θ along pitch and angle R_θ along roll. One has the relationship as

$$\theta_h = \arctan\left(\frac{\tan R_\theta}{\tan P_\theta}\right), \tag{7.9}$$

$D_{\shortparallel} = \frac{1}{2}\rho S_{FP} v_{\shortparallel}^2(t)$ and $D_{\perp} = \frac{1}{2}\rho S_{FP} v_{\perp}^2(t)$ are the fuselage drags in the parallel and perpendicular directions, $a_{\shortparallel} = \|\mathbf{a}\| \cos\theta_h$ and $a_{\perp} = \|\mathbf{a}\| \sin\theta_h$ are acceleration components that are parallel and perpendicular to the head direction [135], [30], respectively. Using (7.6) and (7.8), the power in parallel and perpendicular directions for arbitrary 2D level acceleration is

$$\begin{aligned} P_{\shortparallel}(t) &= \left(\frac{1}{2}\rho S_{FP} v_{\shortparallel}^2(t) + m a_{\shortparallel}\right) v_{\shortparallel}(t), \\ P_{\perp}(t) &= \left(\frac{1}{2}\rho S_{FP} v_{\perp}^2(t) + m a_{\perp}\right) v_{\perp}(t), \end{aligned} \tag{7.10}$$

where $v_{\shortparallel}(t) = v_{i\shortparallel} + a_{\shortparallel} t$ and $v_{\perp}(t) = v_{i\perp} + a_{\perp} t$ are speed components that are parallel and perpendicular to the head, respectively, $v_{i\shortparallel} = \|\mathbf{V}_i\| \cos\theta_h$ and $v_{i\perp} = \|\mathbf{V}_i\| \sin\theta_h$ are two components of initial velocity $\mathbf{v}_0$ in the corresponding direction. Using

(7.7) and (7.10), the total power consumption is

$$P_{total-2D}\left(t\right) = P_{vertical}(t) + P_{\shortparallel}\left(t\right) + P_{\perp}\left(t\right). \tag{7.11}$$

Since the deceleration process is similar to the acceleration process, it will not be repeated here. Together, the total energy for accelerating/decelerating with initial $\mathbf{V}_i$, acceleration/deceleration $\mathbf{a}$ during a time period of τ, using (7.11), is

$$\begin{aligned}
&E_{2D}\left(\mathbf{V}_i, \mathbf{a}, \tau\right) = \int_0^{\tau} P_{total-2D}\left(t\right)\ dt \\
&= P_0\tau + \frac{3P_0}{U_{tip}^2}\left(\|\mathbf{V}_i\|^2\tau + \|\mathbf{V}_i\|\|\mathbf{a}\|\cos\theta_h\tau^2 + \frac{\|\mathbf{a}\|^2\tau^3}{3}\right) \\
&\quad \pm \frac{P_1 v_0}{2\|\mathbf{a}\|}\left(\ln\frac{\left(2v_0^2 + \xi I_u + 2v_0\sqrt{\Re_u}\right) I_l}{I_u\left(2v_0^2 + \xi I_l + 2v_0\sqrt{\Re_l}\right)}\right) \\
&\quad \pm \frac{P_1}{2\|\mathbf{a}\|}\left(\sqrt{\Re_u} - \sqrt{\Re_l} + \frac{\xi}{2v_0}\left(\arcsin\Im_u - \arcsin\Im_l\right)\right) \\
&\quad + \frac{1}{2}\rho S_{FP}\Phi\left(\tau\right) \pm m a_{\shortparallel} v_{i\shortparallel}\tau + \frac{1}{2}m a_{\shortparallel}^2\tau^2 \\
&\quad + \frac{1}{2}\rho S_{FP}\Psi\left(\tau\right) \pm m a_{\perp} v_{i\perp}\tau + \frac{1}{2}m a_{\perp}^2\tau^2,
\end{aligned} \tag{7.12}$$

where $I_u = \sqrt{1 + \frac{(\|\mathbf{V}_i + \mathbf{a}\tau\|)^4}{4v_0^4}} - \frac{(\|\mathbf{V}_i + \mathbf{a}\tau\|)^2}{2v_0^2}$, $I_l = \sqrt{1 + \frac{\|\mathbf{V}_i\|^4}{4v_0^4}} - \frac{\|\mathbf{V}_i\|^2}{2v_0^2}$, $\xi = \|\mathbf{V}_i\|^2\cos^2\theta_h - \|\mathbf{V}_i\|^2$, $\Re_u = -v_0^2 I_u^2 + \xi I_u + v_0^2$, $\Re_l = -v_0^2 I_l^2 + \xi I_l + v_0^2$, $\Im_u = \frac{-2v_0^2 I_u + \xi}{\sqrt{\xi^2 + 4v_0^4}}$, $\Im_l = \frac{-2v_0^2 I_l + \xi}{\sqrt{\xi^2 + 4v_0^4}}$, $\Phi\left(\tau\right) = v_{i\shortparallel}^3\tau \pm \frac{3}{2}v_{i\shortparallel}^2 a_{\shortparallel}\tau^2 + v_{i\shortparallel}a_{\shortparallel}^2\tau^3 \pm \frac{1}{4}a_{\shortparallel}^3\tau^4$, $\Psi\left(\tau\right) = v_{i\perp}^3\tau \pm \frac{3}{2}v_{i\perp}^2 a_{\perp}\tau^2 + v_{i\perp}a_{\perp}^2\tau^3 \pm \frac{1}{4}a_{\perp}^3\tau^4$, $\tau = \frac{\|\mathbf{v}_f - \mathbf{v}_i\|}{\|\mathbf{a}\|}$ is the acceleration/deceleration time, and the plus and minus sign " $\pm$ " corresponds to the total energy of acceleration and deceleration processes (and hereinafter) denoted by E_{2D-Acc} and E_{2D-Dec}, respectively.

As a special case of the 2D scenario, the ECM for 1D level flight when

$\theta_h = 0$ or π can be derived as

$$
\begin{aligned}
E_{1D}\left(\mathbf{V}_i, \mathbf{a}, \tau\right) = & P_0\tau + \frac{3P_0}{U_{tip}^2}\left(\|\mathbf{V}_i\|^2\tau \pm \|\mathbf{V}_i\|\|\mathbf{a}\|\tau^2 + \frac{\|\mathbf{a}\|^2\tau^3}{3}\right) \\
& \pm \frac{P_1 v_0}{2\|\mathbf{a}\|}\left(\ln\frac{\left(1+\sqrt{1-I_u^2}\right)I_l}{I_u\left(1+\sqrt{1-I_l^2}\right)} + \sqrt{1-I_u^2} - \sqrt{1-I_l^2}\right) \\
& + \frac{1}{2}\rho S_{FP}\Omega(\tau) \pm ma\|\mathbf{V}_i\|\tau + \frac{1}{2}ma^2\tau^2,
\end{aligned}
\tag{7.13}
$$

where $a = \|\mathbf{a}\|$, $\Omega(\tau) = \|\mathbf{V}_i\|^3\tau \pm \frac{3}{2}\|\mathbf{V}_i\|^2 a\tau^2 + \|\mathbf{V}_i\|a^2\tau^3 \pm \frac{1}{4}a^3\tau^4$. Similarly, the plus and minus sign " $\pm$ " corresponds to acceleration and deceleration, respectively.

Compared with the existing models, our model has a closed-form expression and has taken acceleration/deceleration at directions that are parallel and perpendicular to the UAV head into account. Therefore, it is more reasonable and practical. Although (7.12) looks a little complex, to the best of author's knowledge, it is the first and only model with closed-form expression so far.

7.3.2 Further discussion

Analysis of maneuvering parameters

During acceleration/deceleration, T, tilt angle θ_v (also known as rotation angle P_θ along pitch in Fig. 7.1(c)) and θ_h change with the speed, as D is proportional to the speed, and one has

$$
\begin{aligned}
T(t) &= W \times \sqrt{1 + \frac{\left(\rho S_{FP}\left(\|\mathbf{V}_i + \mathbf{a}t\|\right)^2 + 2m\|\mathbf{a}\|\right)^2}{4W^2}}, \\
\theta_v(t) &= \arctan\frac{\rho S_{FP}\left(\|\mathbf{V}_i + \mathbf{a}t\|\right)^2 + 2m\|\mathbf{a}\|}{2W},
\end{aligned}
\tag{7.14}
$$

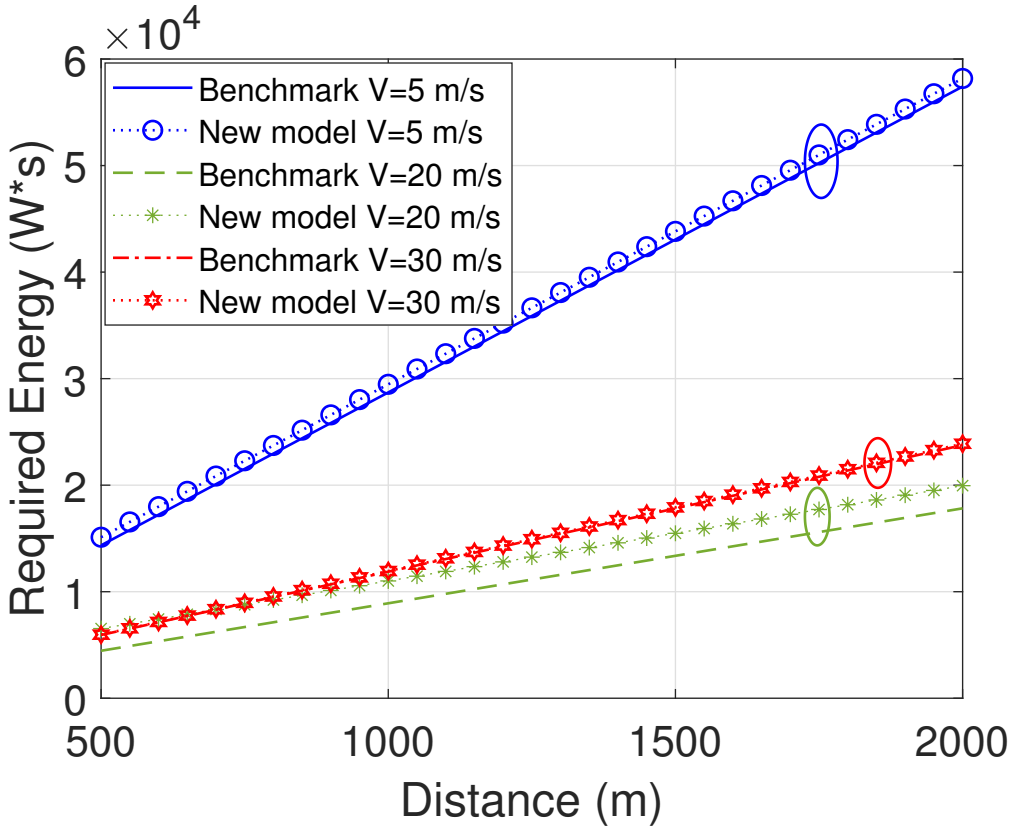

Figure 7.2: Total energy consumption.

Special case

Considering an *acceleration-fly(V)-deceleration* operation [43], [92] of 1D scenarios, where the UAV accelerates from an initial velocity of 0 to V and continues to fly at the speed of V, and finally decelerates from V to 0. The total energy, using (7.2) and (7.13), can be calculated as

$$E = E_{1D}(0, \mathbf{a}_1, \tau_1) + E_v + E_{1D}(V, \mathbf{a}_2, \tau_2). \tag{7.15}$$

where $\tau_1 = \frac{\|\mathbf{V}\|}{\|\mathbf{a}_1\|}$ and $\tau_2 = \frac{\|\mathbf{V}\|}{\|\mathbf{a}_2\|}$. Note that, for a given distance d, E_v exists if and only if $d > \frac{\|\mathbf{v}\|^2}{2\|\mathbf{a}_1\|} + \frac{\|\mathbf{v}\|^2}{2\|\mathbf{a}_2\|}$.

7.4 Numerical Results and Discussion

In this section, numerical examples are given to validate the derived energy model by comparing it with the models in [49], [53], [135]. Also, for a given distance, we compare the total energy calculated by the new model considering acceleration and deceleration with that calculated by the benchmark model [49] without considering acceleration or deceleration. For acceleration, the new model is also compared with [53] and [135]. In the examples, we set $W = 20$ N [49], $a = \pm 1\text{m/s}^2$, the number of wings and the number of blades are 4, and other parameters of UAV are the same as given in Table I of [49].

Fig. 7.2 shows the total energy consumption versus the distance for different speeds in 1D. One sees that the total energy consumption increases with the distance, but decreases first and then increases with the speed. This is because, when the speed is low, the power consumption is relatively large [49]. As both acceleration and deceleration have been considered in the new model, one can also see that the energy calculated by the new model is larger than that from [49]. For fixed distance at 1500 m, one can see that, when the speed is small (5 m/s) or large (30 m/s), the new model and the model in [49] match better than when the speed is medium. This is due to acceleration, which prolongs the acceleration process to consume more energy.

Fig. 7.3 shows the energy gap between the new model and the model in [49]. In this figure, we fix the distance at 2000 m and vary the acceleration from 1 to 30 m/s^2. One sees that for the speed V changing from 5 m/s to 20 m/s, the gap decreases with the acceleration. This can be explained as follows. For small a, the acceleration/deceleration process increases and the power consumption is relatively large when the speed is low [49] so as to consume more energy; For

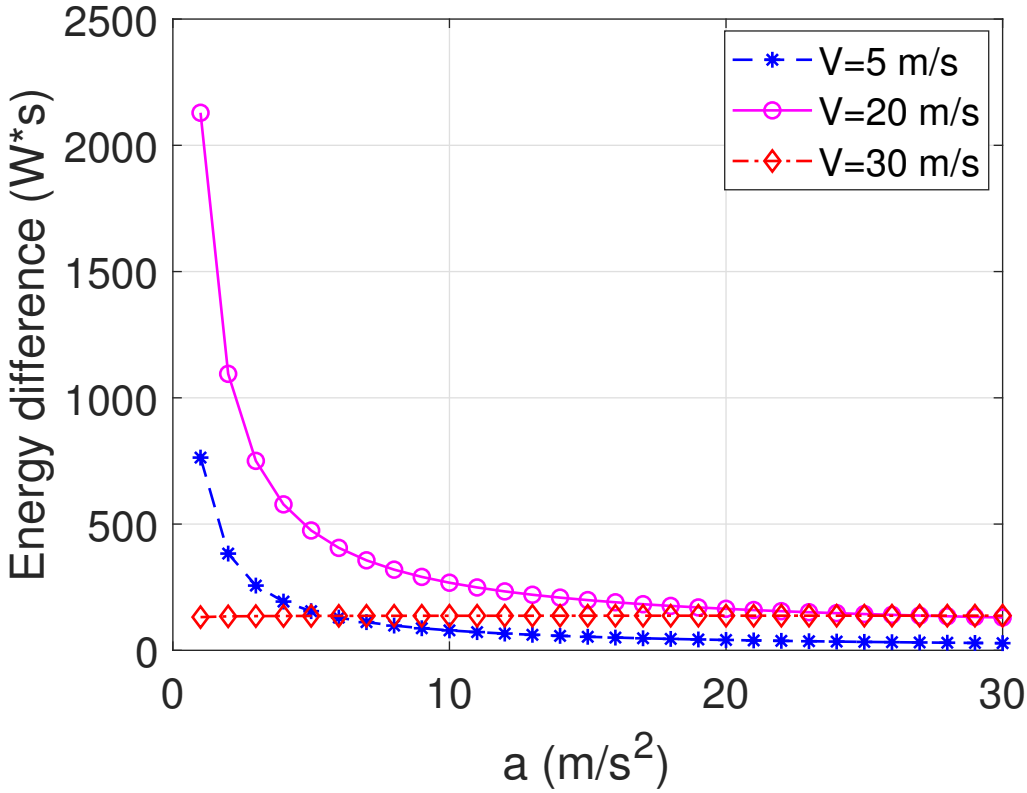

Figure 7.3: Energy gap caused by acceleration.

large a, the time for acceleration/deceleration is short, the energy gap becomes stable. Besides, for fixed a, the energy gap increases with the speed first and then decreases as in Fig. 7.2. When the speed is set as 30 m/s, which is larger than the $maximum - range$ (MR) $speed$ [49], the energy gap changes little with the acceleration. This is due to the fact that, when the speed is larger than the MR speed, higher power consumption is needed [49] so that the difference caused by acceleration is relatively small compared with the total energy consumption. This is why the new model and the model in [49] match well when the speed is 30 m/s.

Fig. 7.4 compares the total energy consumption of the new model with those in [53] and [135]. In the figure, (7.13), [53, eq. (A.8)] and [135, eq. (4)]

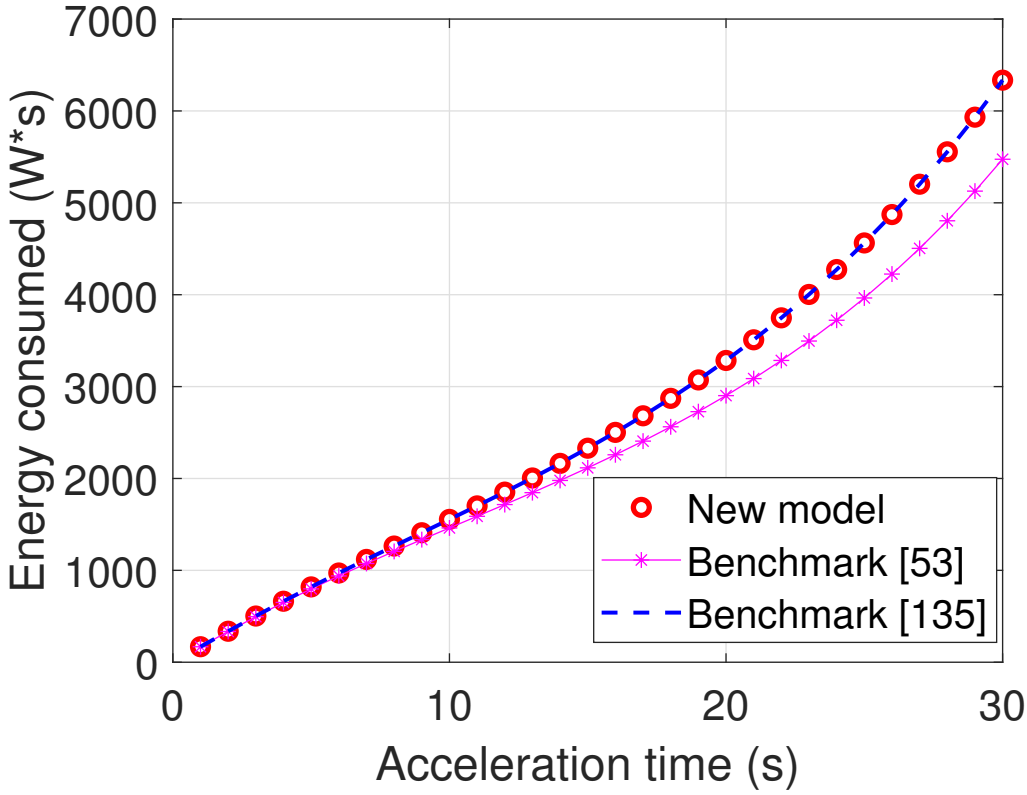

Figure 7.4: 1D scenario.

are used, $a = 1$ m/s^2, and other parameters are the same as Table 1 in [49]. One can see that the energy consumption increases with the acceleration time, and the energy consumption calculated by the new model is the same as that calculated by [135, eq. (4)]. However, [135, eq. (4)] is complex to use and does not have closed-form expression. In [53], even if D is considered, the pull force T could remain unchanged so as to cause the change of a, i.e., $a < 1$ m/s^2 as time goes on. In our work, D increases with the acceleration time so that T also increases to keep a. As a result, it consumes more energy. Note that when the speed is small, D is also small. This is why the three curves overlap at the beginning.

Fig. 7.5 investigates the total energy consumption of the new model and

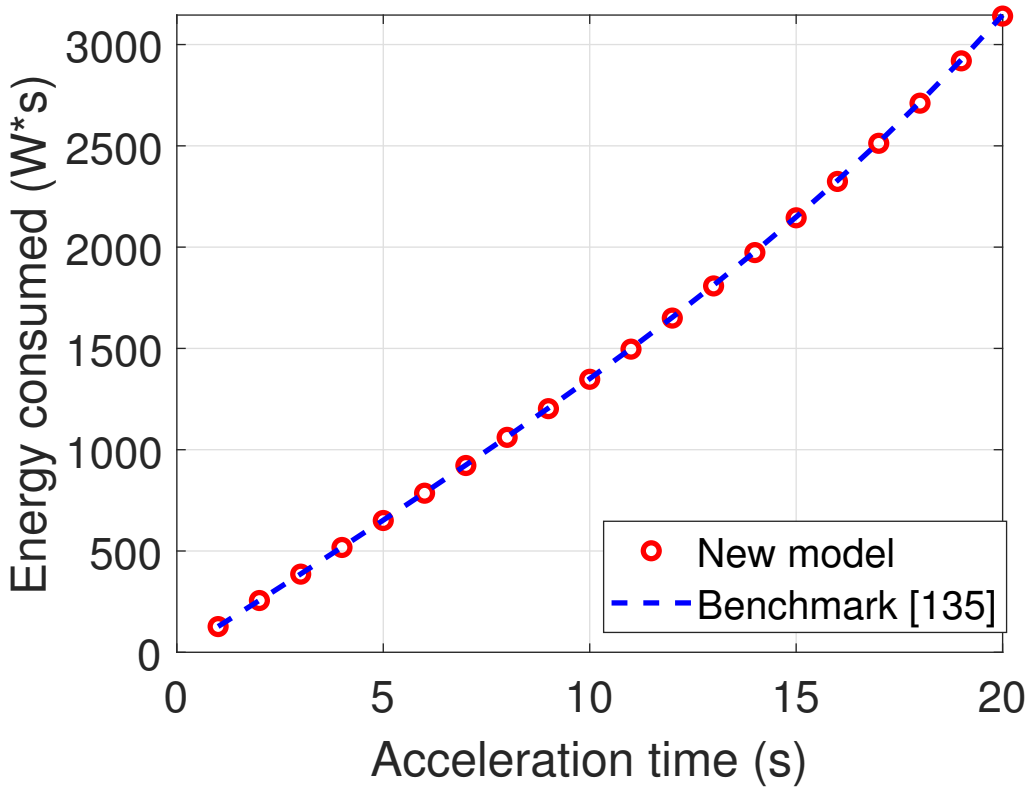

Figure 7.5: 2D scenario.

that in [135] for a 2D case. In the figure, (7.12) is used and $v_{\parallel} = 10$ m/s, $a_{\parallel} = 0$ m/s^2, $v_{\perp} = 0$ m/s, $a_{\perp} = 1$ m/s^2. One sees that two curves match well, similar to Fig. 7.4. However, [135, eq. (4)] does not have closed-form expression, and acceleration/deceleration that is parallel to the UAV head direction has been largely ignored.

Fig. 7.6 shows the change of the pulling force T and tilt angle θ_v using (7.14). For acceleration, one can see that both T and θ_v increase with t. This is because the fuselage drag increases with the speed during the acceleration process, leading to a gradually increasing T to maintain a. Meanwhile, in order to balance the UAV weight in vertical direction, i.e., $T \cos\theta_v = W$ in (7.8), θ_v also needs

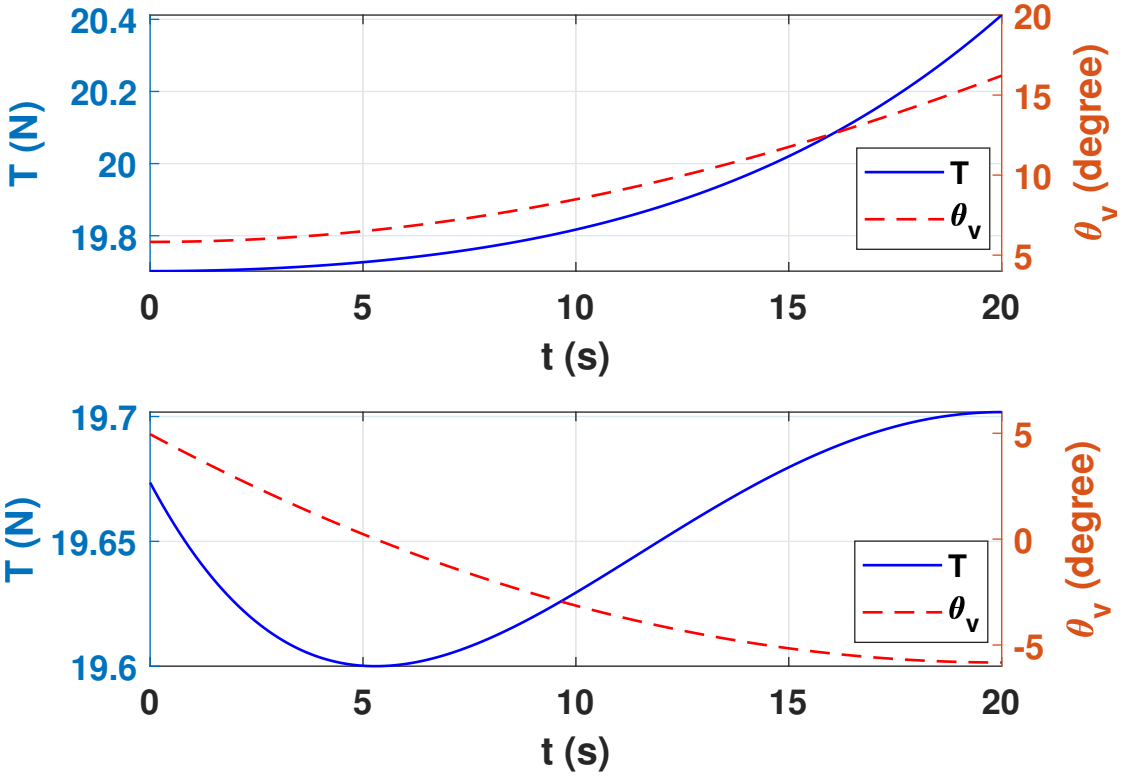

Figure 7.6: T and θ_v change with t in the process of acceleration/deceleration from $v_0(v)$ to $v(v_0)$.

to be increased accordingly. For deceleration, one sees that T decreases first and then increases, while θ_v changes from the velocity direction to the deceleration direction. This can be explained as follows. When the UAV is flying at speed of $v = 20$ m/s, its fuselage drag is $D = \frac{1}{2}\rho S_{FP} v^2$, this drag is large enough to make a deceleration of more than $a = 1$ m/s^2. Thus, a certain amount of T in the same direction of the speed is still needed. However, with the decreasing speed, D gradually decreases. Hence, T also needs to decrease in the direction of the speed. This is why T decreases from time 0 to the 5th second. Also, for balancing the UAV weight, θ_v decreases accordingly. From the figure, when it's nearly the 5th second, T starts to increase. This is because D is not large enough to make a deceleration

of $a = 1$ m/s^2. Hence, a certain amount of T in the opposite direction of the speed is needed. As shown in the figure, the curve representing θ_v changes from positive to negative, which indicates the direction change of T. As T continues to increase, θ_v also needs to be increased, showing a downward curve from 0 to -5.

7.5 Summary

In this chapter, a new ECM considering both acceleration and deceleration as a function of acceleration and time duration has been derived. Numerical results have shown the validity and reliability of the new ECM. The effects of wind and variable acceleration are also important but will be considered as future work.

Chapter 8

Conclusions and Future Work

In this thesis, UAV-enabled WPCNs considering UAV's charging process and propulsion consumption have been studied. For UAV charging, wireless charging from a charging station is studied for the consideration of applications where there is no dedicated landing dock at the charging station for wired charging or it is not convenient or safe for the UAV to land due to the complicated environment surrounding the charging station. However, the UAV charging is not limited by wireless charging. Instead, it includes the wired charging as special cases as clarified where relevant. For UAV propulsion consumption, various manoeuvres such as acceleration and deceleration have also been taken into account. Besides, to further investigate the UAV flight performance and energy consumption, battery-powered UAVs in UAV-enabled WPCNs have been studied where the optimal battery weight for maximizing available energy at the UAV is derived analytically, and a new ECM for rotary-wing UAVs has also been derived.

Next, we first summarize the main findings of the thesis in detail and conclude in Section 8.1. Then, some potential future works are provided in Section

8.2.

8.1 Conclusions

In this section, the main findings of the thesis are summarized and concluded chapter-by-chapter.

- **Chapter 1:** In this Chapter, an overview of UAV-enabled applications in both academia and industry has been presented. In particular, UAV-enabled wireless communications and UAV-enabled WPCNs have been introduced in detail. With the integration of the telecommunication networks and the IoT, UAVs have found a new blue ocean, which is full of opportunities and challenges.

- **Chapter 2:** In this Chapter, some fundamental concepts used in this thesis such as wireless channel model, wireless charging, UAV types and UAV propulsion energy consumption models, etc. have been introduced. Particularly, detailed analysis or mathematical models behind each of these concepts have been presented. Take wireless charging in Section 2.2 as an example, the WPT from a charging station to the UAV, a conversion of RF-to-DC, and the calculation of energy harvested at the UAV have all been demonstrated in detail by mathematical models. Moreover, a comprehensive literature review on UAV-enabled WPT and UAV-aided data collection have been also presented to discuss the start of the art.

- **Chapter 3:** In this Chapter, a UAV-enabled WPT system has been studied, where the UAV is deployed as a mobile energy transmitter to charge a UGV,

i.e., remote sensors. Considering the propulsion power consumption, the UAV is firstly fully charged wirelessly by a BS and then flies towards the remote sensors, followed by discharging. To evaluate the energy transfer efficiency, it is compared with the conventional direct charging without using a UAV. The main contributions and conclusions are summarized as follows:

1. For the UAV-enabled WPT system, a "Load-carry-and-charging" (LCAC) paradigm has been first proposed and compared with the conventional direct charging without using a UAV. In the system, the UAV internal consumption and transmission loss at different stages of the system, including power consumption for hovering during *load* and *charging* stages, power consumption for flying during *carry* stage and transmission loss between the BS and the UAV, and between the UAV and sensors, have been all taken into account. Besides, RF-to-DC conversion efficiency at the UAV and sensors have also been considered.

2. Two new wireless charging schemes have been proposed for UAV-enabled WPT in wireless networks. In the proposed Scheme 1, the UAV stays static when being charged above the BS and discharging above the sensors. While in proposed Scheme 2, instead of hovering above the BS and the sensors, the UAV starts at a distance to the right of the BS and flies at a relative low speed along both sides of the BS within the distance to be charged, and similarly within another distance along both sides of the sensors to discharge. For the Scheme 2, it is a bit more complicated than the Scheme 1, because the charging distance between the BS and the UAV, as well as between the UAV and the sensors, changes periodically with time. For this reason, two algorithms for calculating the energy harvested at the UAV and the energy received at the sensors, have been designed.

3. A critical range within which the proposed schemes have superiority over the conventional scheme has been derived analytically.

In conclusion, the energy transfer efficiency of UAV-enabled WPT is mainly determined by the critical range. Within the critical range, the new proposed schemes show better performance than the conventional direct WPT without using a UAV. This is due to the fact that direct WPT has an increasing transmission loss with distance. Once the transmission loss exceeds the energy cost of using a UAV, the latter shows superiority. However, the critical distance is determined by other system parameters, such as UAV flight height, RF-to-DC conversion efficiency, UAV energy capacity and UAV fight speed, etc.

- **Chapter 4:** On the basis of the work in Chapter 3, the optimal location of UAV in UAV-enabled WPT system has been studied in this Chapter. Different from the previous work, in this chapter we calculate the UAV internal energy consumption using a new analytical propulsion power consumption model for rotary-wing UAVs reported in [49], rather than using the methods in Chapter 3, and a non-linear RF-to-DC conversion model has also been considered. The main contributions and conclusions are summarized as below:

  1. Two different charging schemes for both 1D and 2D topologies in UAV-enabled WPT system have been proposed. In the Scheme 1, the UAV does not charge the sensors until it arrives and hovers at a location above the sensors. This scheme minimizes the transmission loss by having the shortest distance but limits the charging time. For the Scheme 2, the UAV starts to charge sensors before it arrives at the top of sensors, that is, the UAV starts to charge while it is flying close to the sensors.

Although the charging time is extended, it suffers from possible large transmission loss due to a longer distance between the UAV and sensors.

2. According to the combination of two charging schemes and two topologies, four cases have been considered. To derive the optimal UAV location that maximizing the sum-energy received by all sensors, algorithms 1 and 2 have been designed for 1D cases, and algorithms 3 and 4 for 2D cases. Besides, the derived optimal location has also compared with those derived in previous works that ignore the BS charging and UAV internal power consumption.

3. To examine the system performance, different system parameters, such as UAV speed and transmit power, have also been investigated.

In conclusion, the optimal location of the UAV tends to be close to the BS compared with the optimal locations derived in previous works that ignore the BS charging process and the UAV power consumption. For 1D and 2D cases, Schemes 2 shows a better energy efficiency than Scheme 1, possibly because Scheme 2 has a longer charging time than that in Scheme 1 and flying at a relatively low speed consumes less energy than hovering [49]. However, the optimal location is also affected by many other factors, such as the number of sensors, sensors distribution, the UAV flight speed and transmit power.

- **Chapter 5:** Since the critical distance and the optimal location of the UAV have been derived in Chapter 3 and Chapter 4 for UAV-enabled WPT system, this Chapter studies the use of the UAV as a mobile energy transmitter and a data collector in UAV-enabled WPCNs. More specifically, the UAV is first charged from a charging station before it flies to the sensors for data collection. Upon arrival, the UAV first charges the sensors via WPT in

the DL, followed by data transmission from the sensors in the UL. After that, the UAV flies back to the BS to offload data to the BS. To maximize the data offloaded to the BS, the time allocation between above processes is studied. Both distance-dependent path loss and small-scale fading have been considered. The main contributions and conclusions are summarized as follows:

1. The UAV-enabled WPCN has been studied by considering wireless energy transfer from the BS to the UAV, the UAV internal power consumption, WPT from the UAV to sensors, data collection from sensors to the UAV, and the data offloading from the UAV to the BS. To the best of author's knowledge, UAV-aided WPT and data collection considering all these issues has not been studied yet.
2. For the data transmission from the sensors in the UL, two TDMA mechanisms have been studied, i.e., TDMA with equal transmission time for all sensors and TDMA with optimal transmission time.
3. Considering the complexity of the channel, two algorithms have been designed to derive the optimal time allocation for both TDMA mechanisms. Besides, the closed-form expressions of the optimal time allocation have also been derived analytically, but they are determined by the random complex channel coefficient.

In conclusion, when the total task time is fixed, the optimal time allocation in different phases has been derived, and it can maximize the data volume without wasting any time or energy. However, due to the storage capacity limitation of the sensors, it is of great interest and meaningfulness to study the age of information.

- **Chapter 6:** In this Chapter, a battery-powered UAV-enabled wireless com-

munication system has been studied. In this work, a set of batteries on the parking apron are used as energy for different UAV tasks, and an automatic battery replacement mechanism [50] is assumed. Considering the UAV propulsion consumption, we aim to maximize the energy available for communication when the UAV arrives at destination. The main contributions and conclusions are summarized as follows:

1. To quantify the energy available for communication, a LiPo battery-based energy model with maximum battery mass is used to calculated the initial total energy before dispatching. Both vertical and horizontal flight consumption models are used for calculating the energy required for UAV propulsion.
2. The optimal battery weight that maximizes the UAV flight performance has been derived. Both numerical and analytically solutions have been provided.
3. Other system parameters, such as UAV flight height, flight speed and flight distance, have also been examined to provide guidance for system designs.

In conclusion, the optimal battery mass can maximize the energy for communications. However, it is determined by the gross mass of the UAV, vertical/horizontal flight speed, flight height and flight distance. Besides, the optimal battery mass does not necessarily maximize the operation time. This is because larger battery mass makes more energy, but also increases propulsion and hovering consumption, thereby reduces the time for communications.

- **Chapter 7:** Existing energy consumption models for rotary-wing UAVs are either too complex, or do not consider acceleration/deceleration. In this Chapter, a new ECM that overcomes the shortcoming of the current models

has been studied. The main contributions and conclusions are summarized as below:

1. A much simpler and easier to use ECM, as a function of acceleration/deceleration and time duration, has been derived analytically.
2. Both 1D and 2D level flight cases have been considered, and the new ECM has also been compared with existing models to verify the validity and reliability.
3. Other system parameters, such as polling force and tilt angle, have been analyzed in analytical form to provide useful guidance for fight control.

In conclusion, a new, simple and ease-to-use model with closed-form expression as a function of the initial velocity, acceleration and time duration has been derived. Such an ECM is of great importance and meaningfulness for UAV-enabled applications, because it can be used to calculate the energy required for UAV propulsion.

Corresponding to the research objectives in Section 1.2 in Chapter 1, all those five research objectives have been achieved, and the research achievements have also been published, see [J1] to [J5].

8.2 Future Work

So far, we have completed the research works presented from Chapter 3 to Chapter 7, in which all the issues discussed in Section 1.2 in Chapter 1 have been considered and addressed. Some potential future works based on this thesis and current research trend [103, 137, 138] are discussed and suggested.

Inspired by the work in this thesis, some interesting future works are provided as below:

- **Potential future work for Chapter 3**: The work in Chapter 3 focuses on the energy transfer efficiency of UAV-enabled WPT, considering UAV internal energy consumption. However, the power consumption model used to calculate the UAV propulsion energy is simply assumed before the propulsion power consumption model for rotary-wing UAVs was first reported in [49] and thus, it is more practical to consider such a new power consumption model. Besides, only one UAV is considered in the work, and an interesting future work is to extend it to a multi-UAVs case.

- **Potential future work for Chapter 4**: Our work in Chapter 4 considers different cases to study the optimal UAV locations. In the proposed Scheme 2, it is assumed that the UAV flies at a fixed height of x_h and starts at a distance of x_{start} to the left of sensors to charge. In this assumption, x_{start} is determined by the minimum received power at the nearest sensor. However, jointly optimizing x_{start} and x_h can be further investigated. Besides, it is also interesting and challenging to place the UAV at different optimal locations for different sensors by exploiting the UAV's trajectory design, although extra power consumption is needed and it may not be energy-efficient compared with the current schemes.

- **Potential future work for Chapter 5**: On the basis of Chapter 3 and Chapter 4, Chapter 5 further considers the data collection from sensors and data offloading to the BS. Due to the fact that sensors' memory is limited, it is interesting to consider the age of sensing data. Besides, it is impossible for UAV to hover without any fluctuation, especially when it is windy. In this situation, hovering fluctuation [139] needs to be considered for more

practical cases. Moreover, for the cases where near-field wireless charging or wired charging by placing the UAV on the apron is available, the UAV power consumption for vertical flight also needs to be considered.

- **Potential future work for Chapter 6**: The work in Chapter 6 focuses on the optimal battery weight to maximize the available energy when the UAV arrives at the destination. Motivated by the Wing Loong-2H, a UAV which was successfully deployed to restore telecommunications services in China's Henan Province in July 2021, it is interesting and meaningful to extend the work to the case of multi-UAV cooperative coverage, since the usage of multi-UAV is still a growing topic [140] and has not been well studied yet with different wireless communication technologies [141] such as LoRa.

- **Potential future work for Chapter 7**: In Chapter 7, a new ECM for rotary-wing UAV level flight propulsion is studied. However, the effects of wind and variable acceleration are also important and inevitable in practice and thus, it is interesting to study a more practical model with wind effects considered. Besides, since energy is vital in UAV-enabled applications and the new ECM has been derived, new optimization problems considering UAV propulsion consumption with the new derived ECM, such as UAV trajectory optimization and multi-UAV scheduling and cooperation, will be very meaningful future works.

Appendix A

Derivation of Critical Distance in Chapter 3

A.1 Derivation of Critical Distance in (3.31)

In this appendix, we solve the equation to derive the exact critical range in which it shows the superiority for the proposed Scheme 1. Rewriting equation (3.31), we can transform it into a standard form of a cubic equation as

$$BEL^3 - (BC + BEF)\,L^2 + BEH^2L - BCH^2 - BEFH^2 + AD = 0. \tag{A.1}$$

Since A, B, C, D, E and B are constants, (A.1) can be derived in an easier form via the constant transformation $a = BE$, $b = -(BC + BEF)$, $c = BEH^2$ and $d = -BCH^2 - BEFH^2 + AD$, i.e.,

$$aL^3 + bL^2 + cL + d = 0. \tag{A.2}$$

For (A.2), we divide both sides of the equation by a simultaneously, and then it can be transformed into the form of $Cardano$ formula using the variable transformation $L = y - \frac{b}{3a}$ as

$$y^3 + \left(\frac{c}{a} - \frac{b^2}{3a^2}\right) y + \left(\frac{2b^3}{27a^3} - \frac{bc}{3a^2} + \frac{d}{a}\right) = 0. \tag{A.3}$$

Accordingly, the discriminant of the equation root can be expressed via variable transformation $p = \frac{c}{a} - \frac{b}{3a^2}$ and $q = \frac{2b^3}{27a^3} - \frac{bc}{3a^2} + \frac{d}{a}$ as

$$\Delta = \left(\frac{q}{2}\right)^2 + \left(\frac{p}{3}\right)^3. \tag{A.4}$$

It is not difficult to find that $\Delta < 0$ and $p < 0$ in this case. Therefore, three unequal real roots of the equation (A.3) can be obtained according to the $Cardano$ formula as

$$\begin{aligned} y_1 &= 2\sqrt[3]{r}\cos\theta, \\ y_2 &= 2\sqrt[3]{r}\cos\left(\theta + \frac{2\pi}{3}\right), \\ y_3 &= 2\sqrt[3]{r}\cos\left(\theta + \frac{4\pi}{3}\right), \end{aligned} \tag{A.5}$$

where

$$r = \sqrt{-\left(\frac{p}{3}\right)^3}, \theta = \frac{1}{3}\arccos\left(-\frac{q}{2}\right). \tag{A.6}$$

Consequently, the three real roots of the equation (A.2) are

$$\begin{aligned} L_1 &= y_1 - \frac{b}{3a}, \\ L_2 &= y_2 - \frac{b}{3a}, \\ L_3 &= y_3 - \frac{b}{3a}. \end{aligned} \tag{A.7}$$

And the final solutions of the equation (A.2) after reorganizing are

$$
\begin{aligned}
L_1 &= 2\sqrt[3]{\sqrt{-\left(\tfrac{p}{3}\right)^3}}\cos\left(\frac{1}{3}\arccos\left(-\frac{q}{2}\right)\right) - \frac{b}{3a}, \\
L_2 &= 2\sqrt[3]{\sqrt{-\left(\tfrac{p}{3}\right)^3}}\cos\left(\frac{1}{3}\arccos\left(-\frac{q}{2}\right) + \frac{2\pi}{3}\right) - \frac{b}{3a}, \\
L_3 &= 2\sqrt[3]{\sqrt{-\left(\tfrac{p}{3}\right)^3}}\cos\left(\frac{1}{3}\arccos\left(-\frac{q}{2}\right) + \frac{4\pi}{3}\right) - \frac{b}{3a}.
\end{aligned}
\tag{A.8}
$$

By substituting the values of the parameters for simulation, we can find that L_2 is a negative value among the above three roots, which is obviously meaningless in our model because L is a positive number. While L_3 and L_1 are the two values on both the left and right sides of the critical rang $[L_3 \quad L_1]$ we expect, and L_3 is seen as the critical distance.

Appendix B

Derivation of the Integral $\int_0^{\frac{V}{a}} P(t)\,dt$ in Chapter 4

B.1 The Calculation of Integral in (4.5)

In this appendix, we solve the integral $\int_0^{\frac{V}{a}} P(t)\,dt$ to derive the exact energy required when the UAV accelerates from the speed of 0 to V or decelerates from the speed of V to 0. Then the integral can be rewritten by combining (2.11), (2.15) and (4.5) as

$$\int_0^{\frac{V}{a}} P(t)\,dt = \int_0^{\frac{V}{a}} \left[P_0 \left(1 + \frac{3(at)^2}{U_{tip}^2}\right) + P_i \left(\sqrt{1 + \frac{(at)^4}{4v_0^4}} - \frac{(at)^2}{2v_0^2}\right)^{\frac{1}{2}} + \frac{1}{2} d_0 \rho s A (at)^3 \right] dt. \tag{B.1}$$

To do this, we divide it into three integrals as

$$\begin{aligned}\int_0^{\frac{V}{a}} P(t)\,dt &= \int_0^{\frac{V}{a}} P_0\left(1+\tfrac{3(at)^2}{U_{tip}^2}\right)\,dt + \int_0^{\frac{V}{a}} \frac{1}{2}d_0\rho sA(at)^3\,dt \\ &\quad + \int_0^{\frac{V}{a}} P_i\left(\sqrt{1+\tfrac{(at)^4}{4v_0^4}}-\tfrac{(at)^2}{2v_0^2}\right)^{\frac{1}{2}}\,dt \\ &= \left[P_0 t + \frac{P_0 a^2}{U_{tip}^3}t^3\right]_0^{\frac{V}{a}} + \left[\frac{1}{8}d_0\rho sAa^3t^4\right]_0^{\frac{V}{a}} + \int_0^{\frac{V}{a}} P_i\left(\sqrt{1+\tfrac{(at)^4}{4v_0^4}}-\tfrac{(at)^2}{2v_0^2}\right)^{\frac{1}{2}}dt.\end{aligned} \tag{B.2}$$

Now we only need to solve the third one. In doing so, we let $u = \left(\sqrt{1+\frac{(at)^4}{4v_0^4}}-\frac{(at)^2}{2v_0^2}\right)^{\frac{1}{2}}$. Then we have

$$u^2\left(u^2+\frac{a^2t^2}{{v_0}^2}\right)=1, \tag{B.3}$$

$$t=\frac{v_0}{ua}\sqrt{1-u^4},\ t>0, \tag{B.4}$$

$$dt=\frac{-v_0}{au^2}\sqrt{1-u^4}-\frac{2v_0u^2}{a\sqrt{1-u^4}}\,du. \tag{B.5}$$

Taking u as the integral variable, the lower limit and upper limit can be obtained as 1 and $\left(\sqrt{1+\frac{(V)^4}{4v_0^4}}-\frac{(V)^2}{2v_0^2}\right)^{\frac{1}{2}}$. As a result, the third sub-item integral can be expressed as

$$\begin{aligned}\int_0^{\frac{V}{a}} P_i\left(\sqrt{1+\tfrac{(at)^4}{4v_0^4}}-\tfrac{(at)^2}{2v_0^2}\right)^{\frac{1}{2}}dt &= \int_0^{U_l} P_i u\left(\frac{-v_0}{au^2}\sqrt{1-u^4}-\frac{2v_0u^2}{a\sqrt{1-u^4}}\right)du, \\ &= \int_0^{U_l}\frac{-P_iv_0\sqrt{1-u^4}}{au}du-\int_0^{U_l}\frac{2P_iv_0u^3}{a\sqrt{1-u^4}}\,du,\end{aligned} \tag{B.6}$$

where $U_l=\left(\sqrt{1+\frac{(V)^4}{4v_0^4}}-\frac{(V)^2}{2v_0^2}\right)^{\frac{1}{2}}$.

For the first one, we use the variable transformation $z_1 = \sqrt{1-u^4}$, then the lower limit and upper limit of the integral are converted to 1 and $\sqrt{1-U_l{}^4}$ so that one has

$$\int_0^{U_l} \frac{-P_i v_0 \sqrt{1-u^4}}{au} du = \frac{P_i v_0}{2a} \int_1^{\sqrt{1-U_l{}^4}} \frac{z_1{}^2}{1-z_1{}^2} dz_1, \tag{B.7}$$

For the integral above, we continue to use the variable transformation $z_1 = \sin\theta$, then the lower limit and upper limit are converted again to $\frac{\pi}{2}$ and $\arcsin\left(\sqrt{1-U_l{}^4}\right)$ so that one has

$$\begin{aligned} \frac{P_i v_0}{2a} \int_1^{\sqrt{1-U_l{}^4}} \frac{z_1{}^2}{1-z_1{}^2}\, dz_1 &= \frac{P_i v_0}{2a} \int_{\frac{\pi}{2}}^{\theta'} \frac{\sin^2\theta}{\cos\theta}\, d\theta \\ &= \frac{P_i v_0}{2a} \left\{ \left[\ln\tan\left(\frac{\pi}{4}+\frac{\theta}{2}\right) \right]_{\frac{\pi}{2}}^{\theta'} - [\sin\theta]_{\frac{\pi}{2}}^{\theta'} \right\}, \end{aligned} \tag{B.8}$$

where $\theta' = \arcsin\left(\sqrt{1-U_l{}^4}\right)$.

For the second one, we use the same variable transformation $z_2 = \sqrt{1-u^4}$ as in (B.7), then the lower limit and upper limit are changed to 1 and $\sqrt{1-U_l{}^4}$ so that one has

$$\begin{aligned} \int_0^{U_l} \frac{2P_i v_0 u^3}{a\sqrt{1-u^4}} du &= \int_0^{U_l} \frac{P_i v_0}{2a\sqrt{1-u^4}} du^4 \\ &= \int_1^{\sqrt{1-U_l{}^4}} \frac{P_i v_0}{-a} dz_2 \\ &= \frac{P_i v_0}{-a} \left(\sqrt{1-U_l{}^4} - 1\right) \end{aligned} \tag{B.9}$$

Finally, the original integral is solved by substituting (B.6) – (B.9) into (B.2).

Appendix C

Derivation of μ_3^* for the Special Case of One Sensor in Chapter 5

C.1 The First-order Derivative of $\bar{D}_{K,u}$

Taking the first-order derivative of the $\bar{D}_{K,u}$ with respect to μ_3 and let it be zero, one has

$$\frac{\partial \bar{D}_{K,u}}{\partial \mu_3} = 0 \Longleftrightarrow x_1 \ln x_1 = \frac{A_1}{\mu_3},\ x_1 = 1 - A_1 + \frac{A_1}{\mu_3}, \tag{C.1}$$

By observing (C.1), it is very challenging to derive its analytical solution. However, it is found that there is a 'function' in the form of '$x \ln x$' on the left side of the equations above, and it can be replaced by a polynomial derived by curve fitting. In this way, the approximate solution of the equation (C.1) can be obtained, one has

$$x_1 \ln x_1 \approx p_1 {x_1}^2 + p_2 x_1 + p_3, \tag{C.2}$$

where p_1, p_2 and p_3 are coefficients of the approximate polynomial. Using (C.2) and substitute it to (C.1), the optimal μ_3 can be derived as

$$\mu_3^* = \frac{-b_1 \pm \sqrt{{b_1}^2 - 4a_1c_1}}{2a_1}, \tag{C.3}$$

where $a_1 = p_1(1-A_1)^2+p_2(1-A_1)+p_3$, $b_1 = 2p_1A_1(1-A_1)+p_2A_1-A_1$, $c_1 = p_1A_1$.

References

[1] L. Gupta, R. Jain, and G. Vaszkun, "Survey of Important Issues in UAV Communication Networks," *IEEE Communications Surveys and Tutorials*, vol. 18, no. 2, pp. 1123–1152, Nov. 2016.

[2] S. Hayat, E. Yanmaz, and R. Muzaffar, "Survey on Unmanned Aerial Vehicle Networks for Civil Applications: A Communications Viewpoint," *IEEE Communications Surveys and Tutorials*, vol. 18, no. 4, pp. 2624–2661, Apr. 2016.

[3] H. Shakhatreh, A. H. Sawalmeh, A. Al-Fuqaha, Z. Dou, E. Almaita, I. Khalil, N. S. Othman, A. Khreishah, and M. Guizani, "Unmanned Aerial Vehicles (UAVs): A Survey on Civil Applications and Key Research Challenges," *IEEE Access*, vol. 7, pp. 48 572–48 634, Apr. 2019.

[4] Y. Zeng, R. Zhang, and T. J. Lim, "Wireless communications with unmanned aerial vehicles: Opportunities and challenges," *IEEE Communications Magazine*, vol. 54, no. 5, pp. 36–42, May 2016.

[5] I. Guvenc, W. Saad, M. Bennis, C. Wietfeld, M. Ding, and L. Pike, "Wireless communications, networking, and positioning with unmanned aerial vehicles [Guest Editorial]," *IEEE Communications Magazine*, vol. 54, no. 5, pp. 24–25, May 2016.

[6] Y. Zeng, M. Debbah, D. Gesbert, I. Guvenc, S. Jin, and J. Xu, "Integrating UAVs into 5G and Beyond," *IEEE Wireless Communications*, vol. 26, no. 1, pp. 10–11, Feb. 2019.

[7] R. Shahzadi, M. Ali, H. Z. Khan, and M. Naeem, "UAV assisted 5G and beyond wireless networks: A survey," *Journal of Network and Computer Applications*, vol. 189, p. 103114, Sep. 2021.

[8] L. Bai, I. Guvenc, Q. Yu, and W. Zhang, "Special Issue on Unmanned Aerial Vehicles Over Internet of Things," *IEEE Internet of Things Journal*, vol. 6, no. 2, pp. 1636–1639, May 2019.

[9] R. Sokullu and M. A. Akkaş, "Unmanned Aerial Vehicle and IoT as Enabling Technologies for 5G: Frameworks, Applications and Challenges," in *Studies in Systems, Decision and Control*. Springer, 2020, vol. 266, pp. 217–239.

[10] W. Feng, J. Tang, Y. Yu, J. Song, N. Zhao, G. Chen, K. K. Wong, and J. Chambers, "UAV-Enabled SWIPT in IoT Networks for Emergency Communications," *IEEE Wireless Communications*, vol. 27, no. 5, pp. 140–147, Oct. 2020.

[11] X. Cao, P. Yang, M. Alzenad, X. Xi, D. Wu, and H. Yanikomeroglu, "Airborne Communication Networks: A Survey," *IEEE Journal on Selected Areas in Communications*, vol. 36, no. 9, pp. 1907–1926, Aug. 2018.

[12] Y. Zeng, Q. Wu, and R. Zhang, "Accessing from the Sky: A Tutorial on UAV Communications for 5G and beyond," *Proceedings of the IEEE*, vol. 107, no. 12, pp. 2327–2375, Dec. 2019.

[13] "China deploys UAV for telecom restoration in rain-hit Henan - People's Daily Online." [Online]. Available: http://en.people.cn/n3/2021/0723/c90000-9875913.html

[14] "Homegrown emergency UAV aids telecoms restoration in central China - CGTN." [Online]. Available: https://news.cgtn.com/news/2021-07-23/Homegrown-emergency-UAV-aids-telecoms-restoration-in-central-China-127VHvAvb0I/index.html

[15] "Chinese drones provide lifeline network services for flood-stranded residents - Global Times." [Online]. Available: https://www.globaltimes.cn/page/202107/1229363.shtml

[16] A. Al-Hourani, S. Kandeepan, and S. Lardner, "Optimal LAP altitude for maximum coverage," *IEEE Wireless Communications Letters*, vol. 3, no. 6, pp. 569–572, Dec. 2014.

[17] Y. Chen, W. Feng, and G. Zheng, "Optimum Placement of UAV as Relays," *IEEE Communications Letters*, vol. 22, no. 2, pp. 248–251, Feb. 2018.

[18] Y. Zeng, R. Zhang, and T. J. Lim, "Throughput Maximization for UAV-Enabled Mobile Relaying Systems," *IEEE Transactions on Communications*, vol. 64, no. 12, pp. 4983–4996, Dec. 2016.

[19] J. Lyu, Y. Zeng, R. Zhang, and T. J. Lim, "Placement Optimization of UAV-Mounted Mobile Base Stations," *IEEE Communications Letters*, vol. 21, no. 3, pp. 604–607, Mar. 2017.

[20] J. Lyu, Y. Zeng, and R. Zhang, "Cyclical Multiple Access in UAV-Aided Communications: A Throughput-Delay Tradeoff," *IEEE Wireless Communications Letters*, vol. 5, no. 6, pp. 600–603, Dec. 2016.

[21] R. Fan, J. Cui, S. Jin, K. Yang, and J. An, "Optimal Node Placement and Resource Allocation for UAV Relaying Network," *IEEE Communications Letters*, vol. 22, no. 4, pp. 808–811, Feb. 2018.

[22] S. Zhang, H. Zhang, Q. He, K. Bian, and L. Song, "Joint Trajectory and Power Optimization for UAV Relay Networks," *IEEE Communications Letters*, vol. 22, no. 1, pp. 161–164, Jan. 2018.

[23] H. Ju and R. Zhang, "Throughput Maximization in Wireless Powered Communication Networks," *IEEE Transactions on Wireless Communications*, vol. 13, no. 1, pp. 418–428, Jan. 2014.

[24] L. Xie, J. Xu, and R. Zhang, "Throughput maximization for uav-enabled wireless powered communication networks," *IEEE Internet of Things Journal*, vol. 6, no. 2, pp. 1690–1703, Apr. 2019.

[25] Y. Liu, K. Xiong, Y. Lu, Q. Ni, P. Fan, and K. B. Letaief, "UAV-aided Wireless Power Transfer and Data Collection in Rician Fading," *IEEE Journal on Selected Areas in Communications*, 2021.

[26] A. Moheddine, F. Patrone, and M. Marchese, "UAV and IoT Integration: A Flying Gateway," in *2019 26th IEEE International Conference on Electronics, Circuits and Systems (ICECS)*, vol. 19, no. 1. IEEE, Nov. 2019, pp. 121–122.

[27] Y. Pang, Y. Zhang, Y. Gu, M. Pan, Z. Han, and P. Li, "Efficient data collection for wireless rechargeable sensor clusters in Harsh terrains using UAVs," in *2014 IEEE Global Communications Conference (GLOBECOM)*. IEEE, Dec. 2014, pp. 234–239.

[28] S. Arabi, H. Elbiaze, E. Sabir, and M. Sadik, "Tradeoffs for Data Collection and Wireless Energy Transfer Dilemma in IoT Environments," in *2018 IEEE International Conference on Communications (ICC)*, vol. 2018-May. IEEE, May 2018, pp. 1–6.

[29] J. Hou, Z. Yang, and M. Shikh-Bahaei, "Energy-Efficient Data Collection and Wireless Power Transfer Using A MIMO Full-Duplex UAV," Nov. 2018. [Online]. Available: http://arxiv.org/abs/1811.10134.

[30] Y. Zeng and R. Zhang, "Energy-Efficient UAV Communication with Trajectory Optimization," *IEEE Transactions on Wireless Communications*, vol. 16, no. 6, pp. 3747–3760, Jun. 2017.

[31] S. Sekander, H. Tabassum, and E. Hossain, "Statistical Performance Modeling of Solar and Wind-Powered UAV Communications," *IEEE Transactions on Mobile Computing*, vol. 20, no. 8, pp. 2686–2700, Aug. 2021.

[32] X. Lu, P. Wang, D. Niyato, D. I. Kim, and Z. Han, "Wireless Charging Technologies: Fundamentals, Standards, and Network Applications," *IEEE Communications Surveys and Tutorials*, vol. 18, no. 2, pp. 1413–1452, 2016.

[33] M. Lu, M. Bagheri, A. P. James, and T. Phung, "Wireless Charging Techniques for UAVs: A Review, Reconceptualization, and Extension," *IEEE Access*, vol. 6, pp. 29 865–29 884, 2018.

[34] K. Min Naing, A. Zakeri, and O. Iliev, "Wireless Energy transfer to long distance flying Intelligent Unmanned Aerial Vehicles (UAVs) using reactive power transfer techniques," *Journal of Multidisciplinary Engineering Science and Technology (JMEST)*, vol. 7, no. 9, pp. 2458–9403, 2020. [Online]. Available: www.jmest.org

[35] Global Energy Transmission, "Wirelessly powered drone – GLOBAL ENERGY TRANSMISSION," 2016. [Online]. Available: http://getcorp.com/wirelessly-powered-drone/.

[36] J. Xu, Y. Zeng, and R. Zhang, "UAV-enabled wireless power transfer: Trajectory design and energy optimization," *IEEE Transactions on Wireless Communications*, vol. 17, no. 8, pp. 5092–5106, Aug. 2018.

[37] Y. Hu, X. Yuan, J. Xu, and A. Schmeink, "Optimal 1D Trajectory Design for UAV-Enabled Multiuser Wireless Power Transfer," *IEEE Transactions on Communications*, vol. 67, no. 8, pp. 5674–5688, Aug. 2019.

[38] Y. Wu, L. Qiu, and J. Xu, "UAV-Enabled Wireless Power Transfer with Directional Antenna: A Two-User Case (Invited Paper)," in *2018 15th International Symposium on Wireless Communication Systems (ISWCS)*, vol. 2018-Augus. IEEE, Aug. 2018, pp. 1–6.

[39] M. Hua, C. Li, Y. Huang, and L. Yang, "Throughput maximization for UAV-enabled wireless power transfer in relaying system," in *2017 9th International Conference on Wireless Communications and Signal Processing, WCSP 2017 - Proceedings*, vol. 2017-January. IEEE, Oct. 2017, pp. 1–5.

[40] Y. Chen, K. T. Sabnis, and R. A. Abd-Alhameed, "New Formula for Conversion Efficiency of RF EH and Its Wireless Applications," *IEEE Transactions on Vehicular Technology*, vol. 65, no. 11, pp. 9410–9414, Nov. 2016.

[41] J. Xu, Y. Zeng, and R. Zhang, "UAV-Enabled Wireless Power Transfer: Trajectory Design and Energy Region Characterization," in *2017 IEEE Globecom Workshops, GC Wkshps 2017 - Proceedings*, vol. 2018-January. IEEE, Dec. 2018, pp. 1–7. [Online]. Available: http://ieeexplore.ieee.org/document/8269097/

[42] J. Xu, Y. Zeng, and R. Zhang, "UAV-enabled multiuser wireless power transfer: Trajectory design and energy optimization," in *2017*

23rd Asia-Pacific Conference on Communications (APCC), vol. 2018-January, no. 8. IEEE, Dec. 2017, pp. 1–6. [Online]. Available: http://ieeexplore.ieee.org/document/8304077/

[43] H. Yan, Y. Chen, and S. H. Yang, "Analysis of energy transfer efficiency in UAV-enabled wireless networks," *Physical Communication*, vol. 37, p. 100849, Dec. 2019.

[44] M. Jiang, Y. Li, Q. Zhang, and J. Qin, "Joint Position and Time Allocation Optimization of UAV Enabled Wireless Powered Communication Networks," *IEEE Transactions on Communications*, vol. 67, no. 5, pp. 3806–3816, May 2019.

[45] T. Shen and H. Ochiai, "A UAV-Aided Data Collection for Wireless Powered Sensor Network over Rician Fading Channels," in *2019 16th IEEE Annual Consumer Communications Networking Conference (CCNC)*. IEEE, Jan. 2019, pp. 1–5.

[46] H. T. Ye, X. Kang, J. Joung, and Y. C. Liang, "Optimization for Full-Duplex Rotary-Wing UAV-Enabled Wireless-Powered IoT Networks," *IEEE Transactions on Wireless Communications*, vol. 19, no. 7, pp. 5057–5072, Jul. 2020.

[47] F. Wu, D. Yang, L. Xiao, and L. Cuthbert, "Energy Consumption and Completion Time Tradeoff in Rotary-Wing UAV Enabled WPCN," *IEEE Access*, vol. 7, pp. 79 617–79 635, 2019.

[48] Y. Chen, N. Zhao, and M. S. Alouini, "Wireless Energy Harvesting Using Signals from Multiple Fading Channels," *IEEE Transactions on Communications*, vol. 65, no. 11, pp. 5027–5039, Nov. 2017.

[49] Y. Zeng, J. Xu, and R. Zhang, "Energy minimization for wireless communication with rotary-wing UAV," *IEEE Transactions on Wireless Communications*, vol. 18, no. 4, pp. 2329–2345, Apr. 2019.

[50] K. A. O. Suzuki, P. Kemper Filho, and J. R. Morrison, "Automatic Battery Replacement System for UAVs: Analysis and Design," *Journal of Intelligent Robotic Systems*, vol. 65, no. 1-4, pp. 563–586, Jan. 2012.

[51] G. L. Stüber, *Principles of mobile communication: Fourth edition.* Springer International Publishing, May 2017.

[52] I. S. Gradshteyn, I. M. Ryzhik, and R. H. Romer, *Tables of Integrals, Series, and Products*, 7th ed. New York, USA: American Journal of Physics, 2007, vol. 56, no. 10.

[53] Z. Yang, W. Xu, and M. Shikh-Bahaei, "Energy Efficient UAV Communication with Energy Harvesting," *IEEE Transactions on Vehicular Technology*, vol. 69, no. 2, pp. 1913–1927, Feb. 2020.

[54] Q. Wu, Y. Zeng, and R. Zhang, "Joint Trajectory and Communication Design for Multi-UAV Enabled Wireless Networks," *IEEE Transactions on Wireless Communications*, vol. 17, no. 3, pp. 2109–2121, Mar. 2018.

[55] W. Feng, N. Zhao, S. Ao, J. Tang, X. Zhang, Y. Fu, D. K. C. So, and K.-K. Wong, "Joint 3D Trajectory Design and Time Allocation for UAV-Enabled Wireless Power Transfer Networks," *IEEE Transactions on Vehicular Technology*, vol. 69, no. 9, pp. 9265–9278, Sep. 2020.

[56] M. Liu, G. Gui, N. Zhao, J. Sun, H. Gacanin, and H. Sari, "UAV-Aided Air-to-Ground Cooperative Nonorthogonal Multiple Access," *IEEE Internet of Things Journal*, vol. 7, no. 4, pp. 2704–2715, Apr. 2020.

[57] D. Yang, Q. Wu, Y. Zeng, and R. Zhang, "Energy Tradeoff in Ground-to-UAV Communication via Trajectory Design," *IEEE Transactions on Vehicular Technology*, vol. 67, no. 7, pp. 6721–6726, Jul. 2018.

[58] S. Suman, S. Kumar, and S. De, "UAV-Assisted RF Energy Transfer," in *IEEE International Conference on Communications*, vol. 2018-May. IEEE, May 2018, pp. 1–6.

[59] H. J. Visser and R. J. Vullers, "RF energy harvesting and transport for wireless sensor network applications: Principles and requirements," *Proceedings of the IEEE*, vol. 101, no. 6, pp. 1410–1423, Jun. 2013.

[60] L. Xie, Y. Shi, Y. T. Hou, and A. Lou, "Wireless power transfer and applications to sensor networks," *IEEE Wireless Communications*, vol. 20, no. 4, pp. 140–145, Aug. 2013.

[61] X. Lu, P. Wang, D. Niyato, D. I. Kim, and Z. Han, "Wireless networks with rf energy harvesting: A contemporary survey," *IEEE Communications Surveys and Tutorials*, vol. 17, no. 2, pp. 757–789, 2015.

[62] D. Mishra, S. De, S. Jana, S. Basagni, K. Chowdhury, and W. Heinzelman, "Smart RF energy harvesting communications: Challenges and opportunities," *IEEE Communications Magazine*, vol. 53, no. 4, pp. 70–78, Apr. 2015.

[63] M. Y. Naderi, K. R. Chowdhury, and S. Basagni, "Wireless sensor networks with RF energy harvesting: Energy models and analysis," in *2015 IEEE Wireless Communications and Networking Conference, WCNC 2015*. IEEE, Mar. 2015, pp. 1494–1499.

[64] S. Kumar, S. De, and D. Mishra, "RF energy transfer channel models for sustainable IoT," *IEEE Internet of Things Journal*, vol. 5, no. 4, pp. 2817–2828, 2018.

[65] F. Sangare, A. Arab, M. Pan, L. Qian, S. K. Khator, and Z. Han, "RF energy harvesting for WSNs via dynamic control of unmanned vehicle charging," in *2015 IEEE Wireless Communications and Networking Conference, WCNC 2015*. IEEE, Mar. 2015, pp. 1291–1296.

[66] F. Sangare, Y. Xiao, D. Niyato, and Z. Han, "Mobile Charging in Wireless-Powered Sensor Networks: Optimal Scheduling and Experimental Implementation," *IEEE Transactions on Vehicular Technology*, vol. 66, no. 8, pp. 7400–7410, Aug. 2017.

[67] W. Na, J. Park, C. Lee, K. Park, J. Kim, and S. Cho, "Energy-Efficient Mobile Charging for Wireless Power Transfer in Internet of Things Networks," *IEEE Internet of Things Journal*, vol. 5, no. 1, pp. 79–92, Feb. 2018.

[68] N. Zhao, F. R. Yu, and V. C. Leung, "Wireless energy harvesting in interference alignment networks," *IEEE Communications Magazine*, vol. 53, no. 6, pp. 72–78, Jun. 2015.

[69] Z. Wang, R. Liu, Q. Liu, J. S. Thompson, and M. Kadoch, "Energy-Efficient Data Collection and Device Positioning in UAV-Assisted IoT," *IEEE Internet of Things Journal*, vol. 7, no. 2, pp. 1122–1139, Feb. 2020.

[70] S. Liu, Z. Wei, Z. Guo, X. Yuan, and Z. Feng, "Performance Analysis of UAVs Assisted Data Collection in Wireless Sensor Network," in *2018 IEEE 87th Vehicular Technology Conference (VTC Spring)*, vol. 2018-June. IEEE, Jun. 2018, pp. 1–5.

[71] C. You and R. Zhang, "3D Trajectory Optimization in Rician Fading for UAV-Enabled Data Harvesting," *IEEE Transactions on Wireless Communications*, vol. 18, no. 6, pp. 3192–3207, Jun. 2019.

[72] S. Goudarzi, N. Kama, M. H. Anisi, S. Zeadally, and S. Mumtaz, "Data collection using unmanned aerial vehicles for Internet of Things platforms," *Computers and Electrical Engineering*, vol. 75, pp. 1–15, May 2019.

[73] M. Samir, S. Sharafeddine, C. M. Assi, T. M. Nguyen, and A. Ghrayeb, "UAV Trajectory Planning for Data Collection from Time-Constrained IoT Devices," *IEEE Transactions on Wireless Communications*, vol. 19, no. 1, pp. 34–46, Jan. 2020.

[74] H. Q. Pham, M. Camey, K. D. Pham, K. V. Pham, and L. R. Rilett, "Review of unmanned aerial vehicles (UAVs) operation and data collection for driving behavior analysis," in *Lecture Notes in Civil Engineering*. Springer, Singapore, 2020, vol. 54, pp. 1111–1116.

[75] C. Zhan, Y. Zeng, and R. Zhang, "Energy-Efficient Data Collection in UAV Enabled Wireless Sensor Network," *IEEE Wireless Communications Letters*, vol. 7, no. 3, pp. 328–331, Jun. 2018.

[76] C. Zhan and Y. Zeng, "Completion Time Minimization for Multi-UAV-Enabled Data Collection," *IEEE Transactions on Wireless Communications*, vol. 18, no. 10, pp. 4859–4872, Oct. 2019.

[77] J. Gong, T. H. Chang, C. Shen, and X. Chen, "Flight time minimization of UAV for data collection over wireless sensor networks," *IEEE Journal on Selected Areas in Communications*, vol. 36, no. 9, pp. 1942–1954, Sep. 2018.

[78] X. Ma, R. Kacimi, and R. Dhaou, "Fairness-aware UAV-assisted data collection in mobile wireless sensor networks," in *2016 International Wireless Communications and Mobile Computing Conference (IWCMC)*. IEEE, Sep. 2016, pp. 995–1001.

[79] W. Li, L. Wang, and A. Fei, "Minimizing Packet Expiration Loss with Path Planning in UAV-Assisted Data Sensing," *IEEE Wireless Communications Letters*, vol. 8, no. 6, pp. 1520–1523, Dec. 2019.

[80] Z. Jia, X. Qin, Z. Wang, and B. Liu, "Age-based path planning and data acquisition in UAV-Assisted IoT networks," in *2019 IEEE International Conference on Communications Workshops, ICC Workshops 2019 - Proceedings*. IEEE, May 2019, pp. 1–6.

[81] J. Li, H. Zhao, H. Wang, F. Gu, J. Wei, H. Yin, and B. Ren, "Joint Optimization on Trajectory, Altitude, Velocity, and Link Scheduling for Minimum Mission Time in UAV-Aided Data Collection," *IEEE Internet of Things Journal*, vol. 7, no. 2, pp. 1464–1475, Feb. 2020.

[82] J. Chen, F. Yan, S. Mao, F. Shen, W. Xia, Y. Wu, and L. Shen, "Efficient Data Collection in Large-Scale UAV-aided Wireless Sensor Networks," in *2019 11th International Conference on Wireless Communications and Signal Processing (WCSP)*. IEEE, Oct. 2019, pp. 1–5.

[83] C. Zhan and H. Lai, "Energy Minimization in Internet-of-Things System Based on Rotary-Wing UAV," *IEEE Wireless Communications Letters*, vol. 8, no. 5, pp. 1341–1344, Oct. 2019.

[84] C. M. Cheng, P. H. Hsiao, H. T. Kung, and D. Vlah, "Maximizing throughput of UAV-relaying networks with the load-carry-and-deliver paradigm," in *IEEE Wireless Communications and Networking Conference, WCNC*. IEEE, 2007, pp. 4420–4427.

[85] C. Li, S. Zhang, P. Liu, F. Sun, J. M. Cioffi, and L. Yang, "Overhearing protocol design exploiting intercell interference in cooperative green networks,"

IEEE Transactions on Vehicular Technology, vol. 65, no. 1, pp. 441–446, Jan. 2016.

[86] C. Li, H. J. Yang, F. Sun, J. M. Cioffi, and L. Yang, "Multiuser Overhearing for Cooperative Two-Way Multiantenna Relays," *IEEE Transactions on Vehicular Technology*, vol. 65, no. 5, pp. 3796–3802, May 2016.

[87] C. Li, P. Liu, C. Zou, F. Sun, J. M. Cioffi, and L. Yang, "Spectral-Efficient Cellular Communications with Coexistent One- and Two-Hop Transmissions," *IEEE Transactions on Vehicular Technology*, vol. 65, no. 8, pp. 6765–6772, Aug. 2016.

[88] K. Song, B. Ji, Y. Huang, M. Xiao, and L. Yang, "Performance Analysis of Heterogeneous Networks with Interference Cancellation," *IEEE Transactions on Vehicular Technology*, vol. 66, no. 8, pp. 6969–6981, Aug. 2017.

[89] K. Song, B. Ji, C. Li, and L. Yang, "Outage analysis for simultaneous wireless information and power transfer in dual-hop relaying networks," *Wireless Networks*, vol. 25, no. 2, pp. 837–844, Feb. 2019.

[90] C. Di Franco and G. Buttazzo, "Energy-aware coverage path planning of UAVs," in *Proceedings - 2015 IEEE International Conference on Autonomous Robot Systems and Competitions, ICARSC 2015*. IEEE, Apr. 2015, pp. 111–117.

[91] O. Arnold, F. Richter, G. Fettweis, and O. Blume, "Power consumption modeling of different base station types in heterogeneous cellular networks," in *2010 Future Network and Mobile Summit*. Florence, Italy: IEEE, 2010, pp. 1–8.

[92] H. Yan, Y. Chen, and S. H. Yang, "UAV-Enabled Wireless Power Transfer with Base Station Charging and UAV Power Consumption," *IEEE Trans-*

actions on Vehicular Technology, vol. 69, no. 11, pp. 12 883–12 896, Nov. 2020.

[93] Y. Chen, N. Zhao, Z. Ding, and M.-S. Alouini, "Multiple UAVs as Relays: Multi-Hop Single Link Versus Multiple Dual-Hop Links," *IEEE Transactions on Wireless Communications*, vol. 17, no. 9, pp. 6348–6359, Sep. 2018.

[94] R. I. Bor-Yaliniz, A. El-Keyi, and H. Yanikomeroglu, "Efficient 3-D placement of an aerial base station in next generation cellular networks," in *2016 IEEE International Conference on Communications, ICC 2016*. IEEE, May 2016, pp. 1–5.

[95] F. Tang, Z. M. Fadlullah, B. Mao, N. Kato, F. Ono, and R. Miura, "On A Novel Adaptive UAV-Mounted Cloudlet-Aided Recommendation System for LBSNs," *IEEE Transactions on Emerging Topics in Computing*, vol. 7, no. 4, pp. 565–577, Oct. 2019.

[96] X. Liu, Y. Liu, Y. Chen, and L. Hanzo, "Trajectory Design and Power Control for Multi-UAV Assisted Wireless Networks: A Machine Learning Approach," *IEEE Transactions on Vehicular Technology*, vol. 68, no. 8, pp. 7957–7969, Aug. 2019.

[97] F. Tang, Z. M. Fadlullah, N. Kato, F. Ono, and R. Miura, "AC-POCA: Anticoordination Game Based Partially Overlapping Channels Assignment in Combined UAV and D2D-Based Networks," *IEEE Transactions on Vehicular Technology*, vol. 67, no. 2, pp. 1672–1683, Feb. 2018.

[98] F. Tang, Y. Kawamoto, N. Kato, and J. Liu, "Future Intelligent and Secure Vehicular Network Toward 6G: Machine-Learning Approaches," *Proceedings of the IEEE*, vol. 108, no. 2, pp. 292–307, Feb. 2020.

[99] W. Feng, J. Wang, Y. Chen, X. Wang, N. Ge, and J. Lu, "UAV-Aided MIMO Communications for 5G Internet of Things," *IEEE Internet of Things Journal*, vol. 6, no. 2, pp. 1731–1740, Apr. 2019.

[100] J. Kakar, A. Chaaban, V. Marojevic, and A. Sezgin, "UAV-aided Multi-Way Communications," in *2018 IEEE 29th Annual International Symposium on Personal, Indoor and Mobile Radio Communications (PIMRC)*, vol. 2018-Septe. IEEE, Sep. 2018, pp. 1169–1173.

[101] J. I. Hernández-Vega, E. R. Varela, N. H. Romero, C. Hernández-Santos, J. L. S. Cuevas, and D. G. P. Gorham, "Internet of things (IoT) for monitoring air pollutants with an unmanned aerial vehicle (UAV) in a smart city," in *Lecture Notes of the Institute for Computer Sciences, Social-Informatics and Telecommunications Engineering, LNICST*. Springer International Publishing, 2018, vol. 213, pp. 108–120.

[102] E. Bertran and A. Sanchez-Cerda, "On the Tradeoff between Electrical Power Consumption and Flight Performance in Fixed-Wing UAV Autopilots," *IEEE Transactions on Vehicular Technology*, vol. 65, no. 11, pp. 8832–8840, Nov. 2016.

[103] S. H. Alsamhi, F. Afghah, R. Sahal, A. Hawbani, M. A. Al-qaness, B. Lee, and M. Guizani, "Green internet of things using UAVs in B5G networks: A review of applications and strategies," *Ad Hoc Networks*, vol. 117, Mar. 2021. [Online]. Available: https://arxiv.org/abs/2103.17043v1http://arxiv.org/abs/2103.17043

[104] A. Khalili, E. M. Monfared, S. Zargari, M. R. Javan, N. Mokari, and E. A. Jorswieck, "Resource Management for Transmit Power Minimization in

UAV-Assisted RIS HetNets Supported by Dual Connectivity," *IEEE Transactions on Wireless Communications*, pp. 1–1, Jun. 2021.

[105] A. Khalili, S. Zarandi, and M. Rasti, "Joint Resource Allocation and Offloading Decision in Mobile Edge Computing," *IEEE Communications Letters*, vol. 23, no. 4, pp. 684–687, Apr. 2019.

[106] S. Zarandi and H. Tabassum, "Delay Minimization in Sliced Multi-Cell Mobile Edge Computing (MEC) Systems," *IEEE Communications Letters*, vol. 25, no. 6, pp. 1964–1968, Jun. 2021.

[107] A. Khalili, S. Zargari, Q. Wu, D. W. K. Ng, and R. Zhang, "Multi-Objective Resource Allocation for IRS-Aided SWIPT," *IEEE Wireless Communications Letters*, vol. 10, no. 6, pp. 1324–1328, Jun. 2021.

[108] A. Al-Hourani, S. Kandeepan, and A. Jamalipour, "Modeling air-to-ground path loss for low altitude platforms in urban environments," in *2014 IEEE Global Communications Conference, GLOBECOM 2014*. IEEE, Dec. 2014, pp. 2898–2904.

[109] A. Al-Hourani and K. Gomez, "Modeling Cellular-to-UAV Path-Loss for Suburban Environments," *IEEE Wireless Communications Letters*, vol. 7, no. 1, pp. 82–85, Feb. 2018.

[110] M. Monemi and H. Tabassum, "Performance of UAV-Assisted D2D Networks in the Finite Block-Length Regime," *IEEE Transactions on Communications*, vol. 68, no. 11, pp. 7270–7285, Nov. 2020.

[111] P. Machura and Q. Li, "A critical review on wireless charging for electric vehicles," *Renewable and Sustainable Energy Reviews*, vol. 104, pp. 209–234, Apr. 2019.

[112] Y. Rathod and L. Hughes, "Simulating the charging of electric vehicles by laser," *Procedia Computer Science*, vol. 155, pp. 527–534, Jan. 2019. [Online]. Available: https://linkinghub.elsevier.com/retrieve/pii/S1877050919309871

[113] S. Anumula and A. Ganesan, "Wireless power charging of drone using vision-based navigation," *The Journal of Navigation*, vol. 74, no. 4, pp. 838–852, Jul. 2021.

[114] Y. Yan, W. Shi, and X. Zhang, "Design of UAV wireless power transmission system based on coupling coil structure optimization," *Eurasip Journal on Wireless Communications and Networking*, vol. 2020, no. 1, p. 67, Dec. 2020. [Online]. Available: https://jwcn-eurasipjournals.springeropen.com/articles/10.1186/s13638-020-01679-4

[115] Q. Zhang, W. Fang, Q. Liu, J. Wu, P. Xia, and L. Yang, "Distributed Laser Charging: A Wireless Power Transfer Approach," *IEEE Internet of Things Journal*, vol. 5, no. 5, pp. 3853–3864, Oct. 2018.

[116] "— Global Drone Regulations Database." [Online]. Available: https://droneregulations.info/index.html

[117] H. Yan, S.-H. Yang, Y. Chen, and S. A. Fahmy, "Optimum Battery Weight for Maximizing Available Energy in UAV-Enabled Wireless Communications," *IEEE Wireless Communications Letters*, vol. 10, no. 7, pp. 1410–1413, Jul. 2021. [Online]. Available: https://ieeexplore.ieee.org/document/9387395/

[118] H. Yan, Y. Chen, and S.-H. Yang, "New Energy Consumption Model for Rotary-Wing UAV Propulsion," *IEEE Wireless Communications Letters*, vol. 10, no. 9, pp. 2009–2012, Sep. 2021. [Online]. Available: https://ieeexplore.ieee.org/document/9461176/

[119] "UAV Engine Manufacturers — Propulsion Systems for UAVs, UGVs, AUVs, USVs — Unmanned Systems Technology." [Online]. Available: https://www.unmannedsystemstechnology.com/category/supplier-directory/propulsion-power/uav-engines-propulsion-systems/.

[120] J. K. Stolaroff, C. Samaras, E. R. O'Neill, A. Lubers, A. S. Mitchell, and D. Ceperley, "Energy use and life cycle greenhouse gas emissions of drones for commercial package delivery," *Nature Communications*, vol. 9, no. 1, p. 409, Dec. 2018.

[121] Z. Yang, C. Pan, K. Wang, and M. Shikh-Bahaei, "Energy Efficient Resource Allocation in UAV-Enabled Mobile Edge Computing Networks," *IEEE Transactions on Wireless Communications*, vol. 18, no. 9, pp. 4576–4589, Sep. 2019.

[122] M. K. Mohamed, S. Patra, and A. Lanzon, "Designing electric propulsion systems for uavs," in *Lecture Notes in Computer Science (including subseries Lecture Notes in Artificial Intelligence and Lecture Notes in Bioinformatics)*. Springer, Berlin, Heidelberg, 2011, vol. 6856 LNAI, pp. 388–389.

[123] T. Chang and H. Yu, "Improving Electric Powered UAVs' Endurance by Incorporating Battery Dumping Concept," *Procedia Engineering*, vol. 99, pp. 168–179, 2015.

[124] A. Abdilla, A. Richards, and S. Burrow, "Endurance optimisation of battery-powered rotorcraft," in *Lecture Notes in Computer Science (including subseries Lecture Notes in Artificial Intelligence and Lecture Notes in Bioinformatics)*. Springer International Publishing, 2015, vol. 9287, pp. 1–12.

[125] O. Gur and A. Rosen, "Optimizing Electric Propulsion Systems for Unmanned Aerial Vehicles," *Journal of Aircraft*, vol. 46, no. 4, pp. 1340–1353, Jul. 2009.

[126] H. V. Abeywickrama, B. A. Jayawickrama, Y. He, and E. Dutkiewicz, "Empirical Power Consumption Model for UAVs," in *IEEE Vehicular Technology Conference*, vol. 2018-August. IEEE, Aug. 2018, pp. 1–5.

[127] "Li-polymer Battery: Substance or Hype? – Battery University." [Online]. Available: https://batteryuniversity.com/learn/article/the_li_polymer_battery_substance_or_hype.

[128] M. Gatti and F. Giulietti, "Preliminary Design Analysis Methodology for Electric Multirotor," *IFAC Proceedings Volumes*, vol. 46, no. 30, pp. 58–63, 2013.

[129] S. Park, L. Zhang, and S. Chakraborty, "Design space exploration of drone infrastructure for large-scale delivery services," in *Proceedings of the 35th International Conference on Computer-Aided Design*, vol. 07-10-November-2016. New York, NY, USA: ACM, Nov. 2016, pp. 1–7. [Online]. Available: https://dl.acm.org/doi/10.1145/2966986.2967022

[130] J. Zhang, J. F. Campbell, D. C. Sweeney II, and A. C. Hupman, "Energy consumption models for delivery drones: A comparison and assessment," *Transportation Research Part D: Transport and Environment*, vol. 90, p. 102668, Jan. 2021.

[131] A. Thibbotuwawa, P. Nielsen, B. Zbigniew, and G. Bocewicz, "Energy Consumption in Unmanned Aerial Vehicles: A Review of Energy Consumption Models and Their Relation to the UAV Routing," in *Advances in Intelligent Systems and Computing*. Springer Verlag, Sep. 2019, vol. 853, pp. 173–184.

[132] C. W. Chan and T. Y. Kam, "A procedure for power consumption estimation of multi-rotor unmanned aerial vehicle," *Journal of Physics: Conference Series*, vol. 1509, no. 1, p. 012015, Apr. 2020.

[133] H. V. Abeywickrama, B. A. Jayawickrama, Y. He, and E. Dutkiewicz, "Comprehensive Energy Consumption Model for Unmanned Aerial Vehicles, Based on Empirical Studies of Battery Performance," *IEEE Access*, vol. 6, pp. 58 383–58 394, 2018.

[134] Z. Liu, R. Sengupta, and A. Kurzhanskiy, "A power consumption model for multi-rotor small unmanned aircraft systems," in *2017 International Conference on Unmanned Aircraft Systems, ICUAS 2017*. IEEE, Jun. 2017, pp. 310–315.

[135] N. Gao, Y. Zeng, J. Wang, D. Wu, C. Zhang, Q. Song, J. Qian, and S. Jin, "Energy Model for UAV Communications: Experimental Validation and Model Generalization," May. 2020. [Online]. Available: http://arxiv.org/abs/2005.01305

[136] A. Bramwell, G. Done, and D. Balmford, *Bramwell's Helicopter Dynamics*, 2nd ed. Jordan Hill, Oxford, UK : Butterworth-Heinemann, 2001.

[137] X. Jiang, M. Sheng, N. Zhao, C. Xing, W. Lu, and X. Wang, "Green UAV communications for 6G: A survey," *Chinese Journal of Aeronautics*, May 2021.

[138] X. You, C.-X. Wang, J. Huang, X. Gao, Z. Zhang, M. Wang, Y. Huang, C. Zhang, Y. Jiang, J. Wang, M. Zhu, B. Sheng, D. Wang, Z. Pan, P. Zhu, Y. Yang, Z. Liu, P. Zhang, X. Tao, S. Li, Z. Chen, X. Ma, C.-L. I, S. Han, K. Li, C. Pan, Z. Zheng, L. Hanzo, X. S. Shen, Y. J. Guo, Z. Ding, H. Haas, W. Tong, P. Zhu, G. Yang, J. Wang, E. G. Larsson, H. Q. Ngo, W. Hong,

H. Wang, D. Hou, J. Chen, Z. Chen, Z. Hao, G. Y. Li, R. Tafazolli, Y. Gao, H. V. Poor, G. P. Fettweis, and Y.-C. Liang, "Towards 6G wireless communication networks: vision, enabling technologies, and new paradigm shifts," *Science China Information Sciences*, vol. 64, no. 1, p. 110301, Jan. 2021.

[139] S. Suman, S. Kumar, and S. De, "Impact of Hovering Inaccuracy on UAV-Aided RFET," *IEEE Communications Letters*, vol. 23, no. 12, pp. 2362–2366, Dec. 2019.

[140] G. Skorobogatov, C. Barrado, and E. Salamí, "Multiple UAV Systems: A Survey," *Unmanned Systems*, vol. 08, no. 02, pp. 149–169, Apr. 2020.

[141] L. Shi, N. J. H. Marcano, and R. H. Jacobsen, "A Survey on Multi-unmanned Aerial Vehicle Communications for Autonomous Inspections," in *2019 22nd Euromicro Conference on Digital System Design (DSD)*. IEEE, Aug. 2019, pp. 580–587.